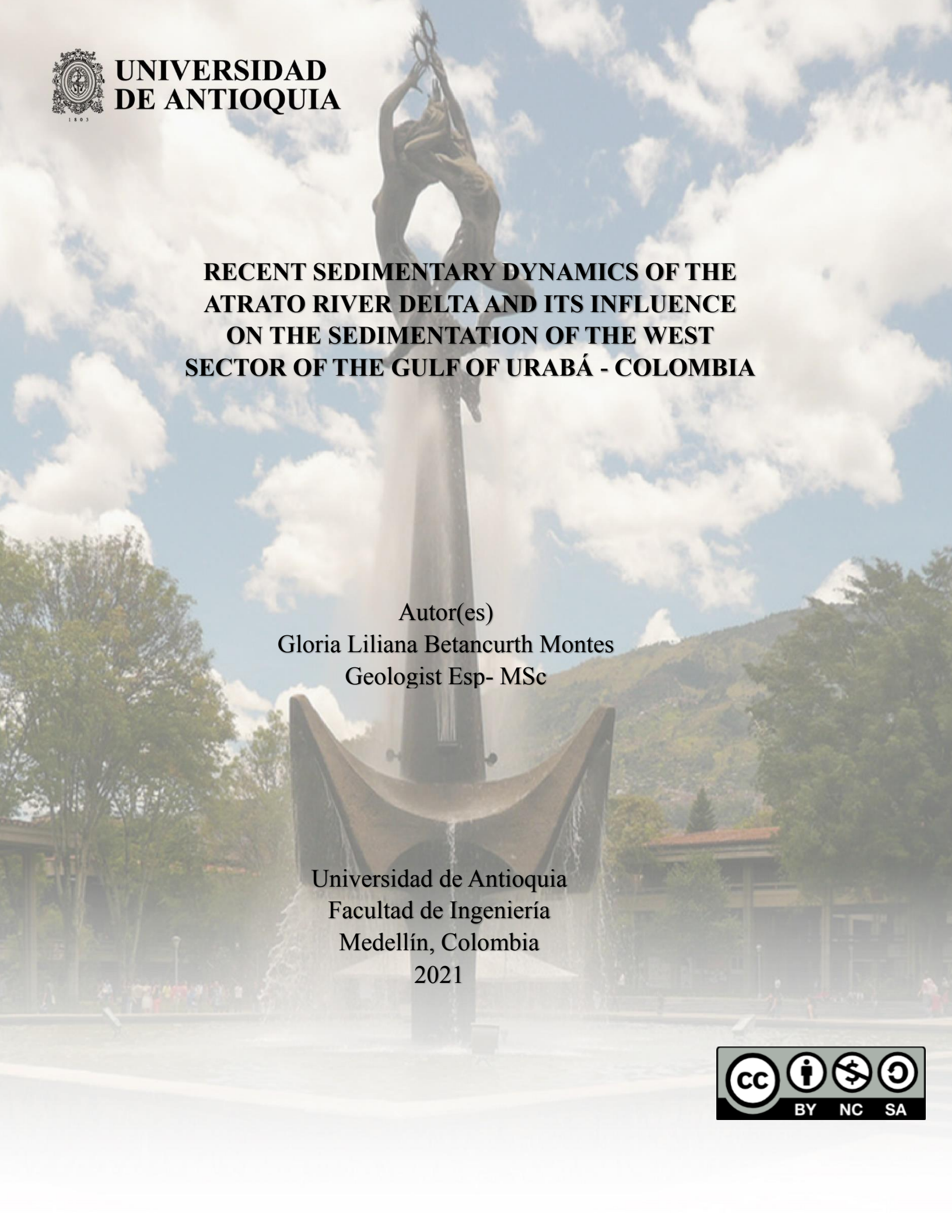

UNIVERSIDAD DE ANTIOQUIA

RECENT SEDIMENTARY DYNAMICS OF THE ATRATO RIVER DELTA AND ITS INFLUENCE ON THE SEDIMENTATION OF THE WEST SECTOR OF THE GULF OF URABÁ - COLOMBIA

Autor(es)
Gloria Liliana Betancurth Montes
Geologist Esp- MSc

Universidad de Antioquia
Facultad de Ingeniería
Medellín, Colombia
2021

RECENT SEDIMENTARY DYNAMICS OF THE ATRATO RIVER DELTA AND ITS INFLUENCE ON THE SEDIMENTATION OF THE WEST SECTOR OF THE GULF OF URABÁ

Gloria Liliana Betancurth Montes

Tesis o trabajo de investigación presentada(o) como requisito parcial para optar al título de:

Doctor en Ingeniería Ambiental

Asesores (a):

Julio Eduardo Cañón Barriga, MSc., PhD.

Línea de Investigación:

Geología ambiental

Grupo de Investigación:

Gestión y Modelación Ambiental GAIA

Universidad de Antioquia

Facultad, de Ingeniería

Medellín, Colombia

2021

Contents

List of figures

List of tables

List of Appendices

Agradecimientos

Desde lo más profundo de mi corazón, agradezco primeramente a la fuerza invisible de todo lo creado, a quien yo llamo Dios.

Agradezco a incontables personas que estuvieron rodeándome en lo académico, lo emocional, lo espiritual, lo material y, en mis más grandes momentos de querer desfallecer. Aquí voy…….

A mi asesor el Dr. Julio Eduardo Cañón por las grandes contribuciones, su extremada paciencia y ecuanimidad.

A la Dra. María Teresa Florez por abrirme el camino y acompañarme en una parte del trayecto.

Agradezco a la Universidad de Antioquia, a El grupo GAIA y a Colciencias por las facilidades administrativas, académicas, económicas y de laboratorio.

A el Dr. Frank Preusser, la Dra. Claire Rambeau, el Dr. Francisco Molina, a mis revisores por tan valiosos comentarios Dra. Valentina Flórez, Dr. Mark Brenner, Dr. Ferreol Solomon.

A Jhon Jairo Ramírez, mi mano izquierda y derecha en campo, por reir de mis desfachateces y por la guitarra en las noches cansadas frente al Río.

A mi esposo y compañero de vida Jorge Molina y a mis dos grandes amores Amelia y Luis Santiago por comprender mis ausencias y acompañarme hasta el "por allá", ellos saben cuánto, pero cuánto los amo.

A mi madre Gabriela, mi hermana Luz Marina, mi hermano Jaime y con ellos, al resto de mis hermanos siempre presentes con su confianza y apoyo durante toda mi vida. Los amo.

A mi parcero Fredy Amaringo por el mutuo apoyo y los valiosos chistes a las 3 am, a Juan Diego Correa, Tatiana Correa, María Cecilia Plested, a mi Gurú Ana María Monsalve.

A mi gente del Delta del Atrato, amorosa, entregada, alegre, fieles guías. Ellos hicieron más que posible este trabajo: Elimeleth Santos, Patrocinio Cuesta, Luis Angel Cuesta y a las comunidades de Bocas del Atrato, Marriaga y el Roto, solo tengo sus sonrisas plasmadas en mis recuerdos.

Río Atrato, te agradezco con mi alma por permitirme nadar en tus aguas, conocer tus sedimentos y sentir esa fuerza deslumbrante de la naturaleza.

Gracias a todos los demás, ellos saben quiénes son, aunque no los nombre en esta lista.

Me agradezco por tener el ímpetu de hacer esta investigación, en las largas jornadas que parecían no acabar.

Acknoledgments

From the bottom of my heart, I first thank the invisible force of all creation, whom I call God.

I thank countless people who have surrounded me academically, emotionally, spiritually, matter, and in my greatest moments of wanting to faint. Here I go…….

To my advisor Dr. Julio Eduardo Cañón for his great contributions, his extreme patience and equanimity.

To Dr. María Teresa Florez for opening the way for me and accompanying me on part of the journey.

I thank the University of Antioquia, the GAIA group and Colciencias for the administrative, academic, economic and laboratory facilities.

To Dr. Frank Preusser, Dr. Claire Rambeau, Dr. Francisco Molina, and my reviewers Dr. Valentina Flórez, Dr. Mark Brenner, Dr. Ferreol Solomón for such valuable comments.

To Jhon Jairo Ramírez, my left and right hand in the field work, for laughing at my impudence and for the guitar on the tired nights in front of the River.

To my husband and partner of life Jorge Molina and to my two great loves Amelia and Luis Santiago for understanding my absences and accompanying me to "over there", they know how much, but how much I love them.

To my mother Gabriela, my sister Luz Marina, my brother Jaime and with them, the rest of my brothers always present with their trust and support throughout my life. I love you.

To my partner Fredy Amaringo for the mutual support and the valuable jokes at 3 am, to Juan Diego Correa, Tatiana Correa, María Cecilia Plested, to my Guru Ana María Monsalve.

To my people of the Delta del Atrato, loving, dedicated, cheerful, faithful guides. They made this work more than possible: Elimeleth Santos, Patrocinio Cuesta, Luis Angel Cuesta and the communities of Bocas del Atrato, Marriaga and el Roto, I only have their smiles reflected in my memories.

Río Atrato, I thank you with my soul for allowing me to swim in your waters, know your sediments and feel that dazzling force of nature.

Thanks to everyone else, they know who they are, even if I do not name them on this list.

I thank myself for having the impetus to do this research in the long journeys that did not seem end.

Abstract

Sedimentary dynamics of the Atrato River Delta (ARD) have geographic, environmental, social and economic significance in this coastal region of Colombia. Complex tectonic and climatic factors formed this delta, with the notoble influence of active faults and relative sea level fluctuations. This thesis provides an interpretative framework to understand late Holocene sedimentation patterns in the ARD and the effects of deposition throughout the western sector of the Gulf of Urabá. To develop this framework, an extensive field survey was conducted in the delta, during which 95 surface sediment samples were collected from the main Atrato River tributaries and six sediment cores we drilled in three swamps and three bays within the delta. Surface samples and sediment cores were analyzed for grain size, mineralogy and geochemistry. Samples were dated and facies described, and all data were used to identify sites of erosion and progradation, sediment provenance, transport regimes and sediments distribution, organic carbon content, weathering intensity, depositional processes and an approach for the paleoenvironmental history of the delta. Ages of surface and shallow sediments in fluvial, lagoonal and marine environments were determined with Infrared Stimulated Luminescence (IRSL), which is a novel technique for this kind of tropical environment. Surface sediments were characterized by fine sandy in the south at floodplain and fine silts and clays toward the north of the delta towards lower delta plain and delta front, with a generally poor sorting. Mineralogical analysis revealed quartz, feldspars, plagioclase, clay minerals, pyroxenes, micas and oxides, reflecting the heterogeneity of bedrock sources. Discriminant diagrams, plotted using the major elements, show sediments derived mostly from rocks formed in the Oceanic Island Arc towards the Continental Island Arc. The chemical index of alteration (CIA) suggests that ARD sediments experienced predominantly intermediate to high chemical weathering effects. Enrichments of Zn, Ni, Cu and Cr along the delta have both natural and anthropogenic causes. Several facies were defined after sediment cores analysis. These facies show alternations of dry and humid periods, with a dominant marine pattern in the late Holocene, between ~1620±130 and ~870±70 a , during which here was waves reworking, under a low to moderate energy fluvial domain, denoted by sandy - silt sediments interbedded with peaty layers. A transitional period with more microtidal effects, but continuous fluvial dominance, was identified between ~ 870±70 a, and ~550±50 a, represented by silty sediments, low organic matter content and shell fragments. The last period indicates a fluvial episode between ~550± 50 a and present, but with some marine incursions, characterized by finer sediments, intermittent coarse sediments and organic matter layers. Grain size, mineralogy and geochemistry of facies enabled inference about past relative sea levels, which dropped during late Holocene to very recent times, but reflect a soft current sea level rise over the delta. Data acquired in this study provided the basis for characterizing sediment dynamics of the ARD, identifying sediment sources, the dominant transport regime and interpreting influence of climate in the late Holocene. The primary data and interpretations from this research constitute an important source of geological and environmental information for future studies in the Urabá region.

I. General framework

Deltas are landforms with great power for natural landscape transformation. This transformation is caused by hydrodynamic energy and geological factors at relatively short geological time scales (Wang et al., 2018; Maselli et al., 2014; Longhitano and Colella, 2007). The short geological changes are measured in months, years, decades or centuries (Vespremeanu-Stroe et al., 2017; Clarke et al., 2014). River delta dynamics are complex and significant in terms of the important influence they have on fluvial and oceanic features because of erosion, sedimentation and morphometric changes (Massuanganhe et al., 2018; Darwishet al., 2017). Research on delta dynamics has increased in the last decades, due to the drastic landscape erosion and progradation changes evidenced in some deltas worldwide in the last century (He et al., 2019; Li et al., 2017; Ballester, 2015).

The Atrato River Delta (ARD), in Colombia, serves as an ideal case of increased erosion, progradation and sedimentation changes over the few centuries. These changes have been identified by several geomorphological and hydrodynamical studies (Blanco-Libreros, 2016; Escobar et al, 2015; Post, 2011; Nieto-Oliveros, 2004), with a special focus on the significant influence of sedimentation in the Gulf of Urabá, mainly supported by hydrodynamic studies (Velazquez, 2013; Escobar, 2011; Bernal, 2007). Nonetheless, there have been no studies aimed at understanding the recent evolution of the sedimentation dynamics of this delta based on the physicochemical and mineralogical characterization of sediments, the analysis of dispersion patterns of the sediments, and the analysis of facies in shallow deposition stratigraphical successions.

The general sedimentation of the ARD in the Gulf of Urabá is evident along its southwest coast. Velásquez (2013) identified the clogging of the Atrato River channels (which hinders the sea-river transport of passengers and cargo) and the decrease of the seabed depth as drivers of very rapid morphological changes that require significant economic investments in dredging. These dredging investments have little technical or scientific justification supported by knowledge of the fluvial and marine sedimentary dynamics.

Previous studies did not emphasize in the characterization of the ARD sediment grain sizes (coarse fraction and fine fraction), mineralogy, geochemistry, geological ages, facies and distribution and the sedimentary stratigraphical successions. This lack of knowledge precludes understanding the evolution and recent sedimentary dynamics of the ARD, leading to the following research questions:

- What is the nature of the sediments accumulated in the main body of the delta?
- Which kind of sediments reaches the interface or delta front at the Gulf of Urabá?
- How do changing morphology, sediment supply and delta dynamics affect the western side of the Gulf of Urabá?
- How did the recent historical sedimentation of the last 2.000 years occur in the ARD?
- What is the conceptual model of the delta´s late Holocene sedimentation based on the analysis of facies?

This thesis provides an interpretative framework to respond to these questions and aims to understand the recent sedimentation patterns of the ARD and the effects of their

deposition over the western sector of the Gulf of Urabá. To achieve this interpretative framework, the author conducted an extensive fieldwork survey in the delta to collect surface sediment samples from the main Atrato River tributaries and drill six sediment cores at three swamps and three bays within the delta. The author conducted the analysis of grain size variations by laser diffraction approach; the semiquantitative analysis of bulk mineralogical composition of the non-clay fraction with X-Ray Difraction-XRD, the geochemical analysis of the total sample with X-Ray Fluorescence; and dating of surface and shallow sediments with the Infrared Stimulated Luminescence (IRSL) technique.

These analyses were the basis to determine the type of sediments distributed along the delta and discharged into the west side of the Gulf of Urabá; the sediment transport patterns; the sediments composition and provenance; the main shallow facies; and a conceptual explanation of the late Holocene and recent sedimentary dynamics of the Atrato Delta.

II. Thesis aim

The aim of this research was to establish the recent sedimentary dynamics (late Holocene) of the Atrato River Delta and its influence on the proximal sedimentation of the west side of the Gulf of Urabá.

III. Specific objectives

To attain the aim, the thesis developed the following objectives:

1) Characterize the grain size, mineralogy, geochemistry and age of surface and shallow sediments of the ARD.

2) Interpret the sedimentation processes of the ARD through the stratigraphy and sedimentological facies in shallow cores.

3) Develop a conceptual scheme to explain the sedimentary dynamics of the ARD

IV. General research question

What sedimentary patterns characterize the surface and shallow sediments that conform the Atrato River Delta?

V. Main reseach hypothesis

The contrasting hypotheses underlying this thesis are: 1) the sedimentary patterns of the ARD in the late Holocene were the result of a uniform, progressive advance of the Atrato River sediment loads as the dominant formative process, or 2) the result of non-uniform, interactive fluvial-marine processes with clear episodes of marine variations recorded in the sedimentary stratigraphical successions.

VI. Document structure

The thesis consists of four main chapters. The first chapter (structured as an article, currently under final revision for publication in the Journal *CATENA*, describes the recent sedimentary dynamics of the delta through the analysis of grain size, mineralogy and geochemistry features of 60 samples of surface sediments taken along current arms of the ARD.

The second chapter (structured as an article, already published in the *Journal of South American Earth Sciences*), describes the dating of surface and core samples, using the Infrared Stimulated Luminescence (IRSL) dating for the first time in sediments of the ARD. This dating constitutes a novel method to date fluvial sediments, useful because of the lack of accuracy for ^{14}C in this kind of environment.

The third chapter (structured as an article submitted for publication in *The Holocene Journal with complements from other article in press in Revista Neogranadina)*, addresses the findings of the previous chapters to interpret facies and proposes a conceptual approximation to the late Holocene sedimentological model in the transition between fluvial and marine environments.

The fourth chapter contains the conclusions of this thesis, divided in terms of each of the objectives attained.

To facilitate the reading of the document, all references are presented after the chapter of conclusions. Furthermore, most of the detailed databases from samples and laboratory analysis, which themselves constitute a contribution to knowledge for the delta, are included as appendices at the end of the document.

1. Chapter 1: Recent sedimentary processes of the Atrato River Delta based on physicochemical characterization of surface sediments

Liliana Betancurth[1], Julio Cañón[1]

[1] *Grupo de Gestión y Modelación Ambiental -GAIA-, Facultad de Ingeniería, Universidad de Antioquia; Medellín, Colombia.*

1.1 Abstract

We studied the modern sedimentation patterns in the Atrato River Delta (ARD) through the analysis of grain size, mineral abundances, chemical weathering and concentrations of major and trace elements in 60 surface sediment samples taken from a novel field survey in the delta over the combination and connection of river beds, floodplains swamps, coastline, and delta front environments. The delta area was divided into six sectors, to cover the main and secondary channels of the ARD and the western side of the Gulf of Urabá, elsewhere related to fluvial and marine environments. Results show that surface sediments of the ARD are heterogeneous in their sedimentary dynamics among sectors and environments, from upstream towards the Gulf of Urabá. Sediments grain size pattern decreases from inner land, in the floodplain towards the bays into Gulf of Urabá. Grain size varies from very fine silt to fine sand (3.123 - 139.3 μm) and from moderately well (0.525 ϕ) to very poorly sorted (2.681 ϕ), from upper delta plain to delta front. Transport regime in the ARD is variable from traction inland, to suspension in the north sector, with the predominance of saltation in the central and east sectors, in the lower delta plain. Mineralogical analysis of sediments shows a dominant mineral phase of quartz, followed by feldspars and plagioclase, clay minerals, pyroxenes, micas and Fe-Mg and Ti oxides, indicative of the heterogeneity of bedrock sources and a mineral distribution affected by sorting, weathering and mineral density. The geochemical composition, compared to Upper Continental Crust (UCC) values and regional geochemistry, shows a depletion of SiO_2, Na_2O, CaO and K_2O, representing significant dilution processes along the delta. The high abundances of other oxides (Al_2O_3, Fe_2O_3, MgO, TiO_2, P_2O_5 and MnO), by contrast, imply oxidation processes and moderate to high weathering. Relatively high concentrations of Organic Carbon (OC), Cl, Na, P and S mainly at bays, indicates the occurrence of a saline wedge and reflect the organic matter degradation, oxidation processes, marine productivity and sediments reworking towards the Gulf of Urabá. The concentrations of heavy metals (Zn, Ni, Cu, Co and Cr) remain high along the delta and indicate both natural and anthropogenic contributions. The tectonic setting and provenance designate the Oceanic Island Arc (OIA) as the main source of sediments. The results offer new insights about sediments type and distribution, transport regime, degree of weathering, tectonic setting and provenance, sediments geochemical classification and reworking, heavy mineral enrichments and the contributions to marine bioproductivity, and are helpful for the modern sedimentary dynamics in the active Atrato River Delta.

Keywords: Atrato River Delta, surface sediments, transport regime, provenance, sedimentary dynamics.

1.2 Introduction

Sediments are the product of the combined effect of factors such as rocks weathering and erosion, catchments morphology and hydrological regimes, transport pathways, mineralogy, geochemical features and reworking (Ouillon, 2018; Guagliardi et al., 2013, Grunsky et al., 2009; Lottermoser, 2007). Sediment sampling is first step in studying grain size, mineralogy and geochemistry for the determination of provenance, history of ancient sedimentary environments and for the interpretation of sedimentation patterns in continental, marine and transitional environments (Li et al., 2019; Viseras et al., 2009).

River sediments in particular, provide an invaluable information on mobility and deposition dynamics, while being indicators of climatic, morphological and anthropic changes (Bhuiyan et al., 2011). Fluvial systems and their deltas transport the weathered materials from high mountains to deltas and oceans (Latrubesse et al., 2005). These fluvial systems and their watersheds are studied to determine patterns of fluvial and sedimentary dynamics of entire basins (Sawakuchi et al., 2018). Deltas are landforms of interest to study geological records linked to oscillations of sea level and environmental changes especially those that occurred in the Holocene (Mateo and Siringan, 2016; Korus and Fielding, 2015; Maselli et al., 2014). Several studies worldwide focused on describing and interpreting sediment deposition mechanisms in deltas, to understand the evolution patterns that occur in these landforms, caused by multiple natural and anthropic factors (Dunn et al., 2018; Olariu and Zeng, 2018; Pennington et al., 2017).

The Atrato River Basin carries a substantial amount of sediments (Montoya, 2010; Álvarez and Bernal, 2007; Restrepo and Kjerfve, 2000) and has a remarkable transport capacity in terms of water discharge and sediment loads (Velásquez and Poveda, 2016; Molina et al., 2014). For instance, the Atrato's ratio of average water discharge to catchment area could be five to six times greater than the ratio for the Amazon River (Escobar et al., 2015; Poveda and Mesa, 1997). Atrato's average discharge has been estimated to range between 4,138 m^3/s (Velásquez, 2013) and 2,174 m^3/s (Velásquez and Poveda, 2016), and the estimated sediment load around 315 $t/km^2/yr$ (Restrepo and Kjerfve, 2000). Sediments transported by the Atrato River end up forming a "bird foot" inner delta over the western flank of the Gulf of Urabá. This river bifurcates into several channels and forms new land in a constant progradation process towards the Gulf, with an erosion occurring along shorelines.

Research in the Atrato River Delta (ARD), has mainly focused on understanding the delta's geomorphology, morphodynamics, and the relationship between vegetation and sediments dispersion (Blanco, 2016; Post, 2011; López and Restrepo, 2007; Nieto-Oliveros-Oliveros, 2004; Vann, 1959). Other studies have focused on the hydrodynamic transport in the Gulf of Urabá, highlighting the direct influence of the sediment plumes from the Atrato into the Gulf (Velásquez, 2013; Escobar, 2011; Álvarez and Bernal, 2007; Bernal et al., 2005).

In the analysis of coastal erosion in the Colombian Caribbean, Posada and Henao (2008) included a characterization of the ARD shoreline. Vélez and Aguirre (2016), determined the influence of the Atrato River on the Gulf of Urabá during the late Holocene, based on the analysis of sediments, total organic carbon TOC, total nitrogen TN, total phosphorus TP, biogenic silica BSi, calcium carbonate $CaCO_3$ and diatoms in two sediment cores taken

on the Gulf. Furthermore, Palacio-Torres et al (2019) and Vallejo et al. (2016) analyzed the impact of terrestrial mining in surface sediments and the historic sediment loads from the Atrato River.

To our knowledge, no other study has focused on sampling and understanding the modern sedimentary dynamics of the ARD by means of analysis of the grain size, mineralogy and geochemistry of surface sediment samples. In this regard, we conducted the first large-scale sedimentary characterization of this delta, aiming at understanding its modern sedimentary processes and dynamics.

1.3 Study Area

The ARD is located in the northwestern part of continental Colombia (between 8° 00" N; 77° 20" W and 8° 15" N; 7° 56" W) (Figure 1.1). This delta is part of a hydrographic basin with an approximate area of 38,000 km^2. The Atrato River flows along 700 km from its headwaters at Plateado hill to the Gulf of Urabá, with a total elevation gradient of 3,000 m. The basin catches sediments from an extensive network of tributaries, composed of 50 rivers and 300 streams (INVEMAR, 2017; Banco de Occidente, 2007). This network provides heterogeneous materials that finally flow into the Gulf of Urabá in the Caribbean Sea (Restrepo, 2014).

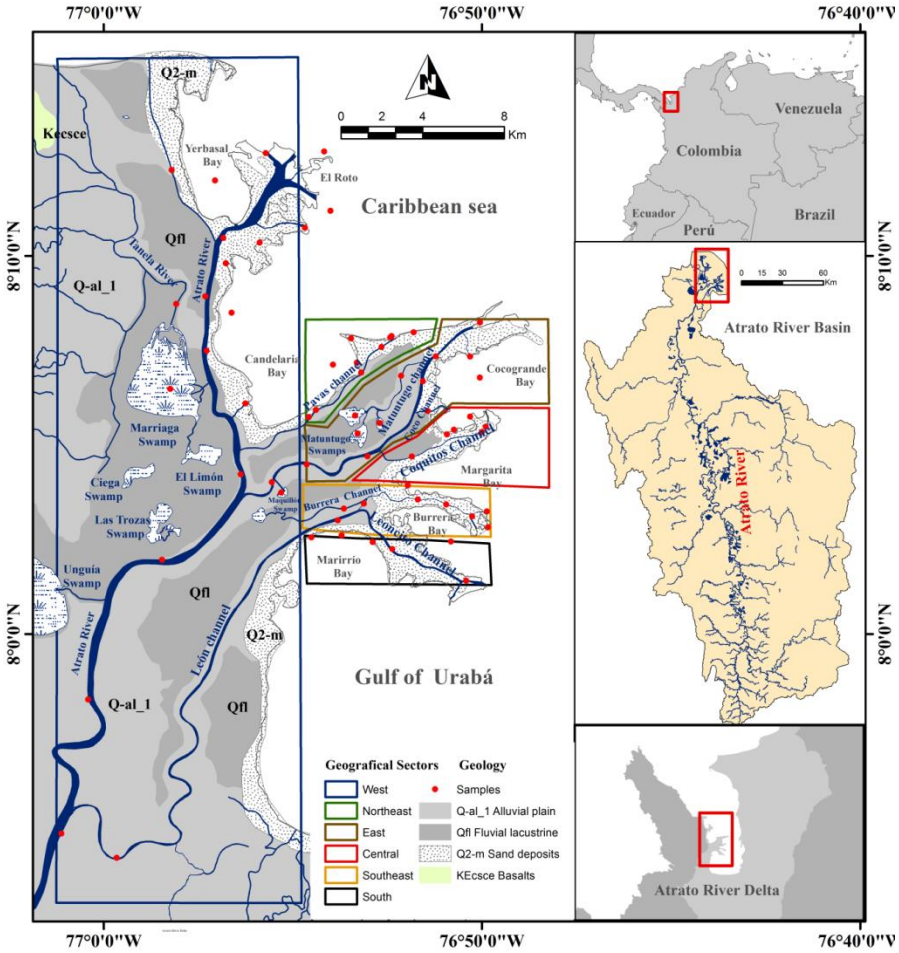

Figure 1.1 Location of collected surface sediment samples in the Atrato River Delta, distributed in geographic sectors.

According to the most accepted classification (Galloway, 1975), the ARD is a "bird foot" type delta, composed of seven main channels that flow into the Gulf of Urabá, and of approximately 11 minor or intermittent channels (closed and connected to the sea in the last 200 years) (Thomas et al., 2007; Nieto-Oliveros, 2004). Some of these channels are navigable, deep enough to enable passage of vessels for cargo transport and passengers to and from the town of Turbo to areas upstream in the the Atrato River (Post, 2011).

The climate in the ARD responds to the Intertropical Convergence Zone (ITCZ), characterized by a dry period between December and February and a rainy period between March and November (Restrepo and López, 2008; Poveda, 2004). Average annual rainfall ranges between 2.500 mm and 3.000 mm and the annual average temperature is 33.8° C, with maxima of 39° C and minima of 16° C (values estimated from stations Sautatá, Turbo, Tanela and Titumate, provided by IDEAM, 2018). The relative humidity varies monthly, displaying a peak in November (86%) and a low in February (80%) (Thomas et al., 2007).

Waves are very variable and strongly influenced by climatic conditions in the Caribbean Sea, especially in the northwest sector of the delta and the Gulf of Urabá (Osorio et al, 2010). Wind patterns throughout the year are bimodal, being stronger in the north and northwest during the dry season and in the south and southwest during the rainy season (Montoya et al., 2010; Roldán, 2007). Tides in the Gulf of Urabá are semidiurnal, with maximum amplitudes of approximately 0.4 m (Correa and Vernette, 2004). Microtides periodically affect the river currents that arrive from the Atrato Delta into the Gulf of Urabá, reversing the river currents towards inland, taking advantage of the low land as observed during field work.

Sea currents in the area vary in response to several factors in the Gulf of Urabá, such as salt stratification and in combination with the phenomenon of advection (flow transport) of the river near the mouths (Escobar, 2011; Montoya, 2010). Surface currents tend to be strong, with maximum and average values of 1.12 m/s and 0.34 m/s, respectively. The velocity of the current decreases progressively with depth, reaching maximum and average speeds < 0.56 and 0.1 m/s (Escobar et al., 2015).

Bedrock in the ARD consists of igneous rocks of basaltic, tonalite and granodiorite composition (Lugo et al., 2003) in the west; basaltic lavas and tuffs intermingled with a variety of sedimentary rocks such as cherts, marls, limestones, mudstones, siltstones and fine sandstones in the southwest (Rodríguez and Zapata, 2012; Bedoya et al., 2007). Towards the west of the ARD there are outcrops of sedimentary marls, claystones, detritic limestones and sandstones composition (Zapata, 2002). Large Quaternary deposits of alluvial and lacustrine nature form the main Atrato River flood plain along the east-central edge of the ARD (Blanco-Libreros, 2016; Post, 2011).

The geomorphological units in the ARD are framed in litoral morphology, controlled by tectonics, fluvial dynamics and marine influence in a combined erosive and accretional pattern (Robertson and Martínez, 1999). Some authors claim a slow growth of the ARD, compared to other smaller deltas present in the eastern of Urabá Gulf and the ocean drift, which does not allow the distribution of atrato river sediments along it (Thomas et al., 2007; Nieto-Oliveros, 2004; Robertson and Martinez, 1999). These claims are supported by historical mapping observations of satellite images and ancient maps, dating from 1817 to 1846 (IGAC, 1985). These maps show a relative stability of this geoform over the past 170 years. The most significant change is the influence on Boca Tarena, which was

replaced by the direct flow of Atrato River to the sea in the El Roto sector, which is not visible on the ancient maps of IGAC. There is also a marked coastal erosive trend in the drainage basins of the Atrato River, supported by the finding of higher sedimentation rates to the northeast of the gulf and not to the proximal area of the delta (Agudelo and Aguirre, 2016).

The location of the ARD could be related to a phenomenon of vasculation or subsidence of sedimentary stratigraphical succession to the west (Chevillot et al., 1993). The tectonic influence could produce a process of "sinking", possibly due to the deposit of river and marine sludge sediments. Both situations incorporate a low probability of the gulf closing, due to sedimentation caused by the Atrato River Delta (Robertson and Martínez, 1999). Nonetheless, the effect of the ARD in the Gulf of Urabá is supported by different hydrodynamic studies developed in the gulf, in terms of the contribution of Atrato River sediments to the system from Bahía Colombia towards the north, and of the decrease in kinetic energy exerted by the currents in the Northwest sector (Escobar, 2011).

From grain size studies of surface sediments, sand deposition was corroborated in the delta mouths (Alvarez and Bernal, 2007), which confirms the relative occurrence of the phenomenon of acretion on the deltaic front. However, the north-south direction of sediment transport casts doubt on the constant deposit of sediments in this delta sector. A cross-cutting factor to the development of the delta is the relative sea level decline around 2400 years ago (Robertson and Martínez, 1999) that had favored the progradation in the northeast direction, that has possibly increased in the last 200 years, with the growth of anthropic activities related to logging and mining (Agudelo and Aguirre, 2016).

The ARD comprises two main geomorphological units: the fluvio-marine plain and the intertidal zone. These units incorporate the alluvial plain, the swamps and marshes (vegetated intertidal planes) of sludge type, and beaches (Blanco, 2016; CIOH, 2008; Thomas et al., 2007). One of the most influential factors in the sedimentary dynamics of the delta is the filling of bays with sediments through cracks, related to the activity of the mouths of the Atrato River, especially in periods of floods (Van, 1959).

The apex of the delta is located at the beginning of the Leon Channel, which bifurcates from the main course of the Atrato River. The León channel exhibits a continuity of approximately 21 km to the northeast, without presenting any significant bifurcations until connecting with the Leoncito channel.

The arms of the southeastern part of the delta (Pichindí, León, Big Coconut, Coco and Matuntugo) carry a portion of the discharge that slowly extends to the sea (Van, 1959). The largest discharge occurs to the north, at the El Roto mouth. Two important channels were recently filled by vegetation and sediments (Pavas and Tarena). Boca Tarena was the main canal until the late 1900s in the northwest section of the Delta, and the Pavas channel in the northeast (Vann and Vannl, 2010; Thomas et al., 2007). The map shows the main geomorphological classification of the ARD in detail (Appendix 1).

Floodplain: this unit is very wide and constitutes the formation of coastal land towards the gulf, due to the accumulation of sediments from the Atrato River. It has a very uniform and flat topography, slightly above sea level. The plain is characterized by the presence of mud-sandy sediments that are deposited in low-energy areas, which form natural dams, especially in flood episodes, when flows increase considerably (Blanco, 2016).

Swamps and marshes: also known as vegetated intertidal planes are the most extended geomorphological unit of the delta, consisting of swamps, marshes and mangrove belts. The unit is located at a relatively lower level than the sea and has flooding zones.

Beaches: the beaches are small and narrow, very contingent on the tidal action and the erosive processes of the bays. Those alternate with mangrove areas.

1.4 Materials and methods

1.4.1 Sediments sampling

We carried out a sampling campaign in November-December of 2017 (Appendix 2). Based on topographic charts of the National Geographic Institute of Colombia - IGAC, scale 1: 25,000, we delimited the delta area in a rectangle of 25 × 15 km, covering 375 km^2. This area included the main river channel and the secondary channels León, Leoncito, Burrera, Coco, Coquitos, Matuntugo and Pavas; the Maquillón, Matuntugo, Marriaga and El Limón Swamps; and the Marirrio, Burrera, Candelaria and Yerbasal Bays. We defined six rectangles within the main area to facilitate further physicochemical analysis by geographic sectors (Figure 1.1).

We defined the six geographical sectors in relation to the river flow direction, considered here as the main driver of sediments deposition and the main contributor of sediments to the the distributary channels, where some of them also include swamps and conform the connection to the bays. The west sector include all the samples distributed along the main Atrato River channel; Marriaga Swamp, Tanela Inlet and El Roto. The northeast sector includes the area drained by Pavas channel and Candelaria Bay. The east sector includes the zone drained by Matuntugo and Coco channels, Matuntugo Swamp and Cocogrande Bay. The central sector comprises the drained area of Coquitos Channel and Margarita Bay. The southeast sector includes the Burrera channel, half of Leoncito Channel and Burrera Bay. Finally, the south sector includes Leoncito Channel and Marirrío Bay.

Overall, we collected 95 surface sediment samples (including duplicates), with an Eckmam dredge (2 - 4 kg weight, at 3 - 5 m water depth). We took 35 samples in the marine area (corresponding to sediments from the Burrera, Candelaria, Margarita, La Paila, Yerbasal, Marirrio and Los Indios Bays); 7 samples in swamps (Matuntugo, Maquillón, Marriaga and El Limón); and 53 samples in main channels (Atrato River, Coco, Coquitos, León, Leóncito, Burrera, Matuntugo, Pavas and Tanela) (Figure 1.1).

We labeled each sample with the code DA (Delta Atrato), followed by a number relative to the sampling. We placed the samples in clear, sealable plastic bags, stored them in Staofoam refrigerators and transported them by car to the GAIA laboratory in Medellín, where the samples were refrigerated until analysis. From the samples set, we chose 60 samples, geographically distributed in the six sectors on which we determine grain size, mineralogy and geochemistry.

1.4.2 Analytical methods

We dried the samples by freeze-drying, using a Labconco Freezone Freeze Dryer, to absorb cold moisture. We homogenized and quartered samples, into subsamples of 200 g, which were labeled and packed to analyze in the laboratories of the University of Freiburg and

Cologne in Germany; the Spectrometry laboratories of the Universidad de Antioquia; and the X-ray Diffraction laboratory of Instituto Tecnológico Industrial Pascual Bravo in Medellín.

We carried out the grain size analyzes for 53 surface sediments at the Laboratories of the University of Köln-Germany, with a Laser Particle Size Analyzer (Beckman Coulter LS13320). We treated an average of 20 g of bulk sample (original grain size <150 μm), with 10% HCl for ~2 hr to remove the carbonate content. We washed samples with distilled water and centrifuged at 2500 rpm for 5 minutes, three times. Subsequently, we treated the samples with 15% H_2O_2 for 24 hours or until the chemical reaction finished, to eliminate the content of Organic Matter. We washed samples with distilled water and centrifuged at 2500 rpm for 5 minutes. Finally, we used a solution of Na_2PO_5 (46 g/l), to disperse the particles.

We did mineralogical analyses of 60 surface samples at the X-ray diffraction laboratory of the Instituto Tecnológico Industrial Pascual Bravo in Colombia. We examined 2 g of bulk sample directly using a Brucker Eco D8 Advance Diffractometer. We fixed the material from random powders prior to grinding. We arranged the material in plastic disk, located in the center of the equipment to scan the minerals in the sediment. We obtained semi-quantitative results for minerals in the non-clay fraction. We analyzed the mineralogy with HighScore Plus Software to obtain a semi-quantitative estimate of major mineralogical fractions, using a the Rietveld full-pattern fitting method (Grunsky et al., 2013; Young, 1993).

We conducted geochemical analysis on 60 samples in the Spectrometry Laboratory of the Department of Materials at the University of Antioquia. We grounded samples in an S-1000 RETCH Centrifugal Ball Mill with zirconium oxide vessel at 3000 rpm, for 5 minutes. A fraction of the powder sample was subjecte calcination at 550° C for two hours, to determine organic matter content by weight Loss On Ignition (LOI) and Organic Carbon (OC) content, Estimated from LOI. We measured 3 g of sample in an ARL OPTIM´X WDRRF Spectrometer/Thermo Sciencific equipment. We obtained results for 10 oxides (SiO_2, Al_2O_3, Fe_2O_3, MgO, Na_2O, CaO, K_2O, TiO_2, P_2O_5, MnO) and 22 trace elements (Cl, S, Ba, V, Cu, Zr, Sm, Cr, Zn, Sr, W, Tb, Ni, Ar, Co, La, Rb, Br, Y, Sc, Ga and Cd).

We entered the results into an Excel database to perform several statistical procedures, including a process of data validation and verification with parametric and non-parametric tests (ANOVA and PCA). We used the Statgraphics (licensed to the Environmental Management and Modeling Research Group - GAIA of the Universidad de Antioquia) and GRADISTAT free software. We used the statistical parameters of mean diameter (Mz), sorting coefficient (σI), skewness (SKI), and kurtosis (KG), based on the Folk and Ward (1957) method of phi values Ø 5, Ø 16, Ø 25, Ø 50, Ø 75, Ø 84, and Ø 95 for the cumulative curves of grain size.

We determined the basic statistics of Mean, Median, Standard Deviation, Maximum and Minimum for the geochemical data. Subsequently, we applied inferential statistics (ANOVA) to determine the significant differences in the analyzed variables, with respect to the categorical variables of four environments (main river channel, secondary channels, swamps and bays) and the six geographical sectors (west, northeast, east, central, southeast, and south). A Principal Components Analysis (PCA) was also carried out to reduce data dimensionality and to find significant relationships among variables (Rencher,

2012; Johnson and Wichern, 2007). The purpose of these analyses was to find possible similarities or differences in terms of natural sources and sedimentological processes in the ARD.

1.5 Results

Surface sediments of the Atrato Delta exhibit distinctive spatial patterns in their physicochemical and mineralogical features. These patterns reflect variability in the dynamics of each geographic sector in terms of: 1) grain size (i.e., Mean (Mz), Sorting (σI) and Skewness (Sk); 2) mineral phase and abundances (%) of quartz, feldspar–plagioclase, Micas, Clays, Pyroxenes, Oxides and accessory minerals; and 3) geochemical features expressed in the different relationships and abundances of major oxides and trace elements that indicate provenance, weathering grade and especially metal enrichment.

1.5.1 Grain size

Grain size, defined with parameters used after applications by Ramadan and Gad (2019) and Martins (2003), confirm that the fluvial environment is the predominant source of the sediments that feed the delta, the connected bays (except for some samples with sorting close to 0.5 and negative swekness, that are characteristic of beach sediments), and the inland swamps (Figure 1.2). In the general background, the mean grain size Mz showed a broad spatial variation, ranging from very fine silt (8.323 ϕ ~ 3.123 μm) to fine sand (2.844 ϕ ~ 139.3 μm). Lowest ϕ values occur in samples located in the sectors south and west. The sorting of the whole set of samples varies from very poorly sorted (2.681 ϕ) to moderately well sorted (0.525 ϕ). The poorly sorted samples are more evident in the west and east sectors (Figure 1.2). Appendix 3 summarizes the statistical parameters and the distribution of size fractions.

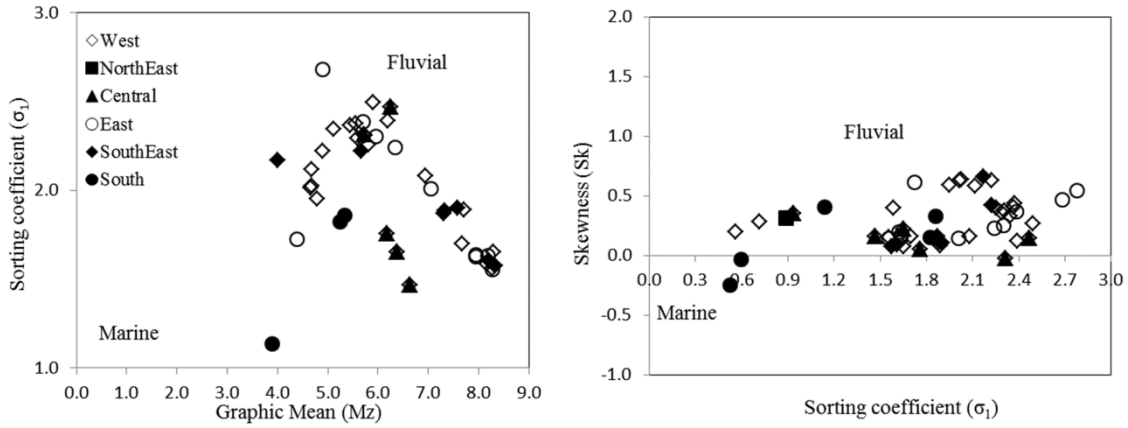

Figure 1.2 Scatter plots of: (a) graphic mean vs. sorting Coefficient. (b) Sorting coefficient vs. skewness, (Ramadan and Gad, 2019; Martins, 2003)

None of the sediments has a mean grain size (Mz) greater than 8.5 ϕ, suggesting a substantial hydrodynamic influence inland (Cai et al., 2012), in which the fine fraction bypasses the delta domain and is further transported and deposited, mostly in the bays connected to the Gulf of Urabá. The ternary diagram shows a depositional context dominated by silty and sandy fractions with no gravel sizes (Figure 1.3).

Grain size percentages for surface sediments in the delta are, on average, distributed as sand (28.7%), silt (58.0%) and clay (13.3%) (Appendix 4).

According to several authors (Kawadi, 2019; Opreanu et al., 2007; and Liu et al., 2006), fluvial sediments evince transportation by different mechanisms, such as rolling or traction, saltation and suspension. For the ARD, the traction populations could relate to the sand size (0 - 4 ϕ), for coarser sediments with higher specific weight, especially in the central, east and west sectors, in the middle of alluvial and marine plain units. Silt diameters cover the mayority of samples and could correspond to sediments transported by saltation (4 - 9 ϕ), which represent the better sorted samples. Nontheless, the particles transported by saltation could include sand, silty sand and silty mud fractions and their grain sizes coverage depend on sediments weight in combination with energy flow. Saltation occurs at the northeast, southeast, south and west sectors in the floodplain. The clay fraction corresponds to the 9 – 15 ϕ particle diameter segments, indicating the sediments transported by suspension (> 9 ϕ), mainly occurring at the south, southeast and northeast sectors in areas of marine plain, swamps and marshes (Figure 1.4)

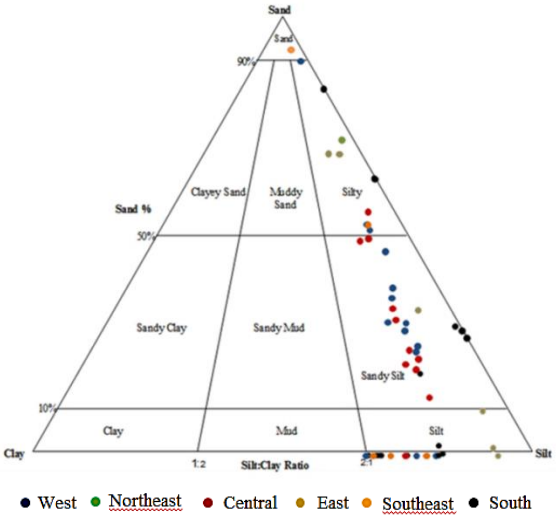

Figure 1.3 Ternary diagram plot for surface sediments distributed by geographical sectors.

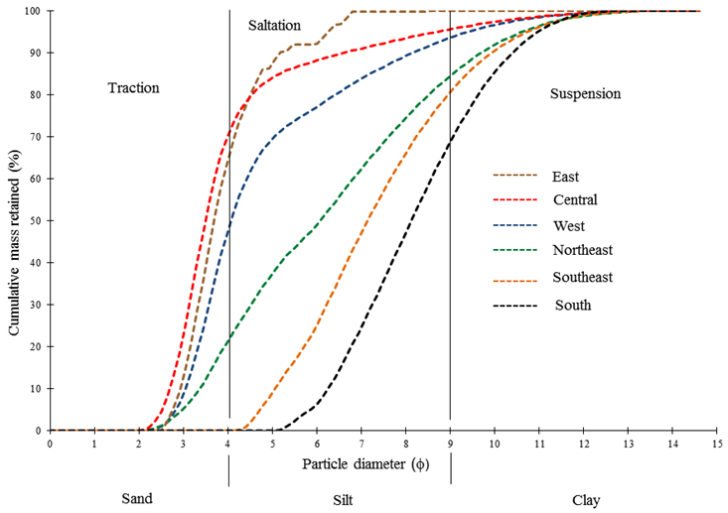

Figure 1.4 Cumulative curves of bulk surface sediments distributed by geographical sectors.

The grain size distribution along the ARD (Figure 1.5) shows that very fine sand dominates over the south, in the Atrato River apex and the first bifurcation to León channel and correspond to the floodplain. This is consistent with the expected coarser size upstream in the Atrato River Basin. Coarse silt sediments cover most of the area along the main Atrato River, up to 2 km north of the Coco channel, the León channel and to the north, around El Roto mouth as part of the floodplain and the influence of waves at coastline in beaches unit.

The medium silt fraction is distributed towards the northwest (Tarena flow and Marriaga Swamp); and the northeast (Candelaria Bay, Matuntugo swamps and the Coco, Coquitos and Matuntugo channels), related to the alluvial plain and some beaches. In the central sector, medium silt is scattered in the Coco Grande, Margarita and Burrera bays and surroundings of the Maquillon swamps in the marine plain geomorphological unit. Some very fine sand is present north of El Roto, Yerbasal Bay, east of Candelaria Bay and in the limits of Marirrio Bay and Leoncito channel, corresponding to the marine plain unit. Fine silt and clay sizes are confined to Maquillon, Matuntugo, El Limón and Marriaga swamps (related to swamps and marshes), as well as some specific small areas towards the Tarena channel (swamps, marshes and beaches), Candelaria, Coco Grande, Burrera Bays and in the Burrera channel mouth, in the marine plain and swamps and marshes .

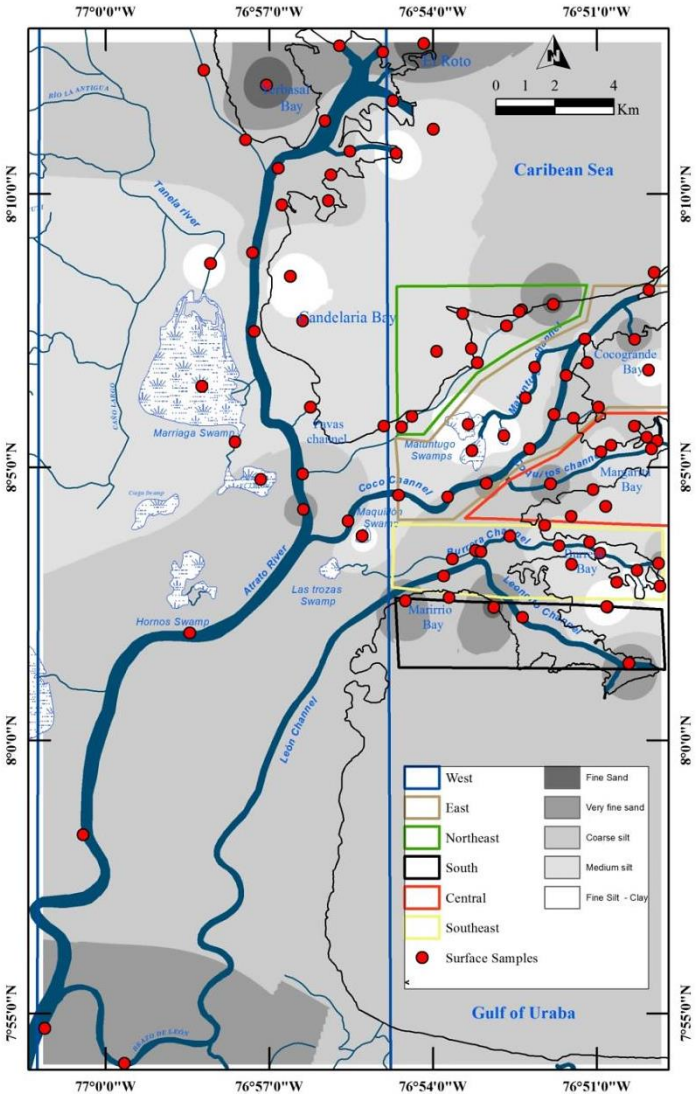

Figure 1.5 Grain size distribution patterns of sand, silt and clay.

1.5.2 Mineralogy

The ARD bulk mineralogy shows quartz as the dominant mineral phase, followed by feldsparts and plagioclase; clay minerals; pyroxenes (diopside, augite); micas and oxides. Additional phases correspond to sporadic accessory minerals such as cristobalite, sylvine, bornite, barite, bernalite, birnessite, cordierite, anorthite, labradorite, zeolite, montmorillonite, muscovite, pyrite, rutile, spinele, phlogopite, halite and perovskite.

The ARD sectors display differences in the mineralogical patterns for the sampled sediments (Table 1.1). The average quartz phase is high in the west sector (alluvial plain) (72%) and low in the south sector (marine plain, swamps and marshes) (47%); the feldspar and plagioclase phases are substantial in the central sector (53%) and southeast sector (31%), in areas of alluvial plain and marshes. The highest clay phases are significant in the east sector (18%) (in marine plain, beaches, swamps and marshes) and remarkably low for the rest of the sectors, with the lowest values in the central and south sectors (1%) (in marine plain, swamps and marshes). The pyroxenes phases do not appear in the central and southeast sectors. Important abundances of pyroxenes occur in the west (18%), northeast (10%) and east (9%) sectors, corresponding to the alluvial plain, marine plain, swamps ad marshes.

Table 1.1 Mineralogical average composition (XRD) of bulk samples. Values are given as relative proportion of mean phases after HighScore plus software analysis (%). (--: not detected or one unique found value). Accessories*: cristobalite, sylvine, bornite, bernalite, birnessite, cordierite, pyrite, rutile, spinele, halite, perovskite.

Mineral Phase	Statistics	Geographical blocks					
		West	Northast	East	Central	Southeast	South
Quartz	Mean	72	60	64	60	63	47
	Max	99	92	97	97	80	60
	Min	34	27	2	8	36	21
Felds+Plag	Mean	19	27	27	53	31	50
	Max	37	44	32	81	36	78
	Min	3	12	19	27	26	38
Micas	Mean	23	-	32	15	-	4
	Max	35	-	40	33	-	-
	Min	6	-	19	4	-	-
Clays	Mean	4	7	18	1	3	1
	Max	20	16	58	2	5	-
	Min	1	1	1	1	2	-
Piroxenes	Mean	18	10	9	-	-	1
	Max	-	15	-	-	-	-
	Min	-	4	-	-	-	-
Oxides	Mean	3	24	4	8	2	-
	Max	4	44	-	13	-	-
	Min	2	8	-	3	-	-
Accesories	Mean	21	19	15	6	27	2
	Max	62	27	45	-	62	3
	Min	1	1	1	-	2	1

According to the representative mineral occurrence diagrams for each sector (Figure 1.6) all analyzed samples contain quartz, feldspar+plagioclase (albite, anortithe, labradorite) and clays (vermiculite, zeolite, illite, montmorrillonite, kaolinite, palygorskite), with at least two peaks for each mineral identified in the XRD patterns. Micas (chlinoclore, plogopite, muscovite, biotite) occur in some samples (with at least two

peaks for each mineral identified in the XRD), mainly at the west, central, east and south sectors, in areas of alluvial and marine plains, being absent at the northeast and southeast sectors, corresponding to marine plain, swamps and marshes.

Pyroxenes (diopside, augite) are not detected in the central and southeast sectors in marine plain and marshes. Oxides (magnetite, iron oxide, titanium oxide, birnesite) are scarce, but present in the northeast sector in marine plain and marshes; small amounts in the west, central and east sectors in areas of alluvial and marine plains and almost absent in the east and south sectors, that correspond to marine plain and marshes. The accessory minerals are distributed along the delta with significant amounts in the west, northeast and southeast sectors (at least one peak identified in the XRD patterns).

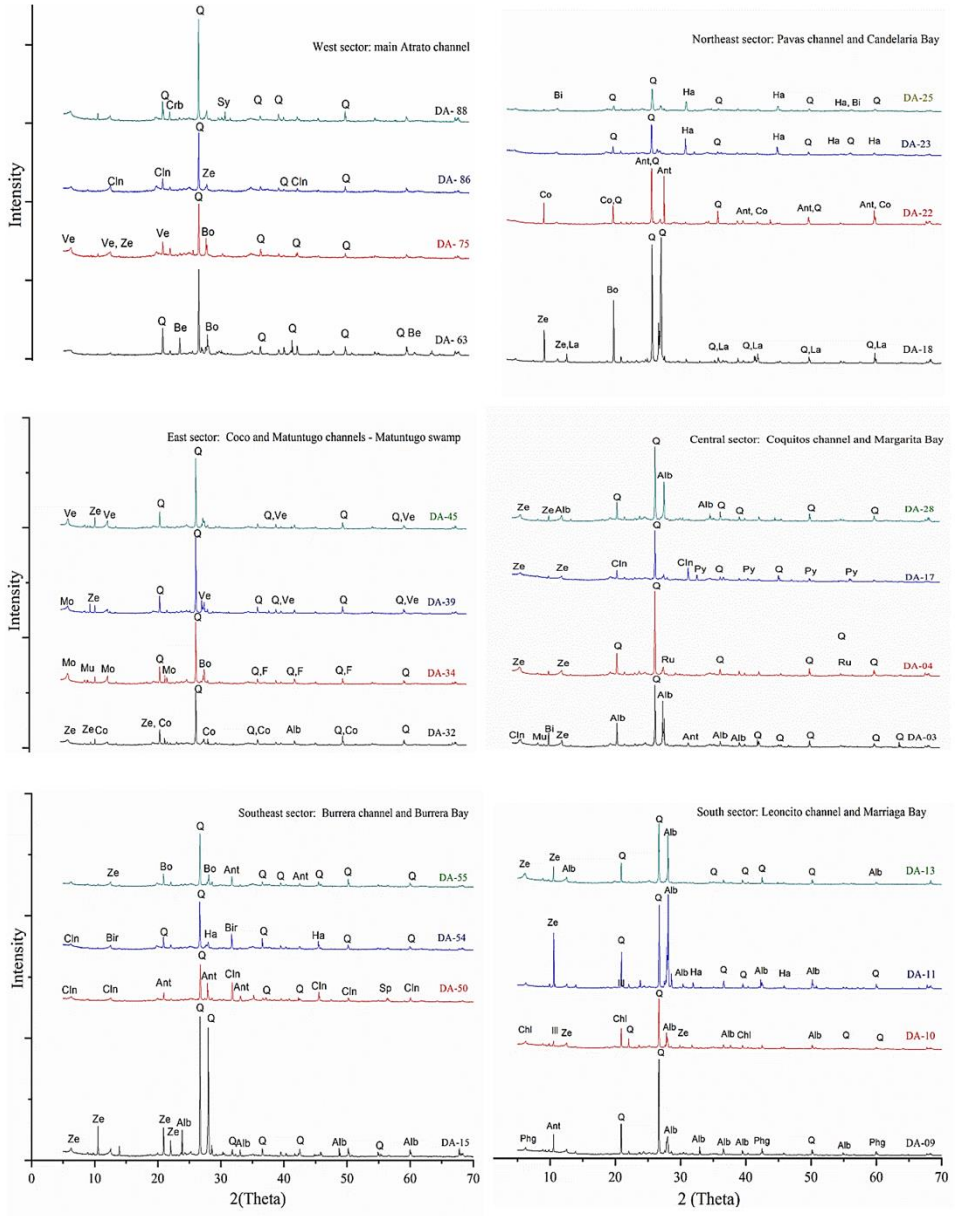

Figure 1.6 Representative X-ray diffraction (XRD) diagrams for bulk samples. Non-oriented powders (2 Theta- Cu). Four selected samples for each geographic sector. Mineral fractions: Q (Quartz); Crb (Chistobalite); Sy (Sylvine); Clh (Chlinoclore); Ve (Vermiculite); Bo (Bornite); Be (Bernalite); Bi (Birnessite); Co (Cordierite); Ant (Anorthite); La (Labradorite); Ze (Zeolite); Mo (Montmorillonite); Mu (Muscovite); Fe Feldspar); Alb (Albite); Py (Pyrite); Ru (Rutile);Sp (Spinele); Phg (Phlogopite); Ha (Halite).

1.5.3 Geochemistry

Average abundances of major elements (in wt%) for all the sediment samples are: SiO_2 (45.48%), Al_2O_3 (19.06 %), Fe_2O_3 (9.29 %), MgO (3.54 %), Na_2O (2.53 %), CaO (2.53 %), K_2O (1.40 %), TiO_2 (0.78 %), P_2O_5 (0.27%) and MnO (0.13%).

The average abundances of main trace elements (in ppm) for all the sediment samples are: Cl (9798.93), S (6571.03), Ba (643.26), Sr (226.64), Cu (207.26), Cr (193.26), Zn (137.41), Ni (109.43), Co (52.38) and Rb (34.69). These abundances show variable distribution patterns along the entire area and are more evident in the statistical parameters of the geographic sectors (Appendix 5 and Appendix 6).

The univariate ANOVA (Table 1.2), indicates the existence of significant differences by environment (i.e., main river, secondary channels, swamps, bays) and by geographical sectors (northwest, west, east, central, southeast and south) for concentrations of oxides Fe_2O_3, MgO, Na_2O, K_2O and TiO_2 (Kolmogorov-Smirnov test application).

Table 1.2 ANOVA for oxides in surface sediments. Confidence of 95%

Oxides	Sector		Environments		Significant differences
	F	Pvalue	F	P value	
SiO_2	1.39	0.2463	1.68	0.1838	No
Al_2O_3	0.78	0.5671	0.71	0.5503	No
Fe_2O_3	2.54	0.042*	0.36	0.7831	By sector
MgO	4.68	0.0017*	7.56	0.0003*	For both
Na_2O	2.94	0.0226*	3.54	0.022	For both
CaO	1.73	0.1488	2.18	0.1033	No
K_2O	2.8	0.0283*	8.05	0.0002*	For both
TiO_2	0.47	0.7968	4.01	0.013	For both
P_2O_5	1.85	0.1237	0.51	0.6776	No
MnO	1.16	0.3419	1.17	0.3316	No

We analyzed the spatial variability of the major elements (oxides) through box and whisker plots for the six geographical sectors (Appendix 7). None of the sectors displays a normal distribution. Central and northeast sectors show the greatest variability in the geochemical characteristics of the analyzed samples, whereas variability is smaller in the west, east and south sectors.

The central and west sectors present high values of SiO_2, Al_2O_3, Fe_2O_3, MgO, K_2O, TiO_2 and MnO. High values of CaO, TiO, P_2O_5 and MnO are evident in the northeast and east sectors. In almost all the analyzed sectors, the median value is very close to the average (Appendix 8).

Since most of the trace elements in the surface sediments do not fit the statistical assumptions for normality, we used the non-parametric Kruskal-Wallis test to analyze the significant differences, by comparing their medians. We did not detect significant differences for environments or geographic sectors, except for Cl and Sr that are higher in the marine environment compared to inland values (Table 1.3).

Table 1.3 ANOVA for trace elements in surface sediments. Confidence of 95%.

Elements	Sector P value	Environment p value	significant differences
Cl	0.019*	0.033*	for both
S	0.09	0.0619	No
Ba	0.1062	0.1714	No
Cu	0.3865	0.095	No
Cr	0.21	0.052	No
Zn	0.2147	0.8943	No
Sr	0.1281	0.023*	for environment
Ni	0.2123	0.1125	No
Co	0.0933	0.2854	No

This homogeneity indicates that the ion concentrations of these elements are not affected by factors such as transport, weathering, grain size, or anthropogenic activities in specific sectors.

The average concentration of heavy metals Cr (193.26 ppm), Ni (109 ppm and Co (52 ppm) is relatively high, compared with regional values. The delta has relatively high average values of Cr, especially in the northeast sector (230 ppm); Ni in the southeast sector (128 ppm) and Co in the northeast sector (68 ppm). Other metals such as Cu and Zn show also relatively high average values, greater than 100 ppm throughout the delta, mainly in the northeast sector (Cu: 698; Zn: 208), the southeast sector (Cu: 249; Zn:161) and the central sector (Cu: 207; Zn:185) (Figure 1.7).

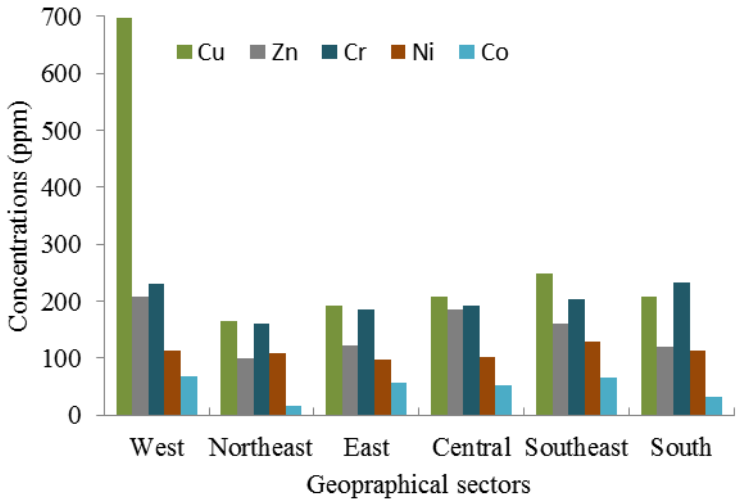

Figure 1.7 Mean trace element concentrations for metals distributed in geographical sectors

High concentrations of heavy metals likely relate to both natural values in parent rocks and pollution phenomena due to anthropic activities, such as mining upstream of the ARD (Palacios et al., 2019). High natural values are supported by the concentration of some trace elements in the bedrock, reported in other studies of potential geochemistry anomalies in the north of Colombia (Prieto et. al., 2009; Muñoz and Güiza, 2005).

Average values of trace elements such as Cl (9798 ppm), Na (25346ppm), S (6571ppm), P (2667ppm) and Ba (643 ppm) are high throughout the delta. This is especially clear in

the northeast and southeast sectors due to the marine influence on the bays, where the saline wedge could play a role in degradation of the organic matter, oxidation processes, marine productivity and sediments reworking (Liguori, et al., 2016; Griffith and Paytan, 2012) (Figure 1.8).

We used the Cr/Ni ratio to identify sediment provenance in a fluvial-marine context (Adikaram et al., 2019; Garver et al., 1996). Both elements show high concentrations along the delta, with Cr averages 199 ppm and Ni averaging 110. The Cr/Ni ratios vary from 1.4 to 2.7, indicating mafic rocks as one source of sediments in the delta. This assumption is consistent with the local geology for the south and west side of the delta, related to basalts and lava breccias from the Santa Cecilia Complex (Méndez et al, 2006).

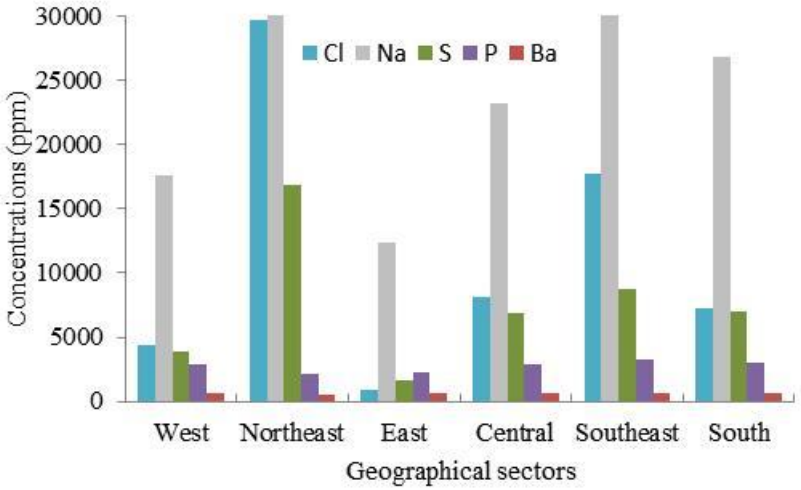

Figure 1.8 Mean concentrations for Cl, Na, S, P and Ba thresholds in geographical sectors

A comparison with UCC values shows that the surface sediments at the delta have lower SiO_2 and high Al_2O_3, Fe_2O_3 and MgO. Concentrations of Na_2O are in general lower, except for the northeast sector; whereas CaO and K_2O are lower in all the delta samples, which is consistent with the relative significance of the CIA found for the target area, as compared with other areas worldwide (Cai et al., 2012). TiO_2, P_2O_5 and MnO are slightly higher in all sectors (Figure 1.9).

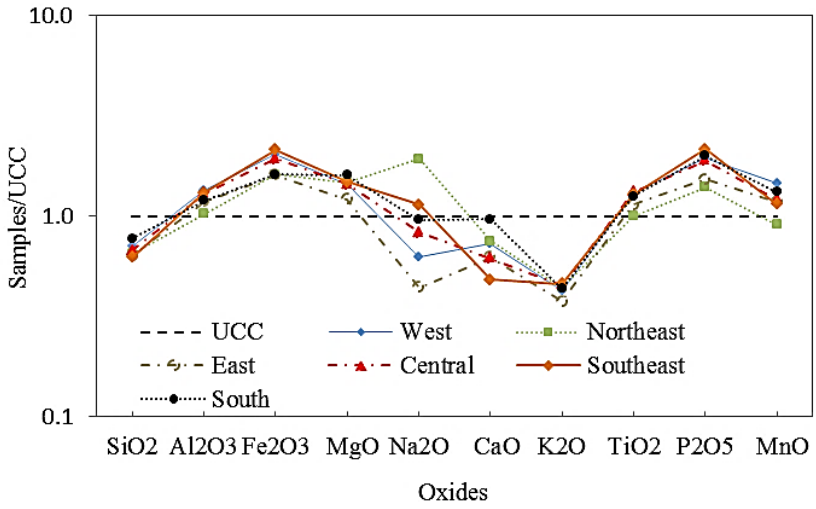

Figure 1.9 Oxides average concentration (wt%) compared to Upper Continental Crust mean values, (Rudnick and Gao, 2003).

Comparison of trace elements with UCC (Gallet et al., 2014; Wedepohl, 1995; Taylor and McLennan, 1985), shows an enrichment of Cl, S, Cu, Cr, Zn, Ni and Co, with the exception of low values for Ba (very similar to UCC), Sr and Rb. In addition, we observe a depletion of Rb in the entire delta, mainly in the northeast sector, probably due to the effect of chemical weathering of granitic rocks, such as the Mandé Batholite, and also due to the high solubility of Rb in natural conditions (Tanaka and Watanabe, 2015) (Figure 1.10). The general permanent enrichment of trace elements indicates that they are not significantly affected by carbonate dilution in marine areas and that the hydrodynamics does not exert direct control over the chemical composition of surface sediments in the delta (Cai et al., 2012).

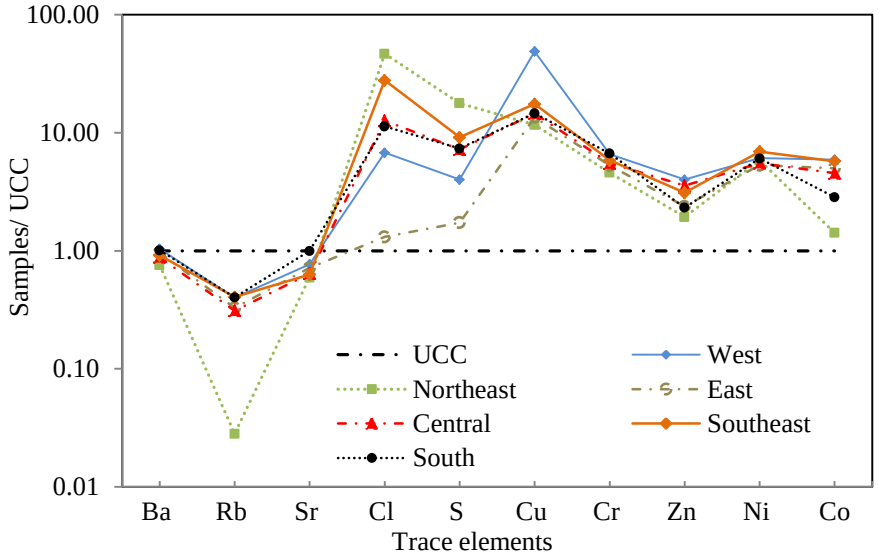

Figure 1.10 Trace elements average concentration (wt%) compared to Upper Continental Crust mean. (Rudnick and Gao, 2003).

1.5.4 Principal Component Analysis (PCA)

We applied PCA to determine the possible correlations among the variables and to group the data. PCA allowed us to assemble the variables according to the variance explained either by common sources or by sedimentological or geochemical processes (Mil-Homens et al., 2014). Furthermore, PCA enabled us to relate factors such as the environments (fluvial, swamp or marine), the six geographic sectors and the OC content. PCA for major elements shows four components that together explain 73.2% of the variability in the original data (Appendix 9). This analysis illustrates the associations between the geochemical variables of major elements (oxides), trace elements and organic carbon found throughout the delta with environments and geographical sectors (Figure 1.11).

Component 1 (PC1) explains 30.9% of the total variance with a positive score for {OC, Br, S, Cl, Na and sectors} in the northeast and east sectors, coincident with the estuarine - marine environments at Candelaria and Cocogrande Bays with a more endogenic source due to brackish coditions. The large negative scores {Si, Ca, Sr, Mg, Ba and environments} occur in the central, southeast and part of south sectors, along the ends of distributary channels of Coquitos, Burrera and Leoncito, highlighting the mixture between the fluvial inputs (Si, Mg) of allochthonous source and the endogenic lacustrine signatures (mainly marked by Sr, Ca and Ba).

Component 2 (PC2) explains 23.3% of the total variance, characterized by large positive scores of {Fe, Ni, Cu, K, Mg, Co, Cr, Ti, Al, Rb and P} at west, central and part of southeast sectors, indicating a strong incidence of detrital elements {Al, Fe, K, Ti, Mg, Rb} and heavy metals {Cu, Ni, Zn, Co and Cr} in a fluviatile context. The incidence of both natural leaching of heavy metals and anthropogenic sources could be encompassed by this component. PC2 allowed to considerate a more marked allochthonous source in west, central and southeast sectors.

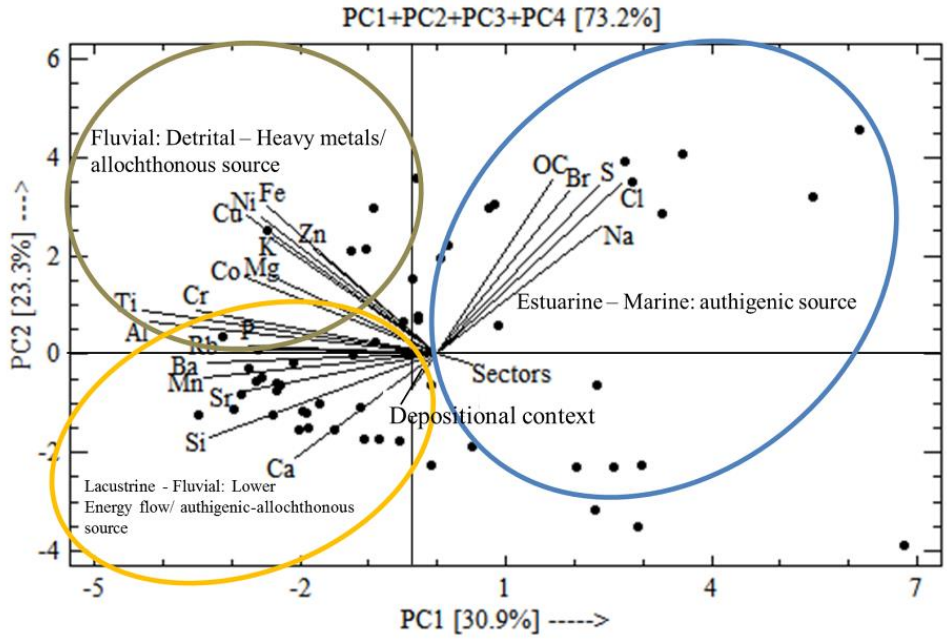

Figure 1.11 Principal component analysis (PCA) for major elements (oxides) and trace elements, environments (river, swamps, bays) and geographic sectors (west, northeast, east, central, southeast, and south). Variables loading on PC1 and PC2.

1.5.5 Chemical index of alteration (CIA)

We applied the CIA, using the molar oxides proportions of Al_2O_3, Na_2O, K_2O and CaO (Nesbitt and Young, 1984) to estimate the degree of weathering in the ARD in relation with the depositional context (swamps, river, bays) and the geographic sectors (Figure 1.12).

We classified the weathering in the delta as predominantly moderate, with regard to the Al/Na ratios (following Nesbitt and Young (1984), and Oni and Olatunji (2017).We found some low (45) and high (83) values of CIA. Moderate average values are in the northeast (59) and south (61) sectors.

Most of the samples in both sectors correspond to open bays (Marirrío and Candelaria), where high CIA values remain in sediments of fluvial sources (Leoncito and Pavas channels).

High mean CIA values occur in sediments in the west (70), east (69), central (69) and southeast (68) sectors. These values represent moderate to intense chemical weathering for these geographic sectors (Appendix 10).

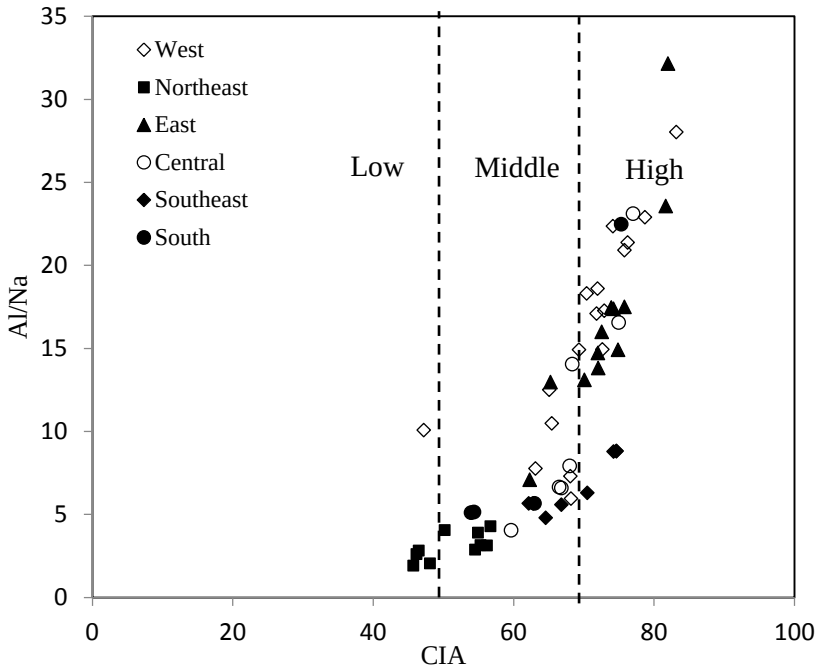

Figure 1.12 Weathering intensity, expressed through Al/Na ratio vs. chemical index of alteration (CIA), after: Nesbitt and Young (1984) and Oni and Olatunji (2017).

1.6 Discussion

Surface sediments of the ARD show heterogeneity grain size, mineralogy and chemical composition among the geographical sectors and depositional context. The variation of physicochemical parameters enables the differentiation of transport regimes, depositional environments and, consequently, of the recent sedimentary dynamics in Quaternary fluvial environments (Hasberg et al., 2019; Mycielska and Ludwikowska, 2011). We discuss the ways to distinguish the transport regime by means of grain size; the minerals distribution patterns; the tectonic setting and provenance based on geochemical characterization; the sediments geochemical classification; and scenarios to classify the sedimentary processes among the ARD.

1.6.1 Sediment transport regime

We determined the ARD sediments transport regime in terms of the relationship between the enery flow and grain size. The average mean grain size values and their distributions along the ARD indicate the occurrence of different energy and depositional conditions (Figure 1.2 Scatter plots of: (a) graphic mean vs. sorting Coefficient. (b) Sorting coefficient vs. skewness,).

Since sorting and skewness parameters depend on the energy flow (Opreanu et al., 2007), sediments with poor sorting and positive skewness reflect low energy, whereas sediments with good sorting and negative skewness reflect high energy. We found that the low to middle energy conditions are the dominant transport regime in the ARD surface sediments (Figure 1.2 Scatter plots of: (a) graphic mean vs. sorting Coefficient. (b) Sorting coefficient vs. skewness, , mainly for the west, southeast and south sectors. This low to middle energy

reflects very poor to poor sorting as the predominant feature in the delta, with the prevalence of a positive skewness.
The surface sediments of the ARD experience traction, saltation and suspension with prevalence of saltation associated with silt grain sizes. The ternary grain size plot (Figure 1.3) shows the variability in energy conditions along the ARD. This plot shows a trend in which the grain size decreases from fine sand to fine silt. This behavior places the surface sediments between the low and middle energy flow.

The particles could experience various means of transport in terms of the occurrence of turbulent flows. Those flows are related to factors such as the river energy, mainly during flooding periods and the the morphological variations of the Atrato River and its branches, in relationship with the speed and flow direction changes. Further, the tidal influence in the marine plain and the affectation due to waves in beaches could also affect the means of transport (Tarena mouth, Candelaria and Matuntugo Bays). We infer that an important reworking of non-consolidated sediments occurs in the areas where saltation is predominant (northeast, southeast and south sectors) and a mixture between fluvial and marine currents occurs, with a direct influence of flow velocity variations (Clarke et al.,2014; Christiansen et al., 2000).

We observe a reduction of coarse fractions from inland towards the Gulf of Urabá. This occurs upstream of the ARD towards the north and east, where sand fractions decrease, a phenomenon observed in most deltas worldwide (Gong et al., 2016; Sibaja-Cordero et al., 2011; Cai et al., 2012 Yevzerov, 2007). Nonetheless, there could be a more complex reason for sediment grain size distribution in the ARD, influenced by a mixture of different fluvial energy flows and marine inputs at the mouths of the Atrato River, which may rework sediments mainly during high tidal periods in the dry season (December–April) (Velásquez, 2013; Tolman, 1997). A drainage network towards the west, descending from the Darien and Baudó hills, could also feed the delta plain and provide the medium–coarse silt fraction around the Marriaga Swamp sector in the north of the ARD.

1.6.2 Drivers of minerals distributions

To determine the drivers of minerals distributions in the ARD, we took into account the relationship of bulk mineral phases (determined by XRD) with the regional and local geology; grain size (mainly sorting); the weathering intensity and the theoretical hardness and density properties for the light and heavy minerals. For instance, quartz and feldspar grains are less dense than heavy minerals, and behave in a different way during transport and deposition.

We addressed some theoretical considerations to understand the drivers of mineral distribution. Regional and local geology are the principal source of fresh minerals that can be weathered, eroded, transported and deposited in catchments. The secondary source of minerals is the weathering and reworking of sediments that contribute to the transformation of minerals into new secondary or low mineralogical phases (Wolf et al.,2019; Martin et al., 2019).

Grain size influences mineralogical variations, mainly for oxides and clays, and is directly related to sorting during fluvial transport (Whitemore et al., 2004). The grain size variability could explain why sorting leads to a preferential enrichment, depletion or absence for specific minerals in different depositional context. Additionally, the mineral

hardness and density are factors that determine the transport mechanisms (Kermani et al., 2015).

Weathering intensity is also a factor that influences the presence of certain minerals (Jian, et al., 2019; Frings and Buss, 2019). Finally, the mineralogical composition is a useful tool to interpret sedimentary processes such as transport, erosion and depositional environments (Ramadan and Gad, 2019).

We used our bulk mineralogical data to analyze the mineral distribution patterns along the delta (Figure 1.13), in terms of main mineralogical phases. Light minerals (quartz, feldspart+plagioclase, clays) are the most abundant in the ARD, whereas heavy minerals (i.e. muscovite, chlorite, biotite, pyroxenes, hornblende and oxides) show a small amount in of sediments. Quartz distribution in the ARD has two main possible sources that explain its enrichment in the west, east and southeast sectors. One likely source is the Batholith of Mandé, of quartzdiorite composition, located at the western side of the ARD (this rock is weathered and transported throughout streams from the Baudó–Darien Mountains and deposited in the delta flood plain).

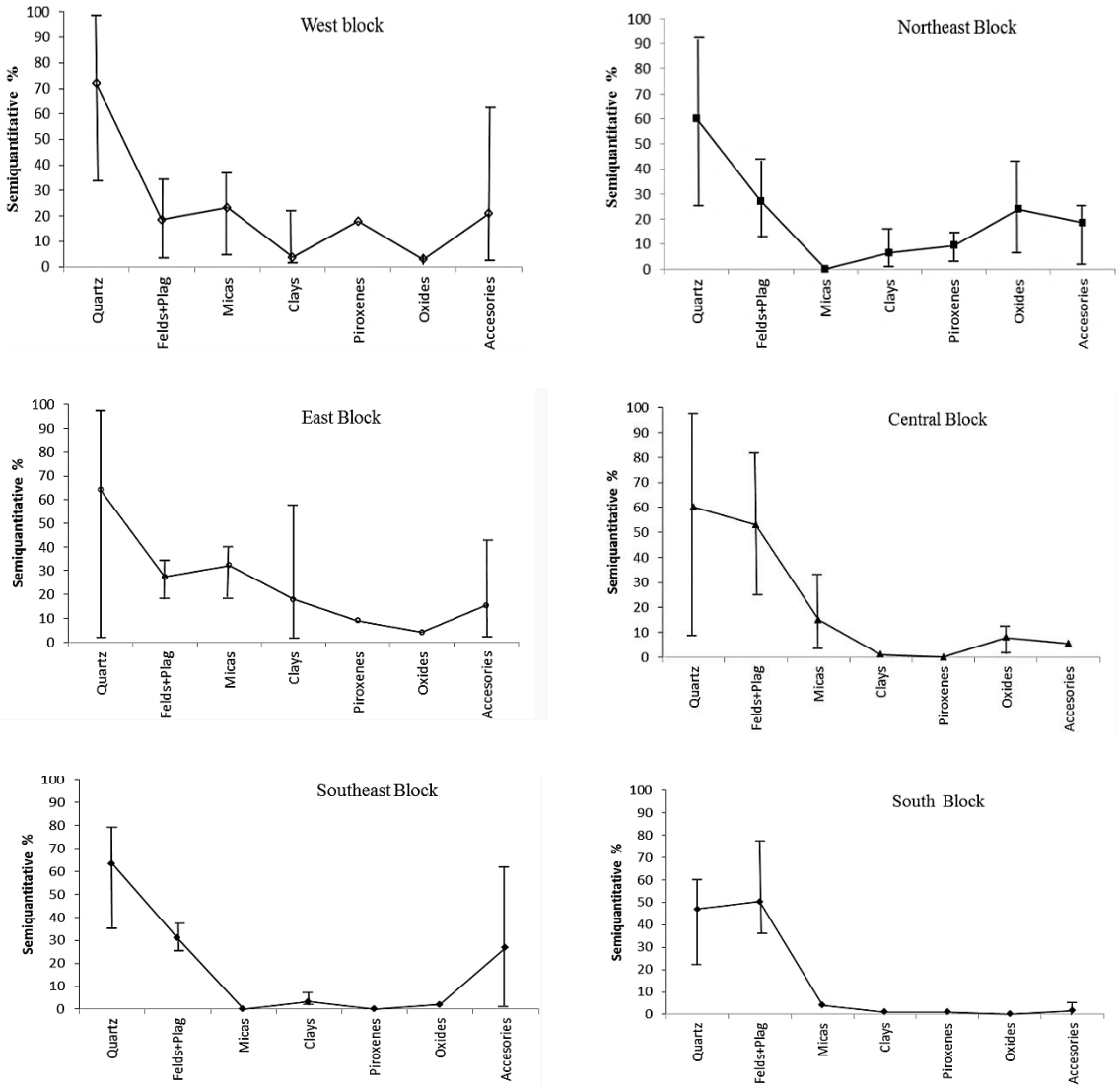

Figure 1.13 Distribution of semiquantitative abundances of the bulk minerals phases in the stream sediments, determined by XRD analysis of sediments in the geographical sectors: average, max and min values, (data from table 1).

The other likely source of minerals in the Atrato River that transports quartz from many types of bedrocks upstream, such as fine sandstones and limestones emplaced southwest of the delta. Since, quartz is the most resistant mineral to weathering (Monnier et al., 2018; Wray and Sauro, 2017; Tanaka and Watanabe, 2015), its presence is expected even in areas with moderate to high weathering. Sorting does not exert a strong control on the quartz distribution in the delta. Furthermore, the hardness (7) and density of quartz (2.6 g/cm^3) strengthen the resistance of this mineral, enabling it to endure long distances in catchments before sedimentation.

The semiquantitative abundances of feldspar+plagioclase (F+P) in the central and south sectors could be explained by the fluvial energy that dissipates towards the east, when the Atrato River bifurcates into four distributary channels in the transition between flood plain, swamps area and the coast. This low energy flow helps to explain the scattering F+P. The sorting differentiation (Kroonenberg, 1994) and grain size reduction of this mineral phase in the mentioned sectors, reinforces the splitting of these minerals. Weathering also influences the secondary formation of minerals derived from this phase and could be significant in the formation of further clay mineral phases. F+P average hardness (~ 6) and density (~ 2.5 - 2.8 g/cm^3) explain its wide distribution in the delta.

Clays are the result of intense weathering and transport, accompanied by grain size reduction (Tanaka and Watanabe, 2015). Clay minerals are moderately distributed in the ARD and could be derived from both primary weathered rocks and alteration during fluvial transport. Limestones and claystones are the primary sources for clay minerals, whereas the alteration of the feldspar in granitic rocks could be the source of secondary clayey phase. Clay minerals have low hardness (~ 1 to ~ 3) and low density (1 – 2.6 g/cm^3). These two features enable a wider distribution along the delta. Weathering intensity is a strong driver for the absence of this phase throughout most of the delta. However, the presence of clay in the east sector could be controlled by sorting and source rather than weathering. However, the bulk mineral detection carried out during this study is insufficient to determine the true amount of clay minerals in the ARD.

Mica is moderate in the west and east sectors and is absent in the northeast and southeast sectors, indicating a fluvial source for this phase. Mica phase could be a secondary product of the alteration of plagioclases from both granite and sedimentary rocks. Micas are minerals that are very sensitive to weathering and alteration, which may explain their low values in the ARD. Mica hardness varies between 2 and 3 and has in general a low density (2.7 – 3.0 g/cm^3), consistent with the effects of transport and sorting in the delta that diminish its presence.

Pyroxenes are in general poor along the delta and their relative enrichment in the west sector is probably a consequence of the basaltic rocks of the Santa Cecilia Complex in the northwest corner of the delta (Garzón, 2012). Basaltic rocks of Santa Cecilia Complex also outcrop to the southeast of the Atrato Basin and could be transported by the Río Sucio River that flows into the Atrato River around 550 km upstream of the delta apex. The pyroxene phase travels along the main Atrato channel towards the northeast and east sectors. The south sector has a very low amount of pyroxene, transported along the León and Leoncito channels. Pyroxenes have a relatively high hardness (5 – 6) and moderate to high density (3.2 – 3.3 g/cm^3) that contributes to a fast deposition or continuous transport by traction or saltation in moderate energy flows, as occur in the Atrato River. As the transport regime dissipates towards the distributary channels, this mineral phase does not

appear on the east sector of the delta. Moderate to high weathering also may account for the scarce amount of this phase along the delta.

Oxides preservation is relatively poor in tropical environments (Johnson, 1990). There is a constant dissolution of ferruginous sediments that can lead to reworking and redeposition of few Fe/Mn Oxides. We consider this to be the reason for the poor presence of oxides phase in the delta. The moderate presence at the northeast sector is likely a consequence of marine Fe sediments from sources in the Gulf of Urabá. The average hardness of oxides (5-6) and their density (4.2 g/cm^3 to 5.5 g/cm^3) also explain their low presence, indicating deposition and low transport.

The distributions of mineral phases indicate the possible transport of low-density minerals over long distances (towards the north of the ARD), scattered into the distributary channels (towards the east). Those minerals could remobilize and deposit in swamps, flood plains and bays. High-density minerals are more concentrated and distributed along the main Atrato River. The incidence of traction, then saltation in the west, northeast and east sectors could cause more rapid deposition of heavy minerals and, consequently, their depletion or absence towards the distributary channels.

We found differences in mineral abundances within geographical sectors and among the geomorphological units. These mineralogical differences demonstrate that another control on the sedimentary dynamics of the ARD is produced by transport regime fluctuations, sorting variations, weathering intensity, punctual reworking and deposition of low-density minerals such as quartz, feldspar+plagioclase and some clays, compared to high-density minerals such as pyroxenes and oxides. Mica phases oscillate between both possible mineral associations, depending on whether they are muscovite, biotite or chlorite type.

1.6.3 Tectonic setting and provenance analysis

We analyzed the tectonic setting from discrimination diagrams, which include the Oceanic Island Arc (OIA), Continental Island Arc (CIAr), Active Continental Margin (ACM) and Passive Margin (PM) settings, to determine the possible sources of sediments and the tectonic setting of the delta ((Bhuiyan et al., 2011; Bhatia, 1983). In this regard, most of the sampled sediments match the OIA towards the CIAr, supported by the (Fe_2O_3+MgO) versus Al_2O_3/SiO_2 and (Fe_2O_3+MgO) versus TiO_2 relationships. This is consistent with the location of the delta in the South American subduction zone at the junction of the oceanic and continental tectonic plates. Even so, some samples from the northeast and east sectors locate within the ACM setting, which is also consistent with regional tectonics (Figure 1.14).

Half the samples tagged as PM are dominated by sediments with low SiO_2 content, corresponding to the west and east sectors (West: 47%, East: 42%). The SiO_2 values relate to detrital-rich material such as quartz, while the samples in the ACM field have high values of Fe_2O_3 (10%) and MgO (3%), reflecting more degraded material and a finer particle size (Bhuiyan et al., 2011).

The samples in the OIA correspond to the central and southeast sectors, characterized by substantial concentrations of Al_2O_3 (20%; 20%) and low in the K_2O/Na_2O ratio for the central and south sectors (0.4; 0.7). The Al_2O_3 values represent intense weathering processes and the relation with mineral phases of phyllosilicates.

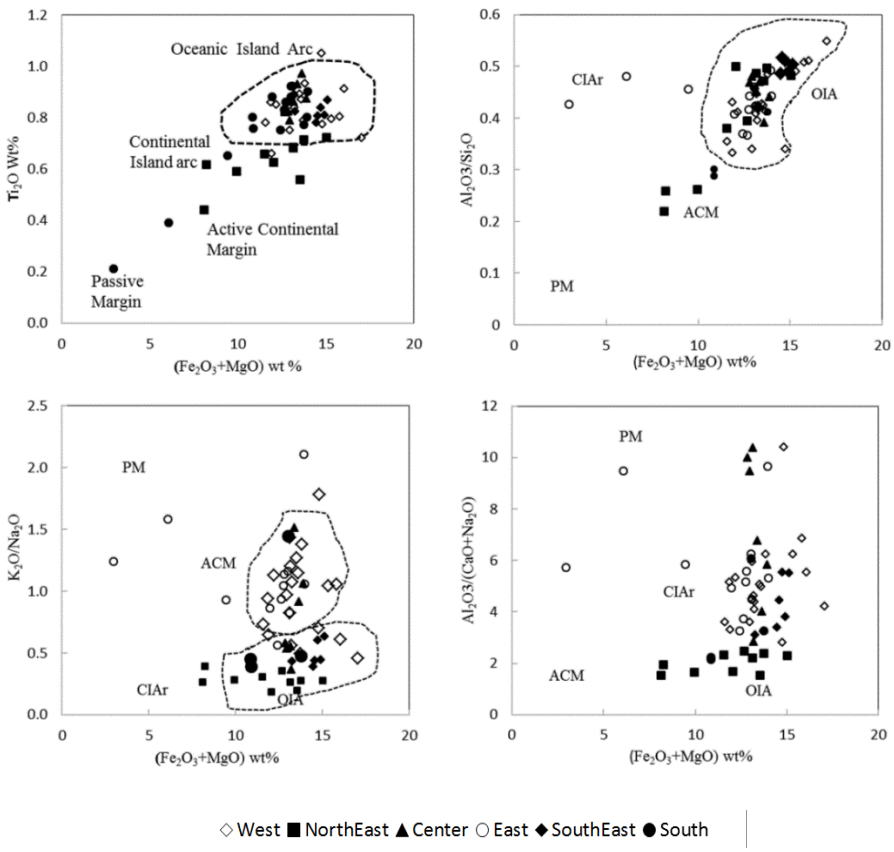

Figure 1.14 Tectonic discrimination diagram for surface sediments of the Atrato River Delta, from the limits established by Bathia (1983), and Roser and Korsch (1986).

From the log plot of chemical oxides and the plot of oxides maturity (Figure 1.15), the sedimentary provenance of the ARD sediments matches the Fe-shale and Graywacke classification. Fe-shale and Graywacke sediments are composed mainly of fine sediments (very fine sand to very find silt to clay) with a mineralogical composition of feldspar, mica, clay and quartz.

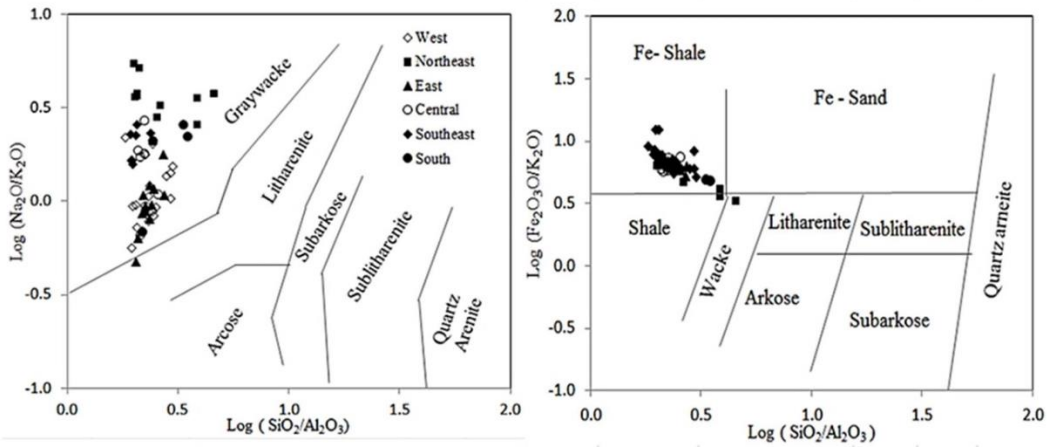

Figure 1.15 Geochemical classification of the Atrato River Delta sediments (a) after Pettijohn et al., 1995 and (b) after Herron, 1988.

The binary plot of sediments in Figure 1.16 enable the identification of rock sources as granite basalt to granite, confirming the predominance of intermediate to felsic rocks,

which are consistent with the andesitic basalt of Santa Cecilia Complex (Rodríguez and Zapata, 2012) and with the granitic rocks of the Batholite of Mandé (Lugo et. al, 2003).

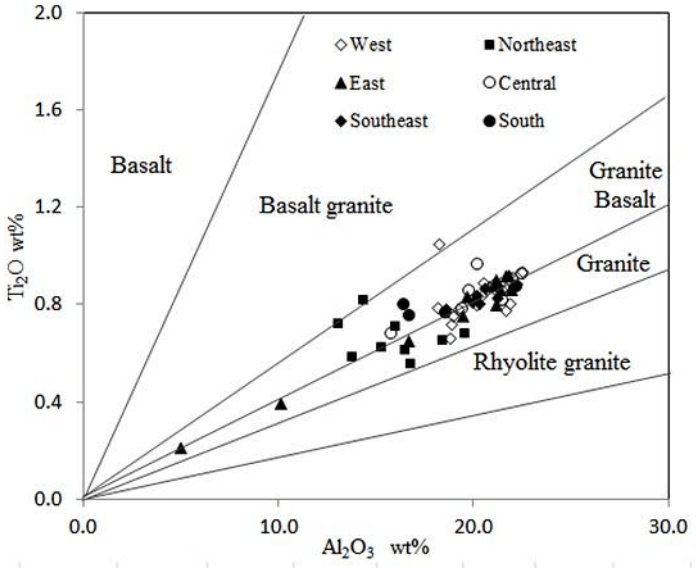

Figure 1.16 Binary plot of Al_2O vs TiO (wt%) in terms of the compositional bedrock field of the ARD.

The geochemistry of the ARD sediments indicates control by various sedimentological factors. For instance, the elevated Fe_2O_3 concentrations (delta average: 9 wt %) indicate the ARD sediments derive from rocks that experience oxidation and leaching during the weathering processes (Mikkel and Henderson, 1983). We identified a silica dilution, represented by moderate to low values of SiO_2 (delta average: 45 wt %). This dilution of silica is supported by the remarkable depletions in K_2O concentrations and the low MgO (compared to UCC values).

Minerals such as feldspar and plagioclase are composed of Al_2O_3, whereas minerals such as olivine, pyroxene and amphibole are composed of TiO_2. Both Al and Ti are unaltered minerals in nature and are resistant to chemical weathering. The average Al_2O_3/TiO_2 radio of 24, identified in the ARD indicates a felsic to intermediate bedrock as one of the main sources of sediments (Hayashi et al., 1997).

1.6.4 Insights into modern sedimentary dynamics in the ARD

The fluvial influence dominates recent sedimentary dynamics along the ARD from inner land to neighboring bays, with possible incursions from of tide/wave/wind towards inland (Escobar et al., 2015; Invemar, 2007). The occurrence of coarser grain size sizes near to some river mouths suggests that tide/wave/wind incursions could contribute to the dispersion and mixing of surficial sediments with marine sediments along west side of the Gulf of Urabá, in river mouths and bays (Figure 1.5). This is similar to the behavior observed in other fluvial systems, such as the Doce and Mekong rivers (Quiaresma et al., 2015; Korus and Fielding, 2015; Unverricht et al., 2013).

The weathering intensity in the ARD is coincident with the moderate to high concentrations for Al_2O_3, Fe_2O_3 and TiO_2, whereas the impoverishment of SiO_2, Na_2O, K_2O and CaO indicates moderate to high weathering. In addition, occurrence of a

feldspars+plagioclase phase indicates high weathering intensity towards altered clay minerals (also distributed in the delta). Therefore, the weathering in ARD is mainly the result of climate conditions associated with a humid, tropical environment. Rainfall in the Atrato Basin (Rodríguez et al.,2010) affects fresh rocks and contributes to the weathering intensity. This weathering favors the erosion and transport of sediments along the Atrato Basin towards the Gulf of Urabá (Blanco and Taborda, 2012; IGAC and INGEOMINAS, 2001).

According to the mean grain size map in the ARD (Figure 1.5) it is a important reduction in grain size at the opening of the apex of the delta, which shows the dissipative power of this landform and the importance of the bifurcation of the flows that it reduces sediment transport capacity.

The moderate to high-energy inputs from the Gulf of Urabá and its hydrodynamic features of a semi-enclosed landform (Escobar, 2015; Montoya, 2010) have the capability to remove (rework) and sort the fine fractions of sediments near the channel mouths, mainly at Burrera, Coquitos, Matuntugo, and El Roto channels.

1.7 Conclusions

This study offers a first interpretation of the grain size distribution, bulk mineralogical phases and geochemistry of surface sediments to understand the transport regime, predominant sedimentary processes and main sources of sediments at the Atrato River Delta.

Physicochemical features of surface sediments in the ARD provide evidence of an active delta with: 1) predominant saltation transport induced by moderate to low energy flow; 2) mineral distribution driven by source type, energy transport, weathering, minerals hardness and density; 3) moderate to high chemical weathering and 4) partial sediment reworking.

The variety of sedimentary processes in the ARD is greater in the west, central and southeast sectors, where major differences in grain size, mineralogy and geochemistry occur. Riverine medium and coarse silt dominate these zones, forming modern deposits that promote progradation along the main distributary mouths that flow directly to the northern and western sides of the Gulf of Urabá and deposit sediments in the delta front.

Tectonic discrimination analysis suggests that most of the sediments in the Atrato Delta belong to rocks derived from the Oceanic Island Arc (OIA). This is consistent with the geology of the west border of the ARD and its relation with the South American Subduction Zone. In this area, the rocks were formed by Oceanic Island Arc terrain accretion towards the continent with the emplacement of granitic and sedimentary rocks.

The Chemical Index of Alteration at the ARD displays a wide range, between 59 and 83, which indicates that the surface sediments originate from moderately to highly weathered igneous and sedimentary sources. This means that sediments experienced a moderate to high degree of chemical weathering after deposition and contribute to the widespread mineral distribution and geochemical variations in the ARD.

The geochemical classification of the ARD surface sediments shows that Graywacke and Fe-shale are the dominant components. In addition, we identified that the main source of

these sediments relates to the trend of intermediate to felsic granite basalt-granite rock. The the Cr/Ni ratios support the identification of mafic rocks such as basalts and lava breccias as possible secondary bedrock sources.

1.8 Acknowledgments

This study was partially supported by the Colombian Administrative Department of Science, Technology and Innovation (COLCIENCIAS, Call 727/2015); as part of the doctoral studies in Environmental Engineering of the first author at Universidad de Antioquia. Samples preparation and laboratory assays were performed by the GAIA Research group of Universidad de Antioquia, Köln University of Germany; XRF Lab of the Materials Engineering Department of Universidad de Antioquia, Ludwig University of Freiburg, and DRX Laboratory of Universidad de Antioquia and Instituto Tecnológico Industrial Pascual Bravo in Medellín. We especially thank Dr. María Teresa Flórez for her academic support and contributions during the research. Special thanks to Dr. Stephen Optiz from University of Köln for laser grain size assays; Dr. Frank Preusser for supporting and advising the first author during her internship in 2018 at Ludwig University of Freiburg; to Pr. Dr. David Dolejts and Pr. Dr. Gertrud Sigmund from Ludwig University of Freiburg for facilitating the use of XRF and XRD Laboratories and for their academic support to the first author in mineralogy and geochemistry issues. We thank the communities of the Atrato Delta region for their hospitality, kindness and support during the field campaigns and project socialization.

2 Chapter 2: First luminescence chronology of late Holocene deposits of the tropical Atrato Delta, Colombia

Liliana Betancurth[1], Frank Preusser[2], Daniela Mueller[2], Claire Rambeau[2], Julio Cañón[1]

[1] *Grupo GAIA, Facultad de Ingeniería, Universidad de Antioquia, Medellín, Colombia*

[2] *Institute of Earth and Environmental Sciences, University of Freiburg, 79104 Freiburg, Germany*

2.1 Abstract

Sediments of the Atrato River Delta, Colombia, were investigated to determine the late Holocene dynamics by using luminescence dating. For this introductory study, near-surface samples were collected along the main river channel and around the main delta body, while sediment cores were drilled at three swamps and in two bays. Altogether, 30 samples were collected to determine ages and accumulation rates in both marine and inland depositional context. The samples proved to be a methodological challenge, but the dating results and derived sediment accumulation rates are conclusive. Relatively constant accumulation rates of less than 2 mm a^{-1} were found for most depositional context of the delta, despite differences expected from the sedimentary facies. A significant increase in accumulation rates, however, was observed in parts of the Atrato Delta and might be related to human activity during early colonisation by Europeans. The contribution of new data and sedimentary information derived from this study may serve as a baseline for future sampling campaigns aimed at gaining more insights into the sedimentary dynamics of the Atrato Delta.

Keywords: Luminescence dating, feldspar, delta deposits, late Holocene, Colombia

2.2 Introduction

Deltas are important indicators of natural and human-induced changes in the interaction between rivers and seas (e.g., Mikhailov and Mikhailova, 2003; Day et al., 2005; Elliott et al., 2019). The natural dynamics in many deltas are strongly influenced by anthropogenic disturbances of the ecological and hydro-morphological conditions in the catchment such as regulation of stream flow and sediment flux (Dolozi et al., 2011; Dunn et al., 2018). Furthermore, the predicted rise of global sea level will likely increase the physical stress on deltas and thereby cause a higher flooding risk in these systems (Syvitski et al., 2009; Alvarado-Aguilar et al., 2012). This is particularly crucial as many deltas are highly populated because of their abundance of natural resources (Evans, 2012; Lauria et al., 2018). Hence, it is indispensable to gain a better understanding of natural dynamics within deltas before the effect of human-induced disturbances can be assessed.

A key question for the investigation of delta dynamics is the assessment of sediment fluxes and deposition at different time scales, in particular for the Holocene. One approach of doing so is dating deposits from different sedimentary units within a delta, using geochronological techniques. The most common means is radiocarbon dating, which was found to be problematic on short (some 100 years) time scales. This is due to the fact that most organic material suitable for dating undergoes several recycling cycles within fluvial systems and may hence significantly overestimate the age of sediment deposition (e.g.,

Hait et al., 1996; Stanley and Hait, 2000; Stanley and Chen, 2000; Stanley, 2001). Furthermore, unconstrained reservoir effects (e.g., Törnqvist et al., 2015), a lack of in-situ material suitable for dating (e.g., Chamberlain et al., 2020) as well as the release of 'old' CO_2 from burning of fossil fuels together with plateaus in the calibration curve (cf. Taylor 2018) can limit the application of radiocarbon dating in deltas.

An alternative to radiocarbon is luminescence dating, enables the direct determination of deposition ages for sediments (cf. Preusser et al., 2008; Rhodes, 2011). It has been shown that even young delta deposits can be dated successfully using this technique (e.g., Shen and Mauz, 2012; Chamberlain et al., 2017; Chamberlain and Wallinga, 2019). Since the pioneering work by Nanson et al. (1991), there have been an increasing number of publications that have used this approach to date the dynamics of deltas. For example, the early to middle Holocene Rhine-Meuse Delta architecture was reconstructed by investigating fluvial and tidal facies deposits (Hijma et al., 2009). For the Mekong Delta, luminescence dating enabled the definition of delta formation as a lateral propagation for the late Holocene with a set of successive emergences of longshore river mouth bars aggrading into the beach ridges (Tamura et al., 2012). This study revealed that the geometry of the Mekong Delta is controlled by the joint effects of tides, waves, the river, and basement features. Chamberlain et al. (2018) showed that a large portion of the Mississippi Delta grew surprisingly constantly during the late Holocene with progradation rates of 100 to 150 m per year, producing 6 to 8 km^2 of land gain per year. Similar studies have been published for the Yangtze River Delta (Nian et al., 2018; Gao et al., 2019; Wang et al., 2019) and several other deltas worldwide, but very little work from South America has been published on this topic so far (e.g. Guedes et al., 2011; Goodbred et al., 2020).

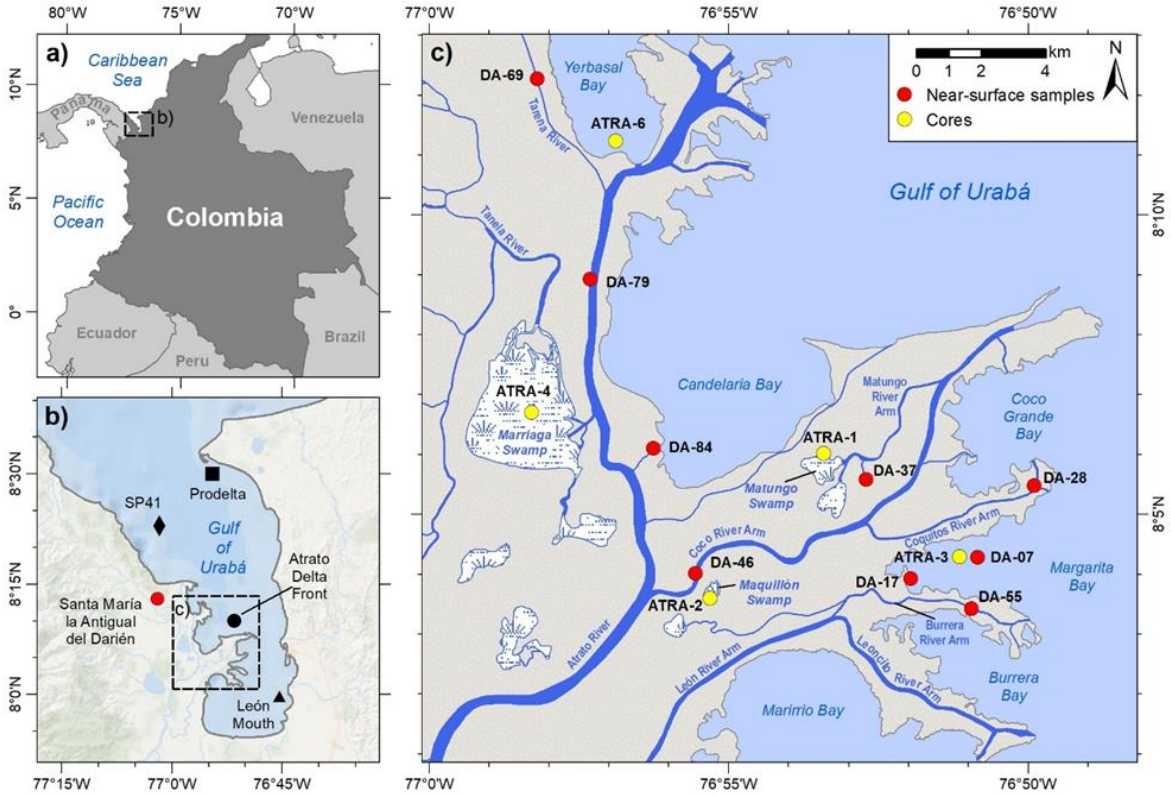

Figure 2.1 a) Location of the study area in north-western Colombia and b) within the Gulf of Urabá. Core locations of previous studies of Rúa et al. (2014, 2016), and Vélez and Aguirre (2016), are shown as mentioned in the text. c) Sediment cores and near-surface samples were collected from across the Atrato Delta (Data source: Agustín Codazzi Geographic Institute of Colombia 2017).

This study focuses on the Atrato Delta, an inner-bay 'bird-foot' delta (Mississippi-type) at the western margin of the Gulf of Urabá in northern Colombia, on the Caribbean Sea (Vernette et al., 2002) (Figure 2.1). The Atrato Delta is fed by the third largest river system of Colombia, in terms of its sediment load in relation to its catchment area size, after the Amazon and Magdalena Rivers. The Atrato River encompasses an area of 38.000 km^2 and comprises more than 150 tributaries. The main channel stretches over more than 700 km and the area receives about 2500 mm of annual precipitation on average, which is mainly falls during the wet season (March to November).

The southern part of the Atrato River valley is characterized by flatlands with the meandering main channel surrounded by jungle and swamps (Thomas et al., 2007). South of the delta plain, the León River arm branches off of the trunk (Atrato River) towards the east and further down-stream separates into two further river arms, the Leoncito and Burrera (Figure 2.1c), which both form individual bird foot deltas. The main river arm of the Atrato continues to the north and forms a large bird foot delta at Yerbasal Bay. The Coco River arm branches off the trunk towards the east further south and also forms a bird foot delta, as does the Coquitos River arm (Figure 2.1c). The Atrato Delta comprises a complex pattern of muddy, intertidal planes with marshes, swamps and mangroves, river-marine plains, flood zones and beaches (Blanco-Libreros, 2016; CIOH, 2009; Thomas et al., 2007), developed over a deltaic plain gradient of $3.07 * 10^{-5}$ mm^{-1} (López and Restrepo, 2007). The bays are filled with sediments through small inlets linked to the Atrato river mouths, mainly during flooding periods (Vann, 1959).

The Atrato Delta occupies an area of 672 km^2 and is situated on a large flat terrain formed by unconsolidated lacustrine and alluvial deposits of the Quaternary (Blanco-Libreros, 2016; Post, 2011), formed by clay and silty detritic sediments of low to medium sorting (IGAC and INGEOMINAS, 2001) Sediments from erosive processes are carried to the delta by channels and inlets (González and Londoño, 2002b; IGAC and INGEOMINAS, 2001). Geological sources of sediments in the Atrato basin are lava flows of basaltic composition, tuffs interspersed with siliceous and calcareous chert, limestones, mudstones, siltstones, and fine-grained sandstones (Rodríguez and Zapata García, 2012; Bedoya et al., 2007). The main intrusive rocks are tonalites to granodiorites with quartzdirites variations (Lugo et. al, 2003; Chakrabarti and Durango, 1979). Secondary sedimentary rocks to the southwest of the delta are marls, claystones, detritic limestones, and fine to medium sandstones (Zapata, 2002; Duque-Caro, 1990; Haffer, 1967).

The delta is delimited to the west by a set of steep mountains and cliffs and to the east by several bays of the Gulf of Urabá. In recent years, substantial progradation of the delta into the gulf has been observed, representing almost 1.8 km^2 of new land formed during the past three decades (Vélez et al., 2020). The delta progradates into the Gulf of Urabá under a microtidal regime that ranges between 0.5 m and 0.7 m (Post, 2011; Vernette et al., 2002),. Information about sea level variations in the Gulf of Urabá during the last 200 years is not conclusive. On one hand, authors such as Gomitz and Lebedeff (1987) mentioned a global sea level rise of 20 cm between AD 1880 and 1980, with a 1 – 2mm a^{-1} increase mentioned by Robertson and Martínez (1999) for our target area. On the other hand, Vélez and Aguirre (2016), mentioned a decrease in sea level rise during the last 100 years.

The Atrato Delta represents a diverse ecosystem and forest reserve, as part of one of the most humid regions of Colombia and has recently been declared a national heritage region.

In addition, the region is in the focus of social-political interests of the national government, as it is economically under-developed. Over the past decades, the area has been affected by social and political conflicts, deforestation, and pollution from gold and platinum mining. To improve the economic situation of the region, an expansion of local harbours is considered at different points in the Gulf of Urabá. However, the navigability of these harbours might be negatively affected by the progradation of the delta even on decadal timescales. Hence, studying the sediment dynamics of the delta in response to both natural and anthropic changes will not only be of scientific value but may also provide important information for policy makers.

Previous research in the region focused on aspects such as heavy metal contamination from mining (Vallejo et al., 2016; Palacios et al., 2018; Palacios-Torres et al., 2019), hydrodynamics in the Gulf of Urabá (Escobar, 2011; Escobar et al., 2015; Rúa et al., 2016), and on the sediment load at the Atrato River mouth (Álvarez and Bernal, 2007). Rúa et al. (2014, 2016) and Vélez and Aguirre (2016) analysed four sediment cores in the Gulf of Urabá and based the chronology of three of their sequences (León Mouth, Prodelta and SP41; Figure 2.1b) on bulk sediment radiocarbon dating. However, these studies considered neither the problem of potential reworking of organic material or reservoir effects, nor the uncertainties of calibration. Hence, the reported deposition rate of between 0.2 and 1-8 cm a^{-1} has to be considered with caution. For the fourth sequence (Delta front/SP26) the chronology was estimated using mercury (Hg) concentrations in the core, which were assumed to rise after the Spanish colonization of the region (Rúa et al., 2014).

The investigations on the Atrato Delta presented here represent one of the first studies to apply luminescence dating to delta sediments in South America. A series of samples was taken from deposits in the main river channel, swamps, the mouth of the delta, and connected bays scattered over the main delta body. The aim was to obtain an overview of the age of deposition in the delta. However, while the ultimate goal was to establish an independent chronology of late Holocene sedimentation in the Atrato Delta, this will ultimately require a more comprehensive approach that includes remote sensing, provenance analyses, and a detailed sedimentology of many samples. Nevertheless, applying luminescence dating is seen as the foundation to understand recent sediment dynamics in this area. In contrast to previous studies, the present contribution focuses mainly on spatial and temporal dynamics in the terrestrial part of the delta. Beside the regional aspects, this study is seen as a first step towards a better understanding of the sedimentation dynamics in tropical deltas.

2.3 Methodology and procedures

2.3.1 Principles and problems of luminescence dating

Luminescence dating utilises a light-sensitive signal present in feldspar and quartz minerals (cf. Aitken, 1998; Preusser et al., 2018; Rhodes, 2011). The signal is released in the form of photons (light) when minerals are exposed to stimulation energy. Within natural surface processes, the stimulation energy will be the light of the sun. The event being dated is the burial of the sediment grains, assuming the latent luminescence signal in the minerals was complete reset (zeroed) during exposure to sunlight, which takes place during sediment transport. Once buried and sealed from light exposure, a new signal is induced by the interaction of ionising radiation originating from radioactive decay and

cosmic radiation within the crystal structure of the target minerals. As a result, latent luminescence increases with time proportionally to the rate of radiation in the sediment.

For dating, two values have to be determined. First, the amount of radiation accumulated since burial and, second, the rate of radiation in the sampled sediment. The first value, the equivalent dose (D_e) in Gray (1 Gy = 1 J kg^{-1}), is quantified by measuring the light emitted by the natural sample during light exposure (Optically Stimulated Luminescence, OSL). This is done in the laboratory using special devices that comprise a stimulation (i.e. diodes of certain colour) and a detection unit (a photon-multiplier). The same aliquot is subsequently exposed to an artificial, energy-calibrated radiation source and the response of the sample is recorded during further optical stimulation. By this procedure, it is possible to describe the function of how radiation is transferred into OSL signals for an aliquot. This allows calculating the radiation dose the sample has absorbed in nature. The second value, the dose rate (D) in Gray per year (Gy a^{-1}), is derived from the concentration of radioactive elements (K, Th, and U) in the sample. From this, the amount of radiation energy is calculated using dose conversion factors considering the samples geometry (grain-size etc.; cf. Guérin et al., 2011) and cosmic radiation is calculated from the geographic position modified by overburden (shielding; Prescott and Hutton, 1994).

For the present study, three issues required consideration. (1) Although the mineral of choice in dating young sediments is quartz, tested sand-sized quartz from the Atrato Delta emitted low to no OSL signal. This phenomenon is known from several other regions where quartz is freshly derived from bedrock (e.g., Preusser et al., 2006; Sawakuchi et al., 2011). Therefore, feldspar was chosen, and IR stimulation was used for D_e determination (Infrared Stimulated Luminescence, IRSL). (2) Feldspar is affected by an instability of the luminescence signal over time (anomalous fading; Wintle 1973), which causes D_e and thereby age underestimation. To correct for this phenomenon, Huntely and Lamothe (2001) have suggested procedures to monitor the signal loss in laboratory experiments (cf. King et al., 2018). It was shown that the effect of fading can be reduced or even eliminated by carrying out a second IR stimulation measurement after the first IRSL but at elevated temperature (post-IR IRSL or pIR; Buylaert et al., 2009). However, the decrease in fading is at the cost of bleachability, i.e. pIR signals require more time to be zeroed than IRSL (Buylaert et al., 2012). (3) The presumption in luminescence dating is that the signal was completely reset by sunlight prior to deposition. However, in river systems dominated by suspended load transport, a high level of light absorption is caused by turbidity in the water column (Ditlefsen, 1992). Hence, a partial resetting of the luminescence signal in at least some grains is to be expected, which will cause overestimation of ages. To assess the level of signal resetting, several approaches have been proposed two of which were applied this study: (a) IRSL and pIR D_e values are compared with a large offset (beyond the difference explained by the potential effect of fading) indicating incomplete resetting of at least the pIR signals (Buylaert et al., 2013). (b) Detecting and correcting for the effect of partial resetting is possible by measuring a large number of individual grains, as each grain will have its own bleaching history (Duller, 1994). The distribution of the individually obtained D_e values may present populations of partially and likely completely reset grains, the latter of which can be extracted and used as the representative for the age determination (cf. Galbraith and Roberts, 2012). Because of the low IRSL intensities of samples from the Atrato Delta, likely caused by a low number of grains emitting IRSL, a few tens of grains were measured at a time to ensure sufficient signal levels.

2.3.2 Sampling and sample preparation

As part of two field campaigns carried out in the delta in 2016 and 2017, nine samples were collected from near surface sediment deposits and five sediment cores were drilled for luminescence dating. Figure 1c shows the locations of the sampling sites and their nomenclature and Table 2.1 lists the details of the sampling context. Near-surface samples were taken with an Eckman dredge at water depths between 1.3 m and 6.0 m, with a riverbed sampling thickness between 3 cm and 5 cm (one of the samples was taken manually from a 0.90 m deep trench). One was taken from a trench excavated by hand. To avoid sunlight exposure, sampled sediments were carefully covered during sampling with a large black blanket, and double bagged in black plastic once sampled.

The five cores (Atra-1: 2.18 m, Atra-2: 2.11 m, Atra-3: 1.70 m, Atra-4: 2.20 m, Atra-6: 1.08 m) were obtained using a Livingstone Bolivia Piston Corer, equipped with black PVC liners. For transportation, the liners were sealed and wrapped in black plastic bags for additional light protection. An initial sample preparation was carried out in the red-light laboratory at EAFIT University of Medellin, Colombia. Cores were split in half lengthwise, and 21 sub-samples for luminescence dating were taken from top, middle, and basal parts of the cores. Samples were weighed, dried at 40°C for 24 hours and sediment water content was obtained (Table 2.2).

Table 2.1 Overview of locations sampled for this study.

Code	Location	Method	Context
ATRA-1	Matungo Swamp	Corer	Swamp on delta plain
ATRA-2	Marquilllón Swamp	Corer	Swamp on delta plain
ATRA-3	Margarita Bay	Corer	Former pro-delta
ATRA-4	Marriaga Swamp	Corer	Swamp on delta plain
ATRA-6	Yerbasal Bay	Corer	In front of new mouth, opened in 2012
DA-07	Margarita Bay	Dredged	Former pro-delta
DA-17	Margarita Bay coast	Dredged	Former pro-delta
DA-28	Coquitos River Arm	Trench	Overbank deposits near channel
DA-37	Matuntugo Swamp	Dredged	Swamp on delta plain
DA-46	Coco River Arm	Dredged	Swamp on delta plain
DA-55	Burrera River Arm	Dredged	Less active river arm
DA-69	Tarena River	Dredged	Main channel until 1990, now inactive
DA-79	Main Atrato Channel	Dredged	Base of the main channel
DA-84	Candelaria Bay coast	Dredged	Small channel that flows towards the bay

Sample preparation was conducted in the laboratory at the University of Freiburg under subdued red-light conditions. Samples were sieved and treated with HCl (30%) and H_2O_2 (30%) to remove carbonates and organic matter, respectively. Depending on grain-size composition, either fine-, coarse-grained or both fractions were chosen for D_e determination. To extract the fine-grained fraction (4-11 µm), sample material was suspended in 0.01 N sodium-oxalate and treated in an ultrasonic bath for ca. 5 min to separate clay coagulates. The fine-grained fraction was divided from the suspension following Stokes' Law (Frechen et al., 1996). For some of these samples, part of the material was treated with hydro-fluorosilicic acid (30% H_2SiF_6) for one week to remove feldspar and obtain a quartz-rich fraction. However, most material vanished during this procedure and the remains did exhibit only a very weak (if any) OSL signal, with a slow decay shape not typical for quartz. For the coarse-grained fraction, material was separated using sodium-poly-tungsten solutions with densities of 2.70 g cm^{-3} to isolate heavy

minerals and 2.58 g cm^{-3} to isolate K-feldspar from quartz and plagioclase. For some samples, quartz was etched in 30% HF for 60 min to remove plagioclase together with the out rim of the quartz grains and tested for OSL response. Due to the absence of suitable OSL signals all further work focused on feldspar.

Table 2.2 Summary data of luminescence dating. Lab code, overburden (depth) corrected for water column, grain-size extracted for luminescence measurements, sediment moisture, concentration of dose rate relevant elements (K, Th, U), dose rate, number of aliquots used for De determination, observed overdispersion (od.) in sand-size samples, model used for data analyses (CAM = Central Age Model, MAM = Minimum Age Model), mean De for IRSL and pIR as well as the resulting ages.

Lab code	Depth (cm)	Grain size (µm)	W (%)	K (%)	Th (ppm)	U (ppm)	D (Gy ka^{-1})	n	od.	Mod.	D_e IRSL (Gy)	D_e pIR (Gy)	Age IRSL (a)	Age pIR (a)
DA-07	115	4-11	81.1	1.13±0.10	3.42±0.19	2.25±0.27	1.49±0.13	5	-	CAM	0.36±0.02	3.92±0.19	240±20	2630±170
DA-17	105	4-11	77.6	0.98±0.10	3.18±0.19	4.05±0.38	1.70±0.16	5	-	CAM	0.17±0.01	1.49±0.08	100±10	860±60
DA-28	60	4-11	76.2	0.94±0.06	2.56±0.15	1.23±0.21	1.11±0.08	5	-	CAM	1.55±0.07	7.95±0.39	1400±100	7160±530
DA-28	60	100-150	76.2	0.94±0.06	2.56±0.15	1.23±0.21	1.13±0.10	40	0.63	MAM	1.43±0.23	-	1040±170	-
DA-37	165	4-11	74.0	1.06±0.07	3.82±0.21	1.50±0.29	1.31±0.10	4	-	CAM	0.97±0.05	5.54±0.29	740±60	4230±340
DA-46	165	4-11	72.9	0.84±0.05	3.02±0.17	1.35±0.22	1.11±0.07	5	-	CAM	1.22±0.06	7.17±0.35	1100±100	6460±390
DA-46	165	100-150	72.9	0.84±0.05	3.02±0.17	1.35±0.22	1.35±0.18	40	0.57	MAM	2.87±0.35	-	2130±270	-
DA-55	165	4-11	76.9	1.09±0.10	3.35±0.19	2.36±0.31	1.45±0.11	5	-	CAM	0.74±0.03	4.88±0.23	510±40	3370±230
DA-69	125	4-11	65.7	0.92±0.07	2.81±0.16	1.63±0.24	1.26±0.08	5	-	CAM	1.33±0.06	6.49±0.31	1060±80	5150±320
DA-79	315	4-11	69.7	0.95±0.07	2.81±0.16	0.98±0.25	1.07±0.10	4	-	CAM	2.09±0.15	11.67±0.47	1960±180	10930±680
DA-79	315	100-150	69.7	0.95±0.07	2.81±0.16	0.98±0.25	1.33±0.18	40	0.53	MAM	2.85±0.34	-	2130±270	-
DA-84	80	4-11	80.8	0.98±0.08	2.97±0.17	1.19±0.25	1.12±0.07	4	-	CAM	1.73±0.09	9.63±0.53	1550±100	8600±530
DA-84	80	100-150	80.8	0.98±0.08	2.97±0.17	1.19±0.25	1.38±0.17	40	0.71	MAM	2.07±0.26	-	1500±200	-
ATRA-1-1	148	63-200	61.2	0.94±0.06	3.39±0.20	1.81±0.24	1.59±0.09	39	0.40	MAM	0.45±0.02	-	280±20	-
ATRA-1-2	152	4-11	88.1	0.87±0.06	3.30±0.19	1.20±0.30	1.03±0.08	5	-	CAM	0.44±0.02	3.26±0.15	430±30	3170±260
ATRA-1-5	195	4-11	55.7	0.95±0.07	3.02±0.17	1.20±0.30	1.25±0.10	5	-	CAM	0.65±0.03	3.61±0.18	520±40	2880±190
ATRA-1-7	241	63-200	68.6	0.84±0.06	3.32±0.22	2.25±0.27	1.53±0.12	40	0.58	MAM	0.89±0.06	-	580±50	-
ATRA-1-10	318	4-11	82.4	1.14±0.08	3.56±0.20	2.02±0.28	1.35±0.10	5	-	CAM	1.00±0.05	3.79±0.18	740±60	2820±180
ATRA-2-1	266	63-200	73.0	0.80±0.06	3.04±0.19	1.48±0.22	1.36±0.11	40	0.45	MAM	0.46±0.12	-	330±90	-
ATRA-2-3	322	4-11	63.5	0.93±0.07	3.30±0.18	1.38±0.26	1.20±0.07	5	-	CAM	1.18±0.05	4.88±0.24	970±70	4000±260
ATRA-2-8	464	4-11	73.6	0.95±0.08	3.25±0.19	1.41±0.24	1.14±0.09	5	-	CAM	1.85±0.09	6.55±0.31	1620±130	5730±460
ATRA-3-1	166	4-11	79.7	1.01±0.07	3.12±0.23	3.40±0.35	1.59±0.13	4	-	CAM	0.24±0.01	2.15±0.12	150±10	1360±120
ATRA-3-3	225	63-200	65.2	1.07±0.08	3.08±0.22	3.38±0.34	1.84±0.18	40	0.46	MAM	0.62±0.09	-	340±50	-
ATRA-3-5	276	63-200	61.8	0.93±0.08	3.23±0.22	3.44±0.34	1.88±0.19	44	0.59	MAM	0.57±0.09	-	330±50	-
ATRA-3-7	323	4-11	97.5	1.05±0.08	2.73±0.16	1.97±0.26	1.15±0.09	5	-	CAM	1.30±0.06	4.99±0.24	1130±90	4350±340
ATRA-4-1	201	4-11	89.1	0.70±0.05	1.96±0.13	0.50±0.12	0.72±0.05	5	-	CAM	0.36±0.02	1.53±0.09	500±40	2120±120
ATRA-4-3	243	63-200	68.0	0.65±0.05	2.21±0.18	1.00±0.27	1.24±0.18	35	0.90	MAM	0.75±0.18	-	630±150	-
ATRA-4-5	279	4-11	88.8	0.83±0.07	2.49±0.15	2.03±0.26	1.10±0.09	5	-	CAM	0.58±0.03	3.68±0.21	530±40	3350±290
ATRA-4-9	360	4-11	53.2	1.02±0.07	3.05±0.17	2.00±0.26	1.49±0.12	5	-	CAM	1.29±0.06	4.63±0.24	870±70	3110±260
ATRA-4-9	360	100-150	53.2	1.02±0.07	3.05±0.17	2.00±0.26	1.64±0.12	40	0.48	MAM	1.43±0.09	-	870±70	-
ATRA-4-12	423	4-11	91.9	1.01±0.08	2.26±0.16	1.59±0.27	1.05±0.08	5	-	CAM	1.18±0.05	3.15±0.15	1130±90	3010±240
ATRA-4-12	423	100-150	91.9	1.01±0.08	2.26±0.16	1.59±0.27	1.30±0.10	40	0.60	MAM	1.87±0.09	-	1680±130	-
ATRA-6-1	130	63-200	55.8	0.99±0.08	3.60±0.24	1.87±0.28	1.68±0.17	40	0.88	MAM	0.26±0.05	-	150±30	-
ATRA-6-3	182	4-11	40.7	0.98±0.07	2.55±0.15	1.63±0.24	1.49±0.11	5	-	CAM	1.27±0.06	6.74±0.32	850±70	4520±350
ATRA-6-3	182	100-150	40.7	0.98±0.07	2.55±0.15	1.63±0.24	1.66±0.18	40	0.33	MAM	0.74±0.11	-	450±70	-
ATRA-6-5	199	63-200	42.6	0.70±0.06	2.34±0.19	3.63±0.33	1.84±0.17	40	0.60	MAM	0.85±0.07	-	460±40	-
ATRA-6-7	231	4-11	86.4	1.03±0.08	2.81±0.17	2.31±0.30	1.29±0.10	5	-	CAM	0.84±0.04	4.92±0.23	650±50	3810±310
ATRA-6-7	231	100-150	86.4	1.03±0.08	2.81±0.17	2.31±0.30	1.48±0.13	40	0.53	MAM	1.24±0.09	-	840±70	-

2.3.3 Measurement procedures

All luminescence measurements were carried out on a Freiberg Instruments *Lexsyg Smart* (Richter et al., 2015), equipped with a Schott BG39 and a AHF BrightLine HC 414/46 detection filter. D_e determination was carried out following the pIR-protocol by Reimann and Tsukamoto (2012) developed for dating young samples (< 500 years). This Single-Aliquot Regenerative Dose (SAR) protocol comprises a preheat at 180°C for 10 s, followed by an initial IRSL stimulation at 50°C for 100 s, and a subsequent second stimulation at 150°C for 120 s. The same procedure was applied to both polymineral fine-grains (10 mm, several hundred-thousand grains) as well as sand-size feldspar extracts (2 mm aliquots, several dozen grains). No 'hot bleach' was added to the protocol to avoid potential thermal transfer and additional sensitivity change. For D_e determination, the initial 20 s of the detected IRSL signal were used after the last 20 s were deducted as background. The performance of the measurement protocol was checked for IRSL in dose

recovery tests (bleached by blue LEDs for 5 min) for samples ATRA-3-3 (applied dose = 5 Gy, n = 12, recovery ratio = 1.05), ATRA-1-7 (1 Gy, n = 6, 1.03), and ATRA-4-12 (2 Gy, n = 6, 1.07).

As initial screening revealed substantial differences in the D_e for IRSL and pIR, a wide range of regenerative dose points were applied within the SAR protocol for the construction of dose response curves. For polymineral fine-grains (PM), four to five aliquot measurements are considered sufficient, but for sand-size feldspar samples (F) 40 aliquots were measured for a statistically solid analysis. The small number of replicate measurements for fine-grains is justified by the fact that the large number of grains on the aliquot will average out any scatter due to partial bleaching or other effects. Overall, despite the rather low IRSL signal level, samples showed quite good SAR performance and only few aliquots had to be rejected as they failed to show recycling ratios within 10% of unity. Following Buckland et al. (2019), recuperation was not considered a useful rejection criterion.

2.3.4 Luminescence performance

Although the luminescence signals of the investigated samples are generally low, they are bright enough to allow proper calculation of D_e values from fine-grains for both the IRSL and the pIR signals (Figure 2.2 a-d). However, the pIR signals from sand grains are close to background (Figure 2.2 e), and for most aliquots the proper calculation of a D_e value was impossible (Figure 2.2 f).

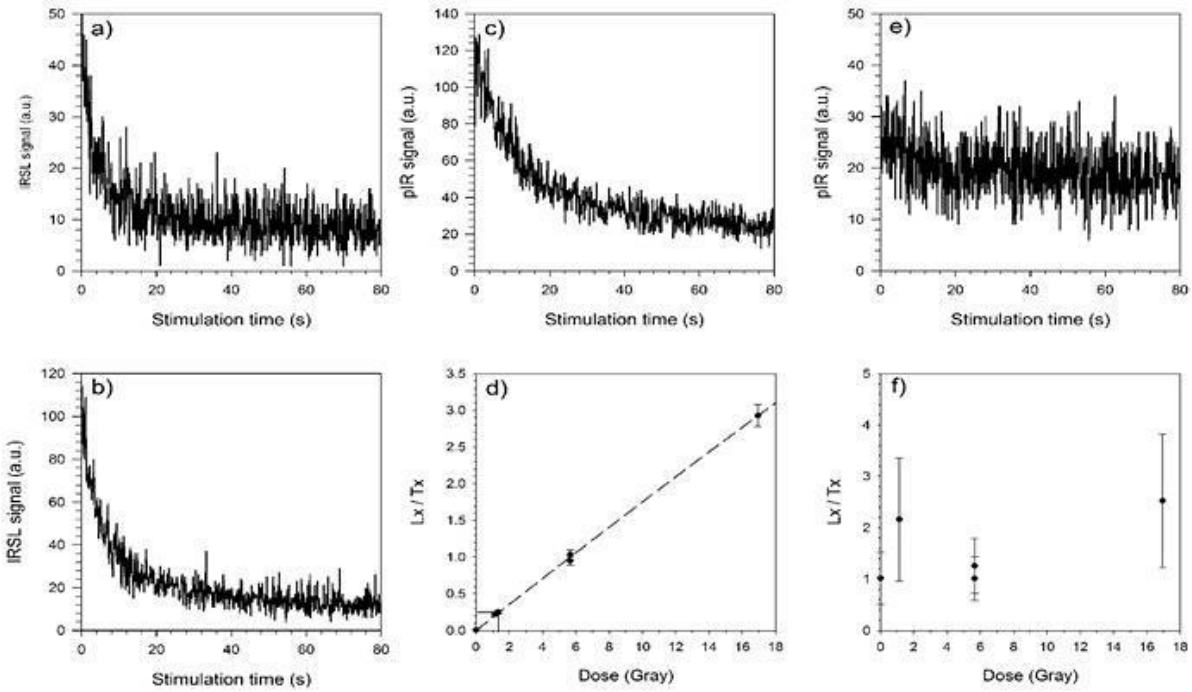

Figure 2.2 Examples characterising the luminescence properties of the investigated samples. Shown is the signal of the natural luminescence. a) IRSL decay curve of K-feldspar sample ATRA-3-3F; b) IRSL decay curve of polymineral fine-grain sample DA-07; c) pIR decay curve of polymineral fine-grain sample DA-07; d) dose response curve of K-feldspar of sample ATRA-3-3F; e) pIR decay curve of K-feldspar sample ATRA-3-3F; f) plot of Lx/Tx measured within the SAR protocol for pIR of example shown in e) does not reveal a clear dose response relation.

Hence, pIR results from sand are not presented. The low luminescence intensities observed are rather unusual for feldspar. It is speculated that this is related to tropical weathering rather than bedrock geology, which is complex in the catchment and comprises a wide range of intrusive, volcanic, and sedimentary rocks.

For fine-grains, average D_e values were calculated using the Central Age Model (CAM; Galbraith et al., 1999), as these measurements reveal little scatter and symmetric distributions. For sand-size grains, D_e distributions are often widely scattered and positively skewed with a distinct population of values at the lower edge (Figure 2.3). Such observations are usually interpreted to represent evidence of differential bleaching of the IRSL signal in the different aliquots, with the lower population likely representing aliquots with fully reset signals at deposition (Olley et al., 1998; Duller, 2008). As values of the lower population scatter due to additional factors such as the effect of micro-dosimetric inhomogeneity (e.g., Mayya et al., 2006), application of a statistical treatment is required. Here, the Minimum Age Model (MAM; Galbraith et al., 1999) is applied as a logged MAM-3 with the R-script of Burow (2019). A critical point when applying this procedure is the selection of an appropriate sigma_b value, which represents the expected scatter present in a well-bleached sample. Unfortunately, no information on well-bleached samples is available from the study area that could function as an analogue. To identify a representative sigma_b value, all obtained D_e distributions were statistically investigated and manipulated by removing outliers at the upper part of the distributions until the parameters skewness and kurtosis reached values likely representing well-bleached samples (cf. Arnold and Roberts, 2009). According to these analyses, the most likely value of sigma_b is 0.20. Sensitivity tests show that even for sigma_b values of 0.15 and 0.25 the MAM D_e values are within the uncertainties of the D_e values calculated using a sigma_b of 0.20 for the vast majority of all samples. Hence, confidence in a sigma_b value of 0.20 as a robust choice was gained.

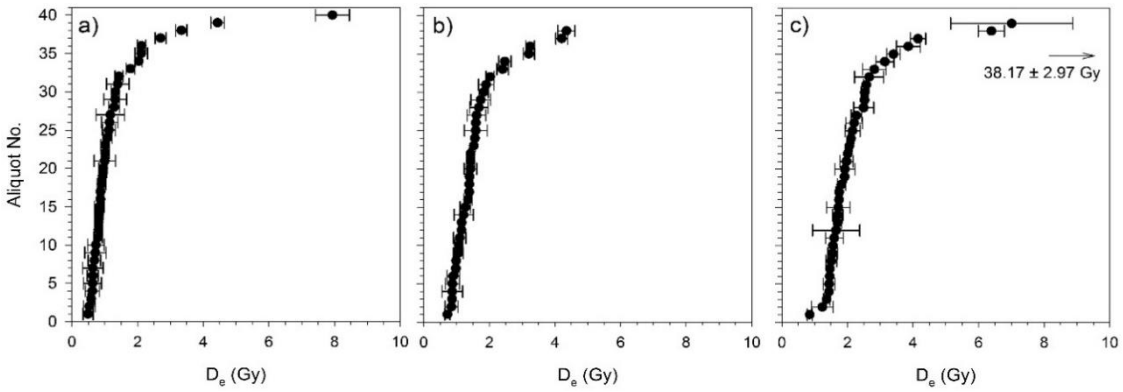

Figure 2.3 De distributions of three selected samples from the study area. De distributions of three selected samples from the study area: a) ATRA-1-7 (od. = 0.58); b) ATRA-6-7 (od. = 0.53); c) ATRA-4-12 (od. = 0.60).

The stability of the different luminescence signals was investigated with storage tests on three previously measured aliquots of two samples. L_n/T_n was determined for prompt measurements and for four different delay times (up to 10 h). The entire procedure was repeated three times to check for reproducibility. Using this procedure, an average (central value) fading rate of -1.13±1.28% per decade for ATRA-3-3 (g-value; normalised to 2 days) was determined, implying that the pIR signal of the investigated samples does not fade. For IRSL, the determined fading rates are 0.92±0.53% (ATRA-3-3) and 1.65±0.47% (ATRA-4-12) per decade. It should be noted that fading rates of about 1% per decade have

been considered by several authors to likely represent a measurement artefact rather than a fading signal (e.g., Thiel et al., 2011a,b; Li et al., 2014). Applying a fading correction will increase IRSL D_e values by ca. 10%. A fading correction has not been applied for the following reasons; 1) the large uncertainty associated with the calculated fading rate will introduce a large systematic uncertainty on the age estimates from a measurement artefact, and 2) the correction will overall lead to only minor changes in the age values that are not very relevant for this study, in particular not for the calculation of sediment depositions rates.

2.3.5 Dose rate calculation

The concentration of K, Th, and U was determined using Neutron Activation Analyses (NAA) by Bureau Veritas Laboratories, Canada (www.bvlabs.com). The performance of this laboratory was blind tested using certified reference material (GeoPT13 'Köln Loess'; Potts et al., 2003 and http://iageo.com/uok-loess/) together with the samples to be measured. Calculation of dose rates was carried out with ADELEv2017 software (https://add-ideas.com). An a-value of 0.07±0.02 was assumed and sediment water content with a 10% uncertainty was applied. For cosmic dose calculation, following Prescott and Hutton (1994), overburden was calculated from the amount of sediment cover plus half the water depth (due to the lower density) at sampling time where applicable. For samples taken with a dredge (all DA samples but DA-28), no direct depth control was feasible and a general depth of 30 cm was assumed.

2.3.6 Age-depth models and accumulation rate calculation

Age-depth models were determined using the CRAN *rbacon* package in R (Blaauw and Christen, 2018). While most commonly used for radiocarbon-based chronologies, *rbacon* works with any type of numerical ages (Blaauw and Christen, 2011), and was therefore applied to cores ATRA 1, 2, 4 and 6 using the IRSL ages produced in this study. For comparison with sedimentation rates of the Gulf of Urabá, previously published radiocarbon ages for three sediment cores were also included in this study (Rúa et al., 2016; Vélez and Aguirre, 2016; Table 2.3, Figure 2.1b), although potential problems regarding the accuracy of the ages obtained (bulk sediments, reservoir effect not taken into account) was always given full consideration.

Two of these cores, Prodelta and SP41, are located close to the entrance of the Gulf of Urabá. The core León Mouth is located, by contrast, in the south of the Gulf of Urabá, at the mouth of the León River, southeast of the Atrato Delta (Figure 1.1b). Radiocarbon ages from literature were calibrated using the IntCal13 calibration curve (Reimer et al., 2013) integrated in *rbacon* and for comparison, with Oxcal 4.3 usings the same calibration curve (Bronk Ramsey, 2009;Table 2.4).

Age-depth models were computed with *rbacon* using Bayesian statistics by dividing a sediment core in vertical slices (by default at 5 cm intervals) and estimating accumulation rates through a series of Markov Chain Monte Carlo iterations. *rbacon* requires prior information, i.e. an estimate of accumulation rate fitting a gamma distribution. For age-depth models with relatively constant sedimentation rates, it will propose the most likely estimates for mean accumulation rates. However, for cores with hiatuses or distinct changes in accumulation rates, this information has to be supplied. *rbacon* ultimately provides age estimates for each cm of the core, including minimum and maximum 95%

confidence ranges, and weighted mean ages representing the 'best age fit' for each depth. Accumulation rates are recalculated for each cm of the investigated cores from the weighted mean ages produced by *rbacon* per cm depth, and summarized by their range (minimum, maximum) and mean values (Table 2.4).

Table 2.3 Calibrated radiocarbon ages for the Leon mouth, Prodelta (Rúa et al., 2016) and SP41 (Vélez and Aguirre, 2016) cores. Note: the Prodelta core published by Rúa et al. (2016) corresponds to core SP9 presented in Rúa et al. (2014) and Vélez and Aguirre (2016), and the Leon Mouth core to core SP43 presented in Rúa et al. (2014).

Core	Depth	^{14}C Age (a)	Age * (cal. a)	Age ** (cal. a)
	92	125 ± 35	275 - 9	253 - 13
Leon Mouth #	112	135 ± 40	282 - 5	272 - 31
	205	230 ± 35	425 - …	378 - 139
Prodelta #	49	140 ± 35	282 - 5	262 - 7
	113	390 ± 35	511-318	511 - 325
	200	960 ± 35	933-792	954 - 768
SP41 $	99	2325 ± 35	2456 - 2184	2410-2167
	190	2525 ± 35	2746 - 2490	2770-2622
	220	2845 ± 35	3063 - 2866	2988-2800

Data from Rúa et al. (2016).
$ Data from Vélez and Aguirre (2016); depths graphically determined.
* Individually calibrated dates, Program Oxcal 4.3 using IntCal 13, 95.4% confidence interval (https://c14.arch.ox.ac.uk).
** Age-depth model ages, CRAN *rbacon* package in R with IntCal 13, 95% confidence interval.

Table 2.4 Accumulation rates based on rbacon weighted average ages per cm; *this study; **data from Rúa et al. (2016); ***data from Vélez and Aguirre (2016). For ATRA 4, values in italics show alternative accumulation rates estimated by comparison to values determined for the other cores of this study and tested for validity using the CRAN *rbacon* package in R (Figure 2.4).

Core	Depth considered (cm)	Min. (mm a^{-1})	Max. (mm a^{-1})	Average (mm a^{-1})
ATRA-4*	0-82	16.7	25.0	20.0 *(10.0)*
ATRA-4*	161-225	1.1	1.2	1.1 *(2.0)*
ATRA-6*	0-108 (entire core)	1.7	2.3	2.0
ATRA-2*	0-211 (entire core)	1.6	2.1	1.9
ATRA-1*	0-218 (entire core)	3.3	5.3	4.7
ATRA-3*	0-118	4.5	5.6	5.1
Leon Mouth**	entire core	9.1	11.1	10.1
Prodelta**	entire core	2.0	2.2	2.1
SP41***	entire core	1.6	2.3	2.1

2.4 Results

In the following, investigated cores are presented from southeast to northwest. Firstly, core location is described, followed by sedimentological observations and interpretations, dating results, and a discussion of the age of surface samples taken in proximity to the core location. All sediment logs are presented together with the results of IRSL dating in Figure 4. The pIR ages are between 4 to more than 10 times greater than the IRSL ages (Table 2.2). As such cannot be explained by the low observed fading rates in the samples, the offset is thought to be caused by partial resetting of the pIR signal. Hence, the pIR ages for the silt fraction are not further discussed. Subsequently, accumulation rates resulting from the IRSL dating results are presented.

2.4.1 Sediment description and IRSL dating

Core ***ATRA-3*** was taken at a water depth of 3.2 m from Margarita Bay (Figure 2.1), where a substantial plume of sediment enters the sea, according to satellite images and our field observations. The plume originates from different river arms that prograde into the bay area (Burrera and Coquitos river arms). The lower part of the core (170-108 cm depth), consists of silt and clay predominantly, whereas the upper part (< 108 cm) comprises mainly clay with some silt at the very top. Considering the location of the core, the sedimentary environment is interpreted as shallow marine, in which the lower (older) part of the core seems to have been closer to the fine-grained sediment plume, whereas the upper (younger) part might have been more distant. The fining upward trend is likely explained by the delta arm prograding into the bay and the sediment input hence moving away from the sampled site, bypassing laterally. The basal IRSL age of the core is 1130±90 a (ATRA-3-07 PM), whereas two identical ages of 330±50 a (ATRA-3-05 F) and 340±50 a (ATRA-3-03 F) have been determined for the middle part of the sequence.

The age of the top sample is 150±10 a (ATRA-3-01 PM) and is consistent with IRSL ages of two samples dredged close-by from sediments (dark gray muds) of Burrera Bay (DA-07 PM: 240±20 a) and (DA-17 PM: 100±10 a). Sample DA-55 (dark gray mud with roots and some calcareous remains) was taken from a less active Burrera River Arm, characterized by slow flow and consequently low sediment transport. An IRSL age of 510±40 a (PM) implies low sedimentation at this spot. Two IRSL ages of sample DA-28 of 1400±100 a (PM) and 1040±170 (F) were determined for homogenous silty clay (likely overbank deposits) sampled in a trench of the Coquitos River Arm. These dating results imply that this arm has existed for at least 1000 a.

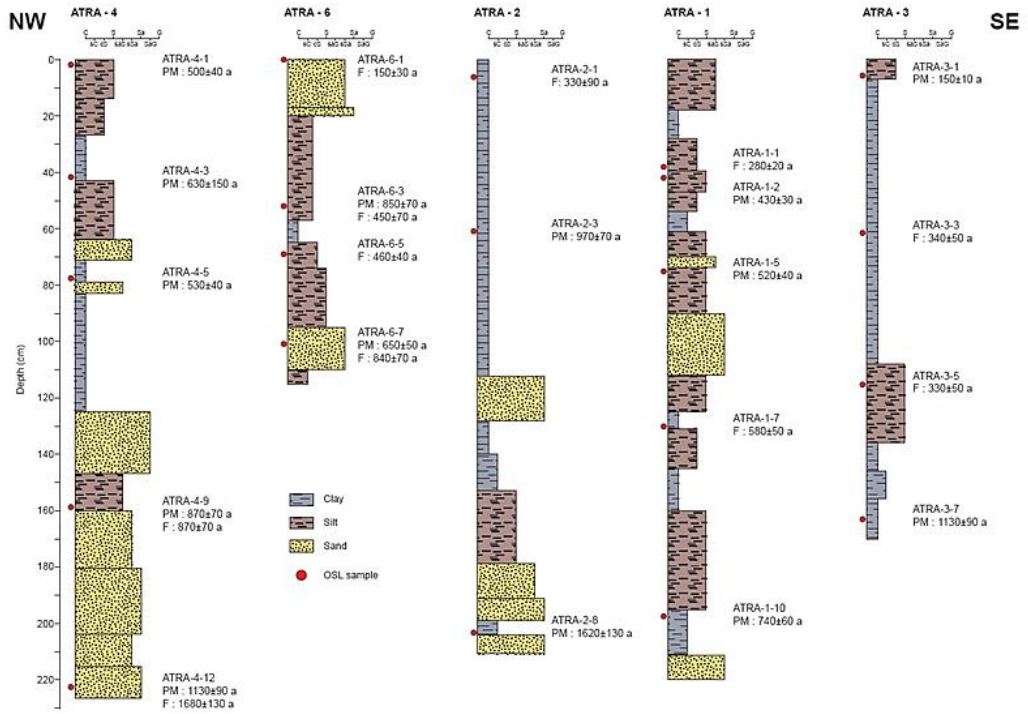

Figure 2.4 Sediment logs of all investigated cores together with IRSL ages.

ATRA-1 is located in the Matungo Swamp, near its shore at a water depth of 2.2 m. Water depth in the centre of the swamp reaches more than 6 m. The swamp is drained by the Matungo River Arm that joins the larger Coco River Arm to the northeast (Figure 2.1). The

sediment sequence comprises clayey to sandy sediment with a high content of organic material, likely representing the flooding of the swamp from the main channel. The lowermost IRSL age is 740±60 a (210 cm, ATRA-1-10 PM), followed by ages of 580±50 a (132 cm, ATRA-1-07 PM), 520±40 a (87 cm, ATRA-1-05 PM), 430±30 a (43 cm, ATRA-1-02 PM), and 280±20 a (40 cm, ATRA-1-01 PM). An IRSL age of 740±60 a (DA37 PM) was determined for a sample dredged from a small nameless swamp with a water depth of 3 m, neighbouring the larger Matungo Swamp. The higher IRSL age of the swamp bottom compared to the age determined for the larger swamp implies this area was less affected by sediment input through flooding.

ATRA-2 comes from the Maquillón Swamp that reaches a depth of more than 7 m. Coring was conducted in a narrow, widely overgrown channel at a water depth of 5.2 m. The lower part of the sediment sequence (211-153 cm) consists of silt and sand, whereof the latter being an indicator for relatively high-energy flows. The upper part (< 153 cm) consists entirely of clay with an increaseing in organic matter content towards the top. This likely represents overbank deposition in a more distal environment with regard to the main channel. The IRSL age of the basal part of the sequence is 1620±130 a (ATRA-2-8 PM), the upper middle part is dated to 970±70 a (ATRA-2-3 PM), and the top dates to 330±90 a (ATRA-2-1 F). A sample (DA-46; dark gray mud) taken by dredging the river channel of the Coco River Arm from a water depth of 3 m gave inconsistent IRSL ages of 1100±100 a (PM) and 2130±270 a (F) that are discussed below.

ATRA-4 was taken from the centre of the Marriaga Swamp, at a water depth of 4 m. The swamp is located to the west of the main Atrato River channel. The sediment sequence is comprised of a mainly sandy lower part (227-125 cm) and a predominantly silty to clayey upper part <125 cm). As in ATRA-3, this sequence likely represents a series of flooding events that occurred closer to the main plume in the lower (older) part of the core, and farther from the plume in the upper (younger) part of the core. The 160 – 147 cm section has shell fragments (not determinable) in a sandy silt matrix. The lowermost IRSL ages (ATRA-4-12) are 1130±90 a (PM) and 1680±130 a (F). The upper part of the coarser part has two identical ages of 870±70 a (ATRA-4-9 for both PM and F), followed by three ages of 530±40 a (ATRA-4-5 PM), 630±150 a (ATRA-4-3 F), and 500±40 a (ATRA-4-1 PM).

ATRA-6 was taken in Yerbasal Bay at a water depth of 2.5 m, in front of a new mouth of the Atrato River that, based on Google Earth satellite images and according to the inhabitants of the area, opened at the end of 2012. This area is, according to our observations, characterised by a quite strong but only surficial (< 3 m) fluvial current that terminates in a relatively calm bay. The very bottom of the core comprises clayey silt (> 5 cm thickness), followed by relatively coarse material (10 cm silt and sand). The middle part is quite fine-grained (mainly silty clay), the upper part (above 17 cm) consists again of coarse grains (sand and sandy silt). IRSL ages (ATRA-6-7) for the coarser part are 840±70 a (F) and 650±50 a (PM), whereas the middle part has two consistent feldspar ages of 460±40 a (74 -75 cm, ATRA-6-5) and 450±70 a (57-62 cm, ATRA-6-3). For the upper sample, an additional non-consistent age of 850±70 a was determined using PM. The age of the uppermost part of the sequence (2-6 cm, ATRA-6-1) is 150±30 a. Three samples have been taken via dredging in the wider vicinity of this core. Sample DA-69 (dark gray mud) is from an abandoned channel (called ‘Tarena’) with very slow water flow at the time of sampling, taken at a water depth of 2.2 m. The sample is a dark gray mud with an IRSL age of 1060±80 a (PM). Sediment from the base of the main channel of the Atrato River (DA-79, gray mud) was taken by dredging at a water depth of 6 m, where the channel has a

width of 250 m and shows a high flow. Two consistent ages of 1960±180 a (PM) and 2130±270 a (F) for gray mud has been determined. The final sample (DA-84) was taken to the east of the main channel, from a small channel that flows into the Candelaria Bay, at a water depth of 1.3 m. The silty to sandy sediment revealed consistent IRSL ages of 1550±100 a (PM) and 1500±200 a (F).

2.4.2 Accumulation rates

For ATRA- 2 and 6, the age-depth model outputs of *rbacon* suggest relatively similar accumulation rates of about 1.9, and 2.0 mm a^{-1}, respectively, whereas ATRA -1 is faster than ATRA-2 and 6 at 4.7 mm a^{-1} (Figure 2.5; Table 2.4). Calculations using radiocarbon ages from León Mouth, Prodelta, and SP41 cores provided accumulation rates of 10.1, 2.1, and 2.1 mm a^{-1}, respectively, although in the case of León Mouth, the large range of radiocarbon ages induces great uncertainties (Figure 2.5). These results are in accordance with the rates obtained with the luminescence technique, especially considering the uncertainties in bulk radiocarbon dating highlighted previously. By contrast, comparison between bottom and top ages for cores ATRA-4 and ATRA-3 suggests either a sharp change in accumulation rate and/or the presence of depositional hiatuses.

For core ATRA-3, a change of sedimentary units is observed between the two lower samples (ATRA3-3, ATRA-3-7). ATRA3-5 was taken from a sandy unit, ATRA-3-7 was obtained from clayey facies. This change in sedimentary pattern is reflected in a ca. 1000 - difference of the IRSL samples. Therefore, only the top part of the core (0-136 cm) was considered in the age-depth model and an apparent accumulation rate of 5 mm a^{-1} was calculated (Table 2.4). Unfortunately, with only one age for the lower part of ATRA-3, calculating accumulation rates below 136 cm is unfeasible.

For ATRA-4, the sedimentary record and individual IRSL ages suggest division of the core. Ages of around 500 a were obtained for the top 125 cm of more-or-less fine-grained facies whereas the lower part of the core consists of predominantly coarse-grained and significantly older deposits. An initial run with *rbacon* on individual portions defined by the IRSL dates obtained for the upper (U, 0-82 cm) and lower (L, 161-225 cm) parts of the core (Table 2.2) returned accumulation rates of ca. about 20 and 1 mm a^{-1} respectively.

These results are very different from all accumulation rates calculated for the other cores, and from those estimated for the core delta front (close to the Atrato Delta; Figure 2.1) at 2.7 mm a-1 to 10–15 mm a-1 (Rúa et al., 2016). Furthermore, large uncertainties of the individual IRSL ages introduce high uncertainties into the calculation. The pre-setting of the age-depth model with accumulation rate estimates of 10 mm a-1 for U and 2 mm a-1 for L, which correspond to the maximum and minimum accumulation rates observed in the other cores, also provided a coherent age-depth model (Figure 2.5). These prior accumulation rates for ATRA-4 may therefore be more in accordance with local sedimentary patterns. For discussion purposes, two age-depths models, both involving a change in accumulation rate at 125 cm depth (Figure 2.4), but using either the original *rbacon* assessment for accumulation rates of ca. 20 and 1 mm a^{-1} or the prior values of ca. 10 and 2 mm a^{-1} for U and L, respectively, are presented for ATRA-4 (Figure 2.5).

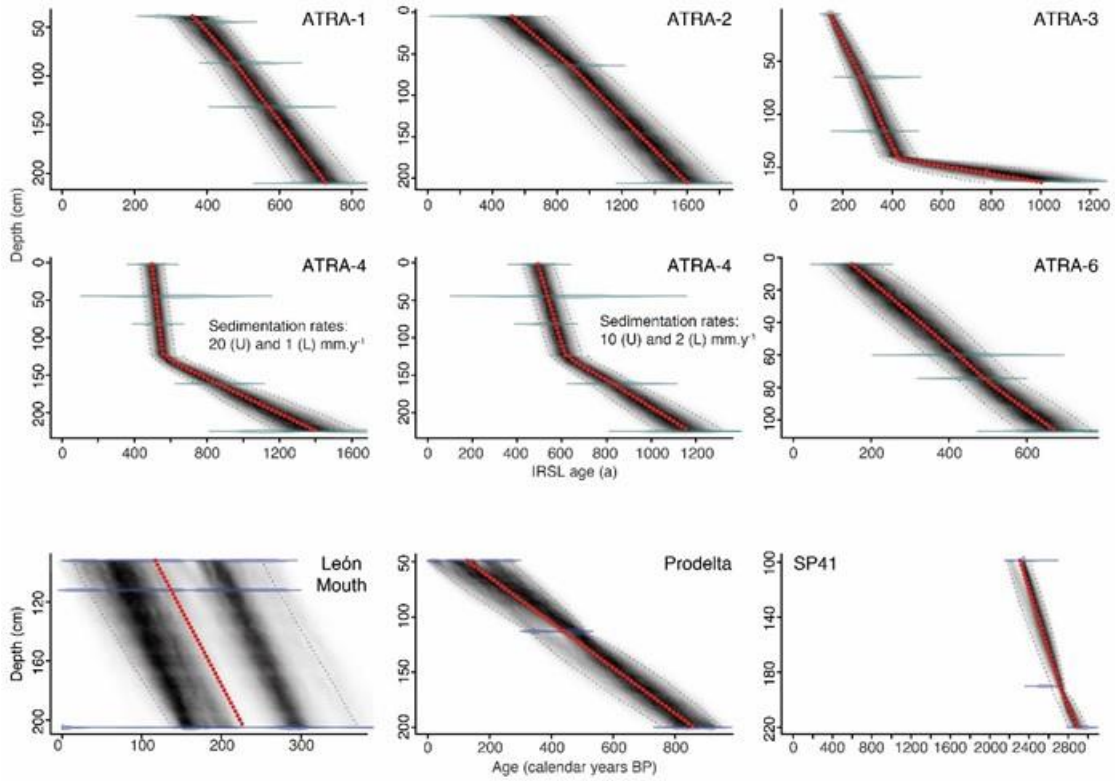

Figure 2.5 Age-depth models calculated using rbacon, (Blaauw and Christen, 2018). Accumulation rates for cores ATRA-1, 2, 6, León Mouth (LM), Prodelta and SP1 are estimated by the software alone. For ATRA-3 and 4, a hiatus of 10 years is integrated at times of suspected changes in accumulation rates (major shifts in IRSL ages; Table 2.2), to allow for a modification in accumulation patterns while reflecting sedimentation breaks that are either very short or non-existent (Blaauw and Christen, 2011). For ATRA-3 prior accumulation rates were estimated by running independent simulations using dates from the lower and upper part of the core, respectively (Table 2.4). For ATRA-4 prior accumulation rates were first estimated the same way (left-hand scenario) then manually changed to 10 and 2 mm a-1 for the upper (U) and lower (L) parts of the core, respectively (right-hand scenario). Breaking points in accumulation rates for ATRA-3 and ATRA-4 are based on major facies changes (Figure 2.4) below the last date included in the upper part of the cores, and this way set at 136 cm and 125 cm depth relative to the surface of the core, respectively. All other parameters were kept to default values (Blaauw and Christen, 2011). Individual IRSL dates are shown in light blue. Calibrated 14C dates are shown in dark blue. Gray stippled lines indicate the 95 % confidence intervals for the age–depth model; the red dotted curve shows the 'best fit' based on the weighted mean age for each depth as calculated by rbacon.

2.5 Discussion

2.5.1 Reliability of the dating results

The major problem that may interfere with reliable dating of the investigated samples is whether or not the IRSL signal was fully bleached at the time of deposition. For sediments from the modern Mississippi Delta, Shen and Mauz (2012) reported residual signals equivalent to ca. 100 a for both sandy quartz and fine silt-sized quartz. Chamberlain et al. (2017, 2018) and Chamberlain and Wallinga (2019) report lower residuals for quartz from the Mississippi and Ganges-Brahmaputra deltas. However, in the present study, IRSL ages from feldspar and polymineral fractions were determined and usually produce significantly higher residual ages (e.g. Fuchs et al., 2005). The quite large difference between IRSL and

pIR ages found in the present silt-size samples implies that the amount of bleaching was likely restricted during sediment transport, possibly due to a high sediment load that limits bleaching of luminescence signals (Ditlefsen 1992).

This leaves two approaches to investigate the signal resetting, namely the assessment of residual doses in the youngest samples in a sequence and the check for consistency of the entire data set. IRSL ages for the top samples of two cores were 500±40 a (ATRA-4-1 PM) and 330±90 a (ATRA-2-1 F). However, these samples were collected in swamps and it is likely that these ages reflect rather low to negligible deposition at the coring location. This could be a consequence of to either temporal closures of the connection channels or by an increasing distance to the sediment source caused by vegetation growth and progradation of the delta. In ATRA-03, the IRSL age of the top sample is 150±10 a (ATRA-3-1; PM) and similar values were found for sediments dredged close-by (DA-07: 240±20 a; DA-17: 100±10 a). As the river mouths (Coquitos and Burrera river arms) and thereby the sediment supply moved away from the ATRA-3 coring location, deposition may have ceased. Hence, the apparent ages could both represent the real ages of deposition as well as residual signals. ATRA-06 is from an area where a channel became re-activated only a few years ago (around 2012). The top sand layer of this core consists of a mixture of coarse marine sediments with silty fluvial sediments. These likely formed in the bay under a strong confluence of fluvial and marine currents and can be interpreted as a result of this re-activation. In this case, the apparent IRSL age would represent a residual. However, as the present current in this area is quite strong, an alternative scenario is to assume that the opening of the new channel first induced erosion. In this case the IRSL age might represent the true age of deposition. In summary, a definitive conclusion about the resetting of the luminescence signals prior to deposition cannot be drawn from the assessment of the youngest, investigated samples.

Inspection of the entire data set (Figure 2.4), reveals mainly good internal consistency, with few exceptions. In ATRA-06, the polymineral IRSL age of sample ATRA-6-7 (650±50 a) is slightly lower tha for the feldspar fraction (840±70 a). The D_e distribution for feldspar (Figure 2.3) shows a distinct lower edge, which is commonly considered to be indication of a reliably bleached proportion of grains and is therefore picked up by the MAM. One explanation for the apparent D_e distribution is permeation of younger, fine grains from overlying units into older, coarser sediment underneath, by to the influence of a strong current that moved the fine, younger sediment, to a deeper stratum. Also, IRSL ages of another sample from the same core, ATRA-6-3, are clearly inconsistent with each other (PM: 850±70 a, F: 450±70 a) and, considering all ages determined for this core, over-estimation of the age determined for the fine grain fraction is the very likely explanation. In this case, no other explanation than partial bleaching is available. A further inconsistency is observed for the basal sample in ATRA-04 (ATRA-4-12). The fine grain IRSL age (1130±90 a) is significantly lower than the age for the sand fraction (1680±130 a). As for ATRA6-7, this could be explained by post-sedimentary percolation of fine grains from above.

In conclusion, unambiguous evidence for partial bleaching is limited to one fine grain age (ATRA-6-3 PM). Although some effect on the age estimates cannot be ruled out, the following interpretation of the dating results assumes a non-significant effect on the entirety of the data set. In this context, it has to be noted that if the effect of partial bleaching were similar in all samples (e.g. 150 a), it would not affect the calculation of deposition rates, which is the main purpose of the present study.

2.5.2 Synopsis of the Atrato Delta dynamics

Age-depth models highlight the presence of three depositional behaviours. Accumulation rates around 2 mm a^{-1} are by far the most frequent, as found in ATRA-2, ATRA-6, Prodelta, and SP41 c, and possibly in the lower part of ATRA-4. Higher accumulation rates of around 5 mm a^{-1} are recorded in both ATRA-1 and ATRA-3. The highest calculated accumulation rate (ca. 10 mm a^{-1}) is recorded in the previously studied core of León Mouth, which relates to sediments originating from the León River on the opposite site of the Gulf of Urabá. A similar or even higher accumulation is assessed for the upper part of ATRA-4.

Steady accumulation rates for ATRA-1, 2 and 6 imply a relatively small influence of the type of sediment, and especially of sand deposition (Figure 2.4) on overall accumulation rates. This is furthermore stressed by the fact that the lower part of ATRA-4, being sandy, has far lower accumulation rates than the upper part, dominated by silt and clay. It is likely that alternations of sand and mud in the studied cores, represent lateral variations in depositional environments. The presence of shell fragments (found in ATRA- 4 at 160 cm depth), indicates a marine influence and possibly closer proximity of this location to the coast at 870±70 a. Accumulation rates estimated for ATRA-2 and ATRA-6 are very similar to those recalculated for the Prodelta and SP41 cores. Meanwhile, accumulation at ATRA-1 and most of ATRA-3 is more than twice as high, although not as high as the accumulation rate estimated for León Mouth (~ ca. 10 mm a^{-1}).

The similarity between accumulation rates in ATRA-2, ATRA-6, possibly the lower part of ATRA-4, and those reported in Prodelta and SP41, may be related to similar deposition context, for example in open waters of the gulf. By contrast, higher accumulations in ATRA-1, ATRA-3, and the upper part of ATRA-4, may indicate local preferential accumulation, potentially linked to more active river arms or to other factors as observed for León Mouth, where increased deposition at the mouth of the León River was linked to local parameters (Bernal et al., 2005). However, an evolution in sediment input, for example caused by climate variability or land-use change, could also partly explain variations in the recorded accumulation rates, as can be seen nowadays in places such as the swamps of Maquillón (ATRA-2) and Marriaga (ATRA-4), whose connections with the Atrato are through inlets that respond to increases in sediment loads.

All higher accumulation rates relate to the time after ca. 730 a (Figure 2.6), if no offset by partial bleaching is assumed. Increased sedimentation in four of the core locations could have been triggered by at least two factors. One factor is the subsidence and consequent tilting of the Urabá block to the west (Robertson and Martínez, 1999) that could promote sediment supply from the Atrato River towards the Gulf of Urabá. The second factor could be the enhanced anthropic activity in the catchment areas of rivers draining into the gulf (Rúa et al., 2014; Vélez and Aguirre, 2016). The very high accumulation rates recorded at León Mouth cover the period ca. 230 – 120 years ago, and at ATRA-4 the period around 600 - 500 years ago. In particular, the Spanish colonization in the 16th century is likely to have had a marked impact on the landscape. The city of Santa María la Antigua del Darién (Figure 2.1b), just to the northwest of the study area, was founded in AD 1510 by Spanish ’conquistadors‘, who were searching for gold in the region (Bénat-Tachot, 2015). Drainage from the north into the Marriaga Swamp at a time of presumed enhanced soil

erosion linked to this settlement and the exploitation of surrounding landscape may have contributed to the very high accumulation rates at the top of the ATRA-4 core.

The Tanela River feeds the Marriaga Swamp and is the main connection to villages to the north (inhabitants also report the negative impact of high sediment accumulation of this river on shipping to the Marriaga area). The age estimated for the start of high accumulation rates at ATRA-4 is ca. 575 or 630 years ago (AD 1443 - 1388), with accumulation rates of 20-10 mm a^{-1} that predate the settlement of Santa María la Antigua del Darién and the commencement of enhanced anthropogenic activity in this region. This can be a consequence of age over-estimation caused by partial bleaching or to a misplacement of the change in accumulation rates at 125 cm depth, originally based on sedimentological changes. Indeed, the lowest date linked to high accumulation rates at ATRA-4 is located at 82 cm depth, with an individual IRSL age of 530 ± 40 a (AD 1488-1528). Such an age would well fit with the time of activity at Santa María la Antigua del Darién. The high sedimentation period at ATRA-4 lasted between ca. 40 and 140 years, depending on the chosen accumulation rates and depth of change (Figure 2.6).

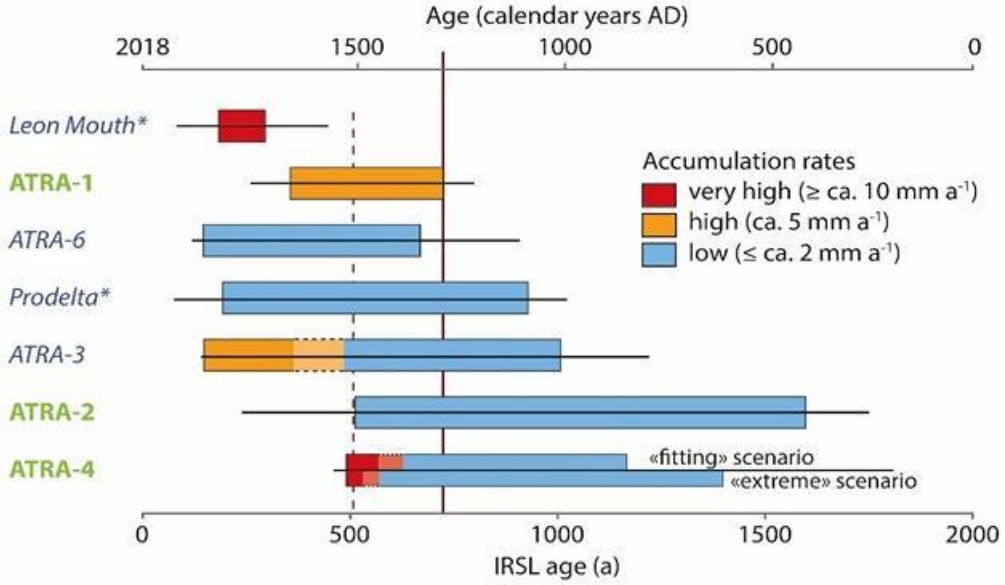

Figure 2.6 Accumulation rate patterns in the study area. Black lines reflect the total extent of the period recorded in each core including. Colour boxes correspond to portions of the core for which accumulation rates were obtained using rbacon (Figure 2.5). Dotted lines and shaded colours correspond to periods for which accumulation rates vary depending on chosen depths for rate breaks. ATRA-3: difference between assumed break at 136 cm depth based on facies changes = older limit; break at oldest date for the upper part of the core = younger limit. ATRA-4: difference between assumed break at 125 cm depth based on facies changes = older limit; break at oldest date for the upper part of the core = younger limit. 'Fitting scenario' refers to prior accumulation rates of 10 mm a-1 and 2 mm a-1 for the upper and lower part of the core, respectively, in accordance with sedimentation rates calculated from other cores. 'Extreme scenario' refers to prior accumulation rates of 20 mm a-1 and 1 mm a-1 for the upper and lower part of the core, respectively, according to rbacon prior calculations on separate core sections. Red line corresponds to the start of calculated higher accumulation rates at ca. 730 a. Dotted red line corresponds to settlement time at Santa María la Antigua del Darién. Green labels for cores correspond to present terrestrial locations, whereas blue labels relate to cores currently located in the gulf.

However, all scenarios are coherent with the early abandonment of the town (ca. AD 1525), followed by a more or less rapid reclamation of settled land by natural vegetation,

which would have led to soil re-stabilization. Continuous gold exploitation in other parts of the Atrato River catchment, especially to the south, increased agricultural pressure (deforestation/cultivation) and dredging to improve transportation infrastructure, all of which could have induced enhanced erosion rates and therefore a general higher sediment supply along the main river channel and into the Gulf of Urabá during the past few centuries. In fact, gold mining has been identified by Palacio et al. (2018) as one of the main factors affecting the Atrato River dynamics and water quality with associated mercury pollution. Pollution due to mining is suspected to have induced the rise in mercury observed in sediments from the Gulf of Urabá in the recent past (Rúa et al., 2014; the Gulf of Urabá is therein called Darién Gulf). However, while human activity appears a plausible explanation, the observed pattern in accumulation rates may also result from natural dynamics of the delta (i.e. tectonics, precipitation and sediment availability) or bias through the sampling strategy.

Ages for the near-surface samples (DA) and the cores give further insights into the pre-colonial, hence likely undisturbed, sedimentation dynamics within the Atrato Delta. The IRSL ages calculated for DA-79 (1960±180 a PM and 2130±270 a F) are from the base of the channel of the Atrato River. Either no sedimentation took place during the last 2000 years, or sediment was eroded under high flow currents, or was dredged. Dates for DA-84 (1550±100 a PM and 1500±200 a F) as well as DA-69 (1060±80 a PM) suggest that the present morphology of the Candelaria and Yerbasal Bay was at least partly established some 1500 to 1000 years ago. The IRSL ages for DA-46 (1100±100 a PM and 2130±270 a F) and DA-28 (1400±100 a PM and 1040±170 a F) indicate sediment deposition towards the Coco Grande and Margarita bays before 1000 a. Some deposition around this time is also recorded in the basal parts of ATRA-2 and ATRA-3 (Figure 2.4) The date of surface sediment (gray mud) DA-37 (740±60 a PM) suggests a displacement of sedimentation northwards towards Coco Grande Bay as the period ca. 1000-700 years ago is a time of slow sedimentation or sedimentary hiatuses at ATRA-3, located southeast of DA-37. In core ATRA-1, situated to the northwest of DA-37, high accumulation rates are recorded from ca. 730 - 360 a. Sedimentation concurrently still occurred at ATRA-2, but at low rates and some deposition probably also took place south of Margarita Bay up to ca. 500 a (DA-55). During that period, sedimentation, albeit with lower accumulation rates, is also recorded in ATRA-6 (Figure 2.4).

High accumulation rates then established in Margarita Bay (ATRA-3), sometime between 410 and 370 a, while sedimentation ceased at ATRA-1. León Mouth, close to the eastern shore of the Gulf of Urabá, also records very high accumulation rates some 200-300 years ago (based on radiocarbon ages), although large uncertainties are apparent in the age-depth model (Figure 2.5) and therefore in accumulation rate calculations. Surface sample DA-07 (240±20 a), the top of cores ATRA-3 (150±10 a) and ATRA-6 (150±30 a), and surface sample DA-17 (100±10 a) are the youngest dates recorded in this study, but it remains unclear if these reflect partial bleaching.

2.5.3 Atrato Delta late Holocene accumulation rates compared to other tropical to subtropical deltas

Late Holocene sediment accumulation rates have been determined for several deltas worldwide, in a variety of different geomorphic, hydrological, and climatic environments. Most studies estimate the accumulation rates through the analyses of ^{210}Pb and ^{137}Cs in the sediments, thus limiting the time window of observation to, at most, the last century. Only

few other studies used radiocarbon and OSL techniques to determine accumulation rates and, hence, considered the time scales in the present study (Table 2.5 Overview of sediment accumulation rates determined for tropical to subtropical deltas worldwide).

Table 2.5 Overview of sediment accumulation rates determined for tropical to subtropical deltas worldwide. Bengal = delta of Brahmaputra, Ganges and Meghna. Climate zones follow Köppen classification as used by Chen and Chen (2013).

Delta name	Climate zone	Catchment size (km^2)	Dating method	Period (years ago)	Accum. rate ($cm\ a^{-1}$)	Depositional context	Reference
Amazonas	Tropical Rain Forest (Af)	6'150,000	^{14}C	700-1800	0.4 – 0.76	Shelf	Sommerfield et al. (1995)
Atrato	Tropical Rain Forest (Af)	38'000	IRSL	< 700 700-1500	≤0.2 0.2–1.0	Swamps and bays	This study
Bengal	Humid Subtropical (Cwa)	1'720'000	^{14}C	2300-1200	0.13 -1.19	Lower delta plain	Allison and Kepple (2001)
Mahakam	Tropical Rain Forest (Af)	75'000	^{14}C	700-1700	0.97-1.0	Alluvial deltaic mangrow system	Storms et al. (2005)
Mekong	Tropical Monsoon (Am)	900'000	^{14}C	< 1000	032-0.63	Bay and prodelta	Ta et al. (2005)
Pearl River	Humud subtropical (Cfa)	452'000	^{210}Pb	<1800	0.26-1.52	Delta and estuary	Zhang et al. (2005)
Yangtze	Humud subtropical (Cfa)	1,808,500	OSL	<2000	4.8	Incised valley	Nian et al. (2018)

The average sediment accumulation rate of less than 2 mm a^{-1} found for the Atrato Delta, although low compared with the Mekong (Ta et al., 2005) or Yangtze (Nian et al., 2018) Deltas, is similar to the rates reported for the Mahakam (Storms et al., 2005), Pearl (Zhang et al. (2005), Bengal (Allison and Kepple., 2001) and the Amazon shelf (Sommerfield et al., 1995). Nevertheless, despite efforts that went into producing the data reported here, the complexity of the investigated region may require further sampling strategies to consolidate the findings of our study. In general, the observed sedimentation rates in tropical and subtropical deltas seem to be of a similar order of magnitude. Furthermore, the sedimentation rates in the Atrato Delta are relatively large, given the small catchment area of the river in comparison with other deltas. This aspect highlights the natural capacity of the rainy environment of the Atrato to carry large sediment loads. Based on the results gathered in our study, we suggest that further sampling surveys are needed, mainly focused on areas upstream of the delta and around the delta apex, confirm our descriptions of the delta evolution in the late Holocene.

2.6 Conclusions

Despite challenging luminescence characteristics of the investigated samples, i.e. the absence of OSL signals in quartz and limited ISRL response from feldspar, the presented chronology shows an internal consistency of ages and is in general agreement with previously published data. From the methodological point of view, partial bleaching of the pIR signal appears to be highly problematic for the silt-sized samples investigated here, in

particular as it is not possible to extract a fraction of well-bleached grains because of the large number (thousands) of grains on an aliquots. It remains unclear why there is no pIR response from the sand-sized feldspar extract, but IRSL produced useful results with negligible fading. It is hence the most suitable method to date the Atrato Delta.

This is the first chronologic assessment of the Atrato Delta itself and thus, provides new insights into the local sedimentary dynamics during the late Holocene. It is noteworthy that the observed accumulation rates in the Atrato Delta, although low (<2 mm a^{-1}), are similar to those of other tropical deltas. The higher area of accumulation might be explained by anthropogenic interference in the region, dating back to the first Spanish settlement in the XVI Century. Nevertheless, caution might be exercised in the interpretation of the data, since it remains unclear whether some of the reconstructed low accumulation rates represent the general characteristics of this particular delta or are due to bias introduced through the sampling strategy. In this regard, the tested dating procedures have proven to be appropriate for the inherent characteristics found in the sediments, whereas there is still plenty of room for future field campaigns to improve sampling strategies that will complement further the complex sedimentological features.

2.7 Acknowledgements

This project is part of the doctoral research of the first author, funded by the Colombian Administrative Department of Science, Technology and Innovation (COLCIENCIAS, Convocatoria 727/2015). Freiburg University provided financial and logistical support for luminescence sample preparation and analysis. Special thanks to the Doctoral Program in Environmental Engineering at Universidad de Antioquia; to GAIA Research group; and to the civil authorities and communities of the Atrato Delta Region for their support during the field campaigns. We thank Eafit University at Medellín – Colombia, for allowing the use of the luminescence preparation laboratory for sampling in Colombia. We thank Elizabeth L. Chamberlain and an anonymous reviewer for their constructive comments on a previous version of the manuscript that helped to improve the document.

3 Chapter 3: Facies and depositional context of late Holocene sediments on the Atrato River Delta, Colombia

Liliana Betancurth[1], Julio Cañón[1]

[1] *Grupo de Gestión y Modelización Ambiental -GAIA-, Facultad de Ingeniería, Universidad de Antioquia; Medellín, Colombia.*

3.1 Abstract

The Atrato River Delta (ARD) is a landform that evolves under the interaction of fluvial and marine environmental conditions. A fluvial environment occurs in the southern portion of the ARD, including the last evidence of meanders and the first avulsion at the delta apex of the Atrato River. The fluvio-marine environment occurs in the north, with the presence of parallel channels, marshes, swamps and mangroves, within an estuarine system. We used six sediment cores, drilled in three swamps and three bays in the delta, to interpret the late Holocene sedimentation history and depositional conditions of the ARD through the analysis of sediments grain size, mineralogy, organic matter (OM) content, geochemistry and dating. Results show the existence of several facies, from the distal upper delta plain to the lower delta plain and delta front, encompassing poorly sorted sequences of sediments from fine sand to coarse silt that points to moderate and high transport energy, intense reworking processes, and a marine period. Presence of OM is constant along the sequences and indicates gradual change from the influence of fluvial channels infill toward estuarine and marine deposits. Sporadic small concretions of iron oxides also occur in the middle depth of some sediment sequences and mark the fluctuation range of the unsaturated zone, whereas the clayey and silty sediments of the Atrato River forman extensive, low delta floodplain intercepted by the three swamps, in the delta front and neighboring bays east of the delta. The facies identified in this study reveal sedimentary dynamics with two well defined periods: a prevalent marine environment in the late Holocene (<1680±130 to 870± 70 a), and a fluvial environment (around ~ 550 ±70 a - to present), within a transition period (~ 740 ±60 to 550±50 a), characterized by intermittent marine incursions.

Keywords: Shallow sediments, facies, swamps, bays, Atrato River Delta

3.2 Introduction

Sedimentary facies are good descriptors of depositional conditions and help to define the sedimentological architecture, of deltas (Olariu and Zeng, 2018; Rossi and Steel, 2016; Purkait and Das, 2014). Most deltas display the notable influence of their fluvial inputs compared to the influence of tides and marine waves (Zoccarato et al., 2018; Korus and Fielding, 2015; Bhattacharya and Giosan, 2003). In consequence, rivers are primary controls on the morphology and architectural facies of inner deltas, followed by tides and marine waves. However, several studies worldwide emphasize the significance of transitional facies to classify specific episodes in the evolution of deltas (Purkait and Das, 2014; Neidhardt et al., 2013; Khalifa and Catuneanu, 2008).

Fluvial deltas constitute one of the most relevant transitional features in terms of morphological and depositional conditions in which fluvial currents interact with sea tides and waves (Edmonds et al., 2011; Dolozi et al., 2011; Brown, 2010). The mixture of fluvial and marine inputs produces unique conditions for deposition, (e.g., stratification, organic matter content, sediments grain size), influenced by climatic variations, relative sea level changes and active tectonics (Kopp and Kim, 2015; Nádor et al., 2007).

Late Holocene to modern deltas in coastal systems, in particular, show important variability in terms of the predominant inputs and processes (Rossi and Steel, 2016;Vakarelov and Ainsworth, 2013). Geomorphology is the first point to elucidate the geometry and main possible domain that characterize a delta (Li et al., 2017; Vespremeanu-Stroe et al., 2017; Mateo and Siringan, 2016). Among other factors, the stratigraphy and physicochemical features (grain size, mineralogy and geochemistry) are the main tools to determine the sedimentary dynamics of these landforms.

Tropical deltas are common landforms that affect the evolution and modification of coasts and littoral landscapes, in terms of sediment load and nutrient supply (Restrepo, 2014; Vijith and Shetye, 2012). The Atrato River Delta (ARD), located in tropical northwestern Colombia, has undergone significant geomorphological changes in recent decades (Velez et al., 2020; Post, 2011, Nieto-Oliveros, 2004). The ARD occurs in an inland-sea transition area, where sea erosion and fluvial accretion modify the coastline (Vélez et al., 2020). The accretion in the ARD is mainly a consequence of the sediment discharge of the Atrato River, modulated by middle energy flows and flooding periods occurring on this part of Colombia. Erosion in turn is controlled by marine waves, sea level changes north of the delta and along the west side of the Gulf or Urabá, and by dimished sediment inputs occurring in dry periods (Montoya, 2010; Bernal et al., 2005).

Based on its geomorphologic characteristics, the ARD is frequently classified as a fluvial domain (Galloway, 1975), with microtidal conditions (< 2m) (Correa and Vernette, 2004), and negligible waves (Blanco, 2014). Located in one of the rainiest regions of the world (Poveda and Mesa, 1999), the ARD is cataloged as the primary source of sediments of the Gulf of Urabá (Velásquez, 2013, Escobar, 2011, Bernal, 2005). Nonetheless, no studies have investigated the recent sedimentary dynamics and possible incidence of microtides in the fluvial domain of the ARD.

We examined the interaction between fluvial and marine processes throughout the shallow sedimentary features of the ARD, focusing on the analysis of six 2-m-long sediment cores, drilled from three swamps on the delta floodplain and three bays at the delta front. In addition, we established the depths and dates of late Holocene stratigraphical successions and younger progradating features from dates recently obtained through Infrared Stimulated Luminescence (IRSL) (Betancurth et al., 2020).

3.3 Regional geological and geomorphological setting

The Colombian Pacific zone is a narrow shelf that surrounds a deep trench with a tectonic control. At this point, the Nazca oceanic plate converges with the South American plate at an average rate of 54 mm/a (Sepúlveda and Cabrera, 2018; Salcedo and Pérez, 2016; Monsalve and Mora, 2005; Kellogg and Mohriak, 2001). This convergence produces continuous earthquakes, most of them of low magnitude (Robertson and Martínez, 1999).

The geological Panamá-Chocó block was produced by the accretion of Miocene islands. This island arc collided with the north of South America and formed the Isthmus of Panama at the northwest Colombian boundary (Noriega and Caballero, 2015; Suter t al, 2008; De Porta, 2003; Trenkamp et al., 2002; Duque-Caro, 1990).

The Chocó Basin splits into the Atrato River basin to the north and the San Juan River Basin to the south (Bedoya et al., 2007; Méndez et al., 2006). Both basins lie in the Paleocene

sedimentary deposits over different Cretacic basements formed from remnants of oceanic crust that carried fragments of island arc (Figure 3.1) (Cediel et al. 2003; Kerr et al., 1996a). These fragments have migrated from the Cretacic and collided with the NW continental border of South America to cut the connection between the Pacific and the Caribbean Sea. During that geological process, both the Atrato and the San Juan Basins formed, with particular stratigraphic features and facies.

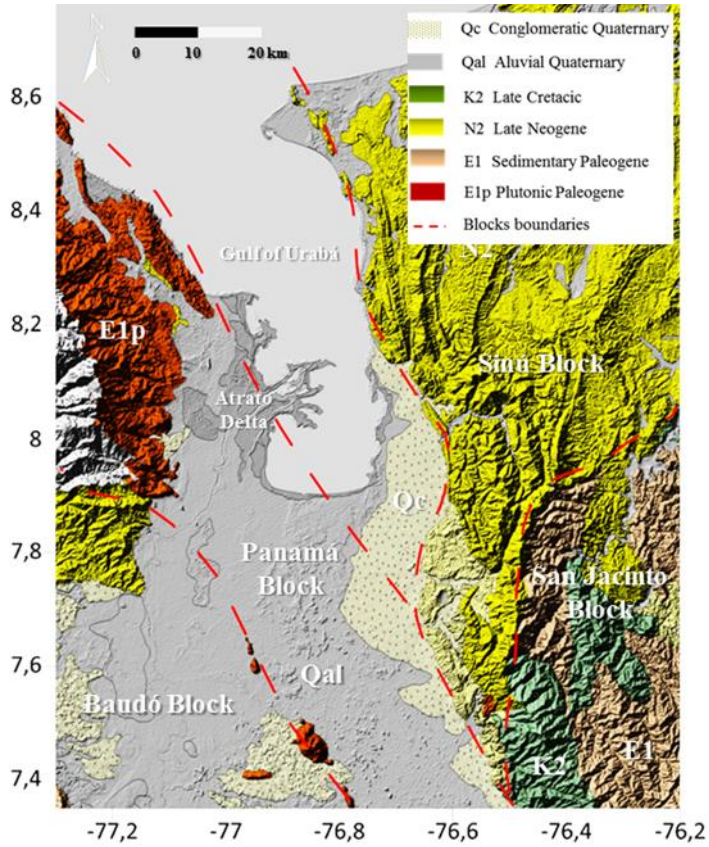

Figure 3.1 Geological regional Blocks of Northwest of Colombia. (Modified from Geological Survey of Colombia, 2015 and Cediel et al., 2003).

The ARD belongs to the oceanic-continental geological unit named Espolón San Blás-Baudó, formed by two belts that correspond to the Serranía de San Blas - Darién and Majé – Baudó; and Chucunaque – Atrato Basins (Parra and Jaramillo,2013). Some authors consider the geological frame of the ARD to be a tectonic unit formed by the Dabeiba and Baudó arches, added to the Northandean block through the Uramita and Ismina Faults (Monsalve and Mora, 2005; De Porta, 2003, Trenkamp et al., 2002).

The geology of the ARD (Figure 3.2) involves adjacent geological units located in the south and west of the delta. These units are the main source of sediments in the Atrato River, related to pyroxene amyloid basalts, porphyry, agglomerated and tuff andesites of basaltic composition, and local lava flows and breccia (Santa Cecilia – La Exis Complex - KECsce) (Rodríguez and Zapata, 2012; Case et al., 1971; Haffer, 1967).

Igneous rocks of tonalite and granodiorite composition are the biggest intrusive unit of the West Cordillera of Colombia (Lugo et. al, 2003; Alvarez et al., 1987). Main minerals are quartz, potasic feldspar, plagioclase, hornblende, biotite and clinopyroxene (Mandé Batholite - Etm).

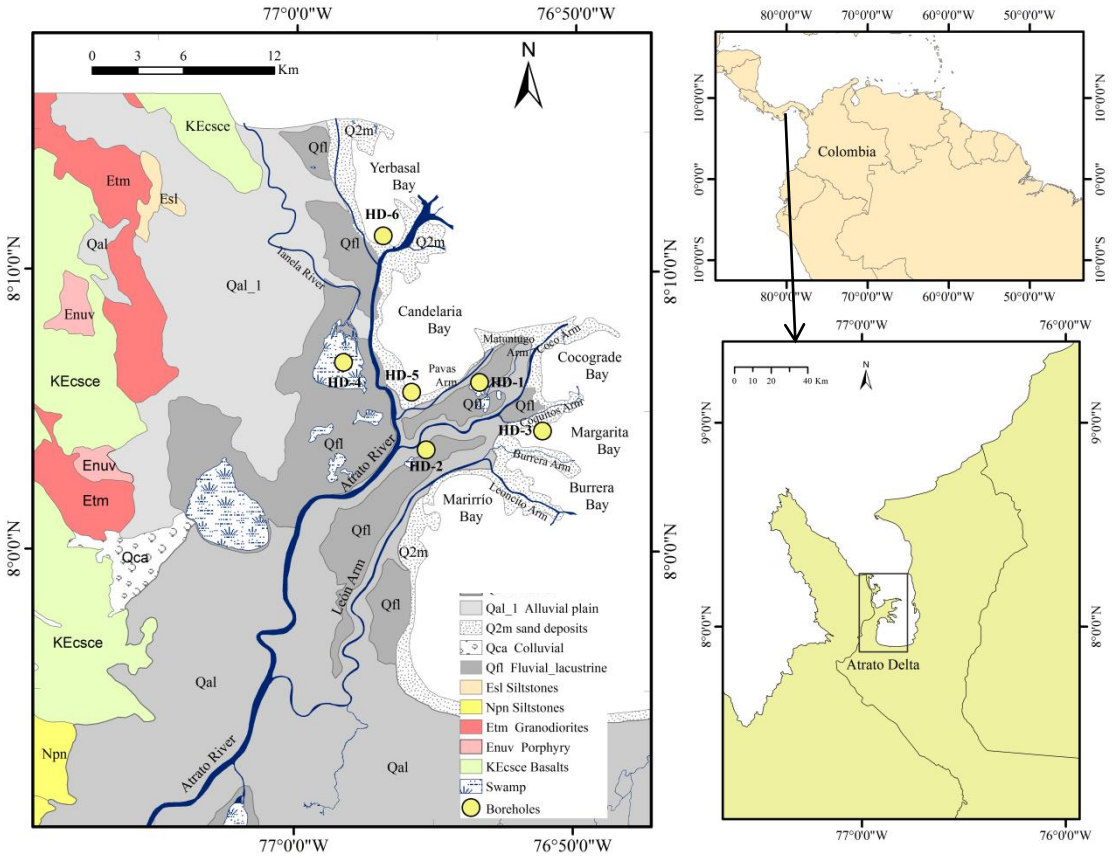

Figure 3.2 Location and geological map of the study area. (Modified from Geological survey of Colombia, 2015).

Sedimentary sequences of siliceous chert, intercalated with siltstone and fine sandstones (Salaquí Formation - Esl), outcrop at the Serranía del Darien (Bedoya et al., 2007; Thomas et al., 2007; Igac and Ingeominas, 2001). The Uva Formation (Enuv) corresponds to claystones, detritic limestone and carbonaceous fine sandstones of a shallow sea setting in terms of algaceous limestone, sandstones and marls (Zapata, 2002; Duque-Caro, 1990; Haffer, 1967).

Recent geology involves widespread *fluvio-lacustrine* (Qfl), non-consolidated deposits, composed of clayey and silty sediments of low to medium sorting, with abundant quartz and mica minerals of late Pleistocene to Holocene age (Igac and Ingeominas, 2001).

The *alluvial Quaternary deposits* (Qal) are deposited in both the channels and adjacent flood plains, as the weathering product of the soils and rocks of the southern and western mountain systems of Baudó-Darién. These are non-consolidated, polymictic, poorly sorted and rounded sediments (González and Londoño, 2002b; Igac and Ingeominas, 2001). Other Quaternary deposits correspond to sand deposits along the shoreface (Q2m) and small *colluvial deposits* (Qca) to the west.

Factors such as littoral landforms, tectonic activity and marine contributions determine the geomorphology of the delta. These factors have shaped the ARD as a system of erosive and cumulative alternations. The main landforms of the ARD are related to vegetated marsh plains of mud type, fluvio-marine plains, flood zones and beaches (Blanco, 2016; CIOH, 2009; Thomas et al., 2007). The vegetated marsh plains are the more extended units, formed by swamps, marshes and mangroves. This unit is relatively below the sea level and prone to floods.

The *fluvio-marine plain* is a unit located near the coast, formed by sediments from the Atrato River. This unit is slightly above sea level. Sediments are of muddy-sandy texture, forming natural levees, mainly during seasonal floods (Blanco, 2016).

The *flood plain* unit includes channels, mangroves and swamps that become flooded mainly during the rainy season, when discharge from the Atrato River increases. *Beach* units, located over the delta front, are few and very narrow, alternating with mangroves along the coastline. These beaches formed by the action of tides and waves in some of the bays.

The delta has had a sedimentary evolution with considerable morphological changes, especially at the coastline. Some sectors progradate, some remained stable, while others receded along the coastline (Vélez et al., 2020; Van, 1959). This behavior is evident in some historical maps that date back 200 years (INVEMAR, 2007) and from Landsat images analyzed in the last few decades (Vélez et al., 2020). As an example, the Tarena mouth in the northwest corner of the delta was located further west, but the entire eastern shore of Tarena Island was eroded, forming Yerbasal Bay around 1960 (INVEMAR, 2007).

The delta's formation was mostly a consequence of the filling of bays with sediments by crevassing related to the active transport through the Atrato River mouths during flooding episodes (Vann and Vannl, 2010). At sites far from the influence of the river mouths, wave erosion from the Gulf, takes control and drives the shoreline landwards.

3.4 Materials and Methods

3.4.1 Drill cores and sediment sampling

For our study, we drilled six (130-220 cm) cores, using a Livingstone Bolivia piston corer operated manually. The cores were located at Marriaga (HD-4), Matuntugo (HD-1) and Maquillón (HD-2) Swamps and at Yerbasal (HD-6), Candelaria (HD-3) and Margarita Bays (HD-5) (Figure 3.2, Table 3.1).

We used 2.5-inch PVC tubes to collect and transport the sediments columns, first by boat from the delta to Turbo town, then by road from Turbo to the GAIA Laboratory in Universidad de Antioquia, Medellín. Cores were stored at 8° C prior to their analysis.

We split each core vertically in half. One-half for sediments description and sampling collection, and the other half stored as a duplicate. We described the sediments following a pre-established format, including the description of thickness, depth, samples, texture, color, plasticity, stickiness, and presence of OM.

Table 3.1 Cores locations at ARD

Samples	N	W	Depth (cm)	Location
HD – 01	8° 06' 01"	76° 53' 40"	209	Matuntugo Swamp
HD – 02	8° 03' 59"	76° 55' 31"	196	Maquillón Swamp
HD – 03	8° 04' 20"	76° 51' 10"	196	Burrera Bay
HD – 04	8° 06' 70"	76° 58' 28"	219	Marriaga Swamp
HD – 05	8° 07' 70"	76° 56' 85"	190	Candelaria Bay
HD – 06	8° 11' 14"	76° 56' 53"	133	Yerbasal Bay

We sampled the core sediments based on the stratigraphic changes determined by visual and tactile inspections, mainly in terms of color and grain size differences. Sediment was sampled every 5 – 10 cm. We also described the six stratigraphic columns to highlight the sedimentology and stratigraphic arrangements, according to different layers.

We determined the water content of the samples by the difference between wet and dry weights after 24 hours at air temperature, using an air extractor. We gently milled the samples in an agate-grinding mill; then we homogenized and quartered the samples to obtain 30 to 70 g per sample (the amount depended on the sediment availability in each stratum of the core).

3.4.2 Analysis of sediment samples

We characterized the stratigraphy and facies of the six cores based on visual and tactile descriptions of thickness, texture (grain size), color (Munshell scale), plasticity, stickiness, OM content, and shell remains. In addition, we analyzed the fine grain size, bulk mineralogical composition and geochemistry. We interpreted the depositional environments according to most typical fluvial, lacustrine and transition fluvial-marine types described previously in deltas worldwide (Akter, 2016; Goodbred et al., 2014; Goodbred and Yoshiki, 2011; Sato and Masuda, 2010; Fitzgerald et al., 2004).We also used the partial analysis of geomorphological units, made in this study (Appendix 12).

We carried out the grain size analyses at the University of Köln in Germany, using a Laser Particle Sizer (Beckman Coulter LS13320). 48 bulk core samples were analyzed as bulk in its original grain size (<150 μm). We treated the samples with HCl 10% during two hours to eliminate carbonate content, until the end of reaction. We washed the samples with distilled water and centrifuged at 2500 rpm during five minutes, three times. We treated samples with 15% H_2O_2 for 24 hours or until the end of reaction if necessary to eliminate the organic matter (OM). We washed and centrifuged the samples three times. Finally, we treated the samples with Na_2PO_5 in a relation of 46g/l. We used this Na_2PO_5 (46 g/l) to disperse and prevent coagulation of particles.

For the grain size, we determined the statistical parameters of mean diameter (Mz), sorting coefficient (σI), skewness (SKI), and kurtosis (KG), based on the Folk and Ward (1957) method of phi values Ø 5, Ø 16, Ø 25, Ø 50, Ø 75, Ø 84, and Ø 95, obtained from the cumulative curves, by using the GRADISTRAT Software. We produced triangular Sand - Silt - Clay diagrams to visualize the grain size distribution in every core (Appendix 11). We also drew the cummulative grain size curves, which indicate the transport means and flow energy.

We determined the main mineral phases of the bulk samples at Instituto Tecnológico Industrial Pascual Bravo in Medellín - Colombia, using a Brucker Eco D8 Advance X-ray

Diffractometer placed 2 g of sample in a horizontal plastic disc. The machine identified the present minerals, recorded in a semi-quantitative database of the minerals phases. We analyzed mineral phases by using the HighScore Plus Software.

For the geochemical characterization, we analyzed samples at the Spectrometry Laboratory at Universidad de Antioquia, using ARL OPTIM´X WDRRF Spectrometer/Thermo Sciencific equipment. Firstly, we ground samples in an S-1000 RETCH Centrifugal Ball Mill with zirconium oxide vessel at 3000 rpm, for 7 minutes.

We submitted 2 – 3 g of sediment to calcination at 550°C for two hours to obtain the weight Loss on Ignition (LOI) and calculate the Organic Carbon (OC) fraction in each sample. OC was determined with the relationship of LOI and the factor 1.724 (LOI/1.724, assuming 58% of C in the Organic matter), which was proposed by Van Benmelen (1890) and reinforced by authors such as Pribyl (2010). We measured around 3 g of samples to obtain 10 oxides (SiO_2, Al_2O_3, Fe_2O_3, MgO, Na_2O, CaO, K_2O, TiO_2, P_2O_5, MnO) and 22 trace elements (Cl, S, Ba, V, Cu, Zr, Sm, Cr, Zn, Sr, W, Tb, Ni, Ar, Co, La, Rb, Br, Y, Sc, Ga and Cd).

We carried out statistical analysis with parametric and non-parametric tests (ANOVA and clusters) for dimension reduction, mainly of geochemical data, using Statgraphics Software (licensed to the Environmental Management and Modeling Research Group - GAIA of the University of Antioquia). We used the GRADISTAT free software for the statistical analysis of grain size data.

For the statistical procedure, we evaluated relationships among the geochemistry of major and trace elements, LOI and OM content in samples throughout a Pearson correlation matrix. As we analyzed the bulk grain size, this variable was not included in the statistical treatment, being not useful to differentiate chemical oxides and trace contents.

We performed a cluster analysis, using Ward's Method and the Euclidian distance, as group linkage method, covering the most dominant oxides and trace elements (Stat point. INC., 1982 - 2006). Samples with a defined cluster indicate similar features with respect to source, weathering, OM content or chemical affinity.

We defined and described the sedimentary facies based on the grain size, mineralogy, geochemistry, OM and additional features such as shells and mica contents, supported by dating previously determined by Betancurth et al. (2020). To complement the determination of facies, we proposed a conceptual sedimentary scheme of the fluvial- marine depositional context of the recent dynamics from the collected sediments cores.

3.5 Results

We described the sedimentary stratigraphical successions of the delta from the six cores collected at the upper delta plain in Maquillón Swamp (HD-2) and Marriaga Swamp (HD-4); the floodplain at Matuntugo Swamp (HD-1); and the delta front (marine) in Margarita Bay (HD-3), Candelaria (HD-5) and Yerbasal (HD-6) bays (

Figure 3.3 a,b).

With visual and textural analyses in the laboratory, we classified the stratigraphic stratigraphical successions as fine sand, coarse silt, medium silt, fine silt and clay. Muddy

stratigraphical successions were double-checked with visual and textural tests and confirmed afterwards by laser diffraction analysis of a set of 48 samples.

The sediments in swamps and marine stratigraphical successions exhibit quite similar textures and compositions, with some notable differences, especially in OM, mineral content and geochemistry. Microfauna were identified as the class bivalves, based on incomplete remains.

3.5.1 Cores description

We described the main physical characteristics of sedimentary stratigraphical successions of each core, including depth, Munsell color, sediments type, OM content, grain size, main mineralogy and geochemical features. We analized some distributed samples along the stratigraphical successions for laser grain size, XRD, bulk mineralogy, XRF, geochemistry and dating. Cores photographs are available at Appendix 13.

Matuntugo Swamp (HD-1). This 209 cm swamp core is located at the lower delta plain, mainly filled by an inlet derived from the Matuntugo channel near Caldelaria Bay. This sequence was drilled at 2.2 mbsl (Fig 3.4 a). Five samples were dated by IRSL method on top, middle and lower part of the sequence.

The sequence consists of laminated silty clay layers, with three coarse silt – fine sand layers (210, 110 and 75 cm depth) and peaty layers. From bottom to top, 8 cm (209 -201 cm) of laminated fine olive gray (Munsell color: 5Y 4/1) silty sand was identified as Sed1-1 without OM or shell fragments (*Sed 1-1*).

Around 93cm (from 200 to 140 cm), there is a laminated dark grey clayey silt (2.5Y 3/0 mainly) with alternations of OM (~ 7%) made of roots and stems. A sample was dated as 740±60 a at 200 cm (*Sed 2-1*). From 140 to 80 cm a sequence of laminated, dark gray silty clay (2.5 y 3/0 - 7,5a 2/0) with two peaty layers (at 120cm and 83cm) was intercepted.

Abundant OM is present along these 60 cm (range 11 – 13% OM). The sediments were dated as 540±50 a, at 125 cm and 520±20 a at 85 cm. Two coarser layers of fine sand are interbedded at 110 cm and 70 cm depth (*Sed 3-1*). The upper 70 cm (70 cm to top) consist of laminated olive gray (5Y 3/1) silt and clay layers with scarce OM and vesicles at 24 cm (*Sed 4-1*). These sediments were dated as 430±30 a, at 45 cm and 280±20 a at 30 cm.

Grain size analyses show the mean grain size Mz at phi scale (ϕ) for sediments varying from very fine silt (8.509) to medium silt (6.440), poorly sorted (standard deviation) and finely skewed sediments and a predominant mesokurtic kurtosis.

After semiquantitative XRD analyses, the main mineralogy shows quartz (67 to 74%), bornite (18%), pyrite (4%), titanium oxide (7%), diopside (17%) and halite (5%). We detected some clay fractions of zeolite (4%), motmorrillonite (4%) and vermiculite (4%).

From the geochemistry, the average concentrations of oxides (in wt%) decrease from SiO_2 (42.06%) to Al_2O_3 (18.40%), Fe_2O_3 (9.64%), MgO (3.17%), Na_2O (1.09%), CaO (1.52%), K_2O (1.35%), TiO_2 (0.75%), P_2O_5 (0.21%) and MnO (0.09%). The SiO_2 concentration decreases from bottom to top (46.7% to 39.1%) and could indicate an increment in the weathering of

modern deposited sediments. Al_2O_3 is variable along the sequence and shows the same decreasing pattern of SiO_2 from bottom to top (20.09% to 16.88%), which is consistent with siliceous and clay mineralogy.

Other oxides do not show special variations along the stratigraphical succession. The ten trace elements in the analysis show an average enrichment sequence (in ppm) of S (2376) > Cl (1706.4)> Ba (637.6)> Cu (231)> Cr (164.6)> Sr (157.2) >Zn (138.2)> Ni (107.4)> Co (62)> Rb (44.8). Heavy metal concentrations of Cu, Cr, Zn and Ni are considerably high in comparison to the reference Upper Continental Crust (UCC) values and regional geochemistry, this outcome is in agreement with the results of surface sediments in chapter 1.

Maquillón Swamp (HD-2). This swamp is located at the upper delta plain, filled by a narrow inlet from Matuntugo Channel. We drilled 196 cm of sediments at 7 mbsl (Fig 3.4 a). From bottom to top, a laminated dark gray (2.5Y 4/0) silty sand of 10 cm thickness was intercepted with abundant mica content (muscovite – sericite) and 4.1% of OM, named as *Sed 1-2*. Further 183 to 120 cm present laminated gray (2.5 y 4/0) silty clay with an increase of OM (9.2%). Sediments were dated to 1620±130 a (*Sed 2-2*).

From 120 cm to top, the stratigraphical succession is very homogeneous, intercalated with thin laminated clay and peaty layers. From 120 to 110 cm, there is a layer of dark brown - black color (7.5A 2/0), with 29.7% of OM, that we classify as peat (*Sed 2-2*). From 110 to 74 cm sediments consist of a laminated clay of dark gray color (5Y 4/1) with leaves and fibers (< 5%). From 74 cm to top, sediment is a dark brown muddy (2.5A 2.5/0) with variable content of OM, that increases to the top (*Sed 3-2*). Two dated samples are on the middle and top of the core: 970±90 a, at 65 cm and 330±90 a at 7 cm.

Laser grain size analyses show the mean grain size Mz at phi scale (ϕ) varying from very fine silt (8.024 ϕ) to very fine sand (3.778 ϕ), very poorly sorted to poorly sorted sediments, with samples that were very fine skewed to fine skewed and one symmetrical. These statistical patterns reflect a predominance of fluvial inputs. However, the kurtosis varies from very leptokurtic to platikurtic, indicating the possible influence of minor tidal reworking (Mateo and Siringan, 2016).

The main bulk mineralogy relates to quartz (13 to 87%), muscovite (37 to 44%), biotite (4 to 32%), magnetite (1 to 3%), orthopyroxene (81%), and calcium oxide (9 %), halite (24 %) and silvine 22%). The detected clay fraction includes Illmenite (9% to 53%), chlorite (11%), kaolinite (8%), montmorrilonite (1%) and vermiculite (1%).

Oxides average concentrations (wt%) decrease from SiO_2 (42.66), Al_2O_3 (17.92), Fe_2O_3 (9.00), MgO (3.47), Na_2O (2.02), CaO (2.04), K_2O (1.33), TiO_2 (0.72), P_2O_5 (0.23) to MnO (0.12). The highest SiO_2 value is at the bottom of the column, in the sandy layer (52.39 wt %). Al_2O_3 concentrations are significantly high (19.06 wt% to 20.43 wt%).

Fe_2O_3 is significantly high at 32 cm (11.34 wt%). The ten trace elements show the follow average enrichment for Cl (6773.3) > S (3706) > Ba (860.5) > Cu (237.8) > Sr (213.3) > Cr (165.8) > Zn (140.1) > Ni (112.1) > Co (59.5) > Rb (43.8). We found significant concentrations of Cu, Cr, Zn, Ni and Co along the stratigraphical succession that are higher to the reference UCC values and regional geochemistry.

Burrera Bay (HD-3). This core, 196 cm deep, reaches 3.2 mbsl (Figure 3.4 b). The bottom consists of 4 cm of dark brown (5y 3/1) thin peaty layer. From 192 cm to 162 cm, the grain size increase to a laminated gray silty sand with mica content and without OM (*Sed 1-3*) and shells fragments (*Sed 2-3*). These sediments were dated at 170 cm with an age of 1130 ±90 a. From 162 to 158 cm, there is laminated gray silty sand with OM (leaves, vegetal nodules) up to 5% (*Sed 3-3*).

From 158 cm to top a very plastic gray clay varies in gray intensities (5Y 4/1, 7.5Y 4/0, 2.5A 4/0) and constitute the major feature for the distinction of layers. From 88 to 77 cm, there is dark gray clay (7.5A 4/0) with < 2% of shell fragments, with an age of 340±50 a, at 70 cm. From 54 cm to 22 cm the clay layer have small, white pink fragments of shell remains (< 5%) (*Sed 4-3*), dated near top as 150±10 a. We analyzed six samples in this core.

The grain size shows a mean Mz at phi scale (ϕ) varying from very fine silt (8.270) to medium silt (6.220), very poorly sorted to poorly sorted sediments, with samples varying from very fine skewed to fine skewed and one symmetrical, and leptokurtic to mesokurtic kurtosis. The OM content varies from 4.1 to 8.9% and seems to be constant in the sequence (based on the analyzed samples).

The OM content is high, considering the marine environment, but reinforces the occurrence of fluvial inputs. The semiquantitave mineralogy of these sediments shows quartz (25% to 88%), albite (1% to 15%), rutile (3%), zinc sulfide (9%), titanium oxide (73%). The clay fraction exhibits illite (28% to 89%), kaolinite (7%), motmorrillonite (1%) and vermiculite (1%).

The geochemical analysis shows the average oxides concentrations (in wt%) for SiO_2 (40.85), Al_2O_3 (19.19), Fe_2O_3 (10.25), MgO (3.56), Na_2O (2.81), CaO (1.51), K_2O (1.56), TiO_2 (0.78), P_2O_5 (0.20) to MnO (0.09). SiO_2 values are relatively stable along the stratigraphical succession, but still low for the expected silica values (range: 39.60 wt% to 40.64 wt%). Al_2O_3 concentrations remain high as in HD-1 and HD -2 cores, ranging from 18.48 wt% to 19.98 wt%.

The Fe_2O_3 concentrations are also high along the sequence and decrease when SiO_2 increases. Other oxides have very similar concentrations along the core. The average concentrations of trace elements (in ppm) are S (15007.5) > Cl (13550) > Ba (548.7) > Cu (234.7) > Cr (184.7) > Sr (175) > Zn (151.5) > Ni (114.5) > Co (59.5) > Rb (47.2). The concentrations of heavy metals are also significant in the sequence Cu, Cr, Zn, Ni and Co.

Marriaga Swamp (HD-4). These sediments were reached at 4 mbsl with a depth of 219 cm (Figure 3.4 a). The bottom consists of almost 18 cm (219 – 201 cm) of very dark brown massive coarse silt (7.5A 4/0), with 20% of OM and 50% of mica (*Sed 1-4*). This layer was dated as 1130±90 a. From 201 to 197 cm is a dark gray (5Y 3/1) a peaty layer was intercepted, mixed with some mica (*Sed 2-4*). From 197 to 177 cm there is laminated dark reddish gray silt (2.5A 4/0) with 6.5% of OM (*Sed 3-4*).

From 177 to 157 cm there is a dark gray (7.5A 4/0) laminated sand with shell fragments of vivalves and mica and OM (*Sed 4-4*). From 157 to top the stratigraphical succession is homogeneous dark gray (5Y 4/1) to dark reddish (2.5A 4/0 muddy (silt – clay) with two sandy layers at 97 and 85 cm; vesicles at 94 cm. Moderate to high OM is distributed along these sediments (7.3 – 10.3%). The OM content diminishes towards the top of the sequence. Four

samples were dated at 159 cm (870±70 a); at 79 cm (530±40 a); at 40 cm (630±150 a) and 10 cm (500±40 a) for *Sed 5-4*. Ten samples were taken for detailed analysis.

Grain size, expressed in Mz (phi scale - ϕ), varies from very fine silt (8.155) to coarse silt (5.522), very poorly sorted to poorly sorted, with very fine skewed to fine skewed and one symmetrical sample and mesokurtic to platikurtic kurtosis. The minerals phases on these sediments present quartz (25 % to 90%), berlinite (23%), halite (7%), Silvine (5%), albite (22% to 72%), cristobalite (9%), pyrite (4%) and titanium oxide (4%). We determined for the clay phase, the presence of zeolite (1% to 3%) and vermiculite (1%).

The oxides at Marriaga swamp show decreasing concentrations (in wt%) from SiO_2 (44.02), Al_2O_3 (18.57), Fe_2O_3 (10.88), MgO (3.27), Na_2O (1.26), K_2O (1.16), CaO (1.63), TiO_2 (0.72), P_2O_5 (0.17) to MnO (0.18). The concentrations of oxides do not have significant variations along the examined sediments. The trace elements enrichment (ppm) is S (11094) > Cl (2901.21) > Ba (506.2) > Cu (260.7) > Sr (172.8) > Cr (159) > Zn (141.2) > Ni (105.2) > Co (73.8) > Rb (36). The sequence also exhibits significant values of Cr, Cr, Zn, Ni and Co.

Candelaria Bay (HD-5). We drilled a 190 cm at 4.3 mbsl. These sediments are an alternation of clay – coarse silty layers with abundant shell remains, mica and low OM. No dates could be taken on this core. From bottom to top, 23 cm (190 – 167cm) consists of laminated black to dark brown gray clay (5Y 2.5/1, 5Y 3/1) with 18% of OM (stems, leaves) and 10% of shell remains. This is an alternation of peaty layers and clay (*Sed1-5*). From 167 to 105 cm the sediments are a homogeneous very dark gray (10Yr 3/1) laminated silty clay layer with white fragments (< 5%) and 8% of OM*, (Sed 2-5*).

From 105 to 95 cm a the layer is a laminated dark gray (5A 3/1) silty clay with iron oxides nodules (10%), fine mica (5%) and OM (5%) (*Sed 3-5*). From 95 to 25 cm there is a very dark gray silt (2.5Y 3/0) with 5% of micas and 2% of white shell fragments (*Sed 4-5*). The upper 25 cm are dark gray silt (7.5A 4/0) with less than 3% of OM and micas *(Sed 5-5*). Six samples were taken for detailed analysis.

Laser grain sizes show the Mz (ϕ) varying from very fine silt (8.103) to coarse silt (5.580), with very poorly sorted to poorly sorted sediments, and with fine skewed predominance. The kurtosis varies from mesokurtic to platikurtic. The OM content varies from 8.5 to 18.2% and increases from top to bottom.

The value of 18.2% matches with a clay layer at 161.5 cm depth that presents a mixture between OM and shell remains. The minerals found on this core involve quartz (46% to 97%), bytownite (49%), pyrite (11 to 13%), coesite (11%), halite (8%), titanium oxide (4%). Clay minerals are zeolite (1 to 8%) and vermiculite (1 to 3%).

The average concentrations of oxides at Candelaria Bay decrease from SiO_2 (34 wt%), Al_2O_3 (15.97 wt%), Fe_2O_3 (11.49 wt%), MgO (3.72 wt%), Na_2O (2.86 wt%), CaO (1.75 wt%), K_2O (1.55 wt%), TiO_2 (0.73 wt%), P_2O_5 (0.16wt%) and MnO (0.11 wt%). The SiO_2 exhibits a significant depletion on this bay with a range concentration between 28.8 wt% and 39.8 wt%. Al_2O_3 concentrations also decrease in comparison with the previous cores values (from 13.6 wt% to 17.8 wt%).

Fe_2O_3 by contrast, exhibits high concentrations (10.9 wt% to 14 wt%) with a particular depletion at 161.5 cm (8.83 wt%). Other oxides have in general little variation along the

stratigraphical succession. However, MgO is specially enriched at 103.5 cm with a concentration of 4.15 wt%. K_2O is also regular along the column, but shows a remarkable enrichment at 130.5 cm with 2.24 wt%. P_2O_5 concentration is high at 15 cm depth with 0.25 wt%. The trace elements concentrations expressed in ppm are S (29471.4) > Cl (17100) > Ba (459) > Cu (261) > Sr (198.6) > Cr (177.71) > Zn (150.71) > Ni (121) > Co (77.7) > Rb (44.7). The concentrations of heavy metals are considerably high for Cu, Cr, Zn, Ni and Co.

Yerbasal Bay (HD-6). This core is the shortest, with only 133 cm depth, intercepted at 2.5 mbsl. From 133 cm to 129 cm a massive dark gray fine sand (5Y 4/1) with 10% of mica is the base of the core (*Sed 1-6*). From 128 to 118 cm a sequence of brown to dark gray (5Y 3/1, 5Y 4/1, 7.5A 3/1) laminated sand with 10 % of fine mica (sericite) and sulfur smell, interbedded with thin peaty layers (*Sed 2-6*).

Next 118 – 110 cm consists in a dark gray (5Y 3/1) laminated sandy silt, with 6.1% of OM content *(Sed 3-6*). From 110 cm to 68 cm there is a succession of banded dark gray clayey silt layers (5Y 3/1, 5Y 3/2, 5Y 4/1), with OM (stems, leaves) from 8.2 to 16% and very destroyed shell fragments *(Sed 4-6*).

From 68 to 20 cm a dark gray brown laminated clayey silt with 6.2 to 8.3% of OM (*Sed 5-6*). This section was dated at 48 cm as 450±70 a. From 20 cm to top, there is a banded dark gray sandy to fine gravel (5Y 4/1), followed by a very homogeneous dark gray sandy silt (5Y 3/1) without OM (*Sed 6-6*).These sediments was dated on top as 150±30 a.

The grain size shows a mean Mz at phi scale (ϕ) varying from fine silt (7.293) to a fine sand (3.451), very poorly sorted to poorly sorted sediments, with samples very fine skewed to fine skewed and one symmetrical. The kurtosis varies from very leptokurtic to platikurtic.

The mineral fraction at Yerbasal Bay involves quartz (41 to 84%), pyrite (12 to 67%), chlinoclore (1 to 39%), albite (27%), muscovite (26%), hornblende (25%), cordierite (21% to 24%), magnesium silicate (23%), protoensatite (20%), hedenbergite (15%), and titanium oxide (13%). The clay phases include zeolite (2 to 13%), montmorrillonite (1%) and vermiculite (1%).

The average concentrations (in wt%) of oxides decrease from SiO_2 (37.92), Al_2O_3 (18.08), Fe_2O_3 (10.21), MgO (3.43), Na_2O (2.28), CaO (2.01), K_2O (1.38), TiO_2 (0.81), P_2O_5 (0.38) and MnO (0.23). The order of average trace element enrichment is S (27112.7) > Cl (12743.6) > Ba (561.2) > Cu (274.1) >Sr (218.6) > Cr (195.4) >Zn (152.5)> Ni (118.1> Co (71.2)> Rb (45.3).

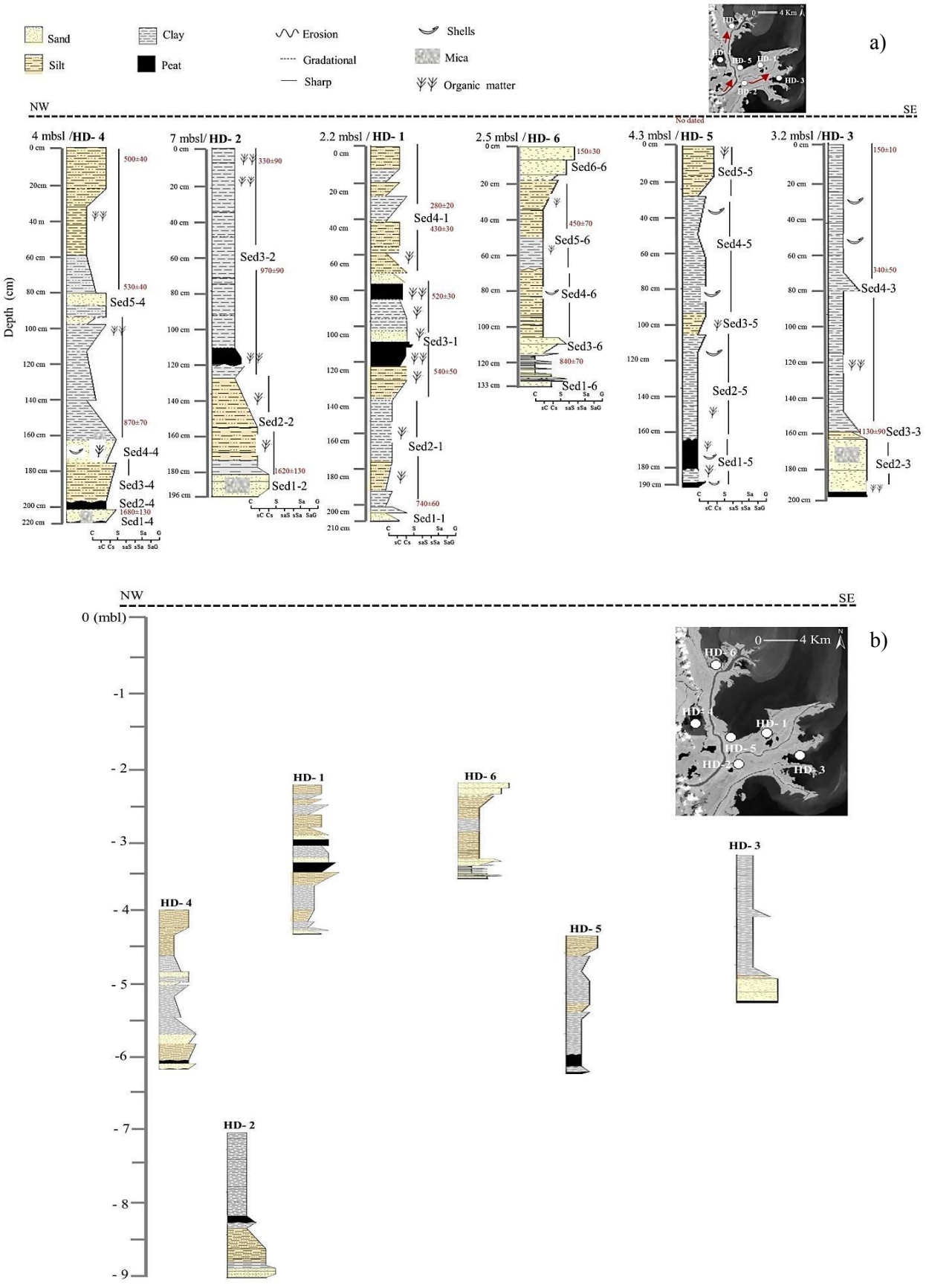

Figure 3.3 a) Sketch logs with measured sedimentological stratigraphical succession in ARD b) Vertical cores locations under sea level.

3.5.1 Grain size distribution

The core displays some variability in grain size and sorting with depth, being clearly coarser in swamps than in bays (Figure 3.4). HD-2 and HD-4 are coarser in depth and become finer to top of the intercepted stratigraphical successions, whereas HD-1 shows a more constant grain size composition from fine silt to clay (6 - >8ϕ), decreasing from bottom to top.

From NW to SE, HD-4 shows the coarser size (coarse silt), between 220 to 180 cm, with an important reduction in grain size at ~210 cm (fine silt). From 180 to 120 cm, the stratigraphical succession is more homogeneous with fine silt. Clay is significant around 90 cm and medium to fine silt is common from the 80 cm to 20 cm depth.

HD- 2 shows coarser sediments (fine sand) from 180 to 160 cm and a constant presence of medium to fine silt from ~ 150 cm to top. HD-1 is the more homogeneous stratigraphical succession with medium silt from 195 to ~ 167 cm; fine silt from ~ 160 to ~ 90 cm and very fine to clay from ~ 90 to 20 cm.

Bay stratigraphical succession show a grain size decrease from NW to SE. Sediments in HD-6 exhibit a coarser character, with important variation from 90 to 80 cm in which milimetric sand laminations intercalate with milimetric peaty mud. Grain size in HD-5 varies from bottom to top, with clay (170cm); fine silt (~168 ~ 90 cm); fine silt (80 – 45 cm) and medium to coarse silt from ~ 45 cm to top. The sampled portion of HD- 3 was done from middle to top of the core and shows a grain size decrease from 115 to 85 cm (medium silt); ~ 85 to 10 cm with very fine silt and some clayey size.

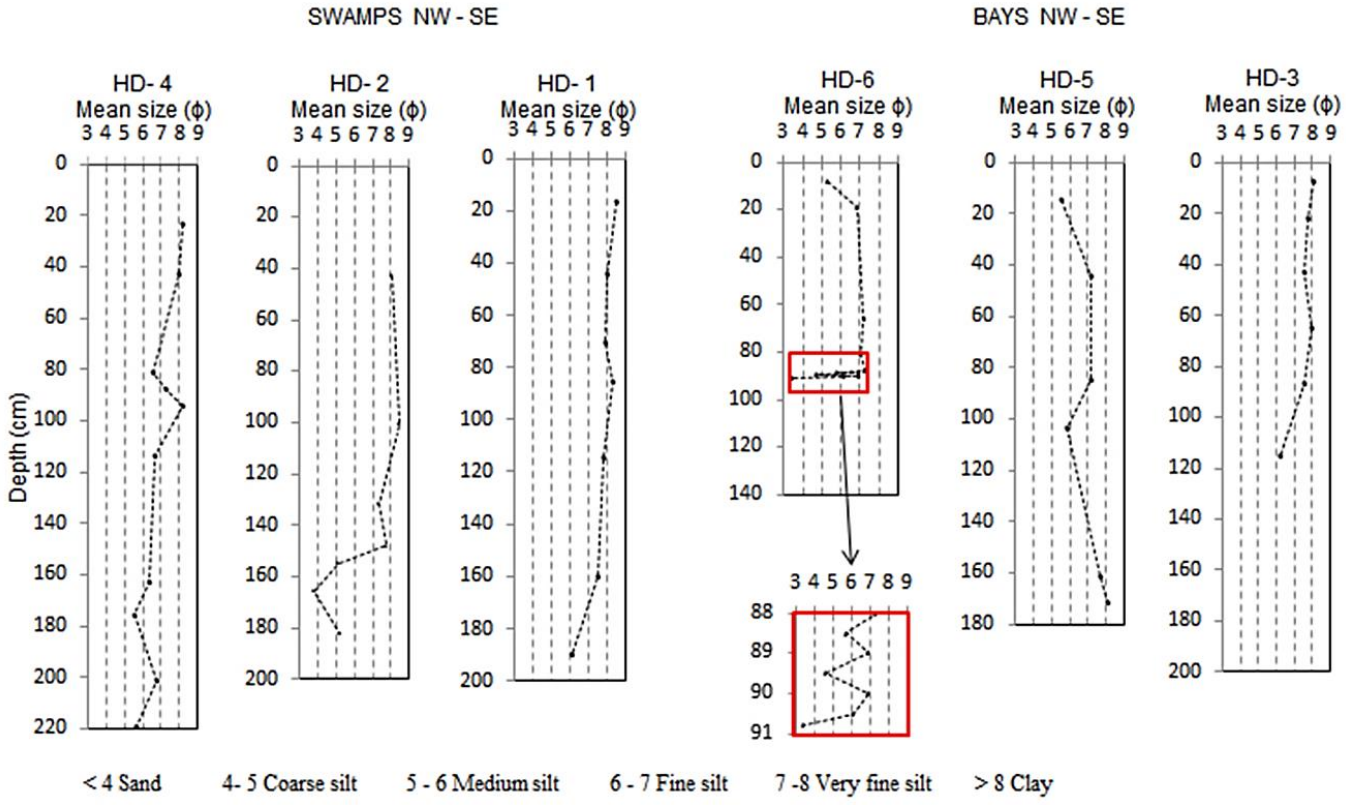

Figure 3.4 Mean grain size distribution in swamps and bays of ARD.

Based on the analysis of grain size curves, the boreholed sediments show evidence of the occurrence of various modes of transport along the core, and a sorting varing from poorly sorted to very poorly sorted. Rolling (sandy samples) have a moderate contribution in the general pattern; whereas saltation and suspension (silty and clayey samples) are the main type of transport, associated with middle to low energy flows (

Figure 3.5).

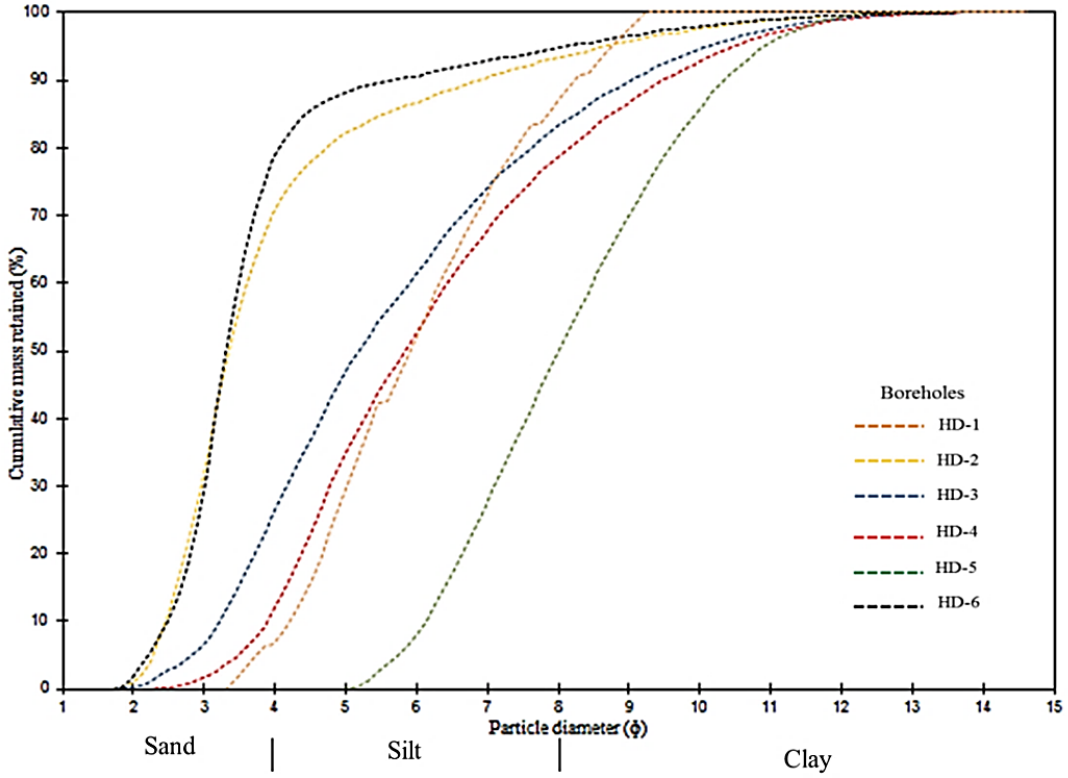

Figure 3.5 Cumulative curves of core sediments.

3.5.2 Mineralogy

Minerals along the different cores have a wide distribution (Figure 3.6) with (high abundances (XRD semiquantitative %) of quartz in HD - 1 (97%) and low in HD-6 (3%). Quartz phase is the most abundant in all the cores, followed by high abundances of feldspar+plagioclase in HD-2 (74%) and HD-4 (72%). also present in the whole cores.

Mica was not detected in HD-1 and HD-3, but has important abundances on the base of HD-4 (219 – 162.5 cm), on top of HD-5 (56 – 25 cm) and the depth of HD-6 (89 cm and 90 cm). The clay phase was detected in all cores with the major abundances in HD-2 (148 cm = 55%) and HD-3 (43 cm = 90%).Pyroxenes are absent in HD-3, HD-4, HD-5 and HD-6, and relatively high in HD-2 (155cm = 80%) and HD- 1(114 = 17%). The oxides phase is important on the middle of HD-1 (160 cm = 8%) and HD-2 (166 cm = 9%); scarce in HD-3, HD-4, HD-5 and HD-6 (1% to 4%).

The accessory minerals (pyrite, muscovite, bornite, rutile, cristobalite, coesite, hedenbergite, silvina, halite, cordierite, and protoenstatite and titanium oxide among other very low traces) are present along the stratigraphical successions with important abundances in HD-5 and HD-6.

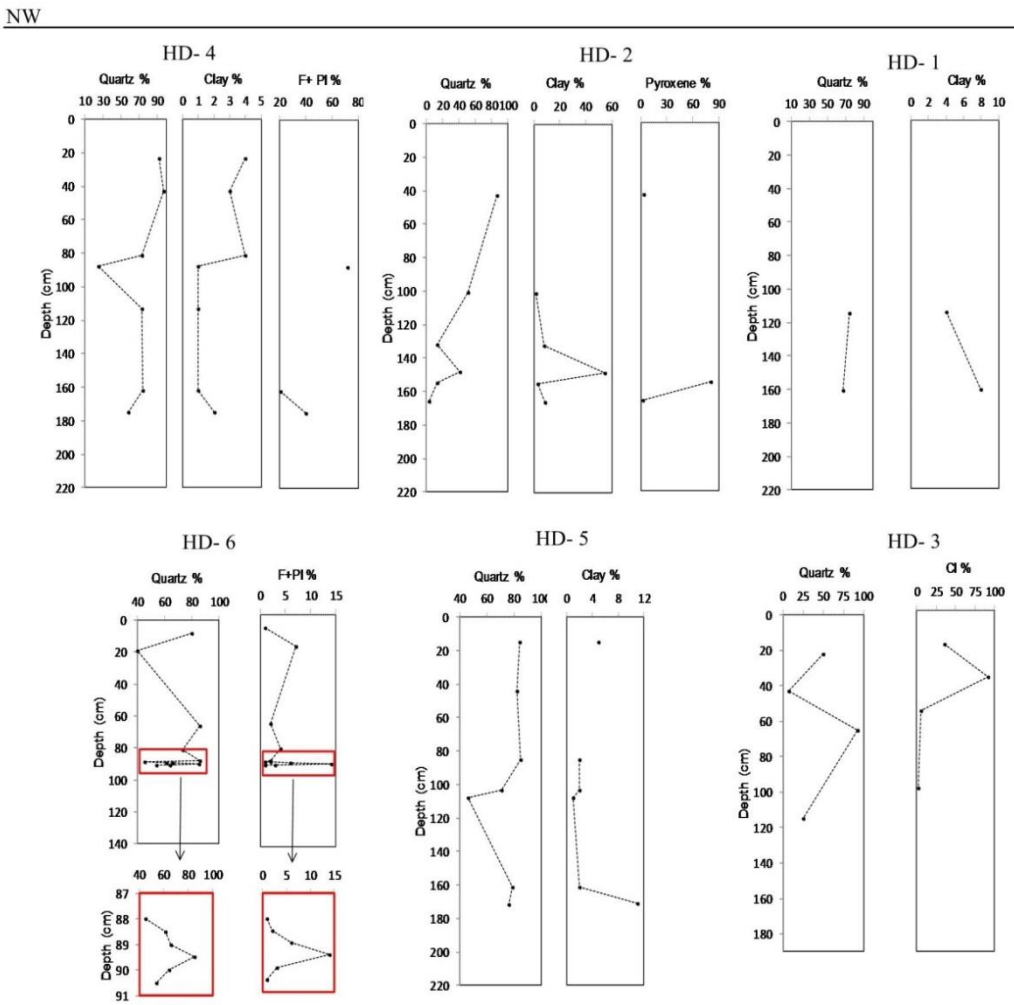

Figure 3.6 Main mineral detected phases in sampled cores after XRD.

3.5.3 Geochemistry and statistical analysis of samples

The correlation matrix in Table 3.2 displays the associations (significance greater than 95%) among pairs of variables. As notable examples, we highlight the high correlations of SiO_2 with Al_2O_3 (0.82), MgO (0.60), Cl (-0.77), S (-0.71) and LOI (-0.86).

Al_2O_3 is positively correlated with MgO (0.50), TiO_2 (0.51) and negatively correlated with Cl (-0.60), S (-0.60) and LOI (-0.82). Cl and S have strong positive correlation (0.74). Heavy metals have in general strong positive correlations among them: Cu/Zn (0.82); Cu/Ni (0.76); Cr/Zn (0.62); Cr/Ni (0.60); Zn/Ni (0.82).

Ti has positive correlation with Cr (0.83), Zn (0.70), Ni (0.65) and Rb (0.69). No significant correlation was found between chemical composition and grain size, except for a weak negative correlation between Na and clay (-0.53), Ca and medium silt (-0.51), and fine silt (-0.52) and Cr with very fine silt (-0.56) and with clay (-0.60). Appendix 14 summarizes the average composition of major elements in the cores and Appendix 15 summarizes the composition of trace elements in the cores.

Table 3.2 Pearson Correlation Matrix. Statistical significance for the Pearson r matrix, Coefficients in bold for p <0.05;. Grain size is expressed as Coarse Sand CS; Medium Sand MS; Fine Sand FS; very fine sand VFS; Very coarse silt VCSi; Coarse Silt CSi;

	Si	Al	Fe	Mg	Na	Ca	K	Ti	P	Mn	Cl	S	Ba	Cu	Cr	Zn	Ni	Co	Rb	LOI	CS	MS	FS	VFS	VCSi	CSi	MSi	FSi
Si	1.00																											
Al	**0.82**	1.00																										
Fe	-0.14	0.05	1.00																									
Mg	**0.60**	0.50	0.15	1.00																								
Na	-0.23	-0.24	0.09	0.46	1.00																							
Ca	0.37	0.16	-0.27	0.40	0.16	1.00																						
K	0.21	0.22	0.19	**0.59**	0.48	0.13	1.00																					
Ti	0.23	**0.51**	0.25	0.06	-0.10	0.17	0.30	1.00																				
P	-0.17	0.06	0.08	-0.36	-0.29	0.30	-0.14	**0.55**	1.00																			
Mn	-0.24	-0.03	0.33	-0.19	-0.09	-0.22	-0.32	0.07	0.17	1.00																		
Cl	**-0.77**	**-0.60**	0.26	-0.20	**0.67**	-0.14	0.17	0.10	0.12	0.16	1.00																	
S	**-0.71**	**-0.60**	0.28	-0.30	0.36	-0.08	-0.01	0.11	0.26	0.37	**0.74**	1.00																
Ba	0.44	0.37	-0.43	0.02	-0.30	0.43	-0.04	0.26	0.27	-0.17	-0.36	-0.43	1.00															
Cu	-0.39	-0.13	0.19	-0.48	-0.22	-0.18	-0.20	0.45	0.40	0.36	0.38	0.43	0.01	1.00														
Cr	0.03	0.21	0.28	0.03	0.10	0.27	0.31	**0.83**	**0.51**	0.01	0.33	0.29	0.12	0.41	1.00													
Zn	-0.24	0.09	0.32	-0.35	-0.21	-0.11	0.05	**0.70**	**0.57**	0.10	0.34	0.28	0.15	**0.82**	**0.62**	1.00												
Ni	-0.32	0.02	0.25	-0.31	-0.03	-0.07	0.07	**0.65**	0.45	0.16	0.47	0.34	0.15	**0.76**	**0.60**	**0.82**	1.00											
Co	-0.05	0.10	**0.68**	0.09	-0.07	-0.02	0.10	0.45	0.26	0.17	0.15	0.26	-0.20	0.34	0.44	0.49	0.39	1.00										
Rb	-0.14	0.13	0.12	-0.21	-0.07	-0.11	0.31	**0.69**	0.39	-0.07	0.30	0.18	0.29	**0.58**	**0.61**	**0.78**	**0.71**	0.34	1.00									
LOI	**-0.86**	**-0.82**	-0.15	**-0.73**	-0.05	-0.42	-0.41	-0.44	0.00	0.11	0.47	0.38	-0.26	0.32	-0.27	0.09	0.18	-0.16	0.03	1.00								
CS	-0.20	-0.14	0.08	-0.05	0.09	-0.18	-0.05	0.02	-0.06	0.06	0.16	0.32	-0.22	0.02	0.04	0.02	-0.02	0.05	-0.02	0.12	1.00							
MS	-0.26	-0.19	0.01	-0.12	0.19	-0.01	-0.10	0.15	0.04	0.09	0.34	0.38	-0.09	0.18	0.17	0.13	0.17	-0.02	0.06	0.16	**0.88**	1.00						
FS	-0.09	-0.14	-0.01	-0.05	0.25	0.42	-0.07	0.22	0.16	0.02	0.38	0.19	0.27	0.26	0.30	0.23	0.36	-0.09	0.12	0.03	0.15	**0.52**	1.00					
VFS	-0.12	-0.17	0.09	0.00	0.30	0.45	-0.05	0.21	0.12	-0.01	0.43	0.21	0.24	0.24	0.37	0.23	0.36	0.04	0.13	0.03	0.04	0.40	**0.94**	1.00				
VCSi	0.17	0.08	0.17	0.36	0.31	0.46	0.18	0.26	0.00	0.00	0.15	0.19	0.04	-0.08	0.49	0.00	0.12	0.29	0.02	-0.31	0.00	0.06	0.19	0.39	1.00			
CSi	0.15	0.12	0.18	0.34	0.25	0.05	0.28	0.18	-0.06	0.17	0.03	0.24	-0.37	-0.15	0.28	-0.14	-0.14	0.25	-0.14	-0.35	-0.03	-0.15	-0.40	-0.33	**0.56**	1.00		
MSi	0.12	0.20	0.01	0.05	-0.13	**-0.51**	0.18	-0.09	-0.14	0.10	-0.30	-0.11	-0.33	-0.21	-0.23	-0.20	-0.36	-0.05	-0.09	-0.14	-0.04	-0.35	**-0.83**	**-0.90**	-0.44	0.38	1.00	
FSi	0.08	0.18	-0.12	-0.10	-0.30	**-0.52**	0.02	-0.23	-0.11	-0.07	-0.38	-0.32	-0.07	-0.17	-0.47	-0.14	-0.31	-0.17	-0.03	0.01	-0.10	-0.39	**-0.77**	**-0.85**	**-0.70**	-0.10	**0.81**	1.00
VFSi	0.01	0.08	-0.21	-0.23	-0.43	-0.47	-0.14	-0.36	-0.09	-0.11	-0.43	-0.40	0.02	-0.13	**-0.56**	-0.15	-0.24	-0.20	-0.05	0.22	-0.16	-0.42	**-0.70**	**-0.78**	**-0.70**	-0.30	**0.62**	**0.92**
Cla	-0.13	-0.10	-0.18	-0.32	**-0.53**	-0.40	-0.26	-0.42	-0.04	-0.06	-0.39	-0.30	-0.06	-0.05	**-0.60**	-0.12	-0.25	-0.11	-0.10	0.39	-0.11	-0.35	**-0.60**	**-0.68**	**-0.74**	-0.34	0.49	**0.76**

The cluster analysis highlights three groups in the dendrogram of Figure 3.7. The analysis explains the clustering for 10 oxides and 10 trace elements, the LOI and grain size (mud %) from a set of 38 core samples.

Group 1 is formed by most of the oxides (SiO_2, Al_2O_3, K_2O, CaO), Ba and Cd, as well as the mud grain size. This group represents the most stable and indicative elements for the major sediment source in the study area, related to siliciclastic mineral. The geochemistry of this group seems to be controlled by muddy content, where high concentrations of SiO_2 and Al_2O_3 depend of to the mud percentage in ARD. This cluster represents the samples of Matuntugo (HD-1) and Marriaga (HD-4), swamps of lagoonal environment.

Group 2 represents associations among heavy metals (Co, Cu, Cr, Zn, Ni), oxides (Fe_2O_3, TiO_2 and P_2O_5) and Rb, indicating processes that occur in a chemically active environment that promotes chemical exchange, heavy metals leaching and the evidence of high weathering. For this cluster, there is a spread group of samples of HD-1, HD-2, HD-3 and HD-5.

Group 3 is formed by elements associated with salinity (Na_2O, Cl, MnO, S and the highest OM content), that are closely related to marine sediments detected at HD-5 and HD-6, characterized by active chemical exchange, bioproductivity in the marine environment and the brackish conditions. Sample HD-2-8 is exceptionally clustered in this group, being the one that contains the highest OM value of all measured samples (OM= 29.7%).

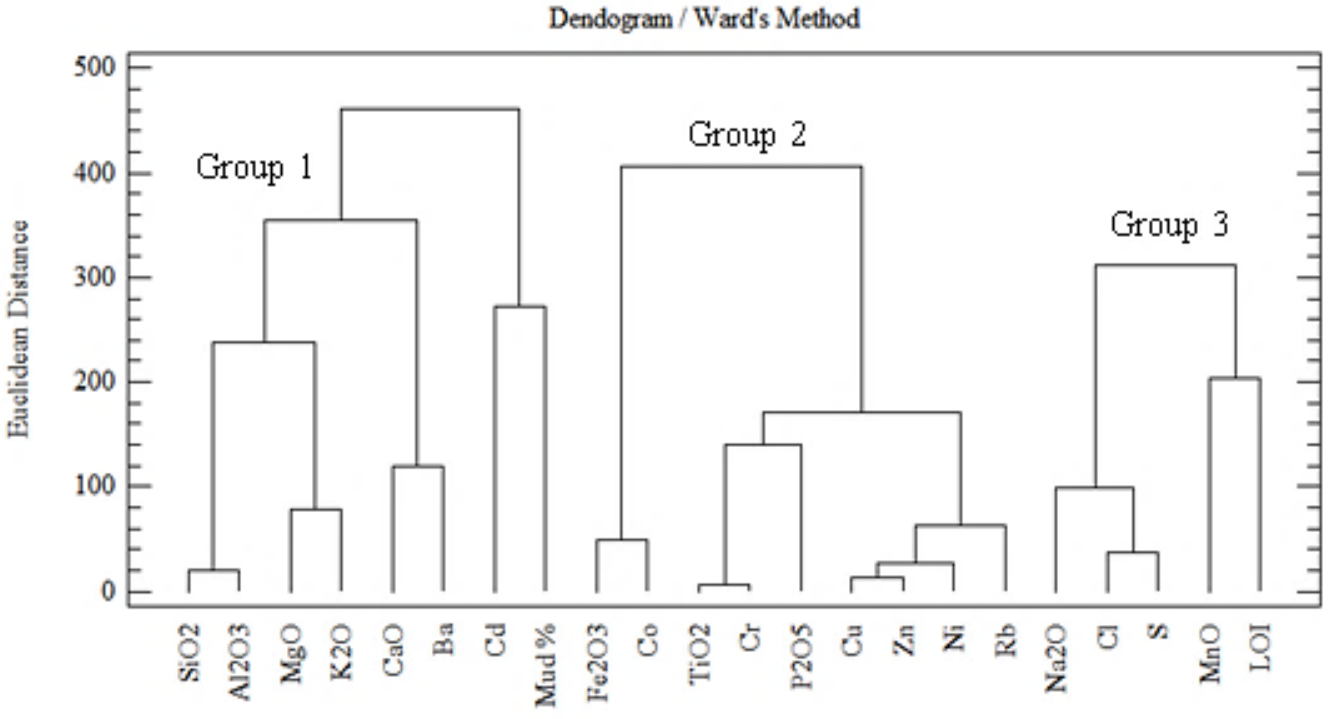

Figure 3.7 Dendrogram from a multivariate cluster analysis of geochemical, grain size and LOI variables.

3.5.4 Sedimentary dynamics

We interpreted our findings, according to Lario et al., (2002) and Tanner (1991a), to determine the depositional context of sediments, using the main grain size and sorting parameters. The depositional context of the ARD is certainly influenced by the tides, supported by the mean grain size–sorting plot (Figure 3.8). Most core samples clustered in the category of "close basin and fluvial storm episodes", but with a transition to "open estuary". Nonetheless, after the identification of facies, there is a set of sediments, mainly the base of some core stratigraphical succession, which are coarser and suggest both high-energy influences with some wave action, possibly acting during low tides.

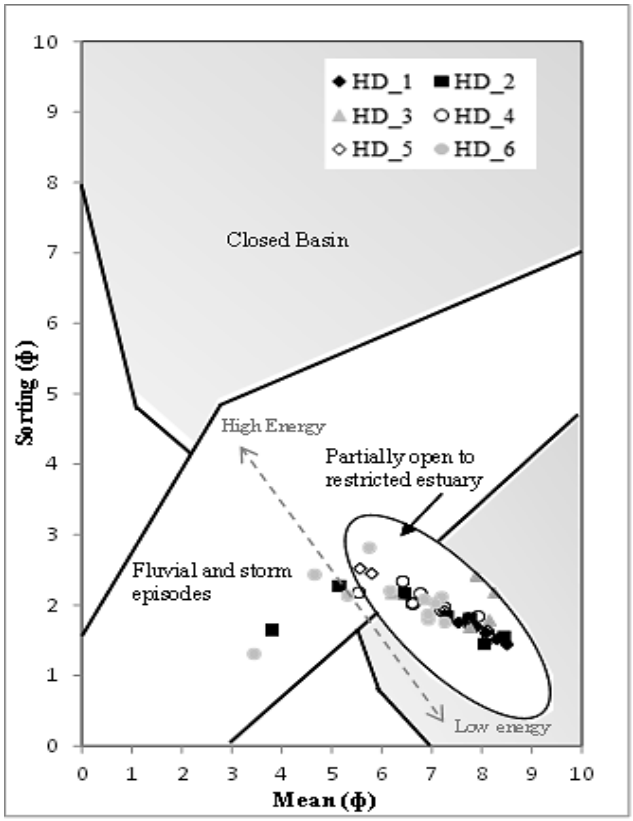

Figure 3.8 Mean grain size vs. sorting to determine depositional conditions. (after: Lario et al, 2002; Tanner, 1991a).

Furthermore, the silt, clay and peaty sediments above fine sand layers in the middle and lower part of the sedimentary stratigraphical successions in all the cores, tend to be more controlled by the river flow domain, with a medium to low energy flow.

According to our grain size analysis, sediments of the ARD are muddy, with poor sorting and a prevalent mesokurtic–platikurtic pattern, with an exceptional leptokurtic pattern (Figure 3.9). We used the relationship of SD (sorting) vs. kurtosis (Mateo and Siringan, 2016), to differentiate among sub-environments and sedimentary processes on the ARD. We found two very close populations of sediments with two isolated samples.

These two populations represent offshore-fluvial (sorting > 1.2 < 1.7, K> 2 < 2.5) and shoreface (sorting > 1.5 to 2.8, K>2.5 <4) environments. Two very fine samples, poorly sorted (< 1.5 > 2.2), leptokurtic and very leptokurtic (>7; <11), indicate an erosional source, possibly associated with a reworking of sediments. This scenario suggests again the dominance of mud with a subordinate sandy population.

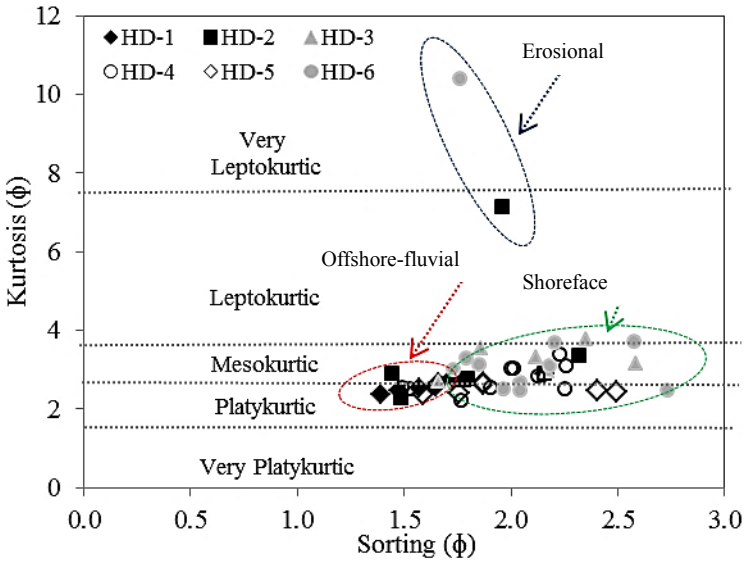

Figure 3.9 Scatter plot of SD (sorting) vs. kurtosis.

3.6 Discussion

The datasets collected and analyzed in this work provide the first insights into the lateral extent and variations of depositional context in the ARD's mixed fluvial-marine environment. We used a suite of sediment variables to distinguish and compare the facies succession, distribution and stratigraphy, supported by grain size, ages, mineralogy and geochemistry. The findings refute previous assumptions about the sedimentary dynamics of the ARD as completely dominated by fluvial processes.

We consider that the presence of spreading channels in the Atrato River reduces the flow discharge and sporadically favors tidal incursions into the channels at the west side of the delta, likely driven by climate seasons and wind direction. To the north, the main Atrato River flow energy is greater and influences the sediments distributions towards Yerbasal Bay and The El Roto mouth, where waves rework the deposited, coarser sand sediments.

3.6.1 Facies distribution and development

Facies were analysed at each location and depositional environment, corresponding to lower delta plain in a fluvial and lagoonal environment (mangrowes and swamps); shoreline-delta front with the marine (waves and tides influence), and the floodplain fluvial contributions (channels, inlets). We presented a first proposal for facies determination based on grain size for each core. The facies nomenclature has the prefix *Sed* followed by the number of facies and finally the number or core (i.e., *Sed1-1*). (Table 3.3).

We classified the stratigraphical succession of late Holocene and modern sediments in the ARD into several environmental facies from the lower 2 m and in a period of last 1680 a to recent. The six cores generally remain into the fine-grain-size classification, from the fine sand to clay with interbedded mud facies (varying within medium to fine silt). The peaty muds not only appear in the inland cores (swamps-fluvial environment), but also into the delta front (bays). In a similar way, laminated sands appear not only in the bays but also in some layers within the swamps.These patterns indicate also the mixed influence of fluvial and marine environments in the delta over time, allowed periodic subaereal exposures for the peat formation, due to the abundant OM.

Matuntugo Swamp (HD-1):

Sed 1-1: Shoreline – delta front (209–201 cm). This 8 cm unit without plant remains or shell fragments, formed by laminated silty sand, represents high-energy conditions that impeded the settling of fine sediments and organic material. These deposits suggest a shoreline environment in the delta front (likely a paleobay). The dated samples reported ages around 740±60 a, for this environment.

Sed 2-1: Lower delta plain-delta front (200 -104 cm). This 93 cm thickness consists of prevalent mud sediments (clayey silt) with moderate OM, indicating the transitional conditions from inland to coastal influence.

Sed 3-1: Floodplain with swamps (140 – 80 cm). The 60 cm thickness sediments consists of laminated dark gray silty clay with high OM content and two peaty layers (at 120cm and 83cm), representing the development of vegetation in freshwater, with a high organic material production *in situ*. This is a period which also represents two significant inputs of siliciclastic sediments, likely related to wet seasons. The dated samples in this stratigraphical succession indicate that this establishment started aroud 540±50 a.

Sed 4-1: Floodplain – Lower delta plain (70 cm to top). These muddy sediments of intercalations of silty and clay layers, with moderate to scarce content of OM, indicate deposition in a progradating environment of moderate to low energy. The dated samples allowed to infer this progradation could start around 520±30 a, and before 430±30 a.

The sedimentary stratigraphical succession in HD-1 is representative of the Lower delta plain, in an environment of shallow waters with fluvial sources and alternation periods of moderate to high energy flow that deposited the silty sand (*Sed 1-1*), followed by a low energy flow period that deposited the clayey silt organic matter sediments (*Sed 2-1*) around 740±60 a. Furthermore, a significant period of subareal exposure allowed the land vegetation growth, represented in the peaty layers of silty clay nature (*Sed 3-1*), around 540±50 a. The upper stratigraphical succession is representative of a period of low energy flow that deposited a stratigraphical succession of silty clay (*Sed 4 -1*) up to 430±30 a.

Further, in terms of the mineralogy in HD-1, we consider that the presence of bornite and pyrite, for instance, could indicate the contributions of sulfides and temporal anoxic conditions, whereas halite may indicate the brackish environment. Despite not having analyzed the clay mineral fraction in detail, after our bulk analysis.

Maquillón Swamp (HD-2):

Sed 1 -2: Shoreline-delta front (196–183 cm). The 13 cm unit without plant remains or shell fragments, but abundant mica, formed laminated silty sand. The presence of fine mica (fine muscovite: sericite), visually ranging from 20 % to 50%, is possibly the signature of fluvial suspended load as the source of mica, mixed with a fluvial input of sand.

Mica deposition requeries low flow conditions, whereas sand requires moderate to high flow. This mixture suggests a combined influence of river flow and tidal period, near an Atrato river inlet that filled a possible paleobay. Some similar facies with mica content occur on the Mekong Delta (Proske et al., 2011).

Sed 2 -2: Lower delta plain–delta front (183 – 120 cm). This 63 cm thick unit shows a silty clay sediment with moderate content of OM representing the transition (transport and deposition) of inland fine sediments seawards, around 1620±130 a.

Sed 3-2: Floodplain with swamps (120 cm – top). The 120 cm thickness sediments of laminated dark gray silty clay with high OM content and one peaty layer (at 110 cm) indicating the development of freshwater vegetation, with important formation of organic material up to 1000 a , just few meters before the determined age of 970±90 a .

Low or no siliciclastic sediments production is evident on this unit as representing a low energy period. The dated samples in this stratigraphical succession could indicate that this establishment started at some point between 970±90 a, and 303±90.

Burrera Bay (HD-3):

Sed 1-3: Floodplain with swamps (196 – 192 cm). The 4 cm peaty layer, represent the distal part of a zone of organic material formation.

Sed 2-3: Lower delta plain–delta front (192 – 162 cm). These 30 cm represent an important change of environment conditions respect to *Sed 1-3*, with a high-energy flow that deposited these sandy sediments, mixed with mica and OM. We interpreted a possible combined influence of tidal movement and a river or inlet outflow.

Sed 3-3: Lower delta plain – delta front (162 – 158cm). This unit of silty sand and low to moderate OM content represents a short transition from an inland condition to marine, above 1130±90 a. This facies is very similar to *Sed 2-3*, but finer and without mica, that could indicate a different source or the temporal decrease of the flow energy, but remaining in the same environment.

Sed 4-3: Floodplain – Lower delta plain (158 cm to top). This thick unit represents a clay succession with moderate spread of OM content and undistingable shell fragments at 77 and 54 cm, which could indicate an intertidal environment. This unit dated at 70 cm (340±50 a) and close to the top (10cm) as 150±10 a, possibly represent these intertidal conditions for around a millennium (the period from 1130±90 a to 150±10 a) .

Marriaga Swamp (HD-4):

Sed 1 -4: Lower delta plain–delta front (219 – 201 cm). This 19 cm of very dark brown massive coarse silt with OM and mica, deposited by a high energy flow conditions in a mixed environment framed by tidal movements and river outflow. These sediments were dated around 1130±90 a, and could be the indication of a paleobay.

Sed 2- 4: Floodplain- with swamps (201 – 197 cm). The 4 cm thick dark brown layer with abundant OM, classified as peat. This thin peat possibly represents a period in subaereal conditions that allowed the establishment of vegetation in a relative sea level variation.

Sed 3 -4: Floodplain (197 -177 cm). This 20 cm thickness laminated dark reddish gray silt with 6.5% of OM indicates the switch of subaereal towards moderate energy flow conditions in freshwater.

Sed 4-4: Shoreline-delta front (177 – 157 cm). The 20 cm unit of dark gray laminated sand with shell fragments of vivalves and mica represents a shallow water environment in intertidal conditions, also fed by fluvial inputs.

Sed 5-4: Floodplain–Lower delta plain (157 cm to top). The muddy sediments of silty and clay layers intercalations, with moderate to high content of OM and two coarse layer of laminated sand (97 cm and 85 cm) indicates the deposition in a progradating environment of moderate to low energy with two defined pulses of high energy represented by the coarse sediments. The four obtained dates indicates a period between 870±70 a and 500±40 a.

Candelaria Bay (HD-5):

Sed 1-5: Lower delta plain – shoreline ((190 – 167cm). This 23 cm of dark brown gray clay, with high OM content (10%) and moderate shell remains content (10%), represents a mix environment of subaereal exposure that allowed the vegetation rise with a tidal incursion. At present, a direct narrow inlet of Atrato main river channel feeds Candelaria bay. If this inlet remained open at the time, could be an explanation for this mixed unit.

Sed 2-5: Floodplain – Lower delta plain (167 – 105cm). The 62 cm thickness sediments of very dark gray silty clay with moderate OM and few shell fragments, indicates a possibly extension of tidal influences in a vegetated zone in a confluence of fresh and brackish waters.

Sed 3-5: Floodplain – with swamps (105 – 95cm). The 10 cm thickness of laminated silty clay, contains oxides nodules (10%), fine mica (5%) and OM. This layer represents subareal conditions under the influence of fluvial inputs of moderate energy.

Sed 4-5: Delta front (95 – 25cm). This 70 cm of laminated dark gray silt with mica and shell fragments represents an environment of waves as the predominant influence.

Sed 5-5: Delta front-shoreline (25 cm to top). The laminated dark gray silt contains few OM and mica, reflecting shoreline deposits with scarce fluvial inputs that carry the OM and mica. This core was not dated, due to the problems with sample treatments.

Burrera Bay (HD-6):

Sed 1- 6: Shoreline–delta front (133 to 129 cm). This 4 cm massive dark gray fine sand with mica (10%) and not OM, could indicate high energy water conditions affected by a fluvial source that supply mica. We consider the incidence of waves for this facies.

Sed 2 -6: Flood plain with swamps (128 to 118 cm). This is a 10 cm brown to dark gray laminated sand with 10 % of fine mica (sericite) and sulfur smell, interbedded with thin peaty layers. These features indicates wetland conditions in standing waters, varying with tidal – waves influence that allowed the deposition of thin sand layers. These conditions date at 840±70 a.

Sed 3 – 6: Floodplain (118 – 110 cm). The 8 cm thickness consists of dark gray laminated sandy silt, with 6.1% of OM, representing the product of fluvial sedimentation seawards.

Sed 4 -6: shoreline–delta front (110 - 68 cm).This 42 cm thick succession of laminated dark gray clayey silt layers with moderate to high OM and destroyed shell fragments, represents a intertidal environment with possible mangrove presence in the shoreline.

Sed 5 -6: Floodplain (68 - 20 cm). The 48 cm of gray brown laminated clayey silt with 6.2 to 8.3% of OM indicates a period of constant fluvial sedimentation, dated for 450±70 a.

Sed 6 – 6: Shoreline (20 cm to top). This 20 cm of bedded dark gray sandy to fine gravel underlying very homogeneous dark gray sandy silt without OM indicates a grain size increasing in high energy flow conditions that did not allow the preservation and deposition of OM, shells and fine sediments. In these terms, the sediments represent wave action in the shoreline. The dated sample near the top of these sediments indicates the prevalence of wave conditions around 150±30 a.

Table 3.3 Idealized facies succession for shallow sediments (2 m depth) in the ARD. The stratigraphical succession reflects the transition and alternations from inland facies of fluvial influence to intertidal - wave conditions with the activation of progradation.

Stratigraphy	Facies name	Sedimentary features	Set average	Organic matter	Interpretation of the depositional environment
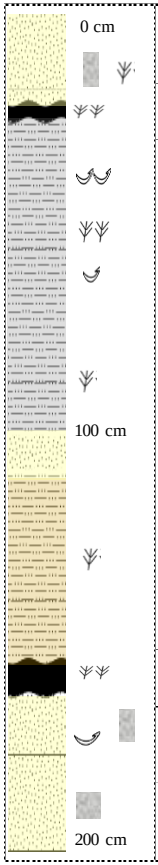	Sed 6-6, Sed5-5	Dark gray - brown ((5Y 2.5/1,,Y 3/1; 5Y 4/1,7.5YR 3/1). Massive coarse to find sand. Laminated silt. Scarce OM and mica.	25	intermitent	Shoreline - Delta front with low fluvial inputs. Waves prevalence
	Sed3-1, Sed3-2, Sed3-5,	Dark reddish brown (2.5Y 3/0 to very dark gray (7.5YR 3/0) laminate silty clay.	10 - 30	Abundant	Flood plain - shallow swamps. Subaereal exposures.
	Sed2-1, Sed2-2, Sed2-3, Sed2-5,Sed4-1,Sed4-3, Sed3-3, Sed3-4, Sed5-4, Sed4-5,Sed 3-6,Sed5-6,	Very dark grey to dark olive grey (2.5YR 4/0, 5Y 4/1, 5Y 3/2) laminated clay. Moderate Shell fragments. Interbedded sandy mm layers. prevalent mud sediments (clayey silt) with moderate OM	5 - 141	Moderate	Floodplain - Lower delta plain:transitional conditions from inland sediment to the coast.
	Sed1-3, Sed1-4,Sed2-4,Sed2-6, Sed4-3	Dark grey to grey brown color (2.5Y 3/0, 2.5Y 4/0, 5Y 3/1). Laminated silty sand. Laminated silty clay. Peaty layers.	10	Abundant	Flood plain - shallow swamps. Subaereal exposures.
	Sed1-5, Sed4-4	Dark gray (7.5YR 4/0). Laminted silty sand. Shells, mica/ Dark brown gray clay, OM (10%), shells.	20	Moderate	Lower delta plain - shoreline: Intertidal conditions. Shallow waters. Moderate vegetation rise.
	Sed1-1, Sed1-2	Dark olive gray (2.5Y 4/0 ; 5Y 3/1). Laminated silty sand Mica > 40%.	40	Absent	Shoreline - Delta front with low fluvial inputs. Waves prevalence

Sand Silt Clay Peat Mica Organic matter Shells

3.6.2 Drivers of sedimentary dynamics in the ARD

All variables measured in the sedimentary stratigraphical successions reveal a specific environmental feature occurred at a particular time from late Holocene to present and explains the nature of sedimentary dynamics on the ARD. The grain size analyses of all the cores show an average distribution in the shallow delta (< 2m depth) of 19.9% clay, 69.2 % silt and 11% very fine to medium sand (Appendix 11). This pattern could explain the general muddy nature of the ARD partially influenced by marine incursions, similar to the features that occur in the Mississippi Delta (Fitzgerald, et al., 2004), the Mekong Delta (Li et al., 2017), the Mahakam Delta (Storms et al., 2005), the Nile Delta (Pennington et al, 2017) instead of a unique fluvial domain. Likewise, we revealed a combined fluvial-tidal delta type (Goodbred and Saito, 2011) for the ARD, based on its landforms that include swamps, marshes, and the absence of meanders in channels within the delta domain. The meandering pattern is visible around the first avulsion of the Atrato River in León Mouth, which forms the delta apex (11 km upstream of the lower delta plain).

The assumption of a fluvial domain based on the bird's foot delta morphology of the ARD (Blanco, 2016; Velásquez, 2013; Post, 2011) is clear in terms of geomorphology and the latest progradation (Vélez et al., 2020). Nonetheless, waves and tides do not necessarily act at the same time and in the same way. Normally, waves only influence the shoreface and coast line sediments, whereas tides could have an influence inland (Goodbred and Saito, 2011; Storms et al., 2005; David et al, 2003), and for ARD in the vicinity of the proximal lower delta plain.

We think the influence of waves in the ARD is not strong in recent times, since the delta exhibits certain geomorphological features not associated to wave control (continuous beach ridge with wide sand beaches, non-steep topography along the coast line, a sedimentary succession of facies of mudy clay-silt, or sporadic reworked sand) (Restrepo, 2008, Fitzgerald et al., 2004; Davis et al., 2003). The most notorious influence of waves occurs to the north in Yerbasal and el Roto mouth and decrease to the south of the delta around the river mouths (Velásquez, 2007; López and Restrepo, 2007).

Some findings in the older sedimentary stratigraphical successions, however, (bottom of cores HD-2, HD-3, HD-4 and HD-6), are consistent with wave influence (coarser sediments of silty sand facies with shell fragments mixed with sandy mica), marking the effect of a relative sea level rise at the time (Khan et al., 2017; Robertson et al., 2003; Robertson and Martínez, 1999), probably mixed with discharges from river mouths and small sediment loads from inlets that fed swamps and bays. From these facies, we infer a fluvial-wave interaction in the delta in the late Holocene.

Mangroves are features of tidal deltas (Ta et al., 2005; Allison et al., 2003) present in the ARD along the riverine channels (Blanco, 2016). Mangroves are established over the channels margins and their permanent presence was also detected at depth in the core stratigraphical successions, as seen in the recurrent presence of OM, similar to the Mekong Delta patterns (Li et al., 2017). This presence supports the idea of a tidal and winds influence (Montoya, 2010) in a brine transition zone towards the fresh waters of the Atrato River. Using the geochemical data, we found particular enrichments of S, Cl, Na, Ba, Br and Ca inland at swamps stratigraphical successions, as well as the presence of halite and silvine as saline minerals.

Climate is also a very important driver of the alternation and distribution of facies in the ARD. Whitin the short period analyzed in the cores, we interpret the direct influence of seasonality, precipitations and warm periods as evident and consistent with the location of ARD within the Intertropical Convergence Zone (ITCZ) (Restrepo and López, 2008). Furthermore, the Monsoonal circulations also influence the warm season precipitation over the eastern tropical Pacific (Amador et. al, 2006), that could affects the sediments distributions and sorting along the delta. Additionaly, the research about the ITCZ migration southwards, occurring in the late Holocene, evince the precipitation decreasing in SouthAmerica (Venezuela and Brazil) and could support the variability in the environments found in the facies, associated with peaty layers, OM and shells content oscilations (Chiessi et. al, 2021; Rúa et. al, 2016, Haug et al, 2001).

The possible marine intrusions into the fresh waters (Sarkar et al., 2009; Bhattacharya, 2006. Posamentier, 2001) are possible, even within the microtidal regime of less than 0.5 cm (and sporadically 1m) at the Gulf of Urabá (Post, 2011; Bernal et al., 2005; Vernette et al., 2002; Tolman, 1997). The low gradient of the ARD and the delta's extended flood plain with absence of significant barriers enables the partial intrusion of sea water into the river. During these intrusions, sediments can experience reverse transport by suspension and can be deposited inland. Wind could be another factor that influences the sea water intrusion, mainly in the dry season, when the wind forces increases towards inland in a NW preferencial direction, but with an average low intensity (range:1.5 - 3.3 m/s.) (Montoya, 2010).

In terms of tectonics, we roughly analyzed the structural control in the Gulf of Urabá exerted by the Uramita fault at the east in a NW/W direction (crossing by near the town of Turbo) and the Murindó Faults at the west in NW/E direction (Figure 3.10). The ARD sediments have a low gradient towards the east that is sufficient to promote the recent progradation of non-consolidated fine sediments.

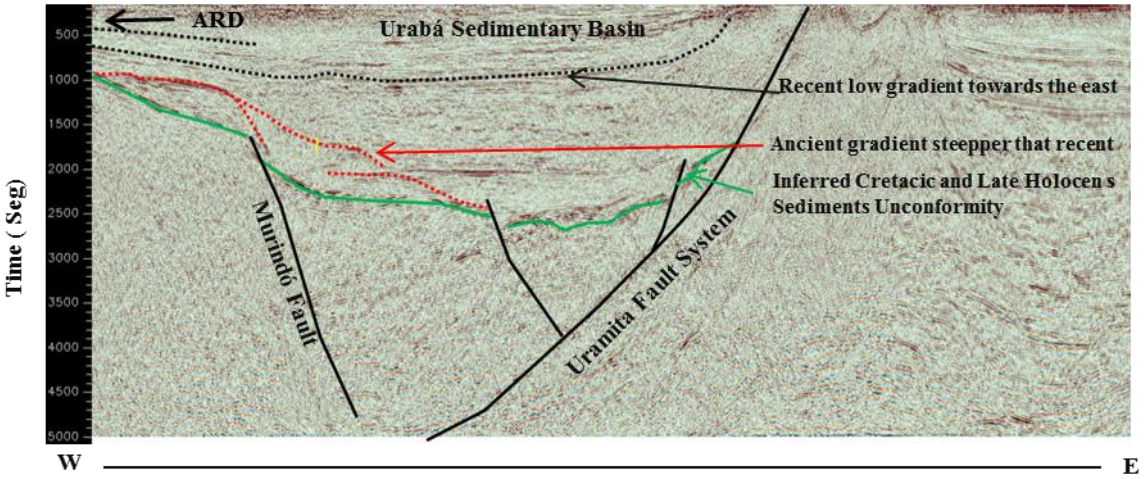

Figure 3.10 Structural control in the Gulf of Uraba by the Uramita and Murindó. Black dotted lines indicate the low gradient of the ARD sediments towards the east of Gulf of Urabá, that promote the recent progradation. Red dotted lines indicate the ancient gradient, steeper than the most recent. The green dotted line indicates the unconformity (contact) between the Cretacic rocks and the Quaternary Sequence (after seismic line 8933. Free scientific information provided by Agencia Nacional de Hidrocarburos).

We used the Digital Terrain Model (DTM) of northwest Colombia (own design with data acquired from the Shuttle Radar Topography Mision - SRTM project from NASA). This DTM represents the local tectonic drivers that affect the north part of the Atrato River Basin, the Baudó - Darién mountain system, the ARD and the Gulf of Urabá (Vargas et al; 2009; Duque -Caro, 1990) . The west side of the ARD represents a compressional portion within the Baudó – Darién Mountains, driven by the Darien Fault System NW/E (Coates et al., 2004) and the Murindó Fault NW/E (Figure 3.11).

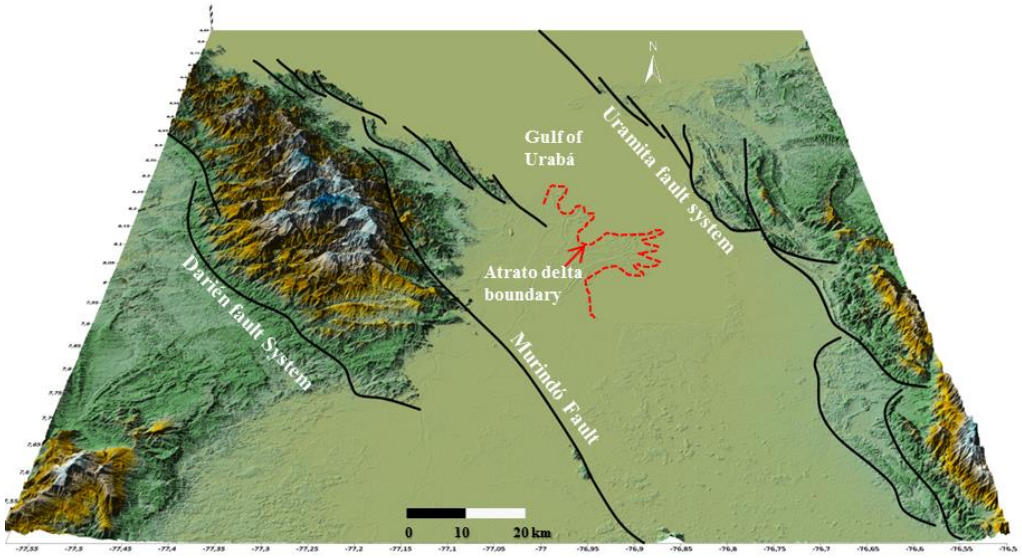

Figure 3.11 Digital terrain model of the target area and the main tectonic structures that drive the ARD sedimentary dynamics and the sink of the Gulf of Urabá (Surfer model, own design after topographic NASA data).

We did not analyze in detail the incidence of tectonic factors in the sedimentary dynamics of the ARD (which is beyond the scope of this research). However, we found support for the structural control excerted by the Darien, Murindó and Uramita faults over the recent progradation and sinking of the Urabá Basin as a result of a compressive tectonic pattern in the Gulf of Urabá.

Relative sea level variations between the middle and late Holocene are reflected in the littoral cordons and beaches that have formed during a sea level that was 2 to 3 m above the modern level, around 3000 a, along the Colombian Caribbean coast (Khan et al., 2017; Vélez et al., 2014; Robertson and Martínez, 1999). The relative sea level drop allowed the progradation of the ARD, which is consistent with the sedimentary deposits we encountered in the cores from the last ~ 800 a. We note the continuous succession of fine sediments (mainly clay, then silt, with sporadic sand laminations) from 130 cm depth to surface. Nonetheless, complementary studies mention a new episode of sea level rise, which occurred in the last century, that affects the coastline worldwide and along the Caribbean sea and could increase up to 86 cm by 2100 (Cronin, 2012; Robertson et al., 2003). A recent sea level rise period could be controlled by the tectonic features of tilting in ARD, similar to the simulations done by Kopp and Kim (2015) in Ganges–Brahmaputra delta.

We consider the occurrence of equilibrium with predominanty low to moderate constant energy flow of the Atrato River that promotes progradation towards the Gulf of Urabá. In this regard, tectonics promote fluvial progradation whereas the relative sea level rise promotes tidal effects towards inland.

3.6.3 Paleoenvironmental interpretations

We classify the sub environments that have dominated the ARD from late Holocene to present based on two cross sections linked through the sedimentary stratigraphical successions. The first cross section involves the sedimentary stratigraphical successions from northwest to southeast (Figure 3.12) and includes the sedimentary succession encountered in the lower delta plain (HD-4 and HD-1) and delta front (HD-5 and HD-3). The second cross section includes the sedimentary stratigraphical successions from south to north (Figure 3.12), associated with the upper delta plain (HD-2), lower delta plain (HD-4) and delta front (HD- 5 and HD-6).

Northwest to Southeast cross section (HD-4, HD-5, HD-1, HD-3). This encompasses several facies (from bottom to top) associated with a peaty layer (floodplain), silts and fine sand (shoreline-delta front) and clays (lower delta plain towards delta front). The lower stratigraphical succession (220~160 cm) is a set of coarse sand interbedded with peaty layers and silt (<1680±130 to 870±70 a). The scarce OM in the lower sediments of Matuntugo Swamp (HD-1) could be interpreted as a marine influence because of its closeness to the open sea at that time, perhaps as a paleobay, which did not allow a subaerial exposure for enough vegetation development. The dated sediments at HD-1 did not match the rest of the dated stratigraphical succession, being younger (< 740±50 a) due to its upper location in terms of sea base level respect to Hd_4, HD-5 and HD-3. In addition, a geomorphological feature that could explain this isolated deposition in HD-1 is that the inlet that feeds the Matuntugo swamp runs from Matuntugo channel around 4.2 km towards the west, and this swamp could be younger than the other lacustrine depositional context in the ARD area (Figure 3.12).

Ages of silt and clay sediments of the intermediate depth (160 – 110 cm) at HD-4, HD-1 and HD-3 range from <1680±130 to 870±70 to 330±50 a. OM content is high at HD-1, which is consistent with the fluvio-lacustrine sedimentation of low-energy flows and intermittent subaerial exposure. The iron oxides nodules, vesicles, mica and scarce OM present at HD-4 indicate more subaereal conditions within a fluvio-lacustrine depositional context with sporadic marine inputs. The sediments in both swamps stratigraphical successions are similar with respect to concentrations of detrital elements (Si, Al, Fe, Na, Ca, K, Ti) and heavy metals. Sulfur is absent in HD-1 and exceptionally high at HD-4 (averaging 17950 ppm), which is consistent with redox conditions. HD-5 and HD-3 middle stratigraphical succession have lower detrital elements concentrations with similar heavy metals abundances registered in swamp sediments. The grain size of the fourth sediment stratigraphical successions consists of thick clays, interbedded with thin to medium fine silt sediments and sporadic sand lenses in swamps.

Upper sediments in the cross section (< 100 cm - surface, dated from ~ 530±40 a to 150± 10 a) grade from silt in HD-4, HD-5 and HD-1 to clay in HD-3. Detrital elements have low concentrations in the whole stratigraphical succession, indicating mainly moderate to low energy flows. However, Cl, Ba and S concentrations increase significantly

from swamps to marine sediments, representing some tidal influence. Low or absent OM in the lower stratigraphical succession indicates scarce periods of aerial exposure or more humid conditions. In these terms, the ARD can be represented by two main environments.

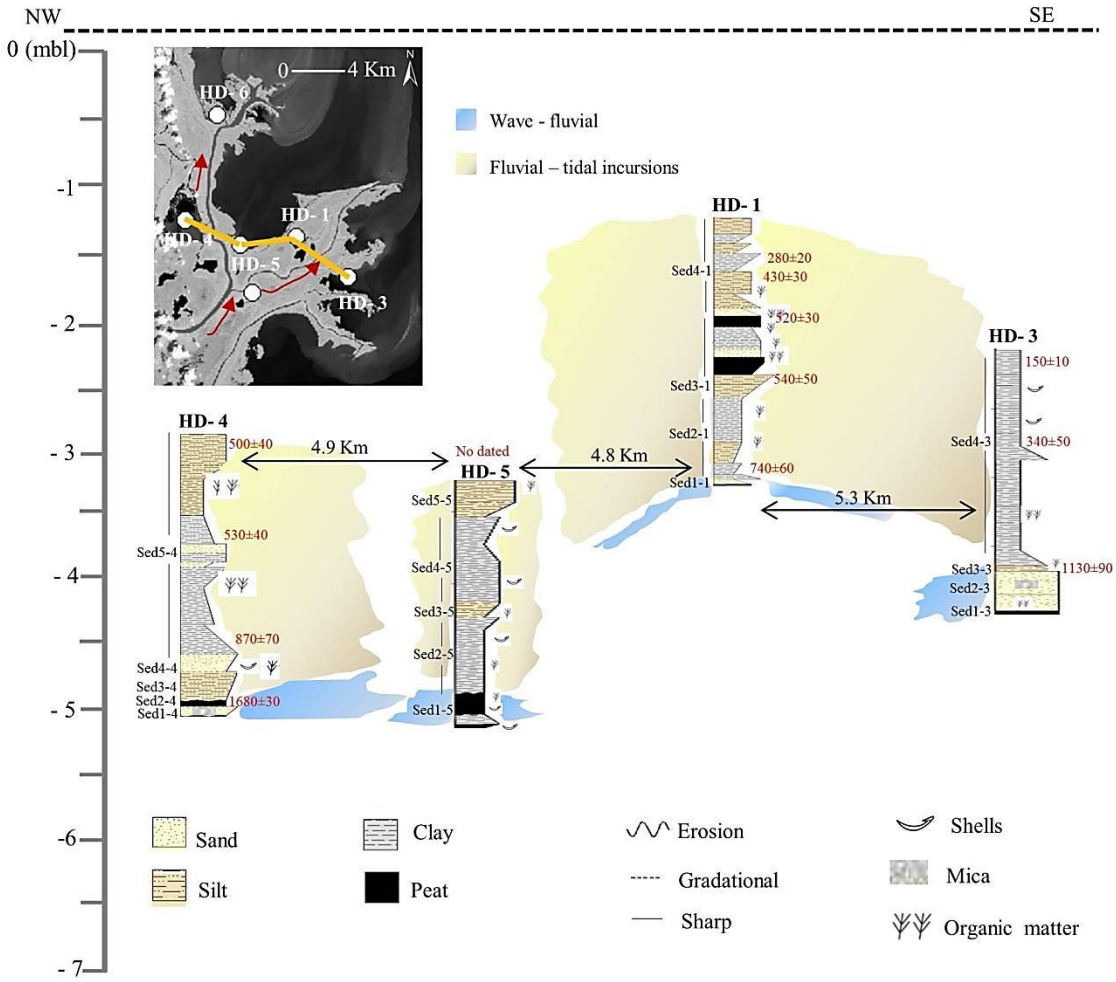

Figure 3.12 Classification of environments from northwest to southeast deposits, based on the interpretation of sedimentary facies and ages.

The first environment is a wave–fluvial domain, represented by facies *Sed1-4, Sed2-4, Sed3-4, Sed4-4, Sed1-1*, *Sed1-5, Sed1-3, Sed2-3, Sed3-3* in the shoreline-delta front. The OM content and presence of shells were significant in the west, decreasing towards the east, where mica appears to reinforce the fluvial inputs. The second environment is an intertidal domain combined with fluvial domains, represented by many facies (*Sed5-4, Sed2-5, Sed3-5, Sed4-5, Sed5-5, Sed2-1, Sed3-1, Sed4-1, Sed4-3*) mainly at the east in the lower delta plain (HD-1, HD-3), which represent a more fluvial environment. This mixed fluvial–tidal domain is also represented by peaty facies (*Sed2-4, Sed1-5, Sed4-1, Sed4-3)* of clay and silt sediments, interbedded with organic fine layers. Upper facies (*Sed5-5*) to the north and central ARD, indicates some wave influence in the deposited sediments.

South to north cross section (HD-2, HD-5, HD-4, HD-6). This trend is associated with fine sand and peaty layers (floodplain), silts (lower delta plain-shoreline) and intercalations of silty, clayey and sandy layers (shoreline-delta front). The lower stratigraphical

succession (220 cm ~180 cm) is a set of coarse sand interbedded with peaty layers and silt (<1680±130 to 870±70 a) at HD-2 and HD-4 (HD-5 could not be dated by the IRSL method, therefore we base its interpretation on facies). The middle stratigraphical succession (~180 ~ 100 cm) ranges from <970±90 a to ~530±40 a, and involves a thick stratigraphical succession of clay with scarce and intermittent OM and shells content, which is consistent with a combination of fluvio-tidal sedimentation of low-energy flow and very rare subaerial exposure. The upper stratigraphical succession, from ~100 cm to the surface, comprises a record from ~ 530±40 a to 150±30 a. The ages of the upper stratigraphical successions are uneven (i.e. HD-2 ~ 970±70 a at 60 cm, HD-4 ~530±40 a at 75 cm, and HD-6 ~480±40 a at 65 cm), due to existing differences in locations respect to sea base level and also to the possible differences between recent deposits caused by progradation and old deposits towards the south in HD-2, showing possible reworking (
Figure 3.13).

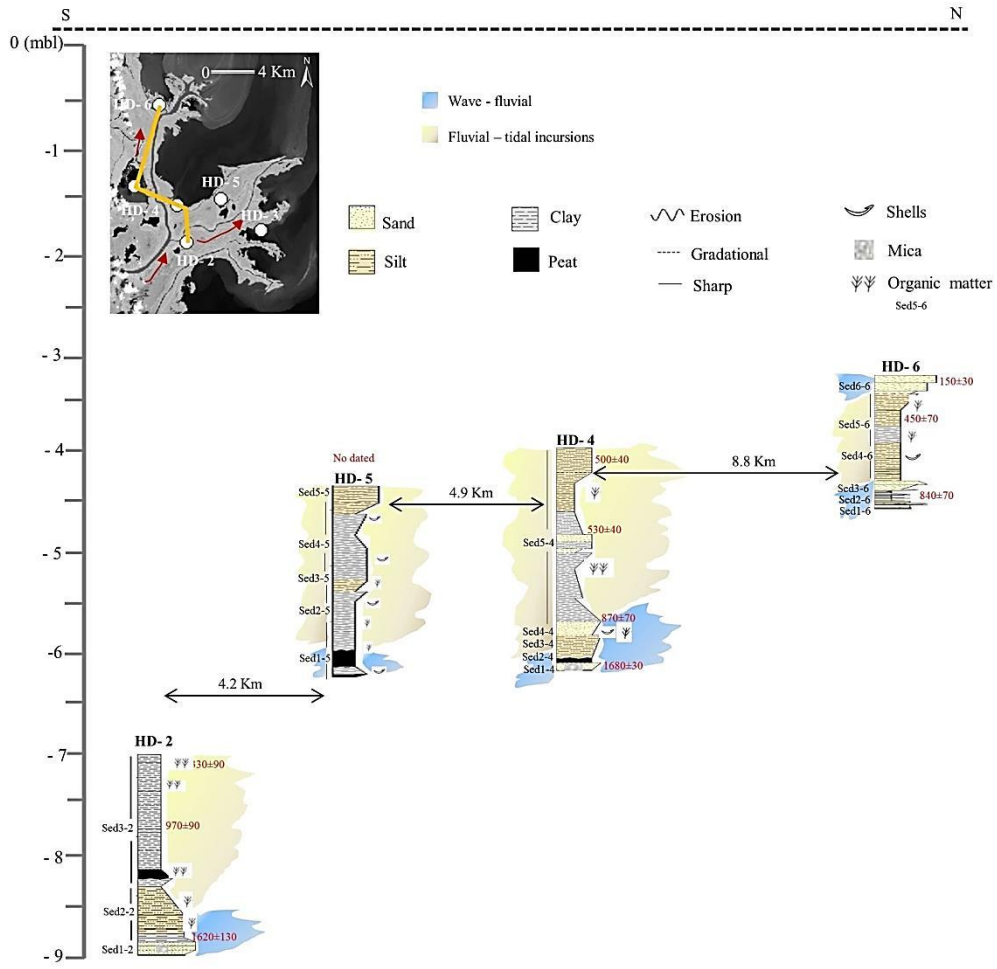

Figure 3.13 Classification of environments from south to north deposits, based on the interpretation of sedimentary facies and ages.

Sediments in both swamps stratigraphical successions (HD-2 and HD-4) are similar with respect to concentration of detrital elements Si, Al, Mg, Na, Ca, Ti and Mn, whereas high values were detected for Fe and low for K and P in HD-4, indicating possible local differences based on sediment inputs and heavy metals. Sulfur was detected in all the cores, being lowest in HD-2 (average of 3706 ppm) and increasing towards the north in

HD-5 (average of 29471 ppm), HD-4 (average of 17950 ppm) and HD-6 (average of 27112 ppm). Those values are consistent with redox conditions today. The upper stratigraphical successions of HD-5 and HD-6 have abundances of heavy metals that are similar to the ones registered in swamp sediments. This is consistent with the homogeneity of the systems for heavy metals leached along the ARD.

The south to north trend sediments indicates two environments. The first environment is a wave-fluvial domain in the late Holocene (<1680±130 to 870±70 a), represented by Facies *Sed1-2, Sed1-4, Sed2-4, Sed3-4, Sed4-4, Sed1-5, Sed1-6, Sed2-6* of sand and silt sediments. The OM content is moderate to high and the shells fragments moderate. The second environment is a fluvial domain with sporadic tidal effects around <870±70 a to ~150±30 a, represented in the mayority of facies (*Sed2-2, Sed3-2, Sed2-5, Sed3-5, Sed4-5, Sed5-5, Sed4-4, Sed4-5, Sed3-6, Sed4-6, Sed5-6, Sed6-6*) of silty sand and clay deposits with colored laminations interbedded, scarce OM layers at the lower delta plain–delta front boundary. This is the thickest stratigraphical successions and relates to the major extension of the floodplain (fluvial sediments) and part of shoreline- delta front (shoreface sediments). This second environment likely determines the establishment of delta progradation that continues today.

3.6.4 Sedimentary shallow architecture of the late Holocene in ARD

We interpreted the deposition patterns and sedimentary dynamics of the last 1680±130 a of ARD, based on i) our geomorphological findings (Appendix 12); ii), the surficial facies found and described in the first chapter of this study, iii) the ages determined by IRSL dating in chapter II of this study and iv) the shallow facies determined in cores. The southern part of the ARD is dominated by fully fluvial facies (floodplain), including the last evidence of meandering morphology and the delta apex (León channel avulsion) that shows the grain size decreasing from coarse sand to silt and clay towards the north, as well as geochemical variations related to dilution (
Figure 3.14).

At the edge of the upper delta plain, the fluvial system losses its meandering condition and splits into several parallel distributary channels towards the east. The swamps and marshes are more spread and the depth of depositional stratigraphical successions of coarse nature (fine sand to silt) in the floodplain (as showed in HD-2) indicate a predominant fluvial domain. The extended distributary channels at the lower delta plain towards the delta front (HD-1, HD-3 and part of HD-4 stratigraphical successions) have developed along a central west to east axis, which defines a preferential orientation of the four main Atrato River channels (Leoncito, Burrera, Coquitos and Matuntugo). Sedimentary deposits are centimeter-scale layers of silty sand and thicker silt–clay interbedded with some peaty layers (at HD-1), being more clayey towards the delta front (HD-5 and HD-3). These layers show a low tide–mild fluvial energy regime (Figure 3.14 b and c).

Towards the north, the fluvial deposits interbeds with coastal and shallow marine sediments, visualized in centimeter-scale stratigraphical succession (at HD-4, HD-5 and HD-6). The presence of peaty levels, identified along both marine and fluvio-lacustrine stratigraphical succession, indicates relatively intermittent humid subaerial conditions along the examined stratigraphical succession. In this sense, the peaty muds in the ARD are

not only present inland in swamps but also in the lower delta plain towards the bays. Meanwhile, the laminated sands could be restricted to wave action in bays.The presence of shell fragments, some minerals such as halite, silvine and the geochemical presence of Na, S, Cl, Ba support the idea of marine incursions towards the delta, in periods with a low fluvial regime.

This marine incursions ocurred around ~1680±130 to ~ 870 ± 70 a, a period when the delta did not prograde towards the Gulf of Urabá and the relative sea level could be higher (Khan et al., 2017; Vélez et al., 2014; Robertson and Martínez, 1999). Further sedimentary dynamics evinced a transition to a strong fluvial dominant period from ~ 870 ± 70 a to ~ 550± 50 a, with finer sediments, abundant organic matter and swamps that could be a relative sea level drop. The most recent deposits indicate a period of relative sea level drop, with a thick stratigraphical succession of fine sediments and the occurrence of continuous progradation with steady marine incursions from ~ 550± 50 a to recent (Figure 3.14).

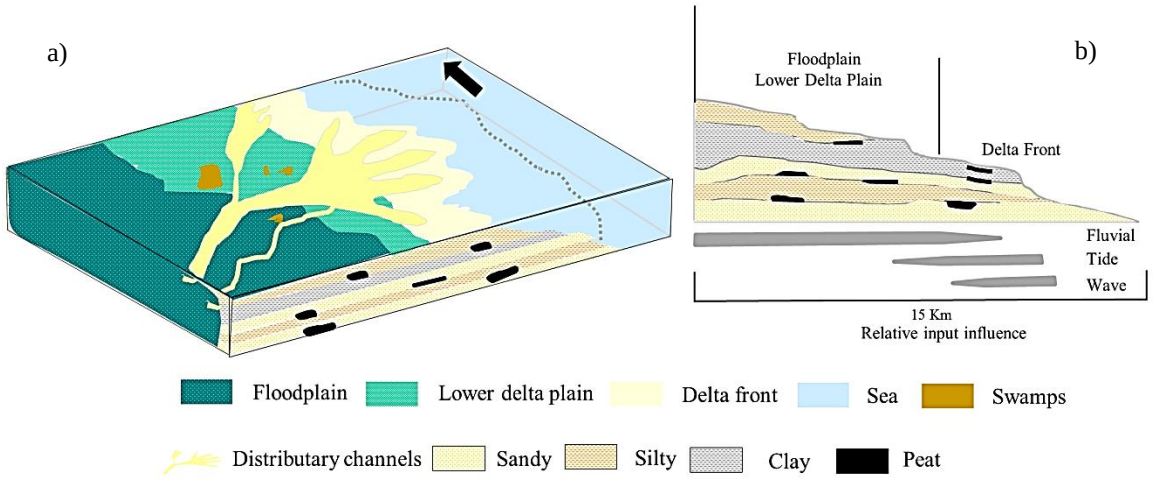

Figure 3.14 Representative depositional sketch of shallow sediments in ARD.a) Planform determined from surface samples b) cross section representing the shallw deposits determined from the cores.

Based on the findings of this thesis, we finally propose two main mechanisms that can explain the two well-differentiated periods in the recent sedimentary dynamics of the ARD. The first mechanism relates to relative sea base level changes, which may have oscillated in the late Holocene as a result of the active tectonics in the Gulf of Urabá. This oscillation could have favored an initial marine influence that was followed by a fluvial-dominated environment in the delta. The second mechanism relates to changes in river energy flow, driven by hydroclimatic factors and temporary flow spreadings into different active channels. This flow energy changes may have reduced the streamflow intensity over an extended period to allow the marine intrusions in the floodplain, followed by a period of larger discharges that switch the dominance towards the fluvial inputs. These two mechanisms are not mutually exclusive and could have occurred simultaneously over the delta front. We expect these findings will provide new ground for future research in the delta.

3.7 Conclusions

We used a multiproxy approach to describe the evolution of the ARD during the late Holocene to present, based on examination of sediment cores to decipher the shallow sedimentary dynamics in this active delta. The identified sedimentary facies (from floodplain, to the lower delta plain and delta front), reveal sedimentary dynamics with two well defined periods: a time of prevalent marine influence in the late Holocene (<1680 ±130 to 870± 70 a), followed by a time of prevalent fluvial influence (around ~ 870 ±70 a - to recent), with a transition period of mixed fluvial inputs and tidal effects (~550±50 a to recent). These dynamics explain the overall delta progradation towards the Gulf of Urabá.

Analysis of subaqueous sediments from the six cores enabled the characterization of grain size, mineralogy, geochemistry, OM content, ages and facies at the central floodplain and delta front of the ARD. The stratigraphical successions and corresponding interpretation of facies revealed an active sedimentary dynamics during the late Holocene, likely associated with relative sea base level changes and variations in river energy flows, in which a marine influence turned into a fluvial influence in the delta.

The lowest stratigraphical successions and facies belong to a marine deposit, in which sandy sediments with intercalations of peaty sediments indicate a shift from a fluvial-estuarine environment a more fluvial–terrestrial one, with a low-relief floodplain system developed mainly at east of the delta. Middle and upper deposits, composed of silty and clayey sediment layers, represent the fluvial distributary channels over bank deposits of the Atrato River, which contribute to the extension of the recent low-relief delta-floodplain. Interbedded sand laminations in the middle and upper parts of the stratigraphical successions reflect the tide incursions towards the fluvial environment.

The ARD is usually described as a bird's foot delta, typical of a fluvial domain. However, the contribution of tidal processes is not negligible and can be found in the marshes and swamps, through features such as the mangrove vegetation in the lower delta plain and the channel mouths, or the presence of shell remains in some fluvio-lacustrine facies. Marine waves contribute to the formation of narrow sand beaches along the coast and thin sand deposits close to some channel mouths, mainly at Leoncito and Matuntugo. The centimeter-thick sand deposits in the bottom and middle sections of the sedimentary stratigraphical succession reflect this contribution. Some recent fine sand deposits with mica content and broken shells reveal the effect of sediment reworking caused by waves.

The fluvial channels distributed over the delta, favor the occurrence of middle to low discharge that temporaly allow the tides to intrude areas of the old distributary channels. This is one of the reasons for the increase in clay deposits between the lower delta plain and delta front (average thickness of 140 cm). Fluctuations from fluvial to microtidal regimes framed the flat topography and even enabled the continued progradation.

The physicochemical composition of sediment samples along the core indicates the possible ocurrence of inland saline water intrusions. High concentrations of Cl, Na, Ba and S in swamps, plus the occurrence of halite, silvine, bornite, pyrite, titanium oxide, calcium oxide, zinc sulfide, silicate and coesite, support this inference. Despite the microtidal regime in the Gulf of Urabá (average < 0.4 m), the flat topography and tidal currents, lead to soft periodic reversals of flow direction towards the lower delta plain.

The stratigraphic correlations between fluvio-lacustrine and marine sediments support the argument of a substantial influence of the Atrato River sediment loads in the sedimentation over the west side of the Gulf of Urabá. This pattern has presumably been prominent for the last ~550±50 a, supported by the increase of finer sediments facies in the middle to upper sediment sections in the six cores. In this context, the shallowness of the Gulf of Urabá favours the current delta progradation. Therefore, inland sediments reworking is moderate to high because of the energy of the river flow, whereas it is moderate to low at the Gulf of Urabá, which overall enables the continuous formation of the bird foot morphology.

3.8 Acknowledgements

This study was supported by the Colombian Administrative Department of Science, Technology and Innovation (COLCIENCIAS, Call 727/2015); as part of the Doctoral Program of the first author in Environmental Engineering at Universidad de Antioquia. We thank the GAIA Research group of Universidad de Antioquia, Köln University of Germany; XRF Lab of the Materials Engineering Department of University of Antioquia, IRLS Freiburg University, and DRX Laboratory of Universidad de Antioquia and Instituto Tecnológico Industrial Pascual Bravo in Medellín for allowing the preparation and laboratory testing of samples. Special thanks to Dr. Frank Preusser for his support and advice with IRSL dating of ARD sediments, during the first author's internship in 2018 at Ludwig University of Freiburg; to Dr. Stephen Optiz from University of Köln for Laser grain size assays; to Dr. María Teresa Flórez from Universidad de Antioquia for her invaluable academic support. Special thanks to the communities of the Atrato Delta region who accompanied and assisted the first author in her field campaigns and project socialization.

4 Chapter 4: General conclusions

For this work, we collected and analyzed a set of surface and core sediment samples from the Atrato River Delta, with the aim of examining the late Holocene and modern sedimentary dynamics of the delta formation in the last 1620 a , with three specific research goals in mind:

i. Characterize grain size, mineralogy, geochemistry and age of surface and shallow sediments collected from the ARD

ii. Interprete the sedimentation processes on the Atrato Delta through stratigraphic analysis and sedimentological facies identified from six drilled shallow cores, and

iii. Develope a conceptual scheme of the shallow sedimentary dynamics on the Atrato Delta and in the western sector of the Gulf of Urabá during the late Holocene.

This section summarizes the main conclusions of the thesis, focusing on the achievements of the proposed objectives.

4.1 Characterization of grain size, mineralogy, geochemistry and age of surface and shallow sediments of the Atrato River Delta.

This thesis offers a first interpretation of sedimentary processes in the ARD through the analysis of grain size distribution, bulk mineralogical phases and geochemistry of surface sediments. The study links the transport regime to the mineralogical distribution, trace element patterns from terrigenous sources (Si, Al, Fe, and Ti), heavy minerals (Cu, Zn, Ni, Co and Cr) and marine ions (Cl, S, Ba), the tectonic setting, sediments provenance and composition.

The physicochemical features of surface sediments on the ARD reflect an active depositional context with saltation as the mean transport mode, controlled by a low to moderate energy flow. The drivers of mineral distribution are sorting, source, weathering, mineral hardness and density. Geochemistry of major and trace elements elucidates the processes of weathering and dilution, the tectonic setting and provenance classification and heavy metal enrichment.

The mineral distributions indicate the transport of low-density minerals over long distances (towards the north of the ARD), scattered into the distributary channels (towards the east). These minerals remobilize and deposit in swamps, flood plains and bays across the delta. High-density minerals are more concentrated and distributed along the main Atrato River channel. The incidence of traction and saltation in west, northeast and east sectors, could control and influence faster deposit of heavy minerals and consequently, their depletion or absence within the distributary channels.

The variability of sedimentary processes in the ARD is more intense in the west, central and southeast sectors, where major differences in grain size, mineralogy and geochemistry occur. Riverine medium and coarse silts dominate these zones, forming modern deposits

that promote progradation along the main distributary river mouths that flow directly to the west side of the Gulf of Urabá and deposit sediments in the delta front.

The CIA at the ARD displays a wide range between 59.55 and 70.11, which indicates the surface sediments originate from moderately to highly weathered igneous and sedimentary sources. These values also indicate moderate maturity of sediments and weathering effects after deposition.

Geochemical classification of ARD surface sediments reveals the intermediate to felsic granite basalt-granite rock as their main source, which agrees with the main composition of Graywacke and Fe–shale, and with the predominant medium- fine grain size. Secondary bedrock sources are supported by the Cr/Ni ratios that indicate mafic rocks such as basalt and lava breccias.

4.2 Interpretation of sedimentation processes of the Atrato River Delta through stratigraphy and sedimentological facies in shallow cores.

The use of the Optically Stimulated Luminescence (IRSL) technique to date fluvial and marine sediments in a tropical environment is one of the novelties of this thesis. The samples had a narrow IRSL feldspar signal but lacked an OSL signal in quartz. However, the chronology showed a consistency of ages, in agreement with ^{14}C ages from nearby sites in the delta and in other studies. The obtained set of ages was essential to interpret the late Holocene sedimentation history of the ARD.

Sediment accumulation rates determined for the ARD represent important findings that complement the interpretation of the sedimentary dynamics of the ARD. Despite apparently low average accumulation rates (<2 mm a^{-1}), they are similar to those of other tropical deltas such as the Orinoco, Irrawaddy and Bengal. These data indicate that the ARD has substantial sediment transport and load competence in terms of its catchment area compared to other deltas.

The analysis of geomorphological features, surficial sediments distribution (facies), shallow facies in cores, and OSL dating, enabled the interpretation of deposition patterns and sedimentary dynamics of the ARD. Full fluvial facies, including the last evidence of meandering morphology and the delta apex (León channel avulsion) dominate the southern part of the ARD. Grain size decreases from coarse sand to silt and clay towards the north. The geochemical variations strongly relate to dilution and weathering. In the zone of the upper delta plain, the fluvial system losses its meandering character and splits into several parallel distributary channels towards the east. The swamps and marshes spread out and the depositional stratigraphical successions of coarse nature (fine sand to silt) in the fluvial-lacustrine depositional context were deposited at a low to moderately mixed (fluvial–wave) energy regime.

The zone of lengthy distributary channels in the lower delta plain towards the delta front has developed along a central west-east axis, defined by the preferential orientation of the four main channels (Leoncito, Burrera, Coquitos and Matuntugo). Sedimentary deposits are centimeter-scaled layers of silty-sand and thicker silt–clay, interbedded with some peaty layers, being more clayey towards the delta front. This succession implies a low tide – weak fluvial energy regime.

Towards the north, the fluvial sediments interbed with coastal and shallow marine sediments, visualized in centimeter-scale stratigraphical successions. Presence of peaty levels, identified along both marine and fluvio-lacustrine stratigraphical successions indicates relatively intermittent humid sub-aerial conditions. Presence of shell fragments and concentrations of some trace elements, support the idea of an incursion of marine sediments towards land, revealing the influence of waves during low fluvial regimes, in a transgression period when the delta did not prograd towards the Gulf of Urabá and the sea level was higher. Further sedimentary dynamics reflect a transition towards a tidal domain, with finer sediments, a relative sea level drop and sporadic low fluvial inputs. Recent dynamics include a sea regression period with a thick stratigraphical succession of fine sediments and the emplacement of continuous progradation with steady tidal incursions.

4.3 Development of a conceptual scheme of the shallow sedimentary dynamics on the Atrato Delta and in the western sector of the Gulf of Urabá during the late Holocene.

This research used a multiproxy approach to describe the evolution of the ARD during the late Holocene, based on the examination of sediment cores to decipher the shallow sedimentary dynamics in this active delta. The sedimentary facies identified in the cores (from floodplain, to the lower delta plain and delta front), reveal a sedimentary dynamics with two clearly defined periods: a prevalent relative base level rise in the late Holocene (<1680±130 to 870± 70 a), followed by a sea level drop started some point after 870± 70 a (stronger around ~ 550 ±70 a to present), with a transition period dominated by a fluvial environment, with intermittent tidal inputs (~ 740 ±60 to 550±50 a). These dynamics explain the overall delta progradation towards the Gulf of Urabá.

The analysis of subaqueous sediments from the six cores enabled the characterization of grain size, mineralogy, geochemistry, OM content, ages and facies at the central floodplain and delta front of the ARD. The stratigraphic stratigraphical successions and corresponding interpretation of facies revealed an active sedimentary dynamics during the late Holocene, when a relative base level rise episode turned to a sea level drop. The lowest stratigraphical successions and facies belong to a period of sea level rise. In this period, sandy sediments with intercalations of peaty deposits indicate a shift from a combined fluvial-estuarine environment toward a more fluvial–terrestrial one, in which a low-relief floodplain system developed, mainly east of the delta. Middle and upper deposits, composed of silty and clayey sediment layers, represent the fluvial distributary channels over bank deposits of the Atrato River, which contribute to the extension of the modern low-relief delta-floodplain. The interbedded sand laminations in the middle and upper parts of the stratigraphical successions reflect the marine incursions towards the fluvial- terrestrial environment.

The ARD is usually described as a bird's foot delta, typical of a fluvial domain. However, the contribution of tidal processes is not negligible and can be found in the marshes, swamps, and extended flood plain, through features such as the mangrove vegetation in the lower delta plain and the channel mouths, or the presence of marine remains in the fluvio-lacustrine facies. Sea waves contribute to form narrow sand beaches along the coast and thin sand deposits close to some channel mouths, mainly at Leoncito and Matuntugo. The centimeter-thick sand deposits in the bottom and middle sections of the sedimentary stratigraphical successions evince this contribution. Some recent fine sand

deposits with mica content and broken shells reveal the effect of sediment reworking by waves.

Large numbers of fluvial channels cause moderate to low discharges distributed among them. In this scenario, it is possible that tides dominate some areas of the old distributary channels, being the dominant driver in new channels, consistent with the microtidal conditions reported in the Gulf of Urabá. This is one of the strongest reasons for the increase in clay deposits between the lower delta plain and the delta front (average thickness of 140 cm). Fluctuations from fluvial to tidal regimes shape the flat topography and promote continued progradation.

The physicochemical composition of sediment samples along the cores indicates the occurrence of inland saline water intrusions. High concentrations of Cl, Na, Ba and S in swamps, plus the mineral occurrence of halite, bornite, pyrite, titanium oxide, calcium oxide, zinc sulfide, sodium, calcium, aluminium silicate and coesite, support this assumption. Despite the microtidal regime in the Gulf of Urabá (average < 40 cm, exceptional 1.6 m), the flat topography and tidal currents lead to periodic reversals of flow direction towards the lower delta plain.

The stratigraphic correlations among cores, using fluvio-lacustrine and marine sediments, illustrate the significant influence of the Atrato River sediments loads in sedimentation on the west side of the Gulf of Urabá. This pattern is presumably prominent for the last ~550±50 a, supported by the increase of finer sediments facies in the middle to upper sediment sections of the six cores. In this context, the shallowness of the Gulf of Urabá favours the current delta progradation. Therefore, the reworking of sediments inland is moderate to high because of the energy of the river flow, whereas it is moderate to low at the Gulf of Urabá, a condition that promotes the continuous formation of the bird foot morphology.

4.4 Future venues of research

Future research should be extended upstream of the delta, to reduce the uncertainties about the Atrato River sedimentary processes in terms of avulsions and bifurcations that had formed the delta. This extension could include additional drilling campaigns and detailed chronology to complement our spatial and temporal resolution.

Complementary surface sediments should be collected in León Channel (the main bifurcation of the Atrato River) to better characterize the sediment transport towards the east side of the delta.

Salinity and pH measurements could be very useful inland to determine the silty wedge boundary along the river channels and swamps.

An issue is the difficulty to find suitable sites for drilling. On the one hand, the river and distributary channels are not adequate to drill, due to the fluvial currents that do not allow installing a stable platform to drill. On the other hand, the flood plain areas are normally flooded and plenty of vegetation, which makes the drilling equally difficult. This was one of the reasons to choose swamps and bays to carry out the cores in relatively calmed waters with good possibilities to drill. Other techniques for stratigraphy and facies recognition,

such as ground-penetrating radar or electrical resistivity tomography, may overcome this difficulty. These techniques could be useful as indirect methods to detail the chrono-stratigraphical stratigraphical succession.

Despite the reliable detection of quartz and feldspar sediments to date with OSL, the technique has proven to be relatively challenging in ARD, although good enough to age the sediments and determine accumulation rates overall, because this dating method has demonstrated to be satisfactory and accurate in other deltas, much more than radiocarbon dating. Therefore, the technique can be used with improved sampling protocols and careful determination of sampling sites, to complement the database gathered in this thesis.

Despite the notable difficulty to get cloud-free photographies and satellite imagery from this region, a detailed multi temporal geomorphological survey that includes the analysis of floodplain inputs in the upper and lower delta plains will be useful to determine the migrations of the Atrato River and its distributary channels over time and to elucidate erosion and accumulation fluctuations.

5 References

Adikaram, M., Pitawala, A., Ishiga, H., and Jayawardana, D. (2019). Geochemistry and grain size distribution of surface sediments of a large semi-enclosed lagoon connected to the western Bay of Bengal. Estuarine, Coastal and Shelf Science, 216(September 2018), 4–13. https://doi.org/10.1016/j.ecss.2018.09.002

Aitken, M.J. (1998). An introduction to optical dating, Oxford University Press, 280 pp.

Akter, J., Sarker, M.H., Popescu, I., Roelvink, D. (2016). Evolution of the Bengal Delta and its prevailing processes. J. Coastal Res. 32, 1212–1226. https://doi.org/10.2112/jcoastres-d-14-00232.1

Allison, M.A., Kepple, E. (2001). Modern sediment supply to the lower delta plain of the Ganges-Brahmaputra River in Bangladesh. Geo-Marine Letters 21, 66–74. https://doi.org/10.1007/s003670100069

Alvarado-Aguilar, D., Jiménez, J.A., Nicholss, R.J. (2012). Flood hazard and damage assessment in the Ebro Delta (NW Mediterranean) to relative sea level rise. Nat. Hazards 62, 1301–1321. https://doi.org/10.1007/s11069-012-0149-x

Álvarez, A.M., Bernal, G. (2007). Estimación del campo de transporte neto de sedimentos en el fondo de Bahía Colombia con base en análisis de tendencia del tamaño de grano. Avances en recursos Hidráulicos 16, 41–50. https://revistas.unal.edu.co

Alvarez, E., Feldhaus, L., Salazar, G., Schmidt-Thomé, M., (1987). Prospección Regional de metales básicos y preciosos en la Cordillera Occidental, Departamentos de Antioquia y Chocó. Ingeominas, Convenio Colombo –Alemán, Proyecto Mandé Fase I, informe Interno, 350 p., Medellín.

Amador, J.A.; Alfaro, E.J.; Lizano, O.G., and Magaña, V.O., 2006. Atmospheric forcing of the eastern tropical Pacific: A review. Progress in Oceanography, 69, 101-142.

Arnold, L.J., Roberts, R.G. (2009). Stochastic modelling of multi-grain equivalent dose (De) distributions: Implications for OSL dating of sediment mixtures. Quat. Geochronol. 4, 204-230. https://doi.org/10.1016/j.quageo.2008.12.001

Ballester, J. L. (2015). Agradación fluvial en la llanura deltaica de Haslital (Alpes Suizos). Análisis de facies sedimentarias y modelización cronoestratigráfica. PhD. Thesis, 1–309.

Banco de occidente. (2007). Deltas y Estuarios de Colombia - Colección Ecológica del Banco de Occidente. Retrieved from http://www.imeditores.com/banocc/deltas/cap6.htm

Bedoya, G., Cediel, F., Restrepo-Correa1, I., Cuartas, C., Montenegro, G., Marin-Cerón, M. I., Mojica, J., Cerón, R. (2009). Aportes al conocimiento de la evolución geológica de las cuencas Atrato y San Juan deltro del arco Panamá- Chocó. Boletín de Geología, 31 (2), 69 -81. http://www.scielo.org.co/pdf/boge/v31n2/v31n2a05.pdf

Bedoya, G., Fabio, C., Isabel, R., Cuartas, C., Mora, C., Montenegro, G., Correa, I. D., Garcpia, E., Muñoz, G., Zuluaga, M. C. (2007). Inventario, compilación, interpretación y evaluación integral de la información geológica, geofísica y geoquímica de la cuenca Atrato y cuenca San Juan. Informe Técnico, 1–143. Retrieved from http://www.anh.gov.co/Informacion-Geologica-y-Geofisica/Tesis/GEOLOGIA, GEOFISICA Y GEOQUIMICA CHOCO 2008.pdf

Bénat-Tachot, L. (2015). Santa María la Antigua del Darién: chronique d'une infortune locale. *e-Spania*, https://doi.org/10.4000/e-spania.25105

Bernal, G., Toro, M., Montoya, L. J., and Garizábal, C. (2005). Estudio de la dispersión de sedimentos del río Atrato y sus impactos sobre la problemática ambiental costera del Golfo

de Uraba. Informe Final de Investigacción, 61. Retrieved from http://www.bdigital.unal.edu.co/2268/1/Bernal-estudio-2005.pdf
Bernal, G.R., Montoya, L.J., Garizabal, C., Toro, M. (2005). La complejidad de la dimensión física en la problemática costera del Golfo de Urabá, Colombia. Gestión y Ambiente 8, 123–135. https://revistas.unal.edu.co/index.php/gestion/article/view/89247
Betancurth, L., Preusser, F., Mueller, D., Rambeau, C., and Cañón, J. (2020). First luminescence chronology of late Holocene deposits of the tropical Atrato Delta, Colombia. Journal of South American Earth Sciences, 102813. https://doi.org/10.1016/j.jsames.2020.102813
Bhatia, M.R. (1983) Plate Tectonics and Geochemical Composition of Sandstone. The Journal of Geology, 91, 611-627. http://dx.doi.org/10.1086/628815
Bhatia, M.R. (1983) Plate Tectonics and Geochemical Composition of Sandstone. The Journal of Geology, 91, 611-627. http://dx.doi.org/10.1086/628815
Bhattacharya, J. P., and Giosan, L. (2003). Wave-influenced deltas: geomorphological implications for facies reconstruction. Sedimentology, 50(1), 187–210. Retrieved from 10.1046/j.1365-3091.2003.00545.x
Bhattacharya, J.P. (2006). Deltas. In: Facies Models Revisited. SEPM Special Publication, vol. 84, pp. 237–292
Bhuiyan, M. A. H., Rahman, M. J. J., Dampare, S. B., and Suzuki, S. (2011). Provenance, tectonics and source weathering of modern fluvial sediments of the Brahmaputra-Jamuna River, Bangladesh: Inference from geochemistry. Journal of Geochemical Exploration, 111(3), 113–137. https://doi.org/10.1016/j.gexplo.2011.06.008
Blaauw, M., Christen, A.J. (2018). rbacon: Age□Depth Modelling using Bayesian Statistics. R package version 2.3.4. https://cran.r-project.org/web/packages/rbacon
Blaauw, M., Christen, J.A. (2011). Flexible paleoclimate age-depth models using an autoregressive gamma process. Bayesian Anal. 6, 457-474. https://doi.org/10.1214/11-BA618
Blanco, J. (2016). Expedición Caribe sur. Antioquia y Chocó costeros. http://www.cco.gov.co/docs/publicaciones/expedicion-caribe.pdf
Blanco, J. F., Taborda, A. (2012). Sediment Exports from the Eastern Basin in the Gulf of Uraba: Climatic and Anthropogenic Influences. Revista Ingenierías Universidad de Medellín, 11(20), 13–30.
Blanco-Libreros, J. F. (2016). Cambios globales en los manglares del golfo de Urabá (Colombia): entre la cambiante línea costera y la frontera agropecuaria en expansión. Actualidades Biológicas, 38(104), 53–70. https://doi.org/10.17533/udea.acbi.v38n104a06
Bronk Ramsey, C. (2009). Bayesian analysis of radiocarbon dates. Radiocarbon 51, 337-360, https://doi.org/10.1017/S0033822200033865
Brown, E.T. (2010). Lake Malawi's response to ''megadrought'' terminations: sedimentary records of flooding, weathering and erosion. Palaeogeogr. Palaeoclimatol. Palaeoecol.. http://doi:10.1016/j.palaeo.2010.01.038
Buckland C.E., Bailey R.M., Thomas D.S.G. (2019). Using post-IR IRSL and OSL to date young (< 200 as) dryland aeolian dune deposits. Radiat. Meas. 126, 106131. https://doi.org/10.1016/j.radmeas.2019.106131
Burow, C. (2019). calc_MinDose: Apply the (un-)logged minimum age model (MAM) after Galbraith et al. (1999) to a given De distribution. Function version 0.4.4. In: Kreutzer, S., Burow, C., Dietze, M., Fuchs, M.C., Schmidt, C., Fischer, M., Friedrich, J., 2019. Luminescence: Comprehensive Luminescence Dating Data AnalysisR package version 0.9.3. https://CRAN.R-project.org/package=Luminescence

Buylaert, J.P., Jain, M., Murray, A.S., Thomsen, K.J., Thiel, C., Sohbati, R. (2012). A robust feldspar luminescence dating method for Middle and Late Pleistocene sediments. Boreas 41, 435–451. https://doi.org/10.1111/j.1502-3885.2012.00248.x

Buylaert, J.P., Murray, A.S., Gebhardt, A.C., Sohbati, R., Ohlendorf, C., Thiel, C., Wastegård, S., Zolitschka B. (2013). Luminescence dating of the PASADO core 5022-1D from Laguna Potrok Aike (Argentina) using IRSL signals from feldspar. Quat. Sci. Rev. 71, 70-80. http://dx.doi.org/10.1016/j.quascirev.2013.03.018

Buylaert, J.P., Murray, A.S., Thomsen, K.J., Jain, M. (2009). Testing the potential of an elevated temperature IRSL signal from K-feldspar, Radiat. Meas. 44, 560–565. https://doi.org/10.1016/j.radmeas.2009.02.007

Cai, G., Miao, L., and Chen, H. (2012). Grain size and geochemistry of surface sediments in northwestern continental shelf of the South China Sea. Enrivon Earth Sci, 1–18. https://doi.org/10.1007/s12665-012-2133-x

Caro, H. D. (1990). The Choco Block in the northwestern corner of South America : Structural , tectonostratigraphic , and paleogeographic implications. Journal of South American Earth Sciences, 3(I), 71–84. https://doi.org/10.1016/0895-9811(90)90019-W

Case, J.E., Duran L.G., López, A., Moore, W.R. (1971): Tectonic investigations in western Colombia and eastern Panama. GSA Bulletin, v. 82, 9, p. 2685-2712, Toulsa. https://doi.org/10.1130/0016-7606(1971)82[2685:TIIWCA]2.0.CO;2

Cediel, F., Shaw R.P., and C. Cáceres. (2003). Tectonic assembly of the Northern Andean Block, in C. Bartolini, R. T. Buffer, and J, Blickwede, eds., The Circum-Gulf of Mexico and the Caribbean: Hydrocarbon habitats, basin formation, and plate tectonics: AAPG Memoir 79, pp.815-848.https://doi.org/10.1306/M79877C37

Centro de Investigaciones Oceanográficas e Hidrográficas, CIOH. (2009). Caracterización físico-biótica del Caribe colombiano. Tomo I. Dirección General Marítima-Centro Investigaciones Oceanográficas e Hidrográficas. Ed. DIMAR, Serie Publicaciones Especiales CIOH Vol. 1. Cartagena de Indias, Colombia. 154 Pp. https://www.cioh.org.co/dev/publicaciones/pdf/caracterizacion_tomo_i_01_capituloI.pdf

Chakrabarti, A. K., Durango, J. (1979). Observations on a porphay copper prospect in Choco,western Colombia. Economic Geology 74, 1687–1692. https://doi.org/10.2113/gsecongeo.74.7.1687

Chamberlain, E.L., Goodbred, S.L., Hale, R., Steckler, M.S., Wallinga, J., Wilson, C. (2020), Integrating geochronologic and instrumental approaches across the Bengal Basin. Earth Surf. Proc. Landf. 45, 56-74. https://doi.org/10.1002/esp.4687

Chamberlain, E.L., Törnqvist, T.E., Shen, Z., Mauz, B., Wallinga, J. (2018). Anatomy of Mississippi Delta growth and its implications for coastal restoration. Science Advances 4, 1–10. https://advances.sciencemag.org/content/4/4/eaar4740

Chamberlain, E.L., Wallinga, J. (2019). Seeking enlightenment of fluvial sediment pathways by optically stimulated luminescence signal bleaching of river sediments and deltaic deposits. Earth Surf. Dynam. 7, 723–736. https://doi.org/10.5194/esurf-7-723-2019

Chamberlain, E.L., Wallinga, J., Reimann, T., Goodbred, S. L., Steckler, M.S., Shen, Z., Sincavage, R. (2017). Luminescence dating of delta sediments: Novel approaches explored for the Ganges-Brahmaputra-Meghna Delta. Quat. Geochronol. 41, 97–111. https://doi.org/10.1016/j.quageo.2017.06.006

Chen, D., Chen, H.W. (2013). Using the Köppen classification to quantify climate variation and change : An example for 1901 – 2010. Environ. Develop. 6, 69–79. https://doi.org/10.1016/j.envdev.2013.03.007

Christiansen, T., Wiberg, P.L., Milligan, T.G., (2000). Flow and Sediment Transport on a Tidal Salt Marsh Surface. Estuarine, Coastal and Shelf Science 50, 315-331. https://doi.org/10.1006/ecss.2000.0548

Clarke, D. W., Boyle, J. F., Chiverrell, R. C., Lario, J., and Plater, A. J. (2014). A sediment record of barrier estuary behaviour at the mesoscale: Interpreting high-resolution particle size nalysis. Geomorphology, 221, 51–68. https://doi.org/10.1016/j.geomorph.2014.05.029

Coates, A.G., Laurel, S., Collins, Aubry, Marie-Pierre, Berggren, William A. (2004). The Geology of the Darien, Panama, and the late Miocene-Pliocene collision of the Panama arc with northwestern South America. GSA. Bulletin. https://doi.org/10.1130/B25275.1

Correa, I., and Vernette, G. (2004). Introducción a la problemática de la erosion litoral en el Urabá (sector Arboletes - Turbo) Costa Caribe Colombiana. Boletin de Investigaciones Marinas y Costeras, 33(ISSN 0122-9761), 7–29. https://repository.eafit.edu.co/handle/10784/1601

Cronin, T. M. (2012). Rapid sea-level rise. Quaternary Science Reviews, 56, 11–30. doi:10.1016/j.quascirev.2012.08.021

Darwish, K., Smith, S. E., Torab, M., Monsef, H., and Hussein, O. (2017). Geomorphological Changes along the Nile Delta Coastline between 1945 and 2015 Detected Using Satellite Remote Sensing and GIS. Journal of Coastal Research, 33(4), 786–794. https://doi.org/10.2112/jcoastres-d-16-00056.1

Davis, R. A., Cuffe, C. K., Kowalski, K. A., and Shock, E. J. (2003). Stratigraphic models for microtidal tidal deltas; examples from the Florida Gulf coast. Marine Geology, 200(1-4), 49 -60. https://doi.org/10.1016/S0025-3227(03)00164-6

Day, J.W., Barras, J., Clairain, E., Johnston, J., Justic, D., Kemp, G.P., Ko, J-Y., Lane, R., Mitsch, W.J., Steyer, G., Templet, P., Yañez-Arancibia, A. (2005). Implications of global climatic change and energy cost and availability for the restoration of the Mississippi Delta. Eco. Eng. 24, 253–265. https://doi.org/10.1016/j.ecoleng.2004.11.015

De Porta J. (2003). La Formación del Istmo de Panamá. Su Incidencia en Colombia. Revista de la Academia Colombiana de Ciencias Exactas Físicas y Naturales, 27(103): 191–216.

Ditlefsen, C. (1992). Bleaching of K-feldspars in turbid water suspensions: A comparison of photo- and thermoluminescence signals. Quat. Sci. Rev. 11, 33–38. https://doi.org/10.1016/0277-3791(92)90039-B

Dolozi, M. B., Kalindekafe, L. S. N., Ngongondo, C., and Dulanya, Z. (2011). A comparative analysis of the distribution, composition and geochemistry of surface sediments in the Linthipe and Songwe River Deltas of Lake Malawi. Journal of African Earth Sciences, 60(3), 93–105. https://doi.org/10.1016/j.jafrearsci.2011.02.002

Duller, G.A.T. (1994). Luminescence dating of poorly bleached sediments from Scotland. Quat. Sci. Rev. 13, 521–524. https://doi.org/10.1016/0277-3791(94)90070-1

Duller, G.A.T. (2008). Single-grain optical dating of Quaternary sediments: why aliquot size matters in luminescence dating. Boreas 37, 589–612. https://doi.org/10.1111/j.1502-3885.2008.00051.x

Dunn, F. E., Nicholls, R. J., Darby, S. E., Cohen, S., Zar, C., and Fekete, B. M. (2018). Science of the Total Environment Projections of historical and 21st century fl uvial sediment delivery to the Ganges-Brahmaputra-Meghna , Mahanadi , and Volta deltas. Science of the Total Environment Journal, 642, 105–116. https://doi.org/10.1016/j.scitotenv.2018.06.006

Duque-Caro H. (1990). The Choco Block in the northwestern corner of South America: Structural, tectonostratigraphy and paleogeographic implications. J. South Amer Earth Sci. 3, 71-84. https://doi.org/10.1016/0895-9811(90)90019-W

Edmonds, D. A., Shaw, J. B., and Mohrig, D. (2011). Topset-dominated deltas: A new model for river delta stratigraphy. Geology, 39(12), 1175–1178. Retrieved from http://doi.org 10.0.4.106/G32358.1

Elliott, M., Day, J.W., Ramachandran, R., Wolanski, E. (2019). A Synthesis: What Is the future for coasts, estuaries, deltas and other transitional habitats in 2050 and beyond? Coasts and Estuaries 1–28. https://doi.org/10.1016/B978-0-12-814003-1.00001-0

Escobar, C. A. (2011). Relevancia de Procesos Costeros en la Hidrodinámica del Golfo de Urabá (Caribe Colombiano). Boletin de Investigaciones Marinas y Costeras, 40(2), 327–346. http://www.scielo.org.co/pdf/mar/v40n2/v40n2a06.pdf

Escobar, C.A., Velázquez, L., Posada, F. (2015). Marine currents in the Gulf of Urabá, Colombian Caribbean Sea. J. Coastal Res. 31, 1363–1375. https://doi.org/10.2112/JCOASTRES-D-14-00186.1

Evans, G. (2012). Deltas: the fertile dustbins of the continents. Proceedings of the Geologists' Association, 123, 397–418. https://doi.org/10.1016/j.pgeola.2011.11.001

Fitzgerald, D. M., Kulp, M., Penland, S., Flocks, J., and Kindinger, J. (2004). Morphologic and stratigraphic evolution of muddy ebb-tidal deltas along a subsiding coast: Barataria Bay, Mississippi River delta. Sedimentology, 51(6), 1157–1178. https://doi.org/10.1111/j.1365-3091.2004.00663.x

Folk, R.L., Ward W.C., (1957). Brazos River bar, a study in the significance of grain size parameters. Journal of Sedimentary Petrology, 27: 3–26. https://doi.org/10.1306/74D70646-2B21-11D7-8648000102C1865D

Frechen, M., Schweitzer, U., Zander, A. (1996). Improvements in sample preparation for the fine grain technique. Ancient TL 14, 15–17.

Frings, P. J., and Buss, H. L. (2019). The Central Role of Weathering in the Geosciences. Elements, 15(4), 229–234. https://doi.org/10.2138/gselements.15.4.229

Fuchs, M., Straub, J., Zöller, L. (2005). Residual luminescence signals of recent river flood sediments: A comparison between quartz and feldspar of fine- and coarse-grain sediments. Ancient TL 23, 25-30. https://doi.or10.14361/9783839403358-fm

Galbraith, R.F., Roberts, R.G. (2012). Statistical aspects of equivalent dose and error calculation and display in OSL dating: An overview and some recommendations. Quat. Geochronol. 11, 1–27, https://doi.org/10.1016/j.quageo.2012.04.020.

Galbraith, R.F., Roberts, R.G., Laslett, G.M., Yoshida, H., Olley, J.M. (1999). Optical dating of single and multiple grains of quartz from Jinmium rock shelter, northern Australia, part 1, Experimental design and statistical models. Archaeometry 41, 339–364. https://doi.org/10.1111/j.1475-4754.1999.tb00987.x

Gallet, S., Jahn B., Van Vliet Lanoë, B., Dia, A., Rosello, E. (2014). Loess geochemistry and its application for particle origin and composition of the upper continental crust, (June). https://doi.org/10.1016/S0012-821X(97)00218-5

Galloway, W.E., (1975). Process framework for describing the morphologic and stratigraphic evolution of deltaic depositional systems. In: Broussard, M.L. (Ed.), Deltas, Models for Exploration. Houston Geological Society, Houston, TX, pp. 87–98.

Gao, L., Long, H., Zhang, P., Tamura, T., Feng, W., Mei, Q. (2019). The sedimentary evolution of Yangtze River delta since MIS3: A new chronology evidence revealed by OSL dating. Quat. Geochronol. 49, 153–158. https://doi.org/10.1016/j.quageo.2018.03.010

Garver, J.I., Royce, P.R., Smick, T.A., (1996). Chromium and nickel in shale of the Taconic foreland: a case study for the provenance of fine-grained sediments with an ultramafic source. J. Sediment. Res. 100, 100–106. http://dx.doi.org/10.1306/D42682C5-2B26-11D7-8648000102C1865D

Garzón Varón, F. (2012). Modelamiento estructural de la zona límite entre la microplaca de Panamá y el bloque norandino a partir de la interpretación de imágenes de radar, cartografía geológica, anomalías de campos potenciales y líneas sísmicas, Master Thesis, Universidad Nacional, 18–157. http://bdigital.unal.edu.co/8848/

Gomitz, V., Lebedeff, S. (1987). Global sea level change during the past century. In: Nummedal, D., et al. (Eds.), Sea Level Fluctuations and Coastal Evolution, vol. 41. Society of Economie Paleontologists and Mineralogists, Special Publication.

Gong, C., Steel, R. J., Wang, Y., Lin, C., and Olariu, C. (2016). Grain size and transport regime at shelf edge as fundamental controls on delivery of shelf-edge sands to deepwater. Earth-Science Reviews, 157, 32–60. https://doi.org/10.1016/j.earscirev.2016.04.002

González, H., Londoño, A. (2002b). Catálogo de las Unidades Litoestratigráficas de Colombia: Batolito de Mandé, Cordillera Occidental, departamentos de Antioquia, Chocó y Risaralda, INGEOMINAS, 20 p.

Goodbred S.L., Saito Y. (2012) Tide-Dominated Deltas. In: Davis Jr. R., Dalrymple R. (eds) Principles of Tidal Sedimentology. Springer, Dordrecht. https://doi.org/10.1007/978-94-007-0123-6_7

Goodbred, S.L., Dillehay, T.D., Mora, C.G., Sawakuchi, A.O. (2020). Transformation of maritime desert to an agricultural center: Holocene environmental change and landscape engineering in Chicama River valley, northern Peru coast. Quat. Sci. Rev. 227,106046. https://doi.org/10.1016/j.quascirev.2019.106046

Griffith, E.M. and Paytan, A. (2012). Barite in the ocean - occurrence, geochemistry and palaeoceanographic applications. Sedimentology 59: 1817-1835. https://doi.org/10.1111/j.1365-3091.2012.01327.x

Grunsky, E. C., Drew, L. J., and Sutphin, D. M. (2009). Applied Geochemistry Process recognition in multi-element soil and stream-sediment geochemical data. Applied Geochemistry, 24(8), 1602–1616. https://doi.org/10.1016/j.apgeochem.2009.04.024

Guagliardi, I., Apollaro, C., Scarciglia, F., and Rosa, R. De. (2013). Influence of particle-size on geochemical distribution of stream sediments in the Lese river catchment, southern Italy. Biotechnol. Agron. Soc. Environ, 17(1), 43–55. https://doi.org/10.1007/s12517-019-4569-8

Guedes, C., Giannini, P.C.F., Sawakuchi, A.O., DeWitt, R., Nascimento Jr, D.R., Aguiar, V., Rossi, M. (2011), Determination of controls on Holocene barrier progradation through application of OSL dating: The Ilha Comprida Barrier example, Southeastern Brazil. Marine Geology 285, 1-16. https://doi.org/10.1016/j.margeo.2011.04.005

Guérin, G., Mercier, N., Adamiec, G. (2011). Dose-rate conversion factors: update. Ancient TL 29, 5-8.

Haffer, J. (1967). Geologic compilation map Northwestern Colombia. Colombian Petroleum Company, Escala 1:500.000.

Hait, A., Das, J., Ghosh, S., Ray, A., Saha, A., Chanda, S. (1996). New dates of Pleisto-Holocene subcrop samples from south Bengal, India. Indian J. Earth Sci. 23, 79-82.

Hasberg, A. K. M., Bijaksana, S., Held, P., Just, J., Melles, M., Morlock, M. A., and Opitz, S. (2019). Modern sedimentation processes in Lake Towuti , Indonesia , revealed by the composition of surface sediments. Sedimentology, 66(May 2015), 675–698. https://doi.org/10.1111/sed.12503

Haug, G.H.; Hughen, K.A.; Sigman, D.M.; Peterson, L.C., and Röhl, U., 2001. Southward migration of the intertropical convergence zone through the Holocene. Science, 293, 1304-1308.

Hayashi KI, Fujisawa H, Holland HD, Ohmoto H (1997). Geochemistry of ~1.9 Ga sedimentary rocks from northeastern Labrador, Canada. Geochim Cosmochim Acta 61(19):4115–4137. https://doi.org/10.1016/S0016-7037(97)00214-7

He, L., Xue, C., Ye, S., Amorosi, A., Yuan, H., Yang, S., and Laws, E. A. (2019). New evidence on the spatial-temporal distribution of superlobes in the Yellow River Delta Complex. Quaternary Science Reviews, 214, 117–138. https://doi.org/10.1016/j.quascirev.2019.05.003

Herron, M.M. (1988). Geochemical classification of terrigenous sands and shales from core and log data. Journal of Sedimentary Petrology 58: 820- 829.

Hijma, M.P., Cohen, K.M., Hoffmann, G., Van Der Spek, A.J.F., Stouthamer, E. (2009). From river valley to estuary: The evolution of the Rhine mouth in the early to middle Holocene (western Netherlands, Rhine-Meuse delta), Neth. J. Geosci. 88, 13–53. https://doi.org/10.1017/S0016774600000986

Huntely, D.J., Lamothe, M. (2001). Ubiquity of anomalous fading in K-feldspars and correction for it in optical dating. Can. J. Earth Sci., 38, 1093–1106. https://doi.org/10.1139/e01-013

Instituto de Investigaciones Marinas y Costeras-INVEMAR (2007). Atlas del golfo de Urabá: una mirada al Caribe de Antioquia y Chocó. Atlas del golfo de Urabá: una mirada al Caribe de Antioquia y Chocó, 188. http://hdl.handle.net/1834/5917

Instituto de Investigaciones Marinas y Costeras-INVEMAR. (2017). Aportes sedimentarios y evolución litoral de la franja oriental del golfo de Urabá, zona de Turbo, 47.

Instituto Geográfico Agustín Codazzi (IGAC), Instituto Colombiano de Geología y Minas (INGEOMINAS). (2001). Investigación integral del Andén Pacífico Colombiano Tomo 1 Geología. Informe Final de Investigacción, 1–168.

Jian, X., Zhang, W., Liang, H., Guan, P., and Fu, L. (2019). Mineralogy, petrography and geochemistry of an early Eocene weathering pro fi le on basement granodiorite of Qaidam basin , northern Tibet : Tectonic and paleoclimatic implications. Catena, 172(July 2018), 54–64. https://doi.org/10.1016/j.catena.2018.07.029

Joeckel, R. M., and Clement, B. A. (1999). Surface features of the Salt Basin of Lancaster County, Nebraska. Catena, 34(3–4), 243–275. https://doi.org/10.1016/S0341-8162(98)00114-3

Johnson, M. J. (1990). Overlooked sedimentary particles from tropical weathering environments. Geology, 18(2), 107–110. https://doi.org/10.1130/0091-7613(1990)018<0107:OSPFTW>2.3.CO;2

Johnson, R.A. and Wichern, D.W. (2007) Applied Multivariate Statistical Analysis. 6th Edition, Pearson Prentice Hall, Upper Saddle River, 794.

Kellogg J.N., Mohriak W.U. (2001) The Tectonic and Geological Environment of Coastal South America. In: Seeliger U., Kjerfve B. (eds) Coastal Marine Ecosystems of Latin America. Ecological Studies (Analysis and Synthesis), vol 144. Springer, Berlin, Heidelberg. https://doi.org/10.1007/978-3-662-04482-7_1

Kermani, S., Boutiba, M., Boutaleb, A., and Fagel, N. (2015). Distribution of heavy and clay minerals in coastal sediment of Jijel , East of Algeria : indicators of sediment sources and transport and deposition environments. Arabian Journal of Geosciences, 1–18. https://doi.org/10.1007/s12517-015-2155-2

Khalifa, M. A., & Catuneanu, O. (2008). Sedimentology of the fluvial and fluvio-marine facies of the Bahariya Formation (Early Cenomanian), Bahariya Oasis, Western Desert, Egypt. Journal of African Earth Sciences, 51(2), 89–103. https://doi.org/10.1016/j.jafrearsci.2007.12.004

Khan, N. S., Ashe, E., Horton, B. P., Dutton, A., Kopp, R. E., Brocard, G., … Scatena, F. N. (2017). Drivers of Holocene sea-level change in the Caribbean. Quaternary Science Reviews, 155, 13–36. doi:10.1016/j.quascirev.2016.08.032

King, G.E., Burow, C., Roberts, H., Duller, G.A.T., (2018). Age determination using feldspar: Evaluating fading-correction model performance. Radiat. Meas. 119, 58–73. https://doi.org/10.1016/j.radmeas.2018.07.013

Kopp, J., and Kim, W. (2015). The effect of lateral tectonic tilting on fluviodeltaic surficial and stratal asymmetries : experiment and theory. Basin Research, 517–530. https://doi.org/10.1111/bre.12086

Korus, J. T., and Fielding, C. R. (2015). Asymmetry in Holocene river deltas: Patterns, controls, and stratigraphic effects. Earth-Science Reviews, 150, 219–242. https://doi.org/10.1016/j.earscirev.2015.07.013

Kroonenberg, S. B. (1994). Effects of provenance, sorting and weathering on the geochemistry of fluvial sands from different tectonic and climatic environments. In Proc. 29th Int. Geol. Congr. Part A. Kyoto, Japan 1992, F. Kumon, K.M. Yu (eds.). VSP Publ., Utrecht (pp. 69-81).

Lario, J., Spencer, C., Plater, A. J., Zazo, C., Goy, J. L., & Dabrio, C. J. (2002). Particle size characterisation of Holocene back-barrier sequences from North Atlantic coasts (SW Spain and SE England). Geomorphology, 42(1–2), 25–42. https://doi.org/10.1016/S0169-555X(01)00071-X

Latrubesse, E.M., Stevaux, J.C., Sinha, R.(2005). Tropical rivers. Geomorphology 70, 187-206. https://doi.org/10.1016/j.geomorph.2005.02.005

Lauria, V., Das, I., Hazra, S., Cazcarro, I., Arto, I., Kay, S., Ofori-Danson, P., Munir, A., Mostafa A.R.H., Barange, M., Fernández, J.A. (2018). Importance of fisheries for food security across three climate change vulnerable deltas. Sci. Total Environ., 640/641, 1566–1577. https://doi.org/10.1016/j.scitotenv.2018.06.011

Li, B., Jacobs, Z., Roberts, R., Li, S.H. (2014). Review and assessment of the potential of post-IR IRSL dating methods to circumvent the problem of anomalous fading in feldspar luminescence. Geochronometria 41, 178-201. https://doi.org/10.2478/s13386-013-0160-3

Li, X., Liu, J. P., Saito, Y., and Nguyen, V. L. (2017). Recent evolution of the Mekong Delta and the impacts of dams. Earth-Science Reviews, 175(March), 1–17. https://doi.org/10.1016/j.earscirev.2017.10.008

Li, Y., Zhang, H., Fu, C., Tu, C., Luo, Y., and Christie, P. (2019). A red clay layer in soils of the Yellow River Delta: Occurrence, properties and implications for elemental budgets and biogeochemical cycles. Catena, 172, 469–479. https://doi.org/10.1016/j.catena.2018.09.015

Liguori, B. T. P., De Almeida, M. G., and de Rezende, C. E. (2016). Barium and its importance as an indicator of (Paleo)productivity. Anais Da Academia Brasileira de Ciencias, 88(4), 2093–2103. https://doi.org/10.1590/0001-3765201620140592

Longhitano, S., and Colella, A. (2007). Geomorphology, sedimentology and recent evolution of the anthropogenically modified Simeto River delta system (eastern Sicily, Italy). Sedimentary Geology, 194(3–4), 195–221. https://doi.org/10.1016/j.sedgeo.2006.06.004

López, S.A., Restrepo, J. D. (2007). Modelos morfodinámicos de los deltas fluviales Colombianos. Boletín de Geología, 29, 103-113. https://revistas.uis.edu.co/index.php/revistaboletindegeologia/article/view/845

Lottermoser, B.G., Pratt, C. (2007). Mobilisation of traffic-derived trace metals from road corridors into coastal stream and estuarine sediments, Cairns , northern Australia, 437–448. https://doi.org/10.1007/s00254-006-0471-2

Lugo, R., Rodríguez, G., Domínguez, E. (2003). Prospección Geológica y Geoquímica Regional en el Área de Mandé. Informe Técnico: Ingeominas, 1–106. https://doi.org/10.1017/CBO9781107415324.004

Martin, A. N., Dosseto, A., May, J. H., Jansen, J. D., Kinsley, L. P. J., and Chivas, A. R. (2019). Sediment residence times in catchments draining to the Gulf of Carpentaria, northern Australia, inferred by uranium comminution dating. Geochimica et Cosmochimica Acta, 244, 264–291. https://doi.org/10.1016/j.gca.2018.09.031

Martins, L. R. (2003). Recent sediments and grain-size analysis. Gravel, 1, 90–105. https://www.ufrgs.br/gravel/1/Gravel_1_08.pdf

Maselli, V., Trincardi, F., Asioli, A., Ceregato, A., Rizzetto, F., and Taviani, M. (2014). Delta growth and river valleys: The influence of climate and sea level changes on the South Adriatic shelf (Mediterranean Sea). Quaternary Science Reviews, 99, 146–163. https://doi.org/10.1016/j.quascirev.2014.06.014

Massuanganhe, E. A., Berntsson, A., Risberg, J., Westerberg, L.-O., Christiansson, M., Preusser, F., Achimo, M. (2018). Palaeogeography and dynamics of the deltaic wetland of Save River, Mozambique. Palaeogeography, Palaeoclimatology, Palaeoecology, 489, 64–73. Retrieved from http://10.0.3.248/j.palaeo.2017.09.021

Mateo, Z. R. P., and Siringan, F. P. (2016). Morphological and Sedimentological Signatures of Late Holocene Prodelta Lobes in Lingayen Gulf, Philippines. Journal of Coastal Research, 32(2), 354–364. Retrieved from 10.2112/JCOASTRES-D-14-00023.1

Mayya, Y.S., Mortekai, P., Murari, M.K., Singhvi, A.K. (2006). Towards quantifying beta microdosimetric effects in single-grain quartz dose distribution. Radiat. Meas. 41, 1032–1039. https://doi.org/10.1016/j.radmeas.2006.08.004

Méndez, C. A., Herrera, J. M., Arciniegas, E. G., Piragua, A., Ramírez, R. I., and Naranjo, J. (2006). Cartografía Geológica En El Área De La Subcuenca Atrato - San Juan, Departamento Del Chocó. Contrato 078 de 2005 Informe de Integración e Interpretación de La Información Geológica de Campo., 94. Retrieved from www.anh.gov.co

Mikhailov, V.N., Mikhailova M.V. (2003). Deltas as indicators of natural and human-induced changes in the regimes of rivers and seas. Water Resour. 30, 602–612. https://doi.org/10.1023/B:WARE.0000007585.01852.ee

Mikkel, S., & Henderson, J. B. (1983). Archean chemical weathering at three localities on the Canadian sheld [J]. Precam. Research, 20, 189-224.

Mil-Homens, M., Vale, C., Raimundo, J., Pereira, P., Brito, P., and Caetano, M. (2014). Major factors influencing the elemental composition of surface estuarine sediments: The case of 15 estuaries in Portugal. Marine Pollution Bulletin, 84(1–2), 135–146. https://doi.org/10.1016/j.marpolbul.2014.05.026

Molina, L. G; Osorio, A.F.; Otero, L. J. (2014). Capacidad de transporte potencial longitudinal de sedimentos a escala intra-anual en Punta Yarumal, Delta del Río Turbo, Golfo de Urabá, a partir de la simulación de un clima marítimo. Boletín de Investigaciones Marino Costeras, 43(2), 213–248.

Monnier, L., Lach, P., Salvi, S., Melleton, J., Bailly, L., Beziat, D., Monniers, Y., Gouy, S. (2018). Quartz trace-element composition by LA-ICP-MS as proxy for granite differentiation, hydrothermal episodes, and related mineralization: The Beauvoir Granite (Echassières district), France. Lithos, #pagerange#. https://doi.org/10.1016/j.lithos.2018.09.024

Monsalve H. and H. Mora, (2005). Esquema geodinámico regional para el noroccidente de Suramérica (modelo de subducción y desplazamientos relativos, Boletín de Geología 27 (44), Universidad Industrial de Santander, https://doi.org/10.18273/revbol

Montoya Jaramillo, L. J. (2010). Dinámica oceanográfica del golfo de Urabá y su relación con los patrones de dispersión de contaminantes y sedimentos., 103. Retrieved from http://www.bdigital.unal.edu.co/5226/1/Cap.1-5.pdf

Muñoz, R. and Güiza, S. (2005). Potencia Geológico Minero en rocas de la corteza oceánica, Plancha 165, Cordillera Occidental, Colombia. Ingeominas, Technical(1), 10.

Mycielska-Dowgiałło E, Ludwikowska-Kędzia M (2011) Alternative interpretations of grain-size data from quaternary deposits. Geologos 17(4):189–203 https://doi.org/10.2478/v10118-011-0010–9

Nádor, A., Thamó-Bozsó, E., Magyari, Á., and Babinszki, E. (2007). Fluvial responses to tectonics and climate change during the Late Weichselian in the eastern part of the Pannonian Basin (Hungary). Sedimentary Geology, 202(1/2), 174–192. Retrieved from http://10.0.3.248/j.sedgeo.2007.03.001

Nanson, G.C., Price, D.M., Short, S.A., Young, R.W., Jones, B.G. (1991). Comparative Uranium-Thorium and thermoluminescence dating of weathered Quaternary alluvium in the tropics of Northern Australia. Quat. Res. 35, 347–366. https://doi.org/10.1016/0033-5894(91)90050-F

Nava-Sanchez, E., Cruz-Orozco, R., and Gorsline, D. S. (1995). Morphology and sedimentology of two contemporary fan deltas on the southeastern Baja California Peninsula, Mexico. Sedimentary Geology, 98(1–4), 45–61. https://doi.org/10.1016/0037-0738(95)00026-5

Neidhardt, H., Biswas, A., Freikowski, D., Majumder, S., Chatterjee, D., and Berner, Z. A. (2013). Sequence stratigraphic interpretation of sediments from the Bengal Delta Plain, West Bengal, India. Applied Geochemistry, 36, 70–82. https://doi.org/10.1016/j.apgeochem.2013.06.017

Nesbitt, H. W.; Young, G. M. (1984). Prediction of some weathering trands of plutonic and volcanic rocks based on thermodynamic and kinetic considerations. Geochimica et Cosmochimica Acta 48, 1523-1534.

Nian, X., Zhang, W., Wang, Z., Sun, Q., Chen, J., Chen, Z., Hutchinson, S.M. (2018). The chronology of a sediment core from incised valley of the Yangtze River delta: Comparative OSL and AMS 14C dating. Mar. Geol., 395, 320–330. https://doi.org/10.1016/j.margeo.2017.11.008

Nieto-Oliveros, M J. (2004). Estudio morfodinámico del delta del río Atrato, Golfo de Urabá, a partir de cartografía histórica y percepción remota. [Tesis de Pregrado en Geología]. [Bogotá]: Universidad Nacional de Colombia. p. 121.

Noriega - Londoño, S., Caballero - Acosta, J. H. (2015). Morfotectónica de la falla Abriaquí y sismicidad histórica asociada con el sismo de 1903 en Frontino, Antioquia. Revista de La Academia Colombiana de Ciencias Exactas, Físicas y Naturales, 39(150), 100. https://doi.org/10.18257/raccefyn.81

Olariu, M. I., and Zeng, H. (2018). Prograding muddy shelves in the Paleogene Wilcox deltas, south Texas Gulf Coast. Marine and Petroleum Geology, 91, 71–88. https://doi.org/10.1016/j.marpetgeo.2017.12.027

Olley, J., Caitcheon, G., Murray, A.S. (1998). The distribution of apparent dose as determined by optically stimulated luminescence in small aliquots of fluvial quartz: implications for dating young sediments. Quat. Sci. Rev. 17, 1033–1040. https://doi.org/10.1016/S0277-3791(97)00090-5

Oni, S. O., Olatunji, A. S. (2017). Depositional environments signatures, maturity and source weathering of Niger Delta sediments from an oil well in southeastern Delta State, Nigeria, 6(3), 259–274. https://doi.org/10.18393/ejss.297245

Opreanu, G., Oaie, G., and PĂuN, F. (2007). The dynamic significance of the grain size of sediments transported and deposited by the Danube. Geo-Eco-Marina, 23–25. Retrieved from http://www.geoecomar.ro/website/publicatii/Nr.13-2007/12.pdf

Osorio, A., Gómez, A., Molina, L., Álvarez, O., Osorio, J. (2010) Bases metodológicas para caracterizar el oleaje local (sea) y de fondo (swell) en el golfo de Urabá. En: XXIV Congreso latinoamericano de hidráulica (2010: Punta del Este, Uruguay). AIIH, p. 12.

Ouillon, S. (2018). Why and how do we study sediment transport? Focus on coastal zones and ongoing methods. Water (Switzerland), 10(4), 1–34. https://doi.org/10.3390/w10040390

Palacios-Torres, Y., Caballero-Gallardo, K., Olivero-Verbel, J. (2018). Mercury pollution by gold mining in a global biodiversity hotspot, the Choco biogeographic region, Colombia. Chemosphere 193, 421–430. https://doi.org/10.1016/j.chemosphere.2017.10.160

Palacios-Torres, Y., de la Rosa, J.D., Olivero-Verbel, J. (2019). Trace elements in sediments and fish from Atrato River: An ecosystem with legal rights impacted by gold mining at the Colombian Pacific. Environ. Pollut., 57 p. https://doi.org/10.1016/j.envpol.2019.113290

Parra N., Jaramillo- Justinico, A. (2006). Geomorfología de la región del Patía. Revista Universidad de Pamplona 1, https://doi.org/10.24054/19009178.v1.n1.2006.109

Pennington, B. T., Sturt, F., Wilson, P., Rowland, J., and Brown, A. G. (2017). The fluvial evolution of the Holocene Nile Delta. Quaternary Science Reviews, 170, 212–231. https://doi.org/10.0.3.248/j.quascirev.2017.06.017

Pettijohn, F.J., Potter, P. E., Siever, R. 1972. Sand and Sandstone. xvi 618 pp., 258 figs. Springer-Verlag, Berlin, Heidelberg, New York. Geological Magazine, 112(2), 203-204. doi:10.1017/S0016756800045945.Pizzuto J. E. (1995). Down stream fining a network of gravel bedded rivers. Water Resources Research. 31, p. 753 -759. https://doi.org/10.1029/94WR0253

Posada Posada, B. O., Henao Pineda, W. (2008). Diagnostico de la erosión en la zona costera del Caribe colombiano. INVEMAR, Serie Publicaciones Especiales, 13, 200.

Posamentier, H.W. (2001). Lowstand alluvial bypass systems: incised vs. unincised. AAPG Bulletin 85,1771–1793.https://doi.org/10.1306/8626D06D-173B-11D7-8645000102C1865D

Post, S. (2011). Morphological modelling of the Atrato river delta in Colombia. Master's thesis, Delft University of Technology, Faculty of Civil Engineering and Geosciences 1–147. https://repository.tudelft.nl

Potts, P.J., Thompson, M., Chenery, S.R.N., Webb, P.C., Kasper, H.U. (2003). An international proficientcy test for analytic geochemistry laboratories – Report round 13 / July 2003 (KölnLoess). GeoPT13 Report 13. http://www.geoanalyst.org

Poveda, G. (2004). La hidroclimatología de Colombia: una síntesis desde la escala inter-decadal hasta la escala diurna. Revista de La Academia Colombiana de Ciencias Exactas, Físicas y Naturales, 28(107), 201–222

Poveda, G., Mesa, O.J. (1997). Feedbacks between hydrological processes in Tropical South America and large scale ocean-atmospheric phenomena. J. Climate 10, 2690–2702. https://doi.org/10.1175/1520-0442(1997)010<2690:FBHPIT>2.0.CO;2

Poveda, G., Mesa, O.J. (1999). La corriente de chorro superficial del Oeste ("del Chocó") y otras dos corrientes de chorro en Colombia: climatología y variabilidad durante las fases del ENSO. Rev. Acad. Col. Cienc., 23(89): 517-528.

Prescott, J.R., Hutton, J.T. (1994). Cosmic ray contributions to dose rates for luminescence and ESR dating: Large depths and longterm time variations. Radiat. Meas. 23, 497–500. https://doi.org/10.1016/1350-4487(94)90086-8

Preusser, F., Degering, D., Fuchs, M., Hilgers, A., Kadereit, A., Klasen, N., Krbetschek, M., Richter, D., Spencer, J. (2008). Luminescence dating: Basics, methods and applications. EandG Quat. Sci. J. 57, 95-149. https://doi.org/10.3285/eg.57.1-2.5

Preusser, F., Ramseyer, K., Schlüchter, C. (2006). Characterisation of low luminescence intensity quartz from Westland, New Zealand Alps. Radiat. Meas. 41, 871-877. https://doi.org/10.1016/j.radmeas.2006.04.019

Pribyl, D. W. 2010. A critical review of the conventional SOC to SOM conversion factor.Department of Soil, Water, Climate, University of Minnesota, United States. Geoderma, 156: 75-83.

Prieto, G.; González- Cubillos L.M., Muñoz, R., Bravo-Guerrero, M., Villamiraz-Meza, F. Y., García-Acosta G., Tabares-Ocampo, L.M., Castellanos-Sanabria, F., Tejada-Avella M. L. (2009). Mapa de anomalías Geoquímicas de Colombia. Escala 1:1'500.000 Ingeominas, Informe Técnico.121

Proske, U., Hanebuth, T. J. J., Gröger, J., and Diêm, B. P. (2011). Late Holocene sedimentary and environmental development of the northern Mekong River Delta, Vietnam. Quaternary International, 230(1–2), 57–66. https://doi.org/10.1016/j.quaint.2009.11.032

Purkait, B., and Das, D. (2014). Distinguishing different sedimentary facies in a deltaic system. Sedimentary Geology, 308, 53–62. https://doi.org/10.1016/j.sedgeo.2014.05.001

Quiaresma, V. D. S., Catabriga, G., Bourguignon, S. N., Godinho, E. and Cardoso Bastos, A. (2015). Modern sedimentary processes along the Doce river adjacent continental shelf. Brazilian Journal of Geology, 47(Decmeber), 635–644. https://doi.org/10.1590/2317 (2015). Modern sedimentary processes along the Doce river adjacent continental shelf. Brazilian Journal of Geology, 47(Decmeber), 635–644. https://doi.org/10.1590/2317

Ramadan, R. S., and Gad, A. (2019). Grain size and mineralogical characteristics of the stream sediments , east of Abu Zeneima area , southwestern Sinai, Egypt. Arabian Journal of Geosciences, 12, 1–17. https://doi.org/10.1007/s12517-019-4362-8

Reimann, T., Tsukamoto, S. (2012). Dating the recent past (<500 years) by post-IR IRSL feldspar - Examples from the North Sea and Baltic Sea coast. Quat. Geochronol. 10, 180–187. https://doi.org/10.1016/j.quageo.2012.04.011

Reimer, P.J., Bard, E., Bayliss, A., Beck, J.W., Blackwell, P.G., Bronk Ramsey, C., Buck, C.E., Edwards, R.L., Friedrich, M., Grootes, P.M., Guilderson, T.P., Haflidason, H., Hajdas, I., Hatté, C., Heaton, T.J., Hoffmann, D.L., Hogg, A.G., Hughen, K.A., Kaiser, K.F., Kromer, B., Manning, S.W., Niu, M., Reimer, R.W., Richards, D.A., Scott, M.E., Southon, J.R., Turney, C.S.M., van der Plicht, J. (2013). IntCal13 and Marine13 radiocarbon age calibration curves 0-50,000 a cal. Radiocarbon 55, 1869–1887. https://doi.org/10.2458/azu_js_rc.55.16947

Rencher, A. C. (2012). Methods of Multivariate Analysis, Second Edition. Wiley-Interscience (Vol. 37). https://doi.org/10.1080/07408170500232784

Restrepo J.D., Kjerfve, B. (2000) Water discharge and sediment load from the western slopes of the Colombian Andes with focus on Rio San Juan. J Geol 108:17–33. https://doi.org/10.1086/314390

Restrepo, J. C. (2014). Dinámica sedimentaria en deltas micromareales-estratificados de alta descarga: Delta del Río Magdalena (Colombia – Mar Caribe). PhD Thesis. Retrieved from http://manglar.uninorte.edu.co/handle/10584/7422

Restrepo, J. D. (2008). Deltas de Colombia: morfodinámica y vulnerabilidad ante el Cambio Global,. Universidad EAFIT, 280.

Restrepo, J. D., López, S. A. (2008). Morphodynamics of the Pacific and Caribbean deltas of Colombia, South America. South American Earth Sciences, 25, 1–21. https://doi.org/10.1016/j.jsames.2007.09.002

Rhodes, E.J., (2011). Optically Stimulated Luminescence dating of sediments over the past 200,000 years. Annu. Rev. Earth Planet. Sci. 39, 461-488. https://doi.org/10.1146/annurev-earth-040610-133425

Richter, D., Richter, A., Dornich, K. (2015). Lexsyg smart — a luminescence detection system for dosimetry, material research and dating application. Geochronometria, 42, 202–209. https://doi.org/10.1515/geochr-2015-0022

Robertson, K., and Martínez, N. (1999). Cambios del nivel del mar durante el holoceno en el litoral caribe colombiano. Cuadernos de Geografía: Revista Colombiana de Geografía, 8(1), 168–198.

Robertson, K., Martinez, N., and Jaramillo, O. (2003). Amenazas naturales asociadas al ascenso del nivel del Mar. Cuadernos de Geografía, XII (1-2), 19.

Rodríguez García, G., and Zapata García, G. (2012). Características del plutonismo Mioceno Superior en el segmento norte de la Cordillera Occidental e implicaciones tectónicas en el modelo geológico del Noroccidente colombiano. Boletín de Ciencias de La Tierra, (31), 5–22.

Rodríguez, N., José Daniel, E., Bernal, N., and Jorge, M. (2010). Cambio climático y su relación con el uso del suelo en los Andes colombianos. http://hdl.handle.net/20.500.11761/31370

Roldán, P . A . (2007). Modelamiento del patrón de circulación de la bahía Colombia, golfo de Urabá- Implicaciones para el transporte de sedimentos. Tesis Recursos Hidráulicos, Univ. Nacional de Colombia, Medellín . 102 p

Roser, B.P., Korsch, R.J. (1986). Determination of tectonic setting of sandstone- mudstone suites using SiO2 content and K_2O/Na_2O ratio. J. Geol. 94, 635e650

Rossi, V. M., and Steel, R. J. (2016). The role of tidal, wave and river currents in the evolution of mixed-energy deltas: Example from the Lajas Formation (Argentina). Sedimentology, 63(4), 824–864. https://doi.org/10.1111/sed.12240

Rúa, A., Liebezeit, G., Molina, R., Palacio, J. (2016). Unmixing progradational sediments in a southwestern Caribbean Gulf through Late Holocene: Backwash of low-level atmospheric jets. J. Coastal Res. 32, 397–408. https://doi.org/10.2112/JCOASTRES-D-14-00216.1

Rúa, A., Liebezeit, G., Palacio, J. (2014). Mercury colonial footprint in Darién Gulf sediments, Colombia. Environ. Earth Sci. 71, 1781–1789. https://doi.org/10.1007/s12665-013-2583-9

Rudnick, R.L., and Gao, S., (2003). Composition of the continental crust, in Rudnick, R.L., ed., Treatise on Geochemistry, Volume 3: Amsterdam, Elsevier, p. 1–64.

Salcedo, E; Pérez, J. (2016). Caracterización sismotectónica de la región del Valle del Cauca y zonas aledañas a partir de mecanismos focales de terremotos. Boletín de Geología, 38(13), 89–107. http://dx.doi.org/10.18273/revbol.v38n3-2016006

Sarkar, A., Sengupta, S., McArthur, J. M., Ravenscroft, P., Bera, M. K., Bhushan, R., … Agrawal, S. (2009). Evolution of Ganges–Brahmaputra western delta plain: Clues from sedimentology and carbon isotopes. Quaternary Science Reviews, 28(25–26), 2564–2581. https://doi.org/10.1016/j.quascirev.2009.05.016

Sato, T., Masuda, F. (2010). Estuarine , Coastal and Shelf Science Temporal changes of a delta : Example from the Holocene Yahagi delta , central Japan. Estuarine, Coastal and Shelf Science, 86(3), 415–428. https://doi.org/10.1016/j.ecss.2009.06.028

Sawakuchi, A. O., Jain, M., Mineli, T. D., Nogueira, L., Jr.Bertassoli, D. J., Häggi, C., … Cunha, D. F. (2018). Luminescence of quartz and feldspar fingerprints provenance and correlates with the source area denudation in the Amazon River basin. Earth and Planetary Science Letters, 492, 152–162. Retrieved from http://10.0.3.248/j.epsl.2018.04.006

Sawakuchi, A.O., Blair, M.W., DeWitt, R., Faleiros, F.M., Hyppolito, T., Guedes, C.C.F. (2011). Thermal history versus sedimentary history: OSL sensitivity of quartz grains

extracted from rocks and sediments. Quat. Geochronol. 6, 261–272. http://dx.doi.org/10.1016/j.quageo.2010.11.002

Sepúlveda-Jaimes, F. J., and Cabrera-Zambrano, F. H. (2018). Tomografía sísmica 3D del nido sísmico de Bucaramanga (Colombia). Revista Boletín de Geología, 40(2), 15–33. https://doi.org/10.18273/revbol.v40n2-2018001

Shen, Z., Mauz, B. (2012). Optical dating of young deltaic deposits on a decadal time scale. Quat. Geochronol. 10, 110–116. https://doi.org/10.1016/j.quageo.2012.01.014

Sibaja-Cordero, J. A., Troncoso, J. S., Gómez-Ramírez, E. (2011). Recent surface marine sediments of Cocos Island in Costa Rica. Journal of Paleolimnology, 46(3), 405–421. https://doi.org/10.1007/s10933-009-9373-0

Simó, J. A., Gàmez, D., Salvany, J. M., Vàzquez-Suñé, E., Carrera, J., Barnolas, A., … Alcalà, F. J. (2005). Arquitectura de facies de los deltas cuaternarios del río Llobregat, Barcelona, España. Geogaceta, 38(1), 171–174. Retrieved from http://dialnet.unirioja.es/servlet/articulo?codigo=1332989andorden=123148andinfo=link

Sommerfield, C.K., Nittrouer, C.A., Figueiredo, A.G. (1995). Stratigraphic evidence of changes in Amazon shelf sedimentation during the late Holocene. Marine Geology 125, 351–371. https://doi.org/10.1016/0025-3227(95)00019-U

Stanley, D.J. (2001). Dating modern deltas: Progress, problems, and prognostics. Annu. Rev. Earth Planet. Sci. 29, 257–294. https://doi.org/10.1146/annurev.earth.29.1.257

Stanley, D.J. Hait, A.K. (2000). Deltas, radiocarbon dating, and measurements of sediment storage and subsidence, Geology 28, 295–298. https://doi.org/10.1130/0091-7613(2000)28<295:DRDAMO>2.0.CO;2

Stanley, D.J., Warne, A.G., Davis, H.R., Bernasconi, M.P., Chen, Z. (1992). Nile Delta: the late Quaternary north-central Nile Delta from Manzala to Burullus Lagoons, Egypt. Natl. Geogr. Res. Explor. 8 (1), 22e51

Stanley, D.J., Zhongyuan Chen, Z. (2000). Radiocarbon dates in China's Holocene Yangtze Delta: Record of sediment storage and reworking, not timing of deposition. J. Coastal Res. 16, 1126–1132. https://www.jstor.org/stable/4300129

Storms, J. E. A., Hoogendoorn, R. M., Dam, R. A. C., Hoitink, A. J. F., and Kroonenberg, S. B. (2005). Late-Holocene evolution of the Mahakam delta , East Kalimantan , Indonesia, 180, 149–166. https://doi.org/10.1016/j.sedgeo.2005.08.003

Suter, F., Sartori, M., Neuwerth, R., Gorin, G. (2008). Structural Imprints at the Front of the Chocó-Panamá Indenter: Field data From the North Cauca Valley Basin, Central Colombia. Tectonophysics 460. 134 - 157 p

Syvitski, J. P. M., Kettner, A. J., Overeem, I., Hutton, E. W. H., Hannon, M. T., Brakenridge G. R., Day J., Vörösmarty, C., Saito, Y., Liviu, G., Nicholls, R.J. (2009). Sinking deltas due to human activities. Nat. Geosci. 2, 681–86. https://doi.org/10.1038/ngeo629

Ta, T.K.O., Nguyen, V.L., Tateishi, M., KobayashiI, I., Saito, Y. (2005). Holocene delta evolution and depositional models of the Mekong delta, southern Vietnam. SEPM, SEPM Special Publication 83, 453–466.

Tamura, T., Saito, Y., Bateman, M.D., Nguyen, V. L., Oanh Ta, T.K., Matsumoto, D. (2012). Luminescence dating of beach ridges for characterizing multi-decadal to centennial deltaic shoreline changes during Late Holocene, Mekong River delta. Mar. Geol. 326–328. https://doi.org/10.1016/j.margeo.2012.08.004

Tanaka, K., and Watanabe, N. (2015). Size distribution of alkali elements in riverbed sediment and its relevance to fractionation of alkali elements during chemical weathering. Chemical Geology. https://doi.org/10.1016/j.chemgeo.2015.05.025

Tanner, W.F. (1991a). Suite statistics: The hydrodynamic evolution of the sediment pool. In: Syvitski, J.P.M. (Ed.), Principles, Methods and Applications of Particle Size Analysis. Cambridge Univ. Press, Cambridge, pp. 225–236.

Taylor, R.E. (2018). Radiocarbon dating in archaeology. In: Smith C. (ed) Encyclopedia of Global Archaeology. Springer, Cham.

Taylor, S.R., McLennan, S.M., (1985). The Continental Crust: Its Composition and Evolution. Blackwell, Oxford. 312 pp. https://doi.org/10.1002/gj.3350210116

Thiel, C., Buylaert, J.-P., Murray, A.S., Terhorst, B., Hofer, I., Tsukamoto, S., Frechen, M. (2011a). Luminescence dating of the Stratzing loess profile (Austria) – Testing the potential of an elevated temperature post-IR IRSL protocol. Quatern. Int. 234, 23–31. https://doi.org/10.1016/j.quaint.2010.05.018

Thiel, C., Buylaert, J.-P., Murray, A.S., Tsukamoto, S. (2011b). On the applicability of post-IR IRSL dating to Japanese loess. Geochronometria 38, 369–378. https://doi.org/10.2478/s13386-011-0043-4

Thomas, Y., Cesaraccio, M., García y, C., M´enanteau, L. (2007). Contribución de la hidrografía histórica al estudio de la cinemática de los fondos marinos: evolución del Golfo de Urabá, Colombia. Bol. Cient. CIOH 25, 110–119.

Thomas, Y.F., García-Valencia, C., Cesaraccio, M., Rojas, X. (2007). Atlas del golfo de Urabá: una mirada al Caribe de Antioquia y Chocó, 12. Instituto de Investigaciones Marinas y Costeras INVEMAR- y Gobernaci´on de Antioquia. Serie de publicaciones especiales INVEMAR, Santa Marta, pp. 75–127.

Tolman, H.L. (1997). User manual and system documentation of WAVEWATCH -III version 1.5. NOAA/NWS/NCEP/OMB, 97 p.

Törnqvist, T.E., Rosenheim, B.E., Hu, P., Fernandez, A. B. (2015). Radiocarbon dating and calibration. IN: Shennan, I., Long, A.J., Horton, B.P. (eds.): Handbook of Sea-Level Research, 349-360.

Trenkamp, R., Kellogg, J. N., Freymueller, J. T., Mora, H. P. (2002). Wide plate margin deformation, southern Central America and northwestern South America, CASA GPS observations. Journal of South American Earth Sciences. 15 (2): 157-171. https://doi.org/10.1016/S0895-9811(02)00018-4

Unverricht, D., Szczuciński, W., Stattegger, K., Jagodziński, R., Le, X. T., and Kwong, L. L. W. (2013). Modern sedimentation and morphology of the subaqueous Mekong Delta, Southern Vietnam. Global and Planetary Change, 110, 223–235. https://doi.org/10.1016/j.gloplacha.2012.12.009

USGS (2018). Landsat Satellite Missions. From:https://www.usgs.gov/land-resources/nli/landsat/landsat-satellite-missions?qt-cience_support_page_related_con=2#qt-science_support_page_related_con. USA.

Vakarelov, B.K. and Ainsworth, R.B. (2013) A hierarchical approach to architectural classification in marginal-marine systems: bridging the gap between sedimentology and sequence stratigraphy. AAPG Bull., 97, 1121–1161.

Vallejo Toro, P. P., Vásquez Bedoya, L. F., Correa, I. D., Bernal Franco, G. R., Alcántara-Carrió, J., and Palacio Baena, J. A. (2016). Impact of terrestrial mining and intensive agriculture in pollution of estuarine surface sediments: Spatial distribution of trace metals in the Gulf of Urabá, Colombia. Marine Pollution Bulletin, 111(1–2), 311–320. https://doi.org/10.1016/j.marpolbul.2016.06.093

Van Bemmelen, J. M. 1890. Über die Bestimmung des Wassers, des Humus, des Schwefels, der in den colloidalen Silikaten gebundenen Kieselsäure, des Mangans u.s.w. im Ackerboden. Die Landwirthschaftlichen Versuchs-Stationen, 37:279–290

Van, J. H. (1959). Landform-vegetation relationships in the Atrato Delta. Annals of the Asssocuation of American Geographers, 5608, 345–360. https://doi.org/10.1111/j.1467-8306.1959.tb01621.x

Vargas Cuervo, G., Castillo, L., Aguilera, R. C., and Jiménez, D. M. (2009). Inventario, Interpretación Y Evaluación De La Información Geológica, Geofísica Y Geoquímica Perteneciente Al Área Libre De La Cuenca De Urabá. Congreso Colombiano de Geología, 1–17. Retrieved from http://archives.datapages.com/data/colombia_acggp/simp10/47.htm

Velásquez, L. (2013). Modelación Del Transporte De Sedimentos En El Golfo De Urabá, Colombia, 132. Retrieved from https://repository.eafit.edu.co/bitstream/handle/10784/1268/VelasquezMontoya_Liliana_2013.pdf?sequence=1andisAllowed=

Velásquez, M., and Poveda, G. (2016). Estimación del balance hídrico de la región Pacífica. Dyna, 86(208), 297–306.

Velez, M. I., Escobar, J., Brenner, M., Rangel, O., Betancourt, A., Jaramillo, A. J., … Moreno, J. L. (2014). Middle to late Holocene relative sea level rise, climate variability and environmental change along the Colombian Caribbean coast. The Holocene, 24(8), 898–907. doi:10.1177/0959683614534740

Vélez-Agudelo, C., Aguirre-Ramírez, N.(2016). Influencia del río atrato en el Golfo de Urabá durante el holoceno tardío, mar caribe colombiano. Boletin de Investig. Mar. y Costeras 45, 73–97.

Vélez-Castaño, J.D., Betancurth-Montes, G.L., Cañón-Barriga, J.E., (2020). Erosion and Progradation in the Atrato River Delta: A Spatiotemporal Analysis with Google Earth Engine. Revista Facultad de Ingeniería Universidad de Antioquia [Online]. Available doi: 10.17533/udea.redin.20200688

Vernette, G., Gayet, J., Echeverry, C., Piedrahíta, I., Correa I. (2002). Introducción a los ambientes deltaicos: Morfología y Sedimentación, En: Geología y Oceanografía del delta del río San Juan. Litoral pacífico colombiano, 1ra Edición, Universidad EAFIT, Medellín, Colombia, 221 p.

Vespremeanu-Stroe, A., Zăinescu, F., Preoteasa, L., Tătui, F., Rotaru, S., Morhange, C., Morhanged, C., Stoicab, M., Hanganu, J., Timar-Gabor, A., Cârdan, I., Piotrowska, N., (2017). Holocene evolution of the Danube delta: An integral reconstruction and a revised chronology. Marine Geology, 388, 38–61. Retrieved from http://10.0.3.248/j.margeo.2017.04.002

Vijith, V., Shetye, S.R., (2012). A stratification prediction diagram from characteristics of geometry, tides and runoff for estuaries with a prominent channel. Estuarine, Coastal and Shelf Science. 98, 101- 107. https://doi.org/10.1016/j.ecss.2011.12.006

Viseras, C., Fernández, J., García-García, F., Soria, J. M., Calvache, M. L., and Jáuregui, P. (2009). Dynamics of sedimentary environments in the accelerated siltation of a reservoir: The case of Alhama de Granada, southern Spain. Environmental Geology, 56(7), 1353–1369. https://doi.org/10.1007/s00254-008-1231-2

Wang, F., Zhang, W., Nian, X., Ge, C., Zhao, X., Cheng, Q., Chen, J., Hutchinson, S.M., (2019). Refining the late-Holocene coastline and delta development of the northern Yangtze River delta: Combining historical archives and OSL dating. Holocene 29, 1439–1449. https://doi.org/10.1177/0959683619854522

Wang, Z., Xian, B., Ma, L., Chao, C., Pu, Q., and Liu, J. (2018). Mapping sediment-dispersal characteristics of Neogene deltas using seismic geomorphology, Liaodongdong area, Bohai Bay Basin, China. Energy Sources Part A: Recovery, Utilization and Environmental Effects, 40(19), 2265–2276. Retrieved from http://10.0.4.56/15567036.2018.1486477

Wedepohl, K. H. (1995). The composition of the continental crust. Geochimica et Cosmochimica Acta, 59(7), 1217–1232.
Whitemore, G.P., Crook, K.A.W., Johnson, D.P., (2004). Grain size control of mineralogy and geochemistry in modern river sediment, New Guinea collision, Papua Guinea. Sediment. Geol. 171, 129–157
Wintle, A.G., (1973). Anomalous fading of thermo-luminescence in mineral samples. Nature 245, 143–144. https://doi.org/10.1038/245143a0
Wolf, D., Ryborz, K., Kolb, T., Calvo Zapata, R., Sanchez Vizcaino, J., Zöller, L., & Faust, D. (2019). Origins and genesis of loess deposits in central Spain, as indicated by heavy mineral compositions and grain-size variability. Sedimentology, 66(3), 1139–1161. https://doi.org/10.1111/sed.12539
Wray, R. A. L., and Sauro, F. (2017). An updated global review of solutional weathering processes and forms in quartz sandstones and quartzites Robert. Earth-Science Reviews. https://doi.org/10.1016/j.earscirev.2017.06.008
Yevzerov, V. (2007). Association of sediments in fluvioglacial deltas (Evidence from Northwesternmost Russia). Lithology and Mineral Resources, 42(6), 505–514. https://doi.org/10.1134/S0024490207060016
Zapata, G. (2002). Geología de las planchas 163 Nuquí, 164 Quibdó, 183 Coquí y 184 Lloró, Departamento del Chocó, escala 1: 100.000. INGEOMINAS, 71 p. Bogotá.
Zhang, G.A.N., Li, X., Sheng, G., Fu, J. (2005). Abundances, depositional fluxes, and homologue patterns of polychlorinated biphenyls in dated sediment cores from the Pearl River Delta, China. Environ. Sci. Technol. 39, 49–56.
Zoccarato, C., Minderhoud, P. S. J., & Teatini, P. (2018). The role of sedimentation and natural compaction in a prograding delta: insights from the mega Mekong delta, Vietnam. Scientific Reports, 8(1), 1–12. https://doi.org/10.1038/s41598-018-29734-7

6 Appendices

Appendix 1. Geomorphological units image of ARD (Invemar, 2007)

Appendix 2. Photographs of field work campains for surface and core samplings, laboratory work and socialization with communities

Appendix 3. Grain size: statistical parameters for selected surface samples

Samples	Samples Type	Textural group	Sediment name	Mean		Sorting		Skewness		Kurtosis	
DA-01	Polymodal, Poorly Sorted	Mud	Coarse Silt	12.07	Medium Silt	3.139	Poorly Sorted	-0.218	Fine Skewed	0.811	Platykurtic
DA-02	Polymodal, Poorly Sorted	Mud	Coarse Silt	10.04	Medium Silt	2.757	Poorly Sorted	-0.162	Fine Skewed	0.945	Mesokurtic
DA-03	Polymodal, Very Poorly Sorted	Sandy Mud	Very Fine Sandy Fine Silt	19.06	Coarse Silt	4.972	Very Poorly Sorted	0.024	Symmetrical	0.668	Very Platykurtic
DA-04	Polymodal, Poorly Sorted	Sandy Mud	Very Fine Sandy Medium Silt	13.86	Medium Silt	3.380	Poorly Sorted	-0.048	Symmetrical	0.785	Platykurtic
DA-08	Polymodal, Moderately Sorted	Muddy Sand	Very Coarse Silty Very Fine Sand	71.05	Very Fine Sand	1.911	Moderately Sorted	-0.352	Very Fine Skewed	1.347	Leptokurtic
DA-09	Trimodal, Moderately Well Sorted	Sandy Mud	Very Fine Sandy Very Coarse Silt	50.24	Very Coarse Silt	1.510	Moderately Well Sorted	0.033	Symmetrical	0.996	Mesokurtic
DA-10	Polymodal, Poorly Sorted	Sandy Mud	Very Fine Sandy Very Coarse Silt	26.26	Coarse Silt	3.542	Poorly Sorted	-0.154	Fine Skewed	0.819	Platykurtic
DA-11	Trimodal, Moderately Well Sorted	Muddy Sand	Very Coarse Silty Very Fine Sand	89.87	Very Fine Sand	1.439	Moderately Well Sorted	0.245	Coarse Skewed	0.924	Mesokurtic
DA-12	Trimodal, Poorly Sorted	Muddy Sand	Very Coarse Silty Very Fine Sand	67.21	Very Fine Sand	2.199	Poorly Sorted	-0.405	Very Fine Skewed	1.262	Leptokurtic
DA-13	Polymodal, Poorly Sorted	Sandy Mud	Very Fine Sandy Very Coarse Silt	24.74	Coarse Silt	3.625	Poorly Sorted	-0.331	Very Fine Skewed	0.776	Platykurtic
DA-14	Bimodal, Very Poorly Sorted	Sandy Mud	Very Fine Sandy Very Coarse Silt	19.75	Coarse Silt	4.662	Very Poorly Sorted	-0.424	Very Fine Skewed	0.900	Mesokurtic
DA-15	Unimodal, Very Poorly Sorted	Muddy Sand	Very Coarse Silty Fine Sand	62.50	Very Coarse Silt	4.501	Very Poorly Sorted	-0.659	Very Fine Skewed	1.628	Very Leptokurtic
DA-18	Unimodal, Moderately Sorted	Muddy Sand	Very Coarse Silty Very Fine Sand	82.15	Very Fine Sand	1.848	Moderately Sorted	-0.314	Very Fine Skewed	1.556	Very Leptokurtic
DA-28	Bimodal, Very Poorly Sorted	Sandy Mud	Very Fine Sandy Very Coarse Silt	13.23	Medium Silt	5.543	Very Poorly Sorted	-0.144	Fine Skewed	0.818	Platykurtic
DA-30	Unimodal, Poorly Sorted	Mud	Fine Silt	3.231	Very Fine Silt	2.940	Poorly Sorted	-0.145	Fine Skewed	0.877	Platykurtic
DA-32	Bimodal, Very Poorly Sorted	Sandy Mud	Very Fine Sandy Very Coarse Silt	19.22	Coarse Silt	5.219	Very Poorly Sorted	-0.369	Very Fine Skewed	0.784	Platykurtic
DA-33	Bimodal, Very Poorly Sorted	Sandy Mud	Very Fine Sandy Very Coarse Silt	12.35	Medium Silt	4.735	Very Poorly Sorted	-0.227	Fine Skewed	0.866	Platykurtic
DA-34	Bimodal, Very Poorly Sorted	Mud	Medium Silt	7.594	Fine Silt	4.029	Very Poorly Sorted	-0.144	Fine Skewed	0.885	Platykurtic
DA-35	Bimodal, Poorly Sorted	Mud	Fine Silt	4.038	Fine Silt	3.081	Poorly Sorted	-0.194	Fine Skewed	0.927	Mesokurtic
DA-36	Unimodal, Poorly Sorted	Mud	Fine Silt	3.456	Very Fine Silt	3.098	Poorly Sorted	-0.148	Fine Skewed	0.867	Platykurtic
DA-37	Bimodal, Poorly Sorted	Mud	Fine Silt	4.076	Fine Silt	3.104	Poorly Sorted	-0.168	Fine Skewed	0.952	Mesokurtic
DA-39	Bimodal, Very Poorly Sorted	Sandy Mud	Very Fine Sandy Very Coarse Silt	16.16	Coarse Silt	4.934	Very Poorly Sorted	-0.248	Fine Skewed	0.855	Platykurtic
DA-41	Polymodal, Very Poorly Sorted	Muddy Sand	Very Coarse Silty Very Fine Sand	33.69	Very Coarse Silt	6.411	Very Poorly Sorted	-0.465	Very Fine Skewed	0.822	Platykurtic
DA-43	Unimodal, Poorly Sorted	Muddy Sand	Very Coarse Silty Very Fine Sand	48.06	Very Coarse Silt	3.299	Poorly Sorted	-0.610	Very Fine Skewed	1.672	Very Leptokurtic

Samples	Samples Type	Textural group	Sediment name	Mean		Sorting		Skewness		Kurtosis	
DA-44	Bimodal, Very Poorly Sorted	Sandy Mud	Very Fine Sandy Very Coarse Silt	15.5953684	Medium Silt	5.221	Very Poorly Sorted	-0.2	Fine Skewed	0.82	Platykurtic
DA-45	Bimodal, Very Poorly Sorted	Sandy Mud	Very Fine Sandy Very Coarse Silt	13.5268481	Medium Silt	4.929	Very Poorly Sorted	-0.16	Fine Skewed	0.83	Platykurtic
DA-46	Bimodal, Very Poorly Sorted	Muddy Sand	Very Coarse Silty Very Fine Sand	33.5687329	Very Coarse Silt	4.664	Very Poorly Sorted	-0.62	Very Fine Skewed	0.95	Mesokurtic
DA-49	Unimodal, Poorly Sorted	Muddy Sand	Very Coarse Silty Very Fine Sand	72.8992153	Very Fine Sand	2.781	Poorly Sorted	-0.54	Very Fine Skewed	2.18	Very Leptokurtic
DA-50	Unimodal, Poorly Sorted	Mud	Mud	3.12268111	Very Fine Silt	2.974	Poorly Sorted	-0.08	Symmetrical	0.9	Platykurtic
DA-53	Trimodal, Poorly Sorted	Mud	Fine Silt	3.39336548	Very Fine Silt	3.046	Poorly Sorted	-0.09	Symmetrical	0.91	Mesokurtic
DA-54	Bimodal, Poorly Sorted	Mud	Medium Silt	5.23896106	Fine Silt	3.729	Poorly Sorted	-0.11	Fine Skewed	0.9	Mesokurtic
DA-56	Bimodal, Poorly Sorted	Mud	Medium Silt	6.21087779	Fine Silt	3.696	Poorly Sorted	-0.11	Fine Skewed	0.93	Mesokurtic
DA-59	Bimodal, Poorly Sorted	Mud	Medium Silt	6.35781601	Fine Silt	3.655	Poorly Sorted	-0.16	Fine Skewed	0.95	Mesokurtic
DA-60	Bimodal, Poorly Sorted	Mud	Fine Silt	3.51086897	Very Fine Silt	2.997	Poorly Sorted	-0.1	Fine Skewed	0.96	Mesokurtic
DA-61	Bimodal, Very Poorly Sorted	Muddy Sand	Very Coarse Silty Very Fine Sand	39.2073866	Very Coarse Silt	4.332	Very Poorly Sorted	-0.59	Very Fine Skewed	1.17	Leptokurtic
DA-63	Unimodal, Moderately Well Sorted	Sand	Moderately Well Sorted Fine Sand	139.311794	Fine Sand	1.472	Moderately Well Sorted	-0.2	Fine Skewed	1.2	Leptokurtic
DA-65	Bimodal, Very Poorly Sorted	Mud	Medium Silt	8.16372544	Medium Silt	4.237	Very Poorly Sorted	-0.16	Fine Skewed	0.86	Platykurtic
DA-69	Bimodal, Very Poorly Sorted	Sandy Mud	Very Fine Sandy Very Coarse Silt	17.8063999	Coarse Silt	4.775	Very Poorly Sorted	-0.39	Very Fine Skewed	0.84	Platykurtic
DA-70	Polymodal, Very Poorly Sorted	Sandy Mud	Very Fine Sandy Very Coarse Silt	16.754045	Coarse Silt	5.628	Very Poorly Sorted	-0.26	Fine Skewed	0.74	Platykurtic
DA-72	Bimodal, Very Poorly Sorted	Sandy Mud	Very Fine Sandy Very Coarse Silt	28.8905489	Coarse Silt	5.084	Very Poorly Sorted	-0.33	Very Fine Skewed	0.96	Mesokurtic
DA-73	Unimodal, Moderately Sorted	Sand	Moderately Sorted Fine Sand	133.996795	Fine Sand	1.644	Moderately Sorted	-0.28	Fine Skewed	1.52	Very Leptokurtic
DA-74	Bimodal, Poorly Sorted	Mud	Medium Silt	4.90791643	Fine Silt	3.243	Poorly Sorted	-0.16	Fine Skewed	0.99	Mesokurtic
DA-75	Trimodal, Poorly Sorted	Mud	Medium Silt	4.81130199	Fine Silt	3.706	Poorly Sorted	-0.08	Symmetrical	0.87	Platykurtic
DA-79	Bimodal, Very Poorly Sorted	Sandy Mud	Very Fine Sandy Very Coarse Silt	20.8836574	Coarse Silt	4.897	Very Poorly Sorted	-0.36	Very Fine Skewed	0.85	Platykurtic
DA-80	Bimodal, Very Poorly Sorted	Sandy Mud	Very Fine Sandy Very Coarse Silt	21.2398176	Coarse Silt	5.181	Very Poorly Sorted	-0.43	Very Fine Skewed	0.8	Platykurtic
DA-82	Bimodal, Poorly Sorted	Mud	Mud	3.18015289	Very Fine Silt	3.142	Poorly Sorted	-0.07	Symmetrical	0.88	Platykurtic
DA-84	Trimodal, Very Poorly Sorted	Sandy Mud	Very Fine Sandy Very Coarse Silt	13.7116339	Medium Silt	5.248	Very Poorly Sorted	-0.12	Fine Skewed	0.86	Platykurtic
DA-85	Unimodal, Very Poorly Sorted	Muddy Sand	Very Coarse Silty Very Fine Sand	38.9052209	Very Coarse Silt	4.069	Very Poorly Sorted	-0.64	Very Fine Skewed	1.29	Leptokurtic
DA-86	Unimodal, Poorly Sorted	Mud	Fine Silt	3.23718239	Very Fine Silt	2.943	Poorly Sorted	-0.15	Fine Skewed	0.87	Platykurtic
DA-87	Bimodal, Very Poorly Sorted	Sandy Mud	Very Fine Sandy Very Coarse Silt	18.8154153	Coarse Silt	4.953	Very Poorly Sorted	-0.38	Very Fine Skewed	0.8	Platykurtic
DA-88	Bimodal, Very Poorly Sorted	Sandy Mud	Very Fine Sandy Very Coarse Silt	23.0824611	Coarse Silt	5.152	Very Poorly Sorted	-0.4	Very Fine Skewed	0.8	Platykurtic
DA-89	Bimodal, Poorly Sorted	Sandy Mud	Very Fine Sandy Very Coarse Silt	36.3819897	Very Coarse Silt	3.868	Poorly Sorted	-0.59	Very Fine Skewed	1.21	Leptokurtic
DA-90	Unimodal, Very Poorly Sorted	Muddy Sand	Very Coarse Silty Very Fine Sand	39.6761347	Very Coarse Silt	4.036	Very Poorly Sorted	-0.63	Very Fine Skewed	1.27	Leptokurtic

Appendix 4. Distribution of size fractions of the selected stream sediments samples

Sample	Sector	Sand %	Silt %	Clay &
DA-01	Central	1.8%	90.7%	7.5%
DA-02		0.0%	92.6%	7.4%
DA-03		34.0%	59.4%	6.7%
DA-04		10.5%	84.1%	5.3%
DA-08		64.5%	35.3%	0.1%
DA-28		21.3%	63.1%	15.5%
	Mean	22.0%	70.9%	7.1%
DA-46	West	50.6%	41.0%	8.3%
DA-60		0.0%	70.8%	29.2%
DA-61		52.6%	40.3%	7.1%
DA-63		94.5%	4.1%	1.3%
DA-65		2.3%	79.6%	18.2%
DA-69		24.2%	63.8%	12.0%
DA-70		31.1%	54.7%	14.2%
DA-72		39.1%	51.7%	9.2%
DA-73		91.9%	6.7%	1.4%
DA-74		0.0%	78.1%	21.9%
DA-75		0.0%	73.8%	26.2%
DA-79		30.9%	58.5%	10.6%
DA-80		34.3%	54.0%	11.7%
DA-82		0.0%	65.8%	34.2%
DA-84		20.1%	65.9%	14.0%
DA-85		53.9%	39.0%	7.1%
DA-86		0.0%	68.1%	31.9%
DA-87		29.1%	59.1%	11.8%
DA-88		36.7%	52.7%	10.6%
DA-89		47.6%	46.0%	6.4%
DA-90		53.8%	39.3%	6.9%
	Mean	33.0%	53.0%	14.0%

Sample	Sector	Sand %	Silt %	Clay &
DA-18	Northeast	73.6%	24.2%	2.3%
DA-09		27.5%	72.5%	0.1%
DA-10		29.1%	70.7%	0.2%
DA-11	South	85.4%	14.6%	0.0%
DA-12		64.5%	35.4%	0.1%
DA-13		30.2%	68.8%	1.0%
	Mean	47.3%	52.4%	0.3%
DA-14		25.6%	63.5%	11.0%
DA-15		70.3%	23.1%	6.6%
DA-50		0.0%	66.5%	33.5%
DA-53	Southeast	0.0%	68.8%	31.2%
DA-54		0.0%	76.1%	23.9%
DA-56		0.0%	79.9%	20.1%
DA-59		0.0%	80.6%	19.4%
	Mean	13.7%	65.5%	20.8%
DA-30		0.0%	68.1%	31.9%
DA-32		31.6%	56.1%	12.3%
DA-33		13.6%	71.9%	14.6%
DA-34		0.3%	81.3%	18.4%
DA-35		0.0%	74.0%	26.0%
DA-36		0.0%	69.0%	31.0%
DA-37	East	0.0%	74.3%	25.7%
DA-39		22.5%	65.2%	12.3%
DA-41		50.0%	39.6%	10.4%
DA-43		56.8%	37.8%	5.4%
DA-44		24.6%	62.3%	13.1%
DA-45		18.9%	67.5%	13.6%
DA-46		50.6%	41.0%	8.3%
DA-49		70.3%	25.3%	4.4%
	Mean	24.2%	59.5%	16.2%

Appendix 5. Summary of statistical parameters for the geochemical variables of oxides in surface

zones	# Samples	Statistics	SiO_2	Al_2O_3	Fe_2O_3	MgO	Na_2O	CaO	K_2O	TiO_2	P_2O_5	MnO
Delta Total	60	Mean	45.48	19.06	9.29	3.54	2.53	2.53	1.40	0.78	0.27	0.13
		Median	47.56	20.09	9.61	3.59	2.07	2.48	1.43	0.81	0.30	0.12
		SD	9.44	3.28	2.04	0.59	1.66	0.96	0.21	0.14	0.08	0.04
		Min	11.85	5.04	2.20	0.78	0.29	0.59	0.36	0.21	0.07	0.03
		Max	62.99	22.57	13.25	4.64	7.07	4.66	1.65	1.05	0.44	0.25
West	22	Mean	47.52	20.57	10.25	3.58	1.77	2.63	1.40	0.84	0.29	0.15
		Median	48.90	20.71	9.98	3.55	1.48	2.74	1.41	0.85	0.31	0.14
		SD	5.94	1.33	1.51	0.28	0.81	0.90	0.15	0.08	0.07	0.04
		Min	34.48	18.20	8.01	3.05	0.77	1.29	0.98	0.66	0.14	0.10
		Max	56.76	22.57	13.25	4.12	3.23	4.66	1.58	1.05	0.41	0.25
Northeast	10	Mean	43.40	15.83	8.16	3.66	5.40	2.70	1.45	0.64	0.21	0.09
		Median	40.46	15.63	8.56	3.66	5.35	2.58	1.46	0.64	0.21	0.09
		SD	13.39	2.04	2.24	0.30	1.03	1.04	0.08	0.10	0.10	0.01
		Min	27.80	13.09	4.69	3.14	3.64	1.58	1.30	0.44	0.10	0.07
		Max	62.99	19.56	11.35	4.24	7.07	4.00	1.55	0.82	0.44	0.11
East	11	Mean	42.52	18.15	8.09	3.02	1.23	2.24	1.23	0.73	0.23	0.12
		Median	47.91	21.13	8.87	3.27	1.26	2.56	0.38	0.83	0.23	0.13
		SD	13.92	5.55	2.59	1.05	0.66	1.01	1.40	0.23	0.09	0.12
		Min	11.85	5.04	2.20	0.78	0.29	0.59	0.36	0.21	0.07	0.03
		Max	53.84	21.98	10.81	4.33	2.75	3.77	1.54	0.92	0.33	0.19
Center	7	Mean	44.81	20.09	9.72	3.58	2.32	2.22	1.49	0.85	0.28	0.12
		Median	45.86	20.22	9.79	3.51	2.71	1.99	1.47	0.86	0.30	0.11
		SD	5.64	2.19	0.35	0.20	1.09	0.67	0.12	0.10	0.09	0.03
		Min	35.02	15.77	9.10	3.37	0.97	1.63	1.32	0.68	0.12	0.09
		Max	51.75	22.48	10.18	3.85	3.90	3.59	1.65	0.97	0.41	0.16
Southeast	6	Mean	41.63	20.17	10.82	3.69	3.19	1.74	1.51	0.82	0.33	0.12
		Median	40.23	20.28	10.94	3.60	3.41	1.49	1.51	0.82	0.32	0.12
		SD	4.49	0.88	1.07	0.51	0.70	0.67	0.09	0.03	0.04	0.02
		Min	38.34	18.60	8.84	3.14	2.30	1.35	1.39	0.78	0.27	0.10
		Max	50.57	21.23	11.88	4.41	3.89	3.08	1.62	0.87	0.38	0.14
South	4	Mean	51.59	18.44	8.16	3.99	2.68	3.46	1.42	0.80	0.30	0.13
		Median	52.08	17.61	8.30	3.96	3.23	3.45	1.44	0.79	0.31	0.13
		SD	5.69	2.66	1.83	0.51	1.13	1.06	0.12	0.05	0.03	0.03
		Min	45.10	16.39	6.25	3.39	0.99	2.43	0.08	0.76	0.26	0.11
		Max	57.09	22.17	9.78	4.64	3.28	4.52	1.27	0.88	0.33	0.17

Appendix 6. Summary of statistical parameters for the geochemical variables of trace elements in surface sediments

Sectors	# Samples	Statistics	Concentrations in ppm									
			Cl	S	Ba	Cu	Cr	Zn	Ni	Sr	Rb	Co
Total delta	60	Mean	9798.93	6571.03	643.26	207.26	193.26	137.41	109.43	226.64	34.69	52.38
		Median	589.50	2615.00	650.50	206.00	197.00	136.00	115.50	248.50	42.50	62.00
		SD	13912.20	8688.44	221.45	62.46	54.94	69.62	29.08	93.07	20.94	28.24
		Min	0.00	0.00	0.00	0.00	0.00	0.00	0.00	0.00	0.00	0.00
		Max	56700.00	36700.00	1020.00	343.00	336.00	573.00	144.00	376.00	63.00	95.00
West	22	Mean	4324.09	3822.41	692.53	698.68	230.27	208.00	113.46	242.64	43.95	68.36
		Median	0.00	1220.00	1560.00	748.00	221.00	196.50	116.00	277.00	46.50	69.00
		SD	7457.17	4882.71	260.09	233.22	54.88	41.87	27.79	93.26	13.88	12.84
		Min	0.00	0.00	0.00	0.00	110.00	154.00	0.00	0.00	0.00	45.00
		Max	24100.00	20300.00	1020.00	1020.00	343.00	336.00	144.00	376.00	63.00	93.00
Northeast	10	Mean	29786.00	16906.00	503.70	166.30	160.10	100.20	108.50	187.20	3.10	16.50
		Median	29050.00	14300.00	519.50	165.00	162.00	107.00	109.00	204.00	0.00	0.00
		SD	17322.50	12895.10	114.01	41.10	38.91	31.65	18.63	110.77	9.80	21.46
		Min	6960.00	1200.00	349.00	105.00	92.00	50.00	72.00	0.00	0.00	0.00
		Max	56700.00	36700.00	648.00	228.00	236.00	135.00	133.00	313.00	31.00	45.00
East	12	Mean	837.50	1647.50	640.50	192.92	185.17	123.08	98.75	226.00	36.00	57.92
		Median	0.00	1093.00	796.00	201.50	205.00	129.50	102.00	264.00	41.50	64.50
		SD	2505.83	1812.30	288.01	62.99	64.17	39.37	32.15	87.96	16.21	20.33
		Min	0.00	303.00	0.00	51.00	47.00	34.00	24.00	62.00	0.00	14.00
		Max	8740.00	7060.00	863.00	292.00	282.00	167.00	136.00	336.00	54.00	89.00
Center	7	Mean	8072.57	6872.57	589.43	207.86	192.86	185.43	102.86	202.43	34.14	52.71
		Median	108.00	1420.00	573.00	229.00	203.00	141.00	118.00	237.00	48.00	62.00
		SD	11703.60	10463.20	322.55	97.74	97.82	179.98	45.83	95.08	23.80	23.38
		Min	0.00	0.00	0.00	0.00	0.00	0.00	0.00	0.00	0.00	0.00
		Max	30600.00	28700.00	930.00	308.00	329.00	573.00	131.00	281.00	53.00	65.00
Southeast	6	Mean	17766.70	8705.00	610.83	249.83	204.00	161.00	128.67	198.83	44.50	66.50
		Median	14850.00	9675.00	623.00	257.00	205.00	161.50	129.50	199.00	53.00	73.00
		SD	6375.16	2903.38	103.44	43.76	13.80	21.63	5.79	14.33	22.92	34.76
		Min	12200.00	4300.00	420.00	187.00	181.00	126.00	118.00	181.00	0.00	0.00
		Max	29400.00	12200.00	727.00	315.00	222.00	186.00	135.00	218.00	62.00	95.00
South	4	Mean	7222.50	6995.00	674.00	208.75	233.25	120.75	112.50	314.50	44.25	33.00
		Median	6045.00	6865.00	657.50	213.50	224.00	128.00	115.50	310.00	43.00	29.00
		SD	7008.34	4815.49	151.63	48.76	29.52	36.77	22.04	44.92	7.09	38.66
		Min	0.00	1450.00	511.00	147.00	211.00	75.00	85.00	274.00	38.00	0.00
		Max	16800.00	12800.00	870.00	261.00	274.00	152.00	134.00	364.00	53.00	74.00

Appendix 7. Box and whisker for oxides and their distribution in geographical sectors

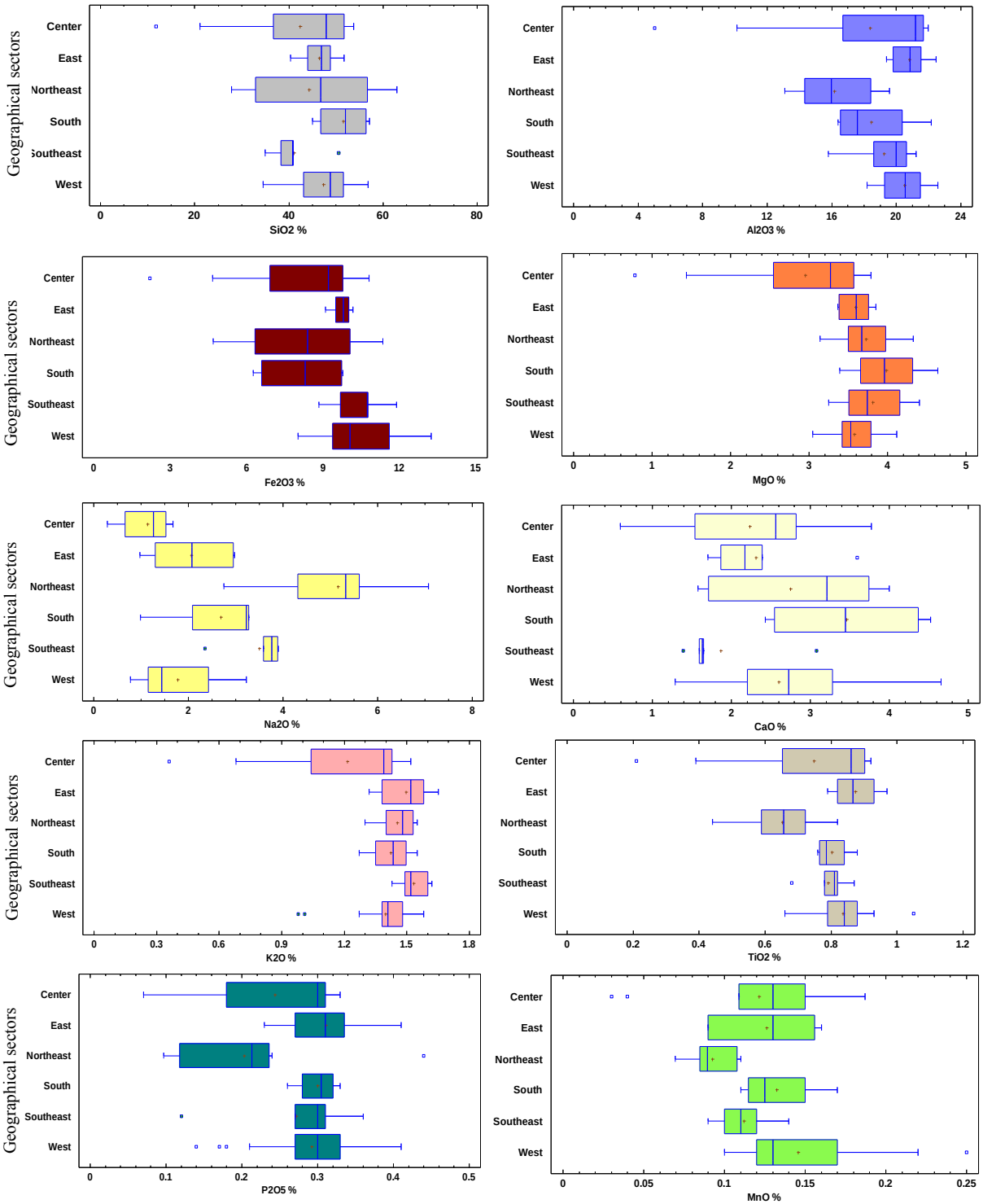

Appendix 8. Box and whisker for trace elements and their distribution in geographical sectors.

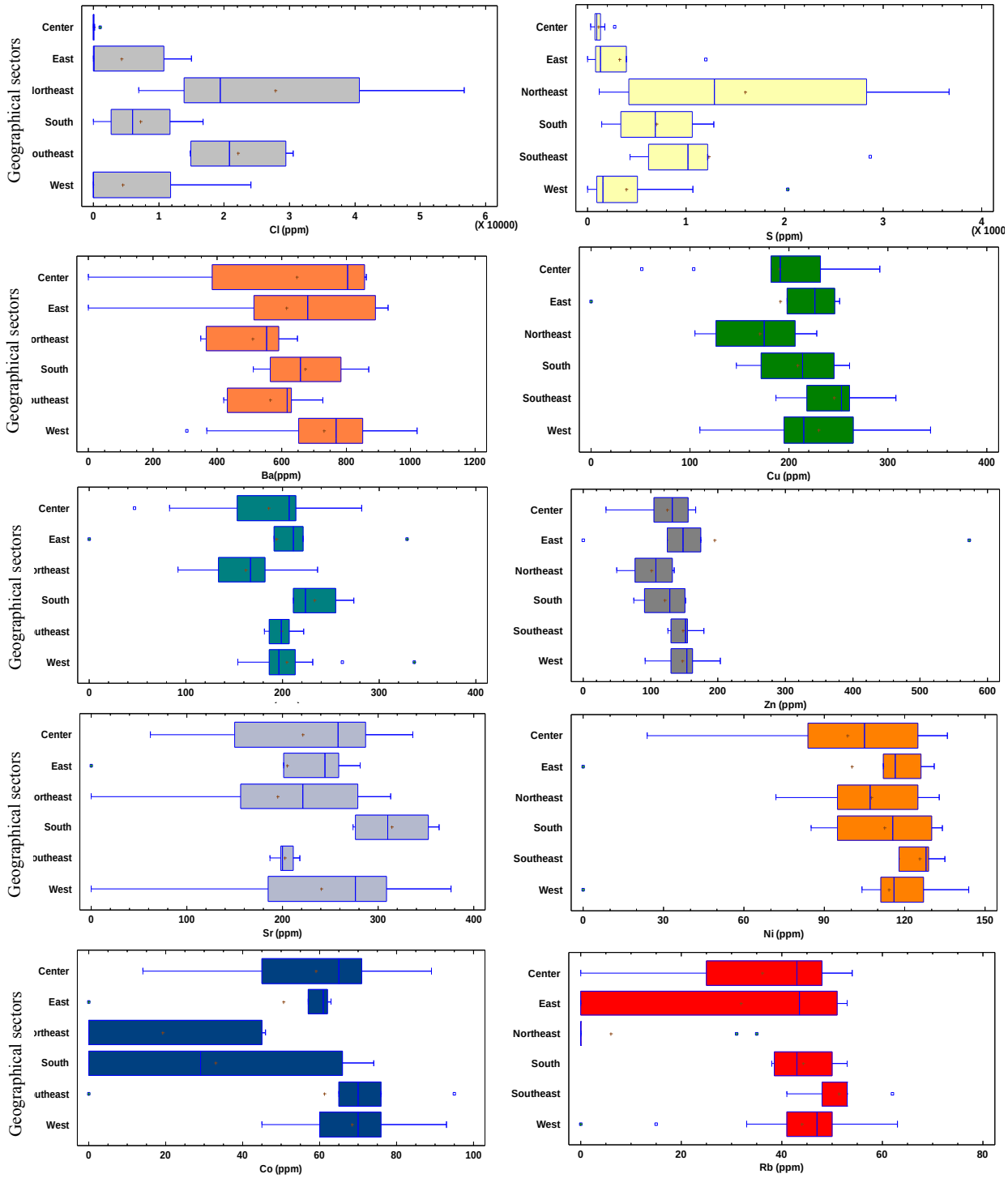

Appendix 9. Principal Components Analysis for major and trace elements: components weights.

	Component 1	Component 2	Component 3	Component 4
Settings	-0.027	-0.066	-0.368	0.132
Blocks	0.037	-0.021	0.032	-0.247
SiO_2	-0.245	-0.164	0.300	0.118
Al_2O_3	-0.312	0.064	-0.065	0.278
Fe_2O_3	-0.183	0.295	-0.185	0.288
MgO	-0.183	0.157	0.346	0.235
Na2O	0.177	0.253	0.322	0.064
CaO	-0.153	-0.206	0.379	0.072
K_2O	-0.178	0.228	0.276	0.114
TiO_2	-0.319	0.085	-0.024	0.210
P_2O_5	-0.204	0.015	-0.061	0.148
MnO	-0.253	-0.049	-0.116	0.322
Cl	0.200	0.340	0.143	0.060
S	0.175	0.334	0.120	-0.021
Ba	-0.248	-0.015	-0.004	-0.298
Cu	-0.207	0.275	-0.092	-0.255
Cr	-0.261	0.085	0.094	-0.154
Zn	-0.133	0.207	-0.120	-0.151
Sr	-0.215	-0.078	0.229	-0.319
Ni	-0.189	0.274	0.088	-0.323
Co	-0.208	0.154	-0.310	-0.092
Rb	-0.241	0.013	-0.108	-0.278
Br	0.143	0.325	0.069	0.031
OC	0.125	0.346	-0.188	0.057

Appendix 10. Chemical alteration features for sediment samples by depositional context and geographical sectors.

Sample	Setting	Blocks	CIA	Mol Sum	A	CN	K
DA-61	Bay	West	72.01	0.32	72.01	22.67	5.33
DA-63	Bay	West	63.13	0.31	63.13	31.18	5.69
DA-65	Bay	West	75.83	0.33	75.83	18.75	5.42
DA-69	River	West	65.48	0.31	65.48	29.56	4.97
DA-70	River	West	72.68	0.47	49.42	18.58	32.00
DA-70D	River	West	74.66	0.33	74.66	19.76	5.58
DA-72	Bay	West	62.81	0.34	62.81	31.29	5.90
DA-73	Bay	West	65.11	0.30	65.11	29.44	5.45
DA-74	Swamp	West	78.74	0.32	78.74	17.33	3.93
DA-75	River	West	76.26	0.32	76.26	19.72	4.02
DA-78	River	West	47.22	0.25	47.22	46.70	6.08
DA-79	River	West	74.17	0.33	74.17	20.68	5.16
DA-82	Bay	West	68.19	0.35	68.19	26.15	5.67
DA-84	River	West	68.10	0.34	68.10	26.25	5.65
DA-85	River	West	69.36	0.31	69.36	25.24	5.40
DA-86	Swamp	West	83.20	0.31	83.20	11.07	5.73
DA-87	River	West	72.94	0.31	72.94	21.90	5.17
DA-88	River	West	71.85	0.31	71.85	22.93	5.22
DA-90	River	West	70.44	0.31	70.44	24.56	5.00
		Mean	**70.11**				
DA-18	Bay	Northeast	46.23	0.42	33.18	38.58	28.24
DA-19	Bay	Northeast	46.55	330.99	46.55	48.40	5.05
DA-20	Bay	Northeast	48.13	153.80	48.13	47.15	4.72
DA-21	Bay	Northeast	56.76	139.53	56.76	38.17	5.07
DA-22	Bay	Northeast	54.99	139.53	56.76	38.17	5.07
DA-23	River	Northeast	54.57	119.74	54.57	39.96	5.47
DA-23D	River	Northeast	56.25	135.21	56.25	38.37	5.38
DA-24	River	Northeast	45.78	118.84	45.78	49.15	5.07
DA-25	River	Northeast	55.36	136.82	55.36	39.39	5.25
DA-26	Bay	Northeast	50.23	251.09	50.23	44.50	5.27
		Mean	**59.55**				
DA-32	River	East	73.96	0.32	73.96	20.83	5.21
DA-33	River	East	72.03	154.23	72.03	22.38	5.60
DA-34	River	East	75.83	0.32	75.83	18.72	5.45
DA-36	Swamp	East	82.00	0.31	82.00	12.19	5.82
DA-37	Swamp	East	81.71	0.31	81.71	12.34	5.95
DA-39	River	East	74.29	0.31	74.29	20.05	5.66
DA-41	River	East	72.56	0.31	72.56	22.31	5.13
DA-43	River	East	65.29	0.31	65.29	29.61	5.09
DA-44	River	East	72.09	0.46	49.00	18.97	32.03
DA-45	River	East	74.89	298.39	50.36	16.88	32.76
DA-46	River	East	70.12	0.32	70.12	25.09	4.79
DA-49	Bay	East	62.32	0.33	62.32	32.34	5.34
		Mean	**69.48**				
DA-01	Bay	Central	70.82	0.31	68.00	25.85	6.15
DA-02	Bay	Central	68.42	0.32	65.50	26.95	6.55
DA-03	Bay	Central	66.84	0.35	66.84	27.27	5.89
DA-04	River	Central	77.06	0.32	77.06	17.48	5.45
DA-08	River	Central	68.37	0.31	68.37	26.80	4.83
DA-17	Bay	Central	59.68	0.36	59.68	34.46	5.86
DA-28	suelo	Central	74.99	280.76	48.19	16.07	35.74
		Mean	**69.46**				
DA-15	Bay	SouthEast	62.20	0.35	62.20	32.66	5.14
DA-50	Bay	SouthEast	66.83	0.55	42.26	20.97	36.77
DA-54	River	SouthEast	64.62	0.35	64.62	29.66	5.72
DA-59	River	SouthEast	74.27	0.33	74.27	19.92	5.81
DA-60	River	SouthEast	70.54	0.54	45.54	19.02	35.44
DA-60D	River	SouthEast	74.66	0.33	74.66	19.79	5.56
		Mean	**68.85**				
DA-09	Bay	South	54.38	0.31	54.38	40.45	5.17
DA-10	Bay	South	63.00	0.34	63.00	31.29	5.70
DA-11	Bay	South	53.95	0.32	53.95	41.60	4.45
DA-13	River	South	75.37	0.32	75.37	19.37	5.26
		Mean	**61.68**				

Appendix 11. Triangular Diagrams of sand, silt, clay (left graphs) and particle diameter distribution (µm) (right graphs) for the six sediment cores.

HD_1 / Matuntugo Swamp

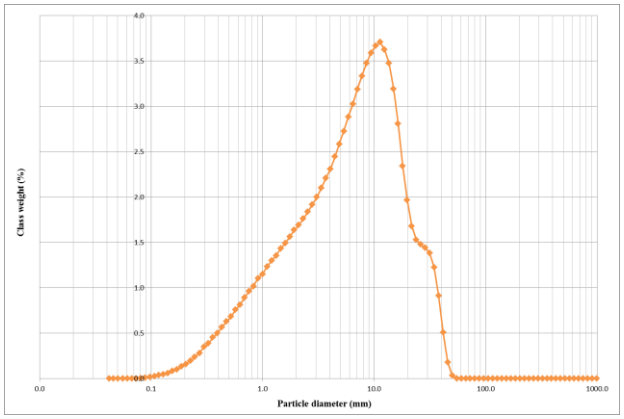

HD_2 / Maquillón Swamp

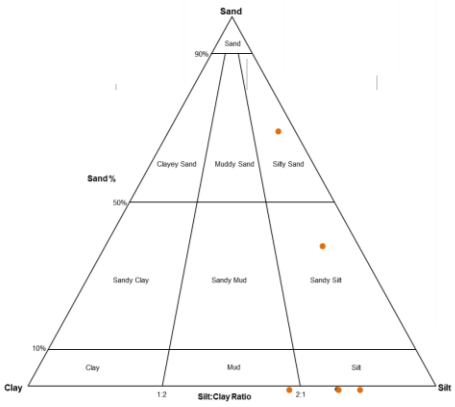

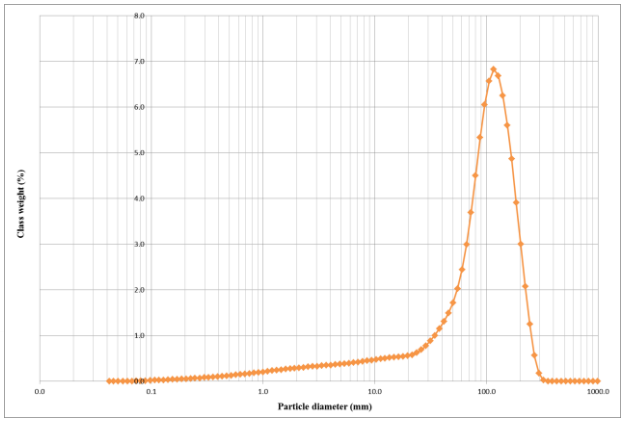

HD_3 / Burrera Bay

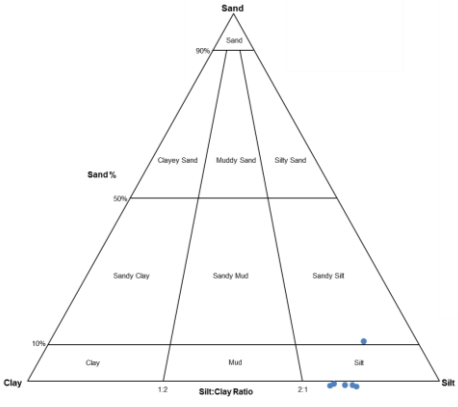

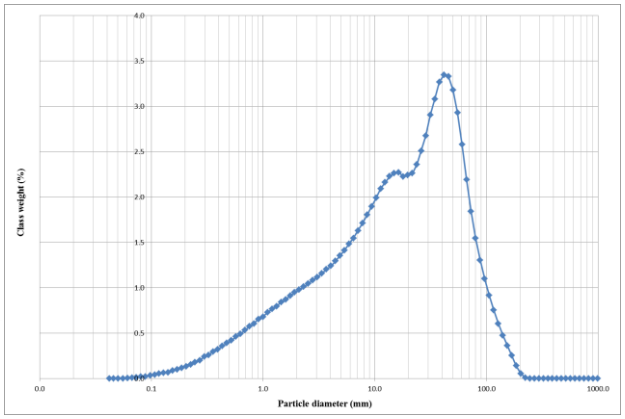

HD_4 / Marriaga Swamp

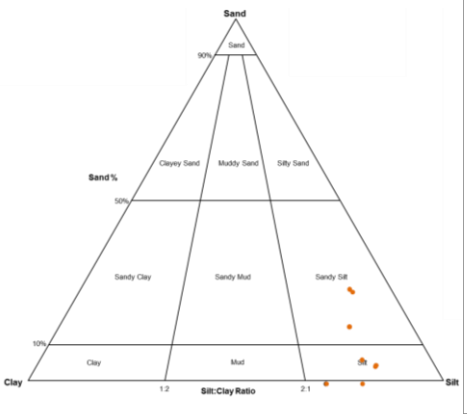

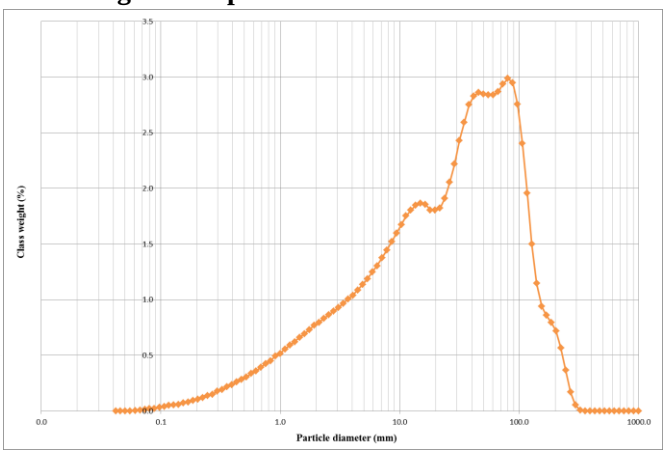

HD_5 / Candelaria Bay

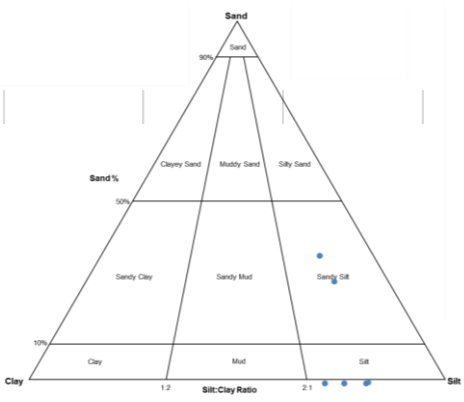

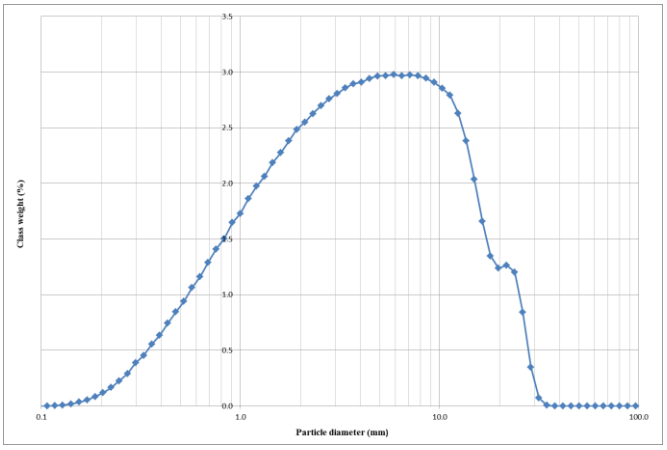

HD-6 / Yerbasal Bay

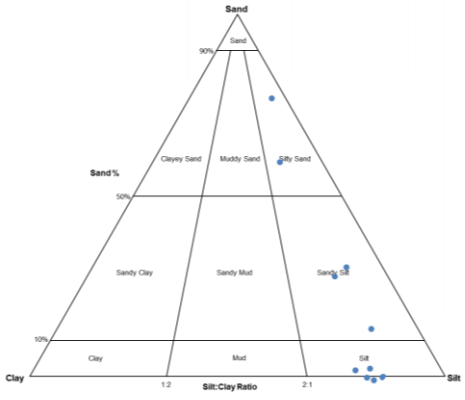

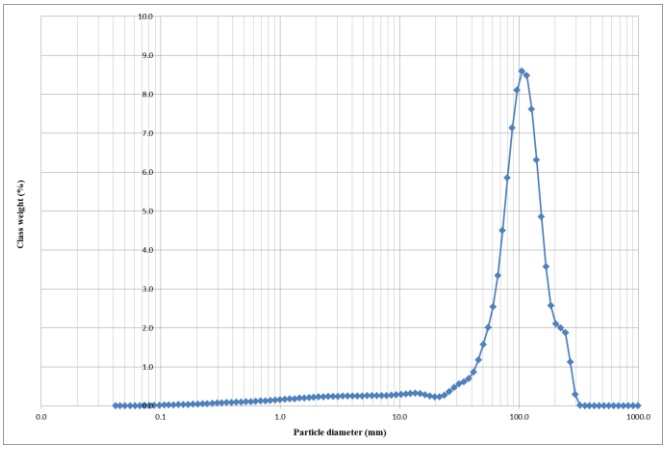

Appendix 12. Geomorphological units and current erosion and progradation analysis in the ARD

We analyzed a set of six Landsat satellite images from USGS Earth Explorer for 1973, 1986, 1996, 2001, 2011 and 2019 to evaluate the recent geomorphological changes occurring in the ARD shoreline in terms of erosion and progradation. We performed a manual digitation of shore polylines per year, from Tarena in the North to Marirrío Bay to the South. We overlapped the polylines by pairs of consequent years to delineate the polygons that represented the loss or gained terrain during every period. Finally, we compared all the obtained areas and calculated the total erosion and progradation areas in km^2 and ha between 1973 and 2019. We used the ArcGis Software for both delineation and calculation. We splited the ARD into three subareas, based on the geomorphological features: 1. Upper delta plain and 2. Lower delta plain as part of Floodplain.3. Delta front.

General Morphological classification of the Atrato River Delta, indicating location of cores and areas of net erosion and net progradation in 46 years. Image source: Landsat imaginery (EOS, 2018).

From the analysis of Landsat images, we classify the morphology of the ARD in three major units: i) the upper fluvial delta plain (south-middle area), ii) the lower delta plain (west-center of delta), and iii) delta front (marine delta).

The main Atrato channel, the delta apex at the beginning of León Mouth, and the bifurcation of the Atrato River at Cocogrande channel, affect the upper fluvial delta, conformed by fluvial levees, meanders, minor channels, large marshes and swamps as major landforms.

The lower delta plain, along the Burrera, Leoncito, Coquitos, Matuntugo channels and the abandoned Pava channel is evident in more linear channels, the mangroves cordons as well as in the presence of marshes and swamps.

The delta front corresponds to a marine environment, bifurcated in the north and east of the delta formed by open coast lobes, closed and abandoned fluvial channels, few small-flooded islands, and eroded beaches along the coastline.

We estimated a net progradation of 1768 Ha and net erosion of 942 Ha in a period of 46 years (1973 -2019). In addition, the linear progradation advance for that period was 1.7 km at Yerbasal bay; 2.2 km at El Roto mouth; 2.8 km at Matuntugo mouth; 1.1 km at Coquitos mouth and 0.98 km at Leoncito mouth.

Appendix 13. Detailed description of sediment core sections.

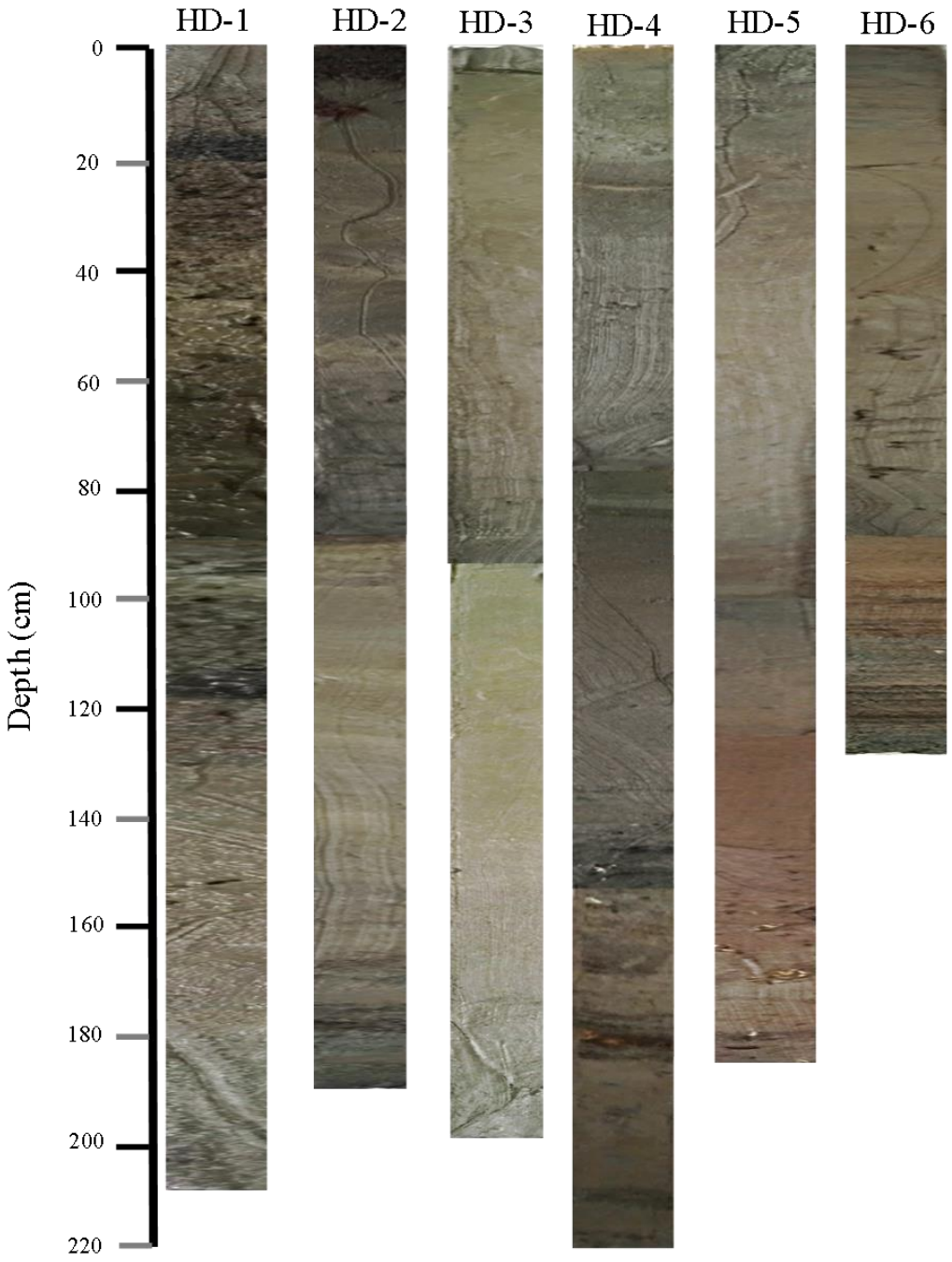

Mosaic of the six sediment cores described below

Appendix 14. Composition and statistics of major elements in cores.

Boreholes	# Samples	Statistics	Concentrations in wt%									
			SiO_2	Al_2O_3	Fe_2O_3	MgO	Na_2O	CaO	K_2O	TiO_2	P_2O_5	MnO
Delta	38	Mean	39.60	17.89	10.27	3.45	2.11	1.80	1.39	0.76	0.25	0.15
		Median	40.90	18.33	10.20	3.55	2.32	1.72	1.42	0.77	0.19	0.12
		SD	6.84	2.47	1.30	0.55	0.79	0.42	0.23	0.09	0.21	0.11
		Min	22.90	9.99	6.77	1.71	0.73	1.05	0.84	0.44	0.09	0.06
		Max	52.39	21.24	14.06	4.36	3.59	2.87	2.24	1.12	1.12	0.70
HD-1	5	Mean	42.06	18.40	9.64	3.17	1.09	1.52	1.35	0.75	0.21	0.09
		Median	41.36	18.17	9.75	3.15	1.05	1.52	1.30	0.74	0.22	0.08
		SD	2.95	1.55	0.38	0.38	0.38	0.03	0.16	0.03	0.06	0.01
		Min	39.18	16.88	9.05	2.68	0.73	1.50	1.22	0.73	0.14	0.08
		Max	46.69	20.09	10.07	3.70	1.71	1.55	1.60	0.79	0.30	0.10
HD-2	6	Mean	42.66	17.92	9.00	3.47	2.02	2.04	1.33	0.72	0.23	0.12
		Median	45.47	19.29	9.01	3.68	1.94	1.77	1.39	0.79	0.25	0.12
		SD	10.21	3.91	1.49	0.79	0.38	0.49	0.24	0.14	0.05	0.04
		Min	22.90	9.99	6.77	1.90	1.59	1.66	0.84	0.44	0.15	0.06
		Max	52.39	20.43	11.34	4.04	2.50	2.76	1.51	0.79	0.28	0.17
HD-3	4	Mean	40.85	19.19	10.25	3.56	2.82	1.51	1.56	0.78	0.20	0.09
		Median	40.60	19.16	10.22	3.70	2.86	1.43	1.53	0.78	0.22	0.10
		SD	1.27	0.80	0.39	0.38	0.19	0.34	0.07	0.02	0.05	0.01
		Min	39.60	18.48	9.91	3.00	2.55	1.22	1.51	0.76	0.12	0.08
		Max	42.62	19.98	10.65	3.85	3.00	1.96	1.66	0.81	0.24	0.10
HD-4	5	Mean	44.02	18.57	10.88	3.27	1.26	1.63	1.16	0.72	0.17	0.18
		Median	45.25	18.13	10.56	3.37	1.31	1.71	1.25	0.76	0.17	0.11
		SD	2.45	1.05	0.48	0.23	0.22	0.16	0.20	0.08	0.09	0.13
		Min	41.16	17.83	10.50	2.86	0.94	1.43	0.90	0.65	0.09	0.10
		Max	46.41	20.37	11.52	3.44	1.50	1.77	1.33	0.78	0.32	0.40
HD-5	7	Mean	34.00	15.97	11.49	3.72	2.86	1.75	1.55	0.73	0.16	0.11
		Median	35.15	16.59	11.00	3.81	3.02	1.72	1.45	0.74	0.15	0.10
		SD	4.72	1.81	1.75	0.33	0.26	0.17	0.32	0.05	0.05	0.02
		Min	28.89	13.62	8.83	3.27	2.44	1.53	1.24	0.62	0.09	0.08
		Max	39.83	17.86	14.06	4.15	3.16	1.95	2.24	0.78	0.25	0.13
HD-6	11	Mean	37.92	18.08	10.21	3.43	2.28	2.01	1.38	0.81	0.38	0.23
		Median	38.31	18.66	10.14	3.65	2.39	1.95	1.44	0.81	0.19	0.19
		SD	7.57	2.77	0.86	0.70	0.75	0.53	0.15	0.12	0.35	0.16
		Min	27.15	14.20	9.08	1.71	0.90	1.05	1.12	0.70	0.10	0.13
		Max	49.00	21.24	11.68	4.36	3.59	2.87	1.52	1.12	1.12	0.70

Appendix 15. Composition and statistics of trace elements in cores.

Boreholes	# Samples	Statistics	Concentrations in ppm									
			Cl	S	Ba	Cu	Cr	Zn	Ni	Sr	Rb	Co
HD-1	5	Mean	1706.40	2376.00	637.60	231.00	164.60	138.20	107.40	157.20	44.80	62.00
		Median	1890.00	0.00	619.00	218.00	159.00	139.00	110.00	161.00	44.00	59.00
		SD	903.21	3754.51	70.94	26.66	13.39	8.32	7.02	13.01	5.17	9.30
		Min	660.00	0.00	539.00	203.00	155.00	125.00	99.00	143.00	38.00	52.00
		Max	2890.00	8590.00	715.00	268.00	188.00	147.00	115.00	171.00	52.00	76.00
HD-2	6	Mean	6773.33	3706.00	860.50	237.83	165.83	140.17	112.17	213.33	43.83	59.50
		Median	6185.00	2750.00	886.00	221.00	172.00	133.00	113.50	199.50	44.50	63.50
		SD	3535.31	2690.49	112.66	45.36	23.09	23.91	8.50	43.66	7.33	19.13
		Min	3160.00	976.00	667.00	202.00	121.00	117.00	96.00	166.00	35.00	35.00
		Max	13300.00	7680.00	977.00	323.00	187.00	179.00	120.00	274.00	51.00	79.00
HD-3	4	Mean	13550.00	15007.50	548.75	234.75	184.75	151.50	114.50	175.00	47.25	59.50
		Median	13200.00	15350.00	524.50	234.00	184.00	148.50	114.00	170.50	45.50	58.50
		SD	1138.71	5682.45	86.43	20.61	15.13	13.43	11.12	30.58	8.66	2.38
		Min	12600.00	8530.00	477.00	216.00	167.00	139.00	102.00	143.00	39.00	58.00
		Max	15200.00	20800.00	669.00	255.00	204.00	170.00	128.00	216.00	59.00	63.00
HD-4	5	Mean	2901.20	11094.00	506.20	260.60	159.00	141.20	105.20	172.80	36.00	73.80
		Median	3320.00	13100.00	502.00	261.00	179.00	142.00	111.00	192.00	36.00	72.00
		SD	1435.88	7484.96	56.96	10.97	37.19	5.40	10.64	38.64	6.12	6.69
		Min	606.00	2630.00	429.00	246.00	104.00	134.00	89.00	111.00	27.00	65.00
		Max	4140.00	18900.00	589.00	273.00	194.00	148.00	115.00	202.00	44.00	81.00
HD-5	7	Mean	17100.00	29471.40	459.00	261.00	177.71	150.71	121.00	198.86	44.71	77.71
		Median	16300.00	24900.00	447.00	248.00	179.00	155.00	121.00	203.00	43.00	13.67
		SD	4029.47	14465.20	69.77	54.41	19.02	12.83	5.63	18.55	6.16	75.00
		Min	12100.00	13300.00	379.00	217.00	147.00	126.00	113.00	173.00	39.00	62.00
		Max	22700.00	48500.00	602.00	376.00	206.00	163.00	127.00	223.00	57.00	104.00
HD-6	11	Mean	12743.60	27112.70	561.27	274.18	195.46	152.55	118.73	218.64	45.36	71.27
		Median	8430.00	22400.00	579.00	262.00	186.00	142.00	113.00	207.00	43.00	72.00
		SD	8115.64	24657.60	122.85	98.79	29.47	46.49	30.06	52.68	11.26	11.92
		Min	1650.00	3610.00	365.00	141.00	172.00	116.00	81.00	149.00	33.00	49.00
		Max	25800.00	64500.00	800.00	537.00	275.00	285.00	197.00	346.00	75.00	95.00